A search for sparticles in zero lepton final states

Russell W. Smith

Submitted in partial fulfillment of the
requirements for the degree of
Doctor of Philosophy
in the Graduate School of Arts and Sciences

COLUMBIA UNIVERSITY
2016

ABSTRACT

A search for sparticles in zero lepton final states

Russell W. Smith

TODO : Here's where your abstract will eventually go. The above text is all in the center, but the abstract itself should be written as a regular paragraph on the page, and it should not have indentation. Just replace this text.

Contents

Contents **i**

1 Introduction **1**

2 The Standard Model **5**

2.1 Overview 5

2.2 Field Content 5

2.3 Deficiencies of the Standard Model 15

3 Supersymmetry **21**

3.1 Supersymmetric theories : from space to superspace 21

3.2 Minimally Supersymmetric Standard Model 24

3.3 Phenomenology 30

3.4 How SUSY solves the problems with the SM 32

3.5 Conclusions 34

4 The Large Hadron Collider **37**

4.1 Basics of Accelerator Physics 37

4.2 Accelerator Complex 40

4.3 Large Hadron Collider 41

4.4 Dataset Delivered by the LHC 43

5 The ATLAS detector **49**

5.1 Magnets 50
5.2 Inner Detector 52
5.3 Calorimetry 56
5.4 Muon Spectrometer 61
5.5 Trigger System 66

6 Object Reconstruction 73
6.1 Primitive Object Reconstruction 73
6.2 Physics Object Reconstruction and Quality Identification 79

7 Recursive Jigsaw Reconstruction 105
7.1 Razor variables 105
7.2 Recursive Jigsaw Reconstruction 110
7.3 Variables used in the search for zero lepton SUSY 116

8 A search for supersymmetric particles in zero lepton final states with the Recursive Jigsaw Technique 123
8.1 Simulation samples 123
8.2 Event selection 125
8.3 Background estimation 132

9 Results 159
9.1 Signal region distributions 159
9.2 Systematic Uncertainties 162
9.3 Limits and Model-dependent Exclusions 164

Conclusion 171
9.4 New Section 171

Bibliography 173

Additional N-1 plots **187**

Compressed region N-1 plots 187

Acknowledgements

Dedication

Chapter 1

Introduction

Particle physics is a remarkably successful field of scientific inquiry. The ability to precisely predict the properties of a exceedingly wide range of physical phenomena, such as the description of the cosmic microwave background [1, 2], the understanding of the anomalous magnetic dipole moment of the electron [3, 4], and the measurement of the number of weakly-interacting neutrino flavors [5] is truly amazing.

The theory that has allowed this range of predictions is the *Standard Model* of particle physics (SM). The Standard Model combines the electroweak theory of Glashow, Weinberg, and Salam [6–8] with the theory of the strong interactions, as first envisioned by Gell-Mann and Zweig [9, 10]. This quantum field theory (QFT) contains a number of particles, whose interactions describe phenomena up to the TeV scale. These particles are manifestations of the fields of the Standard Model, after application of the Higgs Mechanism. The particle content of the SM consists only of six quarks, six leptons, four gauge bosons, and a scalar Higgs boson.

The Standard Model has some theoretical and experimental deficiencies. The SM contains 26 free parameters [1]. We would like to understand these free parameters in terms of a more fundamental theory.

The major theoretical concern of the Standard Model, as it pertains to this thesis, is the *hierachy problem* [11–15]. The light mass of the Higgs boson (125 GeV) should be quadratically dependent on the scale of UV physics, due to the quantum corrections

[1] This is the Standard Model corrected to include neutrino masses. These parameters are the fermion masses (6 leptons, 6 quarks), CKM and PMNS mixing angles (8 angles, 2 CP-violating phases), W/Z/Higgs masses (3), the Higgs field expectation value, and the couplings of the strong, weak, and electromagnetic forces (3 α_{force}) .

from high-energy physics processes. The most perplexing experimental issue is the existence of *dark matter*, as demonstrated by galactic rotation curves [16–22]. This data has shown that there exists additional matter which has not yet been seen interacting with the particles of the Standard Model. There is no particle in the SM which can act as a candidate for dark matter.

Both of these major issues, as well as numerous others, can be solved by the introduction of *supersymmetry* (SUSY) [15, 23–35]. In supersymmetric theories, each SM particles has a so-called *superpartner*, or sparticle partner, differing from given SM particle by 1/2 in spin. These theories solve the hierachy problem, since the quantum corrections induced from the superpartners exactly cancel those induced by the SM particles. In addition, these theories are usually constructed assuming $R-$parity, which can be thought of as the "charge" of supersymmetry, with SM particles having $R = 1$ and sparticles having $R = -1$. In collider experiments, since the incoming SM particles have total $R = 1$, the resulting sparticles are produced in pairs. This produces a rich phenomenology, which is characterized by significant hadronic activity and large missing transverse energy ($E_{\mathrm{T}}^{\mathrm{miss}}$), which provide significant discrimination against SM backgrounds [36].

Despite the power of searches for supersymmetry where $E_{\mathrm{T}}^{\mathrm{miss}}$ is a primary discriminating variable, there has been significant interest in the use of other variables to discriminate against SM backgrounds. These include searches employing variables such as α_T, $M_{T,2}$, and the razor variables (M_R, R^2) [37–47]. In this thesis, we will present the first search for supersymmetry using the novel Recursive Jigsaw Reconstruction (RJR) technique. RJR can be considered the conceptual successor of the razor variables. We impose a particular final state "decay tree" on an events, which roughly corresponds to a simplified Feynmann diagram in decays containing weakly-interacting particles. We account for the missing degrees of freedom associated with weakly-interacting particles by a series of simplifying assumptions, which allow us to calculate our variables of interest at each step in the decay tree. This allows an unprecedented understanding of the internal structure of the decay and additional variables to reject Standard Model backgrounds.

This thesis describes a search for the superpartners of the gluon and quarks, the gluino and squarks, in final states with zero leptons, with 13.3 fb^{-1} of data using the ATLAS detector. We organize the thesis as follows. The theoretical foundations of the Standard Model and supersymmetry are described in Chapters 2 and 3. The Large Hadron Collider and the ATLAS detector are presented in Chapters 4 and 5. The reconstruction of physics objects is presented in Chapter 6. Chapter 7 provides a detailed description of Recursive Jigsaw Reconstruction and a description of the variables used for the particular search presented in this thesis. Chapter 8 presents the details of the analysis, including details of the dataset, object reconstruction, and selections used. In Chapter 9, the final results are presented; since there is no evidence for a supersymmetric signal in the analysis, we present the final exclusion curves in simplified supersymmetric models.

Chapter 2

The Standard Model

2.1 Overview

The Standard Model (SM) is another name for a theory of the internal symmetry group $SU(3)_C \otimes SU(2)_L \otimes U(1)_Y$ and its associated set of parameters. The SM is the culmination of years of work in both theoretical and experimental particle physics. In this thesis, we take the view that theorists construct a model with the field content and symmetries as inputs, and write down the most general Lagrangian consistent with those symmetries. Assuming this model is compatible with nature (in particular, the predictions of the model are consistent with previous experiments), experimentalists are responsible for testing the parameters by measurements.

Additional theoretical background is in **??**. The philosophy and notations are inspired by [48, 49].

2.2 Field Content

The Standard Model field content is

$$\begin{aligned} \text{Fermions} &: Q_L(3,2)_{+1/3}, U_R(3,1)_{+4/3}, D_R(3,1)_{-2/3}, L_L(1,2)_{-1}, E_R(1,1)_{-2} \\ \text{Scalar (Higgs)} &: \phi(1,2)_{+1} \\ \text{Vector Fields} &: G^\mu(8,1)_0, W^\mu(1,3)_0, B^\mu(1,1)_0 \end{aligned} \tag{2.1}$$

where the $(A,B)_Y$ notation represents the irreducible representation under $SU(3)$ and $SU(2)$, with Y being the electroweak hypercharge. Each of these fermion fields has an additional index, representing the three generation of fermions.

We observed that Q_L, U_R, and D_R are triplets under $SU(3)_C$; these are the *quark* fields. The *color* group, $SU(3)_C$ is mediated by the *gluon* field $G^\mu(8,1)_0$, which has 8 degrees of freedom. The fermion fields $L_L(1,2)_{-1}$ and $E_R(1,1)_{-2}$ are singlets under $SU(3)_C$; we call them the *lepton* fields.

Next, we note the "left-handed" ("right-handed") fermion fields, denoted by L (R) subscript, The left-handed fields form doublets under $SU(2)_L$. These are mediated by the three degrees of freedom of the "W" fields $W^\mu(1,3)_0$. These fields only act on the left-handed particles of the Standard Model. This is the reflection of the "chirality" of the Standard Model The left-handed and right-handed particles are treated differently by the electroweak forces. The right-handed fields, U_R, D_R, and E_R, are singlets under $SU(2)_L$.

The $U(1)_Y$ symmetry is associated to the $B^\mu(1,1)_0$ boson with one degree of freedom. The charge Y is known as the electroweak hypercharge.

To better understand the phenomenology of the Standard Model, let us investigate each of the *sectors* of the Standard Model separately.

Electroweak sector

The electroweak sector refers to the $SU(2)_L \otimes U(1)_Y$ portion of the Standard Model gauge group. Following our philosophy of writing all gauge-invariant and renormalizable terms, the electroweak Lagrangian can be written as

$$\mathcal{L} = W_a^{\mu\nu} W^a_{\mu\nu} + B^{\mu\nu} B_{\mu\nu} + (D^\mu \phi)^\dagger D_\mu \phi - \mu^2 \phi^\dagger \phi - \lambda(\phi^\dagger \phi)^2. \tag{2.2}$$

where $W_a^{\mu\nu}$ are the three ($a = 1, 2, 3$) gauge bosons associated to the $SU(2)_L$ gauge group, $B^{\mu\nu}$ is the one gauge boson of the $U(1)_Y$ gauge group, and ϕ is the complex Higgs multiplet. The covariant derivative D^μ is given by

$$D^\mu = \partial^\mu + \frac{ig}{2} W_a^\mu \sigma_a + \frac{ig'}{2} B^\mu \tag{2.3}$$

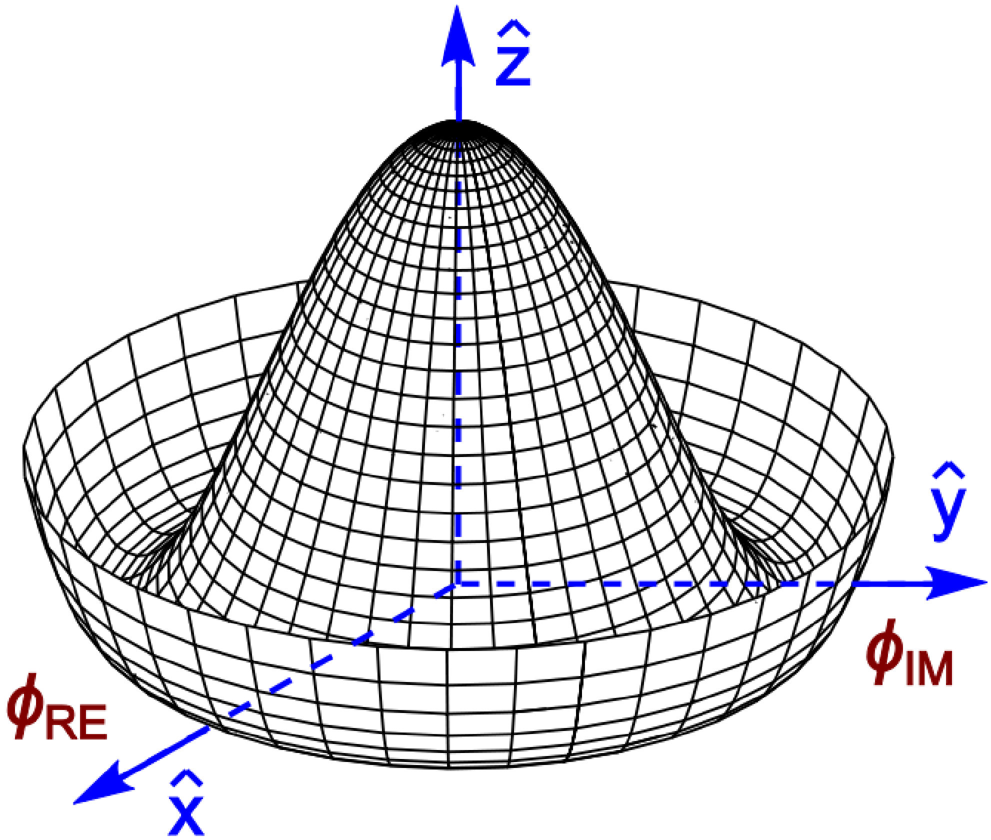

Figure 2.1: Sombrero potential

where $i\sigma_a$ are the Pauli matrices times the imaginary constant, which are the generators for $SU(2)_L$, and g and g' are the $SU(2)_L$ and $U(1)_Y$ coupling constants, respectively. The field strength tensors $W_a^{\mu\nu}$ and $B^{\mu\nu}$ are given by the commutator of the covariant derivative associated to each field

$$\begin{aligned} B^{\mu\nu} &= \partial^\mu B^\nu - \partial^\nu B^\mu \\ W_a^{\mu\nu} &= \partial^\mu W_a^\nu - \partial^\nu W_a^\mu - g\epsilon_{abc} W_a^\mu W_b^\nu, \qquad i = 1, 2, 3 \end{aligned} \tag{2.4}$$

The terms in the Lagrangian Eq. (2.2) proportional to μ^2 and λ make up the "Higgs potential" [50]. As normal (see Appendix **??**), we restrict $\lambda > 0$ to guarantee our potential is bounded from below, and we also require $\mu^2 < 0$, which gives us the standard "sombrero" potential shown in Fig. 2.1.

This potential has infinitely many minima at $<\phi>=\sqrt{2m/\lambda}$ The ground state is *spontaneously* broken by the choice of ground state, which induces a vacuum expection value (VEV). Without loss of generality, we can choose the Higgs field ϕ to point in the real direction, and write the Higgs field ϕ in the following form :

$$\phi = \frac{1}{\sqrt{2}} \exp(\frac{i}{v}\sigma_a\theta_a) \begin{pmatrix} 0 \\ v + h(x) \end{pmatrix}. \tag{2.5}$$

We choose a gauge to rotate away the dependence on θ_a, such that we can write simply

$$\phi = \frac{1}{\sqrt{2}} \begin{pmatrix} 0 \\ v + h(x) \end{pmatrix}. \tag{2.6}$$

Now, we can see how the masses of the vector bosons are generated from the application of the Higgs mechanism. We plug Eq.Eq. (2.6) back into the electroweak Lagrangian, and only showing the relevant mass terms in the vacuum state where $h(x) = 0$ see that (dropping the Lorentz indices) :

$$\begin{aligned} \mathcal{L}_M &= \frac{1}{8} \left| \begin{pmatrix} gW_3 + g'B & g(W_1 - iW_2) \\ g(W_1 + iW_2) & -gW_3 + g'B \end{pmatrix} \begin{pmatrix} 0 \\ v \end{pmatrix} \right|^2 \\ &= \frac{g^2v^2}{8} \left[W_1^2 + W_2^2 + (\tfrac{g'}{g}B - W_3)^2 \right] \end{aligned} \tag{2.7}$$

Defining the *Weinberg* angle $\tan(\theta_W) = g'/g$ and the following *physical* fields :

$$\begin{aligned} W^{\pm} &= \frac{1}{\sqrt{2}}(W_1 \mp iW_2) \\ Z^0 &= \cos\theta_W W_3 - \sin\theta_W B \\ A^0 &= \sin\theta_W W_3 + \cos\theta_W B \end{aligned} \tag{2.8}$$

we can write the piece of the Lagrangian associated to the vector boson masses as

$$\mathcal{L}_{M_V} = \frac{1}{4}g^2v^2W^+W^- + \frac{1}{8}(g^2 + g'^2)v^2Z^0Z^0. \tag{2.9}$$

and we have the following values of the masses for the vector bosons :

$$\begin{aligned} m_W^2 &= \frac{1}{4}v^2 g^2 \\ m_Z^2 &= \frac{1}{4}v^2(g^2+g'^2) \\ m_A^2 &= 0 \end{aligned} \tag{2.10}$$

We thus see how the Higgs mechnanism gives rise to the masses of the $W^{\pm}$ and Z boson in the Standard Model. As expected, the mass of the photon is zero. The $SU(2)_L \otimes U(1)_Y$ symmetry of the initially massless $W_{1,2,3}$ and B fields is broken to the $U(1)_{EM}$. Of the four degrees of freedom in the complex Higgs doublet, three are "eaten" when we give mass to the $W^{\pm}$ and Z_0, while the other degree of freedom is the Higgs particle, as discover in 2012 by the ATLAS and CMS collaborations [51, 52].

Quantum Chromodynamics

Quantum chromodynamics (or the theory of the *strong* force) characterizes the behavior of *colored* particles, collectively known as *partons*. The partons of the Standard Model are the (fermionic) quarks, and the (bosonic) gluons. The strong force is governed by $SU(3)_C$, an unbroken symmetry in the Standard Model, which implies the gluon remains massless. Defining the covariant derivative for QCD as

$$D^\mu = \partial^\mu + i g_s G_a^\mu L_a, a = 1, ..., 8 \tag{2.11}$$

where L_a are the generators of $SU(3)_C$, and g_s is the coupling constant of the strong force. The QCD Lagrangian then is given by

$$\mathcal{L}_{\text{QCD}} = i\bar{\psi}_f D_\mu \gamma^\mu \psi_f - \frac{1}{4} G_{a,\mu\nu} G_a^{\mu\nu} \tag{2.12}$$

where the summation over f is for quarks *families*, and $G_a^{\mu\nu}$ is the gluon field strength tensor, given by

$$G_a^{\mu\nu} = \partial^\mu G_a^\nu - \partial^\nu G_a^\mu - g_s f^{abc} G_b^\mu G_c^\nu, a, b, c = 1, ..., 8 \tag{2.13}$$

where f^{abc} are the structure constants of $SU(3)_C$, which are analogous to ϵ_{abc} for $SU(2)_L$. The kinetic term for the quarks is contained in the standard ∂_μ term, while the field strength term contains the interactions between the quarks and gluons, as well as the gluon self-interactions.

Written down in this simple form, the QCD Lagrangian does not seem much different from the QED Lagrangian, with the proper adjustments for the different group structures. The gluon is massless, like the photon, so one could näively expect an infinite range force, and it pays to understand why this is not the case. The reason for this fundamental difference is the gluon self-interactions arising in the field strength tensor term of the Lagrangian. This leads to the phenomena of *color confinement*, which describes how one only observes color-neutral particles alone in nature. In contrast to the electromagnetic force, particles which interact via the strong force experience a *greater* force as the distance between the particles increases. At long distances, the potential is given by $V(r) = -kr$. At some point, it is more energetically favorable to create additional partons out of the vacuum than continue pulling apart the existing partons, and the colored particles undergo *fragmentation*. This leads to *hadronization*. Bare quarks and gluons are actually observed as sprays of hadrons (primarly kaons and pions). These sprays are known as *jets*, which are what are observed by experiments.

It is important to recognize the importance of understanding these QCD interactions in high-energy hadron colliders such as the LHC. Since protons are hadrons, proton-proton collisions such as those produced by the LHC are primarily governed by the processes of QCD. In particular, by far the most frequent process observed in LHC experiments is dijet production from gluon-gluon interactions, as can be seen Fig. 2.2). These gluons that interact are part of the *sea* particles inside the proton; the simple $p = uud$ model does not apply. The main *valence uud* quarks are constantly interacting via gluons, which can themselves radiate gluons or split into quarks, and

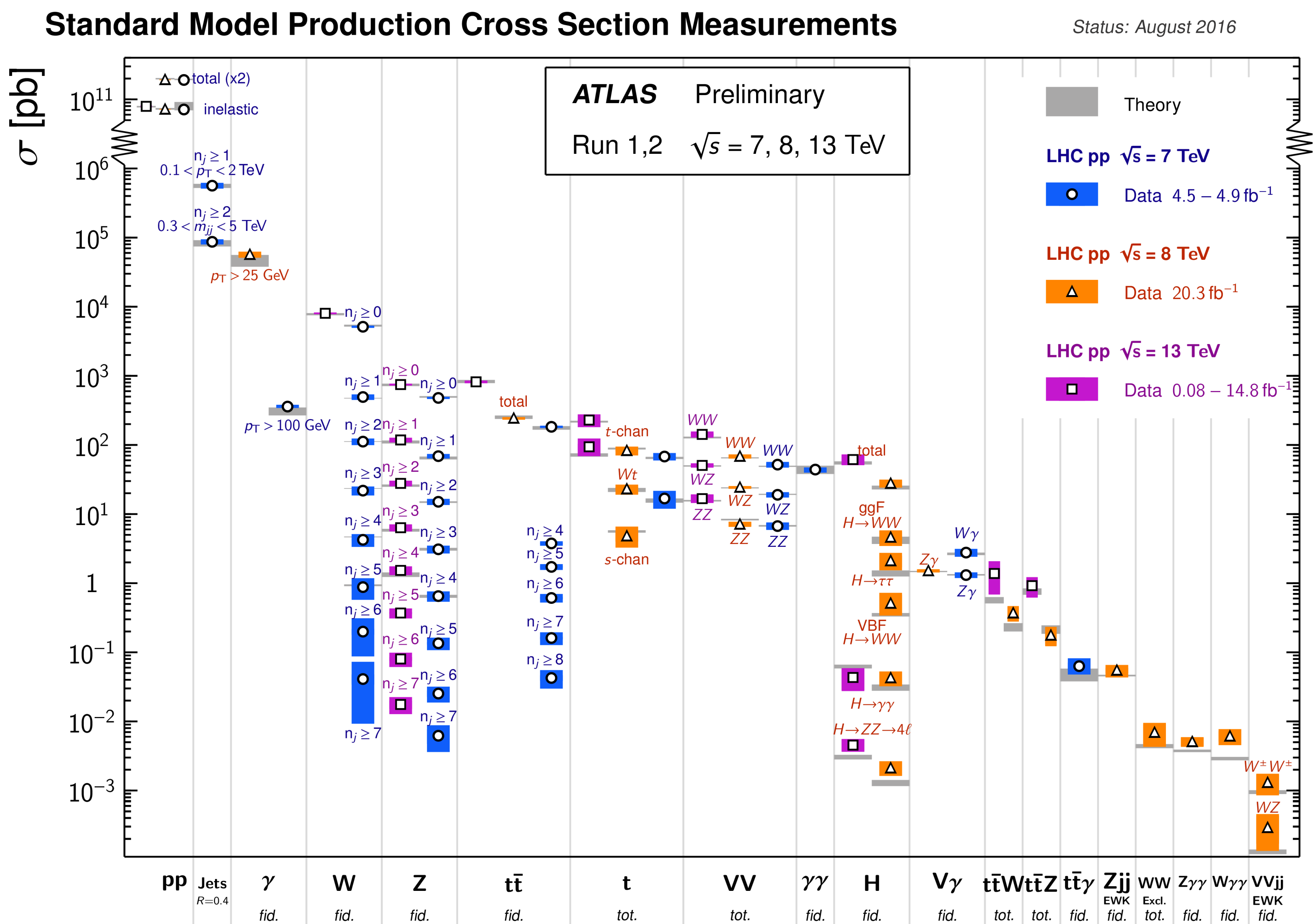

Figure 2.2: Cross-sections of various Standard Model processes

so on. A more useful understanding is given by the colloquially-known *bag* model [53, 54], where the proton is seen as a "bag" of (in principle) infinitely many partons, each with energy $E < \sqrt{s} = 6.5$ TeV. One then collides this (proton) bag with another, and views the products of this very complicated collision, where calculations include many loops in nonpertubative QCD calculations.

Fortunately, we are generally saved by the QCD factorization theorems [55]. This allows one to understand the hard (i.e. short distance or high energy) $2 \to 2$ parton process using the tools of perturbative QCD, while making series of approximations known as a *parton shower* model to understand the additional corrections from nonpertubative QCD. We will discuss the reconstruction of jets by experiments in Ch. 6.

Fermions

We will now look more closely at the fermions in the Standard Model [56].

As noted earlier in Sec. 2.2, the fermions of the Standard Model can be first distinguished between those that interact via the strong force (quarks) and those which do not (leptons).

There are six leptons in the Standard Model, which can be placed into three *generations*.

$$\begin{pmatrix} e \\ \nu_e \end{pmatrix}, \begin{pmatrix} \mu \\ \nu_\mu \end{pmatrix}, \begin{pmatrix} \tau \\ \nu_\tau \end{pmatrix} \tag{2.14}$$

There is the electron (e), muon (μ), and tau (τ), each of which has an associated neutrino (ν_e, ν_μ, ν_τ). Each of the so-called charged ("electron-like") leptons has electromagnetic charge -1, while the neutrinos all have $q_{EM} = 0$.

Often in an experimental context, lepton is used to denote the stable electron and metastable muon, due to their striking experimental signatures. Taus are often treated separately, due to their much shorter lifetime of $\tau_\tau \sim 10^{-13}s$. These decay through hadrons or the other leptons, so often physics analyses at the LHC treat them as jets or leptons, as will be done in this thesis.

As the neutrinos are electrically neutral, nearly massless, and only interact via the weak force, it is quite difficult to observe them directly. Since LHC experiments rely overwhelmingly on electromagnetic interactions to observe particles, the presence of neutrinos is not observed directly. Neutrinos are instead observed by the conservation of four-momentum in the plane transverse to the proton-proton collisions, known as *missing transverse energy*.

There are six quarks in the Standard Model : up, down, charm, strange, top, and bottom. Quarks are similar organized into three generations :

$$\begin{pmatrix} u \\ d \end{pmatrix}, \begin{pmatrix} c \\ s \end{pmatrix}, \begin{pmatrix} t \\ b \end{pmatrix} \tag{2.15}$$

where we speak of "up-like" quarks and "down-like" quarks.

Each up-like quark has charge $q_{up} = 2/3$, while the down-like quarks have $q_{down} = -1/3$. At the high energies of the LHC, one often makes the distinction between the light quarks (u, d, c, s), the bottom quark, and top quark. In general, due to the hadronization process described above, the light quarks, with masses $m_q <\sim 1.5$ GeV are indistinguishable by LHC experiments. Their hadronic decay products generally have long lifetimes and they are reconstructed as jets.[1]. The bottom quark hadronizes primarily through the B-mesons, which generally travels a short distance before decaying to other hadrons. This allows one to distinguish decays via b-quarks from other jets. This procedure is known as *b-tagging* and will be discussed more in Ch.Ch. 5.

Due to its large mass, the top quark decays before it can hadronize. There are no bound states associated to the top quark. The top is of particular interest at

[1]In some contexts, charm quarks are also treated as a separate category, although it is quite difficult to distinguish charm quarks from the other light quarks at high enery colliders.

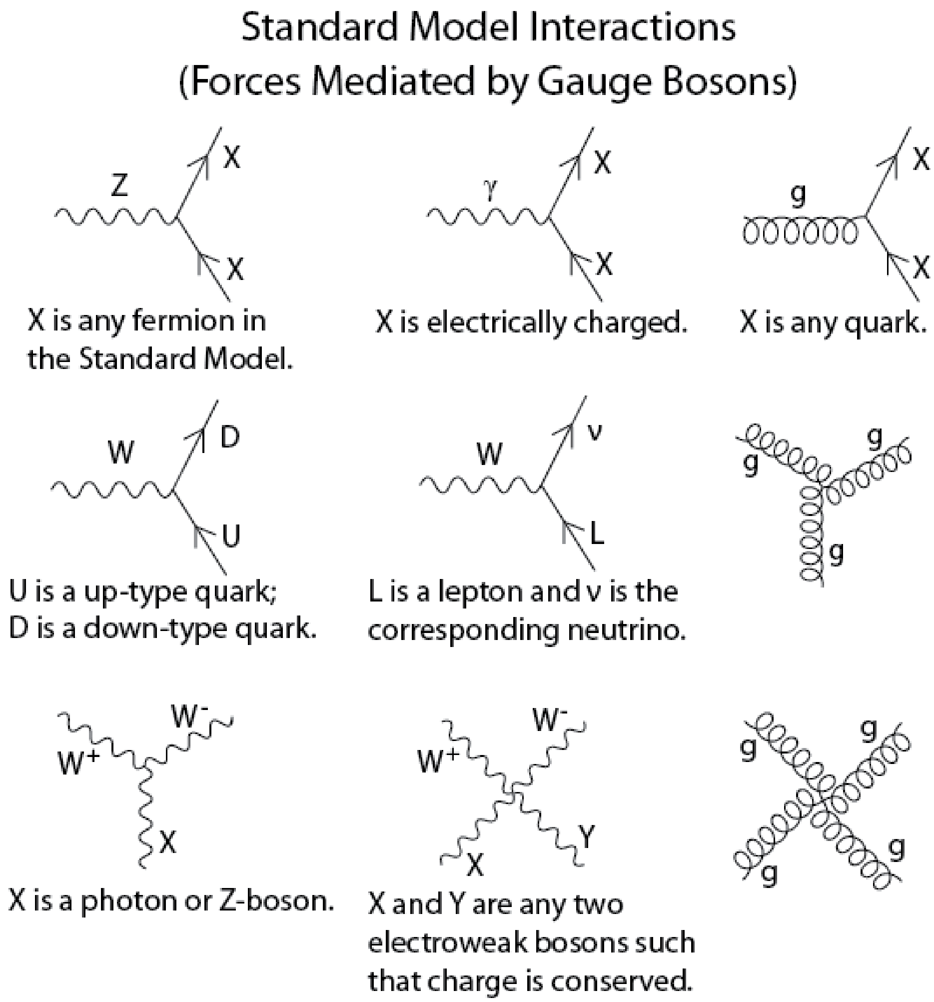

Figure 2.3: The interactions of the Standard Model

the LHC; it has a striking signature through its most common decay mode $t \to Wb$. Decays via tops, especially $t\bar{t}$ are frequently an important signal decay mode, or an important background process.

Interactions in the Standard Model

We briefly overview the entirety of the fundamental interactions of the Standard Model. These can also be found in Fig. 2.3.

The electromagnetic force, mediated by the photon, interacts with via a three-point coupling all charged particles in the Standard Model. The photon thus interacts with all the quarks, the charged leptons, and the charged $W^{\pm}$ bosons.

The weak force is mediated by three particles : the $W^{\pm}$ and the Z^0. The Z^0 can interacts with all fermions via a three-point coupling. A real Z_0 can thus decay to a fermion-antifermion pair of all SM fermions except the top quark, due to its large mass. The $W^{\pm}$ has two important three-point interactions with fermions. First, the $W^{\pm}$ can interact with an up-like quark and a down-like quark; an important example in LHC experiments is $t \to Wb$ The coupling constants for these interactions are encoded in the unitary matrix known as the Cabibbo–Kobayashi–Maskawa (CKM) matrix [57, 58], and are generally known as flavor-changing interactions. Secondly, the $W^{\pm}$ interacts with a charged lepton and its corresponding neutrino. In this case, the unitary matrix that corresponds to CKM matrix for quarks is the identity matrix, which forbids (fundamental) vertices such as $\mu \to We$. For leptons, instead this is a two-step process : $\mu \to \nu_m uW \to \nu_m u\bar{\nu_e}e$. Finally, there are the self-interactions of the weak gauge bosons. There is a three-point and four-point interaction. All combinations are allowed which conserve electric charge.

The strong force is mediated by the gluon, which as discussed above also carries the strong color charge. There is the fundamental three-point interaction, where a quark radiates a gluon. Additionally, there are the three-point and four-point gluon-only interactions.

2.3 Deficiencies of the Standard Model

The Standard Model has been enormously successful. This relatively simple theory is capable of explaining a very wide range of phenomenom, which ultimately break down to combinations of nine diagrams shown in Fig. 2.3 at tree level. Unfortunately, there are some unexplained problems with the Standard Model. We cannot go through all

m_e	Electron mass	511 keV
m_μ	Muon mass	105.7 MeV
m_τ	Tau mass	1.78 GeV
m_u	Up quark mass	1.9 MeV ($m_{\bar{M}S} = 2GeV$)
m_d	Down quark mass	4.4 MeV ($m_{\bar{M}S} = 2GeV$)
m_s	Strange quark mass	87 MeV ($m_{\bar{M}S} = 2GeV$)
m_c	Charm quark mass	1.32 GeV ($m_{\bar{M}S} = m_c$)
m_b	Bottom quark mass	4.24 GeV ($m_{\bar{M}S} = m_b$)
m_t	Top quark mass	172.7 GeV (on-shell renormalization)
θ_{12} CKM	12-mixing angle	13.1°
θ_{23} CKM	23-mixing angle	2.4°
θ_{13} CKM	13-mixing angle	0.2°
δ CKM	CP-violating Phase	0.995
g'	U(1) gauge coupling	0.357 ($m_{\bar{M}S} = m_Z$)
g	SU(2) gauge coupling	0.652 ($m_{\bar{M}S} = m_Z$)
g_s	SU(3) gauge coupling	1.221 ($m_{\bar{M}S} = m_Z$)
θQCD	QCD vacuum angle	∼0
VEV	Higgs vacuum expectation value	246 GeV
m_H	Higgs mass	125 GeV

Table 2.1: Parameters of the Standard Model. For values dependent on the renormalization scheme, we use a combination of the on-shell normalization scheme [59–62] and modified minimal subtraction scheme with $m_{\bar{M}S}$ as indicated in the table [63]

of the potential issues in this thesis, but we will motivate the primary issues which naturally lead one to *supersymmetry*, as we will see in Ch. 3.

The Standard Model has many free paramaters, shown in Tab. 2.1. In general, we prefer models with less free parameters. A great example of this fact, and the primary experimental evidence for EWSB, is the relationship between the couplings of the weak force and the masses of the gauge bosons of the weak force :

$$\rho \equiv \frac{m_W^2}{m_Z^2 \cos^2 \theta_W} \stackrel{?}{=} 1 \tag{2.16}$$

where ? indicates that this is a testable prediction of the Standard Model (in particular, that the gauge bosons gain mass through EWSB). This relationship has been measured within experimental and theoretical predictions. We would like to produce additional such relationships, which would exist if the Standard Model is a

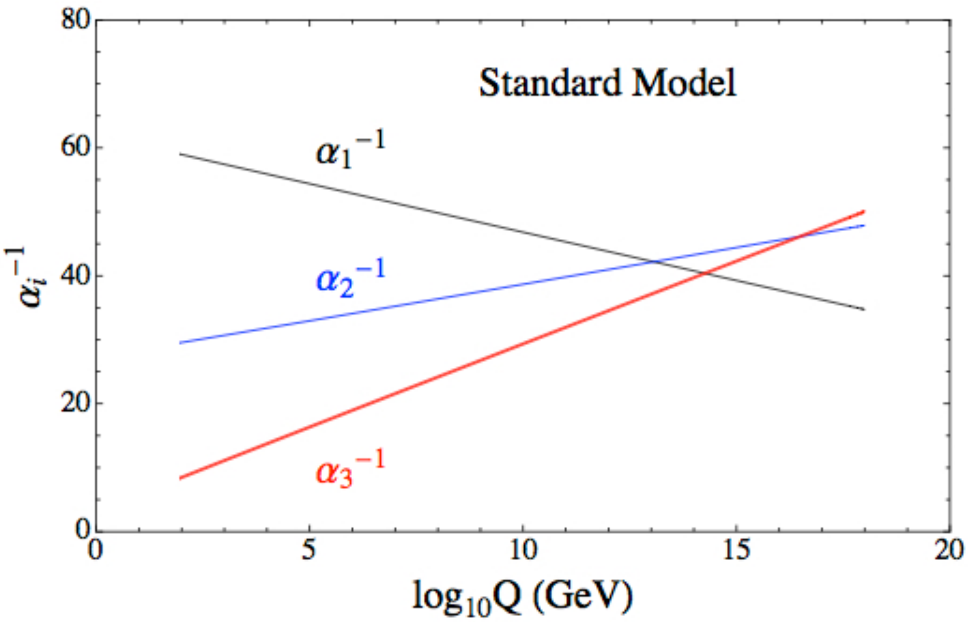

Figure 2.4: The running of Standard Model gauge couplings. The Standard Model couplings do not unify at high energies, which indicates it cannot completely describe nature through the Planck scale.

low-energy approximation of some other theory.

An additional issue is the lack of *gauge coupling unification*. The couplings of any quantum field theory "run" as a function of the distance scales (or inversely, energy scales) of the theory. The idea is closely related to the unification of the electromagnetic and weak forces at the so-called *electroweak scale* of $O(100\text{ GeV})$. One would hope this behavior was repeated between the electroweak forces and the strong force at some suitable energy scale. The Standard Model does not exhibit this behavior, as we can see in Fig. 2.4.

But, the most significant problem with the Standard Model is the *hierarchy problem*. In its most straightforward incarnation, the Higgs scalar field is subject to quantum corrections through loop diagrams, as shown in Fig. 2.5. For demonstration, we use the contributions from the top quark, since the top quark has the largest Higgs Yukawa coupling due to its large mass. In general, we should expect these corrections to quadratically dependent on the scale of the ultraviolet physics, Λ. Briefly assume

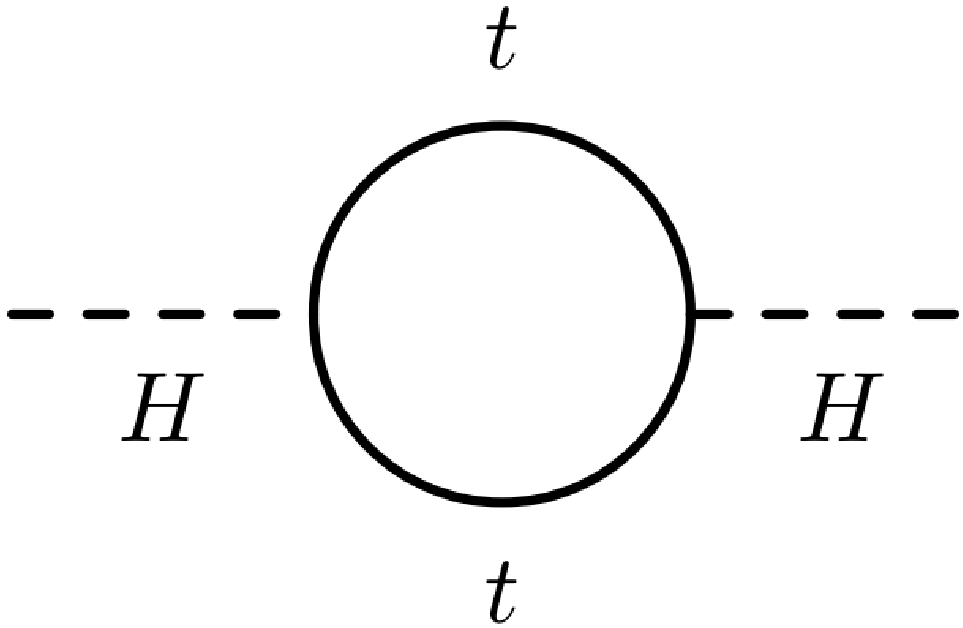

Figure 2.5: The dominant quantum loop correction to the Higgs mass in the Standard Model.

there is no new physics before the Planck scale of gravity, $\Lambda_{\text{Planck}} = 10^{19}$ GeV. In this case, we expect the corrections to the Higgs mass to be

$$\delta m_H^2 \approx \left(\frac{m_t}{8\pi^2 < \phi >_{VEV}}\right)^2 \Lambda_{Planck}^2. \tag{2.17}$$

To achieve the miraculous cancellation required to get the observed Higgs mass of 125 GeV, one needs to then set the bare Higgs mass m_0, our input to the Standard Model Lagrangian, itself to a *precise* value $\sim 10^{19}$ GeV. This extraordinary level of parameter finetuning is quite undesirable, and within the framework of the Standard Model alone, there is little that can be done to alleviate this issue.

An additional concern, of a different nature, is the lack of a *dark matter* candidate in the Standard Model. Dark matter was discovered by observing galactic rotation curves, which showed that much of the matter that interacts gravitionally is invisible to our (electromagnetic) telescopes [16–22]. The postulation of the existence of dark matter, which interacts at least through gravity, allows one to understand these galatic

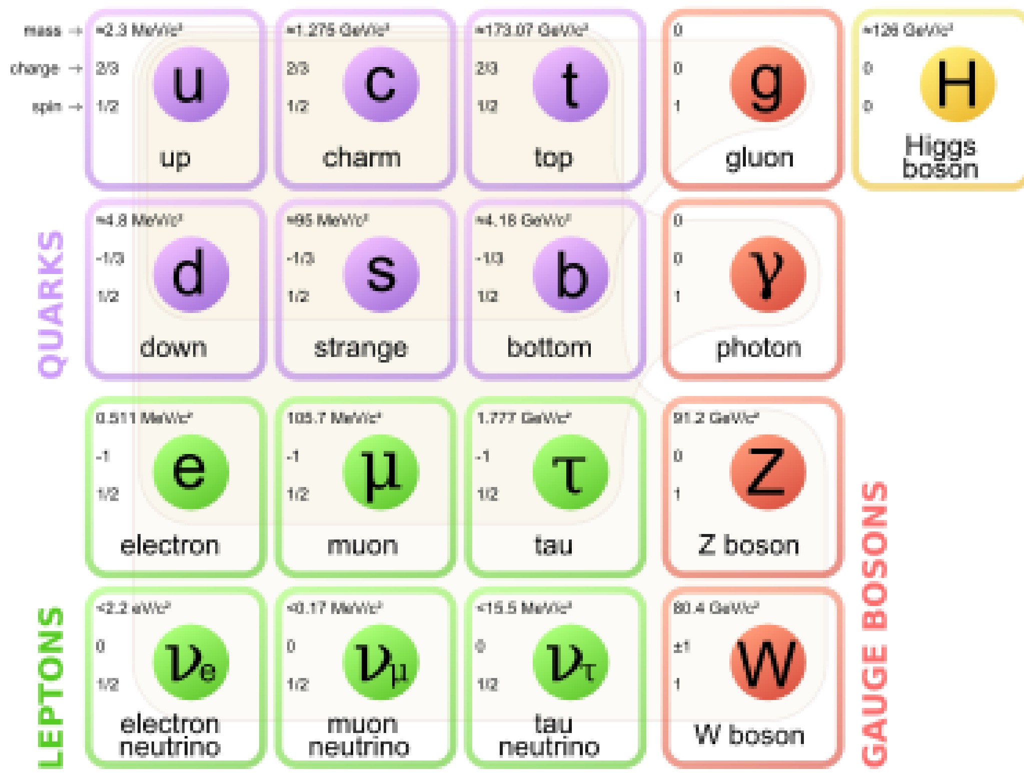

Figure 2.6: Particles of the Standard Model

rotation curves. Unfortunately, no particle in the Standard Model could possibly be the dark matter particle. The only candidate truly worth another look is the neutrino, but it has been shown that the neutrino content of the universe is simply too small to explain the galatic rotation curves [22, 64]. The experimental evidence from the galactic rotations curves thus show there *must* be additional physics beyond the Standard Model, which is yet to be understood.

In the next chapter, we will see how these problems can be alleviated by the theory of supersymmetry.

Chapter 3

Supersymmetry

This chapter will introduce supersymmetry (SUSY) [15, 23–35]. We will begin by introducing the concept of a *superspace*, and discuss some general ingredients of supersymmetric theories. This will include a discussion of how the problems with the Standard Model described in Ch. 2 are naturally fixed by these theories.

The next step is to discuss the particle content of the *Minimally Supersymmetric Standard Model* (MSSM). As its name implies, this theory contains the minimal additional particle content to make Standard Model supersymmetric. We then discuss the important phenomonological consequences of this theory, especially as it would be observed in experiments at the LHC.

3.1 Supersymmetric theories : from space to superspace

Coleman-Mandula "no-go" theorem

We begin the theoretical motivation for supersymmetry by citing the "no-go" theorem of Coleman and Mandula [65]. This theorem forbids *spin-charge unification*. It states that all quantum field theories which contain nontrivial interactions must be a direct product of the Poincaré group of Lorentz symmetries, the internal product of gauge symmetries, and the discrete symmetries of parity, charge conjugation, and time reversal. The assumptions which go into building the Coleman-Mandula theorem are quite restrictive, but there is solution, which has become known as *supersymmetry* [26, 66]. In particular, we must introduce a *spinorial* group generator Q. Alternatively, and equivalently, this can be viewed as the addition of anti-commuting coordinates. Space plus these new anti-commuting coordinates is then called *superspace* [67]. We will not investigate this view in detail, but it is also a quite intuitive and beautiful way to construct supersymmetry [15].

Supersymmetry transformations

A *supersymmetric* transformation Q transforms a bosonic state into a fermionic state, and vice versa :

$$Q\,|\text{Fermion}\rangle = |\text{Boson}\rangle \tag{3.1}$$

$$Q\,|\text{Boson}\rangle = |\text{Fermion}\rangle \tag{3.2}$$

To ensure this relation holds, Q must be an anticommuting spinor. Additionally, since spinors are inherently complex, $Q^\dagger$ must also be a generator of the supersymmetry transformation. Since Q and $Q^\dagger$ are spinor objects (with $s = 1/2$), we can see that supersymmetry must be a spacetime symmetry. The Haag-Lopuszanski-Sohnius extension [66] of the Coleman-Mandula theorem [65] is quite restrictive about the forms of such a symmetry. Here, we simply write the (anti-) commutation relations [15] :

$$Q_\alpha, Q^\dagger_{\dot\alpha} = -2\sigma_{\alpha\dot\alpha^\mu} P_\mu \tag{3.3}$$

$$Q_\alpha, Q_{\dot\beta} = Q^\dagger_{\dot\alpha}, Q^\dagger_{\dot\beta} = 0 \tag{3.4}$$

$$[P^\mu, Q_\alpha] = [P^\mu, Q^\dagger_{\dot\alpha}] = 0 \tag{3.5}$$

Supermultiplets

In a supersymmetric theory, we organize single-particle states into irreducible representations of the supersymmetric algebra which are known as *supermultiplets*.

Each supermultiplet contains a fermion state $|\mathrm{F}\rangle$ and a boson state $|\mathrm{B}\rangle$ These two states are the known as *superpartners*. These are related by some combination of Q and $Q^\dagger$, up to a spacetime transformation. Q and $Q^\dagger$ commute with the mass-squared operator $-P^2$ and the operators corresponding to the gauge transformations [15]: in particular, the gauge interactions of the Standard Model. In an unbroken supersymmetric theory, this means the states $|\mathrm{F}\rangle$ and $|\mathrm{B}\rangle$ have exactly the same mass, electromagnetic charge, electroweak isospin, and color charges. One can also prove [15] that each supermultiplet contains the exact same number of bosonic (n_B) and fermion (n_F) degrees of freedom. We now explore the possible types of supermultiples one can find in a renormalizable supersymmetric theory.

Since each supermultiplet must contain a fermion state, the simplest type of supermultiplet contains a single Weyl fermion state ($n_F = 2$) which is paired with $n_B = 2$ scalar bosonic degrees of freedom. This is most conveniently constructed as single complex scalar field. We call this construction a *scalar supermultiplet* or *chiral supermultiplet*. The second name is indicative, as only chiral supermultiplets can contain fermions whose right-handed and left-handed components transform differently under the gauge interactions (as of course happens in the Standard Model).

The second type of supermultiplet we construct is known as a *gauge* supermultiplet. We take a spin-1 gauge boson (which must be massless due to the gauge symmetry, so $n_B = 2$) and pair this with a single massless Weyl spinor[1]. The gauge bosons transform as the adjoint representation of the their respective gauge groups Their fermionic partners, which are known as gauginos, must also. In particular, the left-handed and right-handed components of the gaugino fermions have the same gauge transformation properties.

Excluding gravity, this is the entire list of supermultiplets which can participate in renormalizable interactions in what is known as $N = 1$ supersymmetry. This

[1]Choosing an $s = 3/2$ massless fermion leads to nonrenormalizable interactions.

means there is only one copy of the supersymmetry generators Q and $Q^\dagger$. This is essentially the only "easy" phenomenological choice, since it is the only option in four dimensions which allows for the chiral fermions and parity violations to be built into the Standard Model. We will not look further into $N > 1$ supersymmtry in this thesis.

The primary goal, after understanding the possible structures of the multiplets above, is to fit the Standard Model particles into a multiplet, and therefore make predictions about their supersymmetric partners. We explore this in the next section.

3.2 Minimally Supersymmetric Standard Model

To construct what is known as the MSSM [15, 68–71], we need a few ingredients and assumptions. First, we match the Standard Model particles with their corresponding superpartners of the MSSM. We will also introduce the naming of the superpartners (also known as *sparticles*). We discuss a very common additional restraint imposed on the MSSM, known as $R-$parity. We also discuss the concept of soft supersymmetry breaking and how it manifests itself in the MSSM.

Chiral supermultiplets

The first thing we deduce is directly from Sec. 3.1. The bosonic superpartners associated to the quarks and leptons *must* be spin 0, since the quarks and leptons must be arranged in a chiral supermultiplet. This is essential, since the chiral supermultiplet is the only one which can distinguish between the left-handed and right-handed components of the Standard Model particles. The superpartners of the quarks and leptons are known as *squarks* and *sleptons*, or *sfermions* in aggregate. (for "scalar quarks", "scalar leptons", and "scalar fermion"). The "s-" prefix can also be added to the individual quarks i.e. *selectron*, *sneutrino*, and *stop*. The notation is to add a $\sim$ over the corresponding Standard Model particle i.e. $\tilde{e}$, the selectron is the superpartner of the electron. The two-component Weyl spinors of the Standard Model must each have their own (complex scalar) partner i.e. e_L, e_R have two distinct partners : $\tilde{e_L}, \tilde{e_R}$. As noted above, the gauge interactions of any of the sfermions are identical to those of their Standard Model partners.

Due to the scalar nature of the Higgs, it must obviously lie in a chiral supermultiplet. To avoid gauge anomolies and ensure the correct Yukawa couplings to the quarks and leptons [15], we must add additional Higgs bosons to any supersymmetric theory. In the MSSM, we have two chiral supermultiplets. The SM (SUSY) parts of the multiplets are denoted $H_u(\tilde{H}_u)$ and $H_d(\tilde{H}_d)$. Writing out H_u and H_d explicitly:

$$H_u = \begin{pmatrix} H_u^+ \\ H_u^0 \end{pmatrix} \tag{3.6}$$

$$H_d = \begin{pmatrix} H_d^0 \\ H_d^- \end{pmatrix} \tag{3.7}$$

we see that H_u looks very similar to the SM Higgs with $Y = 1$, and H_d is symmetric with $+ \to -$ and $Y = -1$. The SM Higgs boson, h_0, is a linear superposition of the neutral components of these two doublets. The SUSY parts of the Higgs multiplets, $\tilde{H}_u$ and $\tilde{H}_d$, are each left-handed Weyl spinors. For generic spin-1/2 sparticles, we add the "-ino" suffix. We then call the partners of the two Higgs collectively the *Higgsinos*.

Gauge supermultiplets

The superpartners of the gauge bosons must all be in gauge supermultiplets since they contain a spin-1 particle. Collectively, we refer to the superpartners of the gauge bosons as the gauginos.

The first gauge supermultiplet contains the gluon, and its superpartner, which is known as the *gluino*, denoted $\tilde{g}$. The gluon is of course the SM mediator of $SU(3)_C$

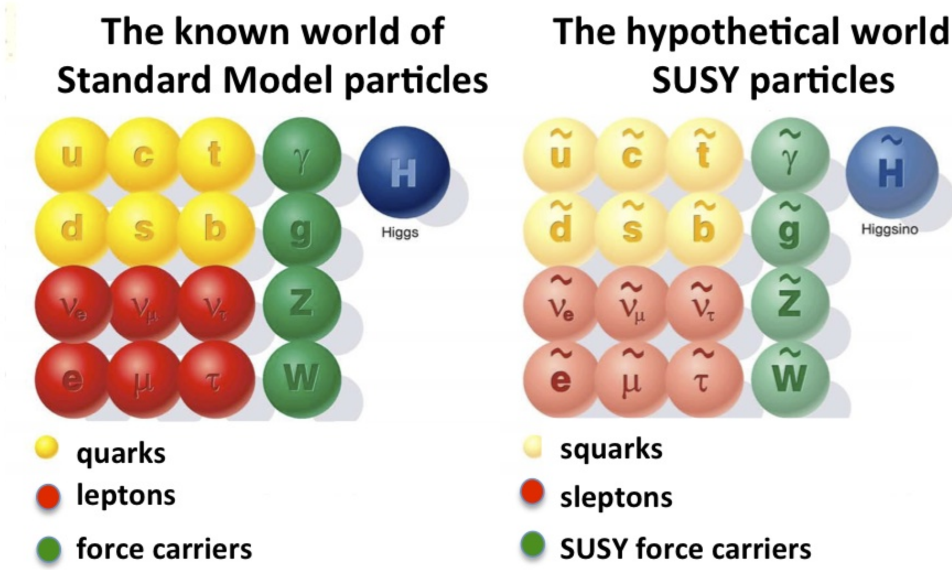

Figure 3.1: Particles of the MSSM

The gluino is also a colored particle, subject to $SU(3)_C$. From the SM before EWSB, we have the four gauge bosons of the electroweak symmetry group $SU(2)_L \otimes U(1)_Y$: $W^{1,2,3}$ and B^0. The superpartners of these particles are thus the *winos* $W^{\tilde{1},2,3}$ and *bino* $\tilde{B}^0$, where each is placed in another gauge supermultiplet with its corresponding SM particle. After EWSB, without breaking supersymmetry, we would also have the zino $\tilde{Z}^0$ and photino $\tilde{\gamma}$.

The entire particle content of the MSSM can be seen in Fig. 3.1.

At this point, it's important to take a step back. Where are these particles? As stated above, supersymmetric theories require that the masses and all quantum numbers of the SM particle and its corresponding sparticle are the same. Of course, we have not observed a selectron, squark, or wino. The answer, as it often is, is that supersymmetry is *broken* by the vacuum state of nature [15].

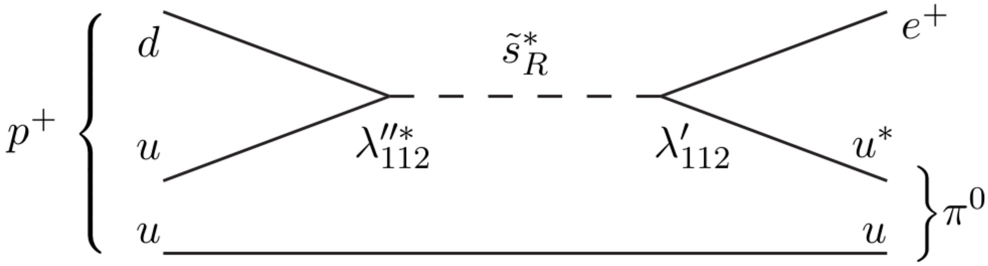

Figure 3.2: This Feynmann diagram shows how proton decay is induced in the MSSM, if one does not impose $R-$parity.

$R-$parity

This section is a quick aside to the general story. $R - parity$ refers to an additional discrete symmetry which is often imposed on supersymmetric models. For a given particle state, we define

$$R = (-1)^{3(B-L)+2s} \tag{3.8}$$

where B, L is the baryon (lepton) number and s is the spin. The imposition of this symmetry forbids certain terms from the MSSM Lagrangian that would violate baryon and/or lepton number. This is required in order to prevent proton decay, as shown in Fig. 3.2[2]. .

In supersymmetric models, this is a $\mathbb{Z}_2$ symmetry, where SM particles have $R = 1$ and sparticles have $R = -1$. We will take $R - parity$ as part of the definition of the MSSM. We will discuss later the *drastic* consequences of this symmetry on SUSY phenomenology

Soft supersymmetry breaking

The fundamental idea of *soft* supersymmetry breaking [15, 34, 35, 72, 73] is that we would like to break supersymmetry without reintroducing the quadratic divergences

[2]Proton decay can actually be prevented by allowing only one of the four potential R-parity violating terms to survive.

we discussed at the end of Chapter Ch. 2. We write the Lagrangian in a form :

$$\mathcal{L}_{\text{MSSM}} = \mathcal{L}_{\text{SUSY}} + \mathcal{L}_{\text{soft}} \tag{3.9}$$

In this sense, the symmetry breaking is "soft", since we have separated out the completely symmetric terms from those soft terms which will not allow the quadratic divergences to the Higgs mass.

The explicitly allowed terms in the soft-breaking Lagrangian are [35]:

- Mass terms for the scalar components of the chiral supermultipletss
- Mass terms for the Weyl spinor components of the gauge supermultipletss
- Trilinear couplings of scalar components of chiral supermultiplets

In particular, using the field content described above for the MSSM, the softly-broken portion of the MSSM Lagrangian can be writen

$$\begin{aligned}
\mathcal{L}_{\text{soft}} = & -\frac{1}{2}\left(M_3\tilde{g}\tilde{g} + M_2\tilde{W}\tilde{W} + M_1\tilde{B}\tilde{B} + c.c.\right) & (3.10)\\
& -\left(\tilde{u}a_u\tilde{Q}H_u - \tilde{d}a_d\tilde{Q}H_d - \tilde{e}a_e\tilde{L}H_d + c.c.\right) & (3.11)\\
& -\tilde{Q}^\dagger m_Q^2\tilde{Q} - \tilde{L}^\dagger m_L^2\tilde{L} - \tilde{u}m_u^2\tilde{u}^\dagger - \tilde{d}m_d^2\tilde{d}^\dagger - \tilde{e}m_e^2\tilde{e}^\dagger & (3.12)\\
& -m_{H_u}^2 H_u^* H_u - m_{H_d}^2 H_d^* H_d - (bH_uH_d + cc). & (3.13)
\end{aligned}$$

where we have introduced the following notations :

1. M_3, M_2, M_1 are the gluino, wino, and bino masses.
2. a_u, a_d, a_e are complex 3×3 matrices in family space.
3. $m_Q^2, m_u^2, m_d^2, m_L^2, m_e^2$ are hermitian 3×3 matrices in family space.
4. $m_{H_u}^2, m_{H_u}^2, b$ are the SUSY-breaking contributions to the Higgs potential.

We have written matrix terms without any sort of additional notational decoration to indicate their matrix nature, and we now show why. The first term Item 1 is the set of mass terms for the gluino, wino, and bino. The second term Item 2, containing a_u, a_d, a_e, has strong contraints from experiments [74, 75]. We will assume that each $a_i, i = u, d, e$ is proportional to the Yukawa coupling matrix : $a_i = A_{i0} y_i$. The third term Item 3 can be similarly constrained by experiments [68, 75–82]. We will assume the elements of the fourth term Item 4 contributing to the Higgs potential as well as all of the Item 1 terms must be real, which limits the possible CP-violating interactions to those of the Standard Model. We thus only consider flavor-blind, CP-conserving interactions within the MSSM.

The important mixing for mass and gauge interaction eigenstates in the MSSM occurs within electroweak sector, in a process akin to EWSB in the Standard Model. The neutral portions of the Higgsinos doublets and the neutral gauginos $(\tilde{H}_u^0, \tilde{H}_d^0, \tilde{B}^0, \tilde{W}^0)$ of the gauge interaction basis mix to form what are known as the *neutralinos* of mass basis :

$$M_{\tilde{\chi}} = \begin{pmatrix} M_1 & 0 & -c_\beta s_W m_Z & s_\beta s_W m_Z \\ 0 & M_2 & c_\beta c_W m_Z & -s_\beta c_W m_Z \\ -c_\beta s_W m_Z & c_\beta c_W m_Z & 0 & -\mu \\ s_\beta s_W m_Z & -s_\beta c_W m_Z & -\mu & 0 \end{pmatrix} \tag{3.14}$$

where $s(c)$ are the sine and cosine of angles related to EWSB, which introduced masses to the gauginos and higgsinos. Diagonalization of this matrix gives the four neutralino mass states, listed without loss of generality in order of increasing mass : $\tilde{\chi}^0_{1,2,3,4}$.

The neutralinos, especially the lightest neutralino $\tilde{\chi}_1^0$, are important ingredients in SUSY phenomenology.

The same process can be done for the electrically charged gauginos with the charged portions of the Higgsino doublets along with the charged winos

$(\tilde{H}_u^+, \tilde{H}_d^+, \tilde{W}^+, \tilde{W}^-)$. This leads to the *charginos*, again in order of increasing mass : $\tilde{\chi}^{\pm}_{1,2}$.

3.3 Phenomenology

We are finally at the point where we can discuss the phenomenology of the MSSM, in particular as it manifests itself at the energy scales of the LHC.

As noted above in Sec. 3.2, the assumption of $R-$parity has important consequences for MSSM phenomenology. The SM particles have $R = 1$, while the sparticles all have $R = -1$. Simply, this is the "charge" of supersymmetry. Since the particles of LHC collisions (pp) have total incoming $R = 1$, we must expect that all sparticles will be produced in *pairs*. An additional consequence of this symmetry is the fact that the lightest supersymmetric particle (LSP) is *stable*. Off each branch of the Feynmann diagram shown in Fig. 3.3, we have $R = -1$, and this can only decay to another sparticle and a SM particle. Once we reach the lightest sparticle in the decay, it is absolutely stable. This leads to the common signature $E_{\mathrm{T}}^{\mathrm{miss}}$ for a generic SUSY signal.

For this thesis, we will be presenting an inclusive search for squarks and gluinos with zero leptons in the final state. This is a very interesting decay channel, due to the high cross-sections of $\tilde{g}\tilde{g}$ and $\tilde{q}\tilde{q}$ decays, as can be seen in Sec. 3.3 [83].

This is a direct consequence of the fact that these are the colored particles of the MSSM. Since the sparticles interact with the gauge groups of the SM in the same way as their SM partners, the colored sparticles, the squarks and gluinos, are produced and decay as governed by the color group $SU(3)_C$ with the strong coupling g_S. The digluino production is particularly copious, due to color factor corresponding to the color octet of $SU(3)C$.

In the case of disquark production, the most common decay mode of the squark in

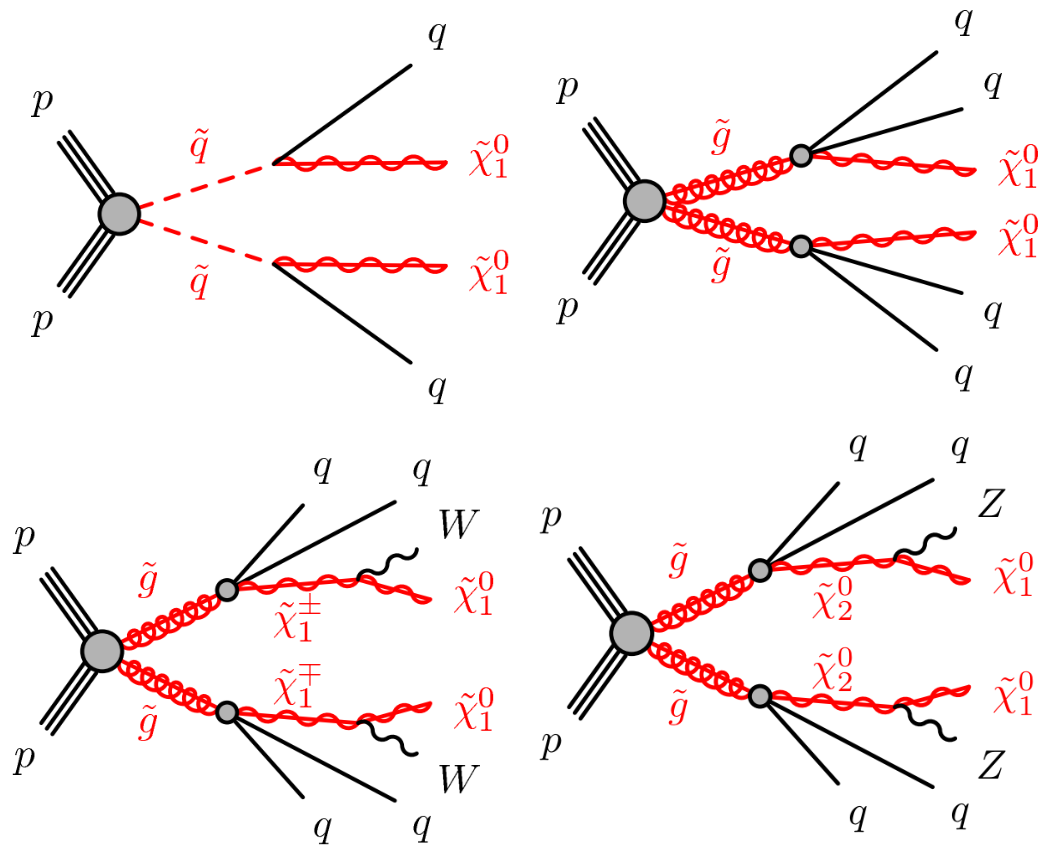

Figure 3.3: SUSY signals considered in this thesis

the MSSM is a decay directly to the LSP plus a single SM quark [15]. This means the basic search strategy of disquark production is two jets from the final state quarks, plus missing transverse energy for the LSPs. There are also cascade decays, the most common of which, and the only one considered in this thesis, is $\tilde{q} \to q\tilde{\chi}^{\pm} \to qW^{\pm}\chi^{0}$.

For digluino production, the most common decay is $\tilde{g} \to g\tilde{q}$, due to the large g_S coupling. The squark then decays as listed above. In this case, we generically search for four jets and missing transverse energy from the LSPs.

In the context of experimental searches for SUSY, we often consider *simplified models*. These models make certain assumptions which allow easy comparisons of results by theorists and experimentalists. In the context of this thesis, the simplified models will make assumptions about the branching ratios described in the preceding paragraphs. In particular, we will often choose a model where the decay of interest

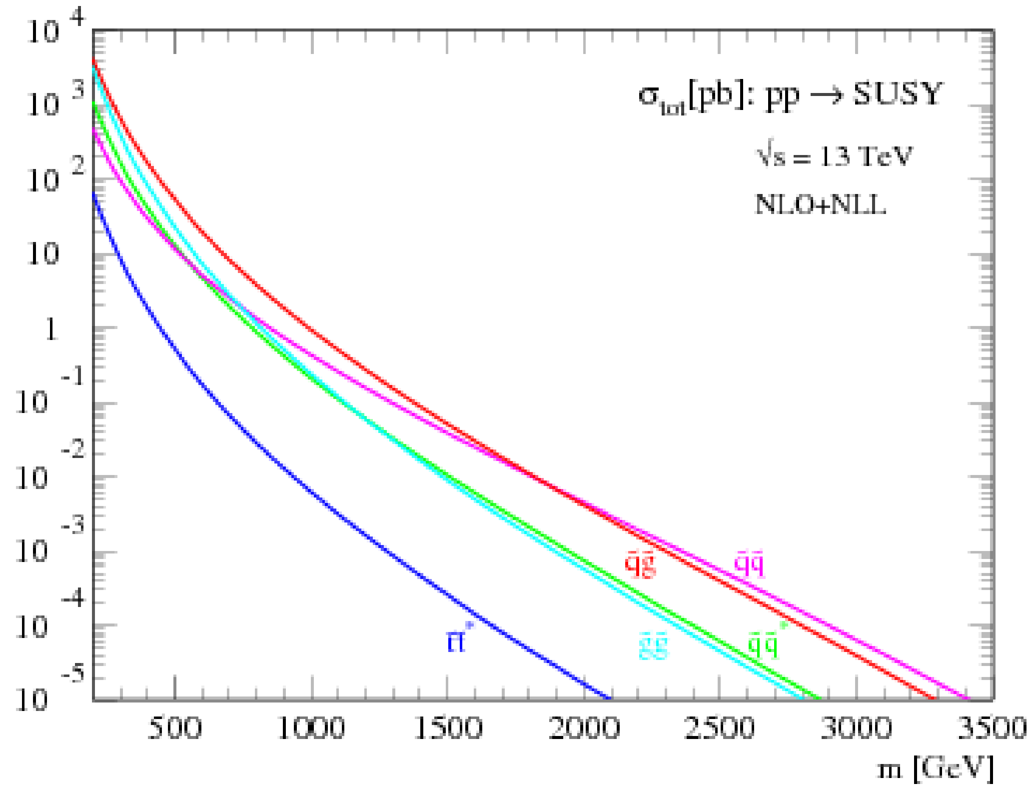

Figure 3.4: SUSY production cross-sections as a function of sparticle mass at $\sqrt{s} =$ 13 TeV.

occurs with 100% branching ratio. This is entirely for ease of interpretation, but it is important to recognize that these are more a useful comparison tool, especially with for setting limits, than a strict statement about the potential masses of sought-after beyond the Standard Model particle.

3.4 How SUSY solves the problems with the SM

We now return to the issues with the Standard Model as described in Ch. 2 to see how these issues are solved by supersymmetry.

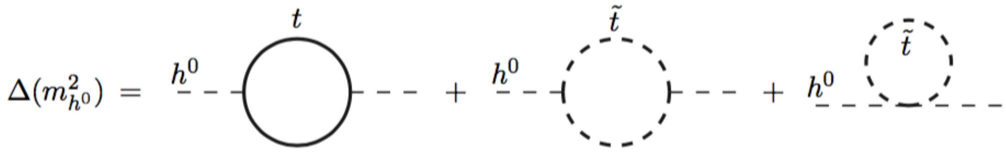

Figure 3.5: Loop diagrams correct the Higgs mass in the MSSM

Quadratic divergences to the Higgs mass

The quadratic divergences induced by the loop corrections to the Higgs mass, for example from the top Yukawa coupling, goes as

$$\delta m_H^2 \approx \left(\frac{m_t}{8\pi^2 {<}\phi{>}_{VEV}} \right)^2 \Lambda^2_{Planck}. \tag{3.15}$$

The miraculous thing about SUSY is each of these terms *automatically* comes with a term which exactly cancels this contribution [15]. The fermions and bosons have opposite signs in this loop diagram to all orders in pertubation theory, which completely solves the hierarchy problem. This is the strongest motived reason for supersymmetry.

Gauge coupling unification

An additional motivation for supersymmetry is seen by the gauge coupling unification high scales. In the Standard Model, as we saw the gauge couplings fail to unify at high energies. In the MSSM and many other forms of supersymmetry, the gauge couplings unify at high energy, as can be seen in Fig. 3.6. This provides additional aesthetic motivation for supersymmetric theories.

Dark matter

As we discussed previously, the lack of any dark matter candidate in the Standard Model naturally leads to beyond the Standard Model theories. In the Standard Model, there is a natural dark matter candidate in the lightest supersymmetric particle [15]

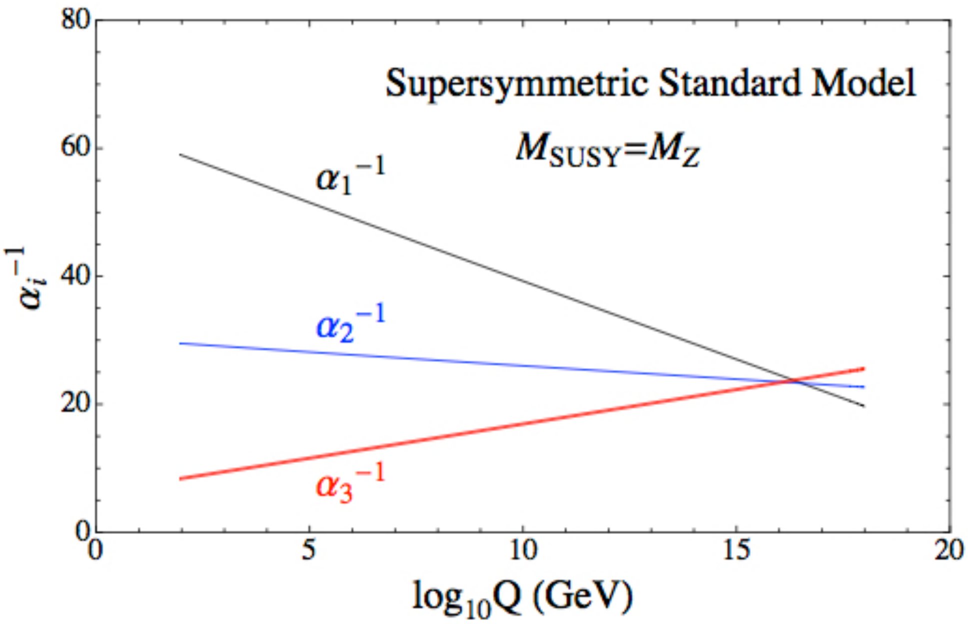

Figure 3.6: The running of Standard Model gauge couplings: compare to Fig. 2.4. The MSSM gauge couplings nearly intersect at high energies.

The LSP would in dark matter experiments be called a *weakly-interacting massive particle* (WIMP), which is a type of cold dark matter [22, 84]. These WIMPS would only interact through the weak force and gravity, which is exactly as a model like the MSSM predicts for the neutralino. In Fig. 3.7, we can see the current WIMP exclusions for a given mass. The range of allowed masses which have not been excluded for LSPs and WIMPs have significant overlap. This provides additional motivation outside of the context of theoretical details.

3.5 Conclusions

Supersymmetry is the most well-motivated theory for physics beyond the Standard Model. It provides a solution to the hierarchy problem, leads to gauge coupling unification, and provides a dark matter candidate consistent with galatic rotation curves. As noted in this chapter, due to the LSPs in the final state, most SUSY

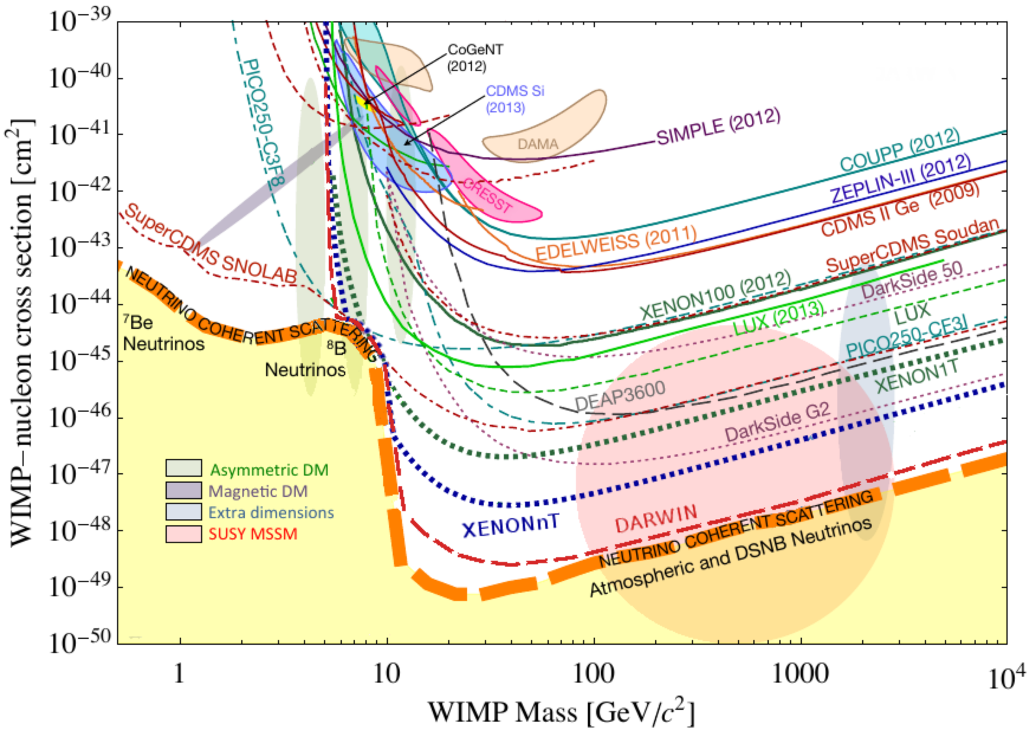

Figure 3.7: WIMP exclusions from direct dark matter detection experiments.

searches require a significant amount of missing transverse energy in combination with jets of high transverse momentum. However, there is some opportunity to do better than this, especially in final states where one has two weakly-interacting LSPs on opposite sides of some potentially complicated decay tree. We will see how this is done in Ch. 7.

Chapter 4

The Large Hadron Collider

The Large Hadron Collider (LHC) produces high-energy protons which collide at the center of multiple large experiments at CERN on the outskirts of Geneva, Switzerland [85]. The LHC produces the highest energy collisions in the world, with a design center-of-mass energy of $\sqrt{s} = 14$ TeV, which allows the experiments to investigate physics at higher energies than previous colliders. This chapter will summarize the basics of accelerator physics, especially with regards to discovering physics beyond the Standard Model. We will describe the CERN accelerator complex and the LHC.

4.1 Basics of Accelerator Physics

This section follows closely the presentation of [86].

Simple particle accelerators simply rely on the acceleration of charged particles in a static electric field. Given a field of strength E, charge q, and mass m, this is simply

$$a = \frac{qE}{m}. \tag{4.1}$$

For a given particle with a given mass and charge, this is limited by the static electric field which can be produced, which in turn is limited by electrical breakdown at high voltages.

There are two complementary solutions to this issue. First, we use the *radio frequency acceleration* technique. We call the devices used for this *RF cavities*. The cavities produce a time-varied electric field, which oscillate such that the charged particles passing through it are accelerated towards the design energy of the RF cavity. This oscillation forces the particles into *bunches*, since particles which are slightly off the central energy induced by the RF cavity are accelerated towards the design energy.

Second, one bends the particles in a magnetic field, which allows them to pass through the same RF cavity over and over. This second process is often limited by *synchrotron radiation*, which describes the radiation produced when a charged particle is accelerated. The power radiated is

$$P \sim \frac{1}{r^2}\left(E/m\right)^4 \tag{4.2}$$

where r is the radius of curvature and E, m is the energy (mass) of the charged particle. Given an energy which can be produced by a given set of RF cavities (which is *not* limited by the mass of the particle), one then has two options to increase the actual collision energy : increase the radius of curvature or use a heavier particle. Practically speaking, the easiest options for particles in a collider are protons and electrons, since they are copiously produced in nature and do not decay[1]. Given the dependence on mass, we can see why protons are used to reach the highest energies. The tradeoff for this is that protons are not point particles, and we thus we don't know the exact incoming four-vectors of the protons. This is a reflection of the "bag model" discussed in Ch. 2, where each proton is actually a bag of incoming quarks and gluons, which individually contribute to the total proton energy.

The particle *beam* refers to the bunches combined. An important property of a beam of a particular energy E, moving in uniform magnetic field B, containing particles of momentum p is the *beam rigidity* :

$$R \equiv rB = p/c. \tag{4.3}$$

[1] Muon colliders are a potential future option at high energies, since the relativistic γ factor gives them a relatively long lifetime in the lab frame.

The linear relation between r and p, or alternatively B and p have important consequences for LHC physics. For hadron colliders, this is the limiting factor on going to higher energy scales; one needs a proportionally larger magnetic field to keep the beam accelerating in a circle.

Besides the rigidity of the beam, the most important quantities to characterize a beam are known as the (normalized) *emittance* ϵ_N and the *betatron function* β. These quantities determine the transverse size σ of a relativistic beam $v \lesssim c$ beam : $\sigma^2 = \beta^* \epsilon_N / \gamma_{\text{rel}}$, where β^* is the value of the betatron function at the collision point and γ_{rel} is the Lorentz factor.

These quantities determine the *instanteous luminosity* L of a collider, which combined with the cross-section σ of a particular physics process, give the rate of the physics process :

$$R = L\sigma. \tag{4.4}$$

The instanteous luminosity L is given by :

$$L = \frac{f_{\text{rev}} N_b^2 F}{4\pi\sigma^2} = \frac{f_{\text{rev}} n N_b^2 \gamma_{\text{rel}} F}{4\pi\beta^* \epsilon_N}. \tag{4.5}$$

Here we have introduced the frequency of revolutions f_{rev}, the number of bunches n, the number of protons per bunch N_b^2, and a geometric factor F related to the crossing angle of the beams.

The *integrated luminosity* $\int L dt$ gives the total number of a particular physics process P, with cross-section σ_{P}.

$$N_{\text{P}} = \sigma_{\text{P}} \int L dt. \tag{4.6}$$

Due to this simple relation, one can also quantify the “amount of data delivered” by a collider simply by $\int L dt$.

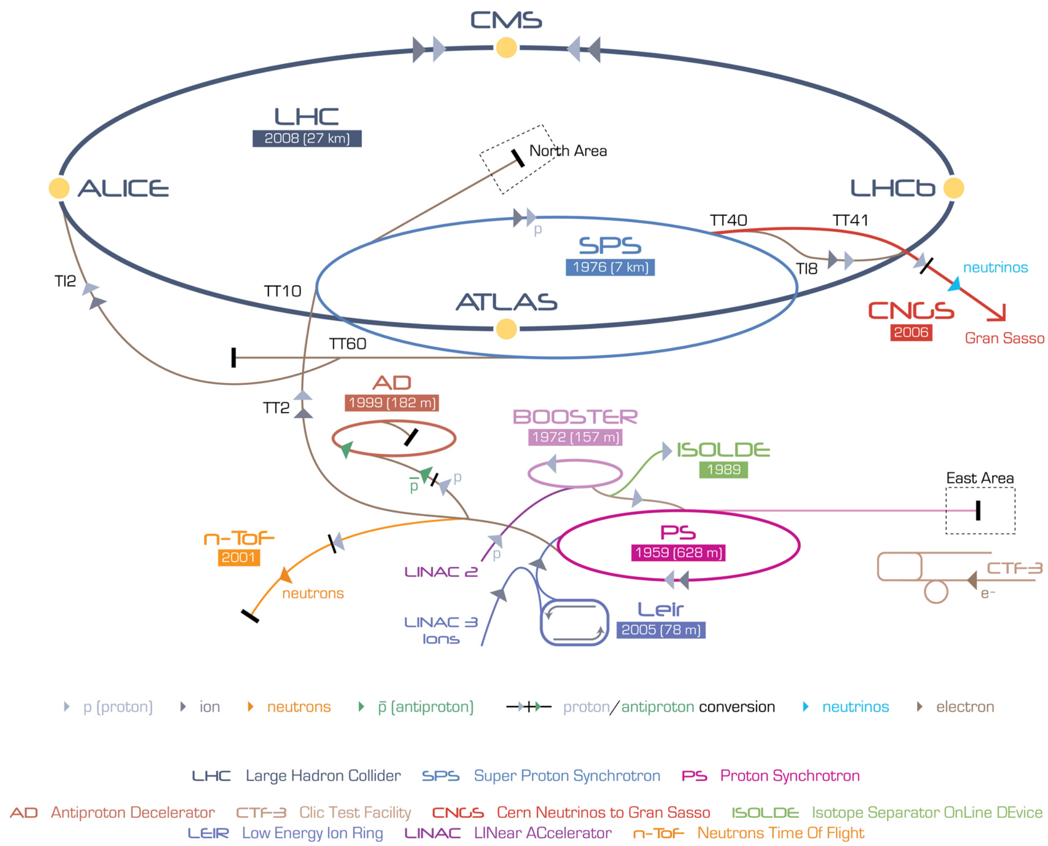

Figure 4.1: The CERN accelerator complex.

4.2 Accelerator Complex

The Large Hadron Collider is the last accelerator in a chain of accelerators which together form the CERN accelerator complex, shown in Fig. 4.1. The protons begin their journey to annilation in a hydrogen source, where they are subsequently ionized. The first acceleration occurs in the Linac 2, a linear accelerator composed of RF cavities. The protons leave the Linac 2 at an energy of 50 MeV and enter the Proton Synchrotron Booster (PSB). The PSB contains four superimposed rings, which accelerate the protons to 1.4 GeV. The protons are then injected into the Proton Synchrotron (PS). This synchrotron increases the energy up to 25 GeV. After leaving the PS, the protons enter the Super Proton Synchrotron (SPS). This is the last step before entering the LHC ring, and the protons are accelerated to 450 GeV. From the SPS, the protons are injected into the beam pipes of the LHC. The process to fill the LHC rings with proton bunches from start to finish typically takes about four minutes.

4.3 Large Hadron Collider

The Large Hadron Collider is the final step in the CERN accelerator complex, and produces the collisions analyzed in this thesis. From the point of view of experimentalists on the general-purpose ATLAS and CMS experiments, the main goal of the LHC is to deliver collisions at the highest possible energy, with the highest possible instantaneous luminosity. The LHC was installed in the existing 27 km tunnel used by the Large Electron Positron (LEP) collider [87]. This allowed the existing accelerator complex at CERN, described in the previous section, to be used as the injection system to prepare the protons up to 450 GeV. Many aspects of the LHC design were decided by this very constraint, and specified the options allowed to increase the energy or luminosity. In particular, the radius of the tunnel was already specified. From Eq.Eq. (4.3), this implies the momentum (or energy) of the beam is entirely determined by the magnetic field. Given the 27 km circumference of the LEP tunnel, one can calculate the required magnetic field to reach the 7 TeV per proton design energy of the LHC :

$$r = C/2\pi = 4.3 \text{ km} \tag{4.7}$$

$$\rightarrow B = \frac{p}{rc} = 5 \text{ T} \tag{4.8}$$

In fact, the LHC consists of eight 528 m straight portions consisting of RF cavities, used to accelerate the particles, and 8 circular portions which bend the protons around the LHC ring. These circular portions actually have a slightly smaller radius of curvature $r = 2804$ m, and require $B = 8.33$ T. To produce this large field, superconducting magnets are used.

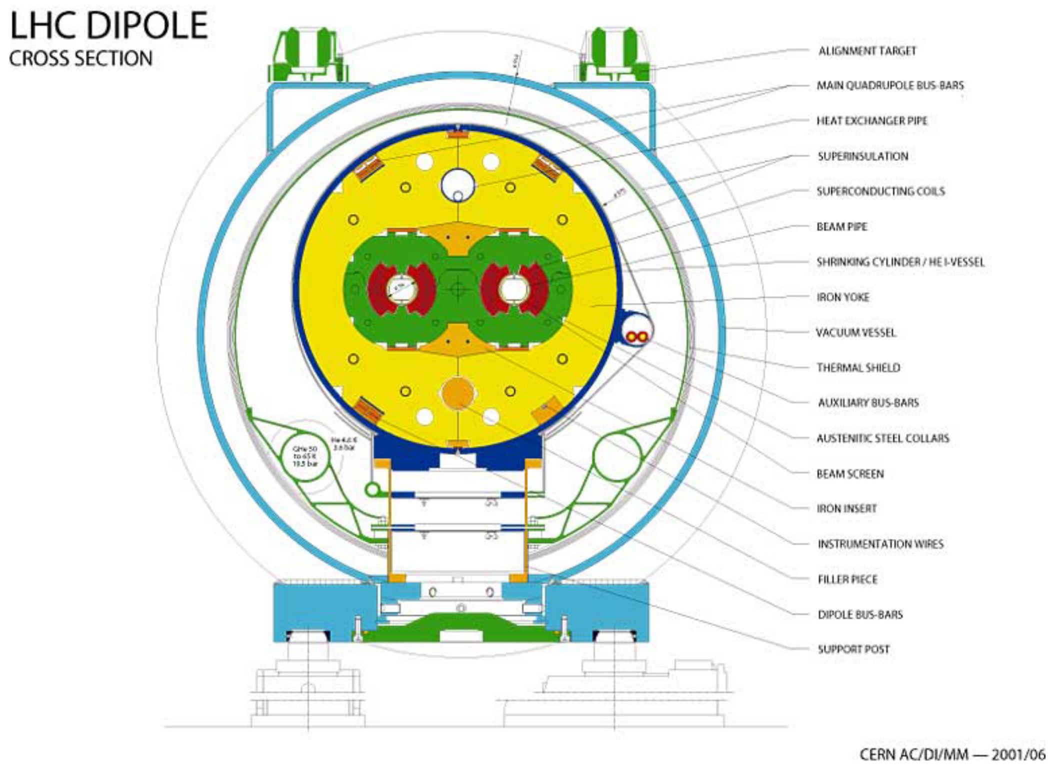

Figure 4.2: Schematic of an LHC dipole magnet.

Magnets

There are many magnets used by the LHC machine, but the most important are the 1232 dipole magnets. A schematic is shown in Fig.Fig. 4.2 and a photograph is present in Fig. 4.3.

The magnets are made of Niobium and Titanium. The maximum field strength is 10 T when cooled to 1.9 Kelvin. The magnets are cooled by superfluid helium, which is supplied by a large cryogenic system. Due to heating between the eight helium refrigerators and the beampipe, the helium is cooled in the refrigerators to 1.8 K.

A failure in the cooling system can cause what is known as a *quench*. If the temperature goes above the critical superconducting temperature, the metal loses its superconducting properties, which leads to a large resistance in the metal. This leads to rapid temperature increases, and can cause extensive damages if not controlled.

The dipole magnets are 16.5 meters long with a diameter of 0.57 meters. There

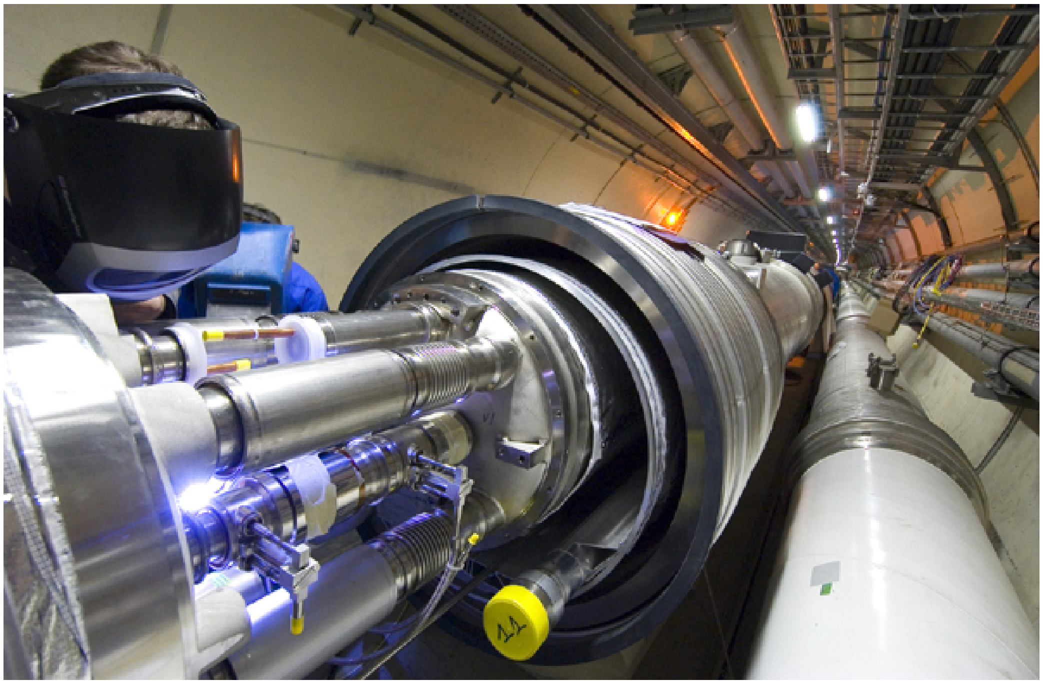

Figure 4.3: Photograph of a technician connecting an LHC dipole magnet.

are two individual beam pipes inside each magnet, which allows the dipoles to house the beams travelling in both directions around the LHC ring. They curve slightly, at an angle of 5.1 mrad, which carefully matches the curvature of the ring. The beampipes inside of the magnets are held in high vacuum to avoid stray interactions with the beam.

4.4 Dataset Delivered by the LHC

In this thesis, we analyze the data delivered by the LHC to ATLAS in the 2015 and 2016 datasets. The beam parameters relevant to this dataset are available in Tab. 4.1.

The peak instanteous luminosity delivered in 2015 (2016) was $L = 5.2\,(11)\,\mathrm{cm}^{-2}\mathrm{s}^{-1} \times 10^{33}$. One can note that the instanteous luminosity delivered in the 2016 dataset exceeds the design luminosity of the LHC. The total integrated luminosity delivered was 13.3 fb^{-1}. In Fig. 4.4, we display the integrated luminosity

Parameter	Injection	Extraction
Energy (GeV)	450	7000
Rigidity (T-m)	3.8	23353
Bunch spacing (ns)	25	25
Design Luminosity ($\mathrm{cm}^{-2}\mathrm{s}^{-1} \times 10^{3}4$)	-	1.0
Bunches per proton beam	2808	2808
Protons per bunch	1.15 e11	1.15 e11
Beam lifetime (hr)	-	10
Normalized Emittance ϵ_N (mm μrad)	3.3	3.75
Betatron function at collision point β^* (cm)	-	55

Table 4.1: Beam parameters of the Large Hadron Collider.

per day for 2015 and 2016.

Pileup

Pileup is the term for the additional proton-proton interactions which occur during each bunch crossing of the LHC. At the beginning of the LHC physics program, there had not been a collider which averaged more than a single interaction per bunch crossing. In the LHC, each bunch crossing (or *event*) generally contains multiple proton-proton interactions. An simulated event with many *vertices* can be seen in Fig. 4.5. The so-called *primary vertex* (or *hard scatter vertex*) refers to the vertex which has the highest Σp_T^2. The summation occurs over the *tracks* in the detector, which we will describe later [**ATL-INDET-PUB-2009-001**]. We then distinguish between *in-time* pileup and *out-of-time* pileup. In-time pileup refers to the additional proton-proton interactions which occur in the event. Out-of-time pileup refers to effects related to proton-proton interactions previous bunch crossings.

We quantify in-time pileup by the number of "primary"[2] vertices in a particular event. To quantify the out-of-time pileup, we use the average number of interactions per bunch crossing $< \mu >$. In Fig. 4.6, we show the distribution of μ for the dataset used in this thesis.

[2] *The* primary vertex is as defined above, but we unfortunately use the same name here.

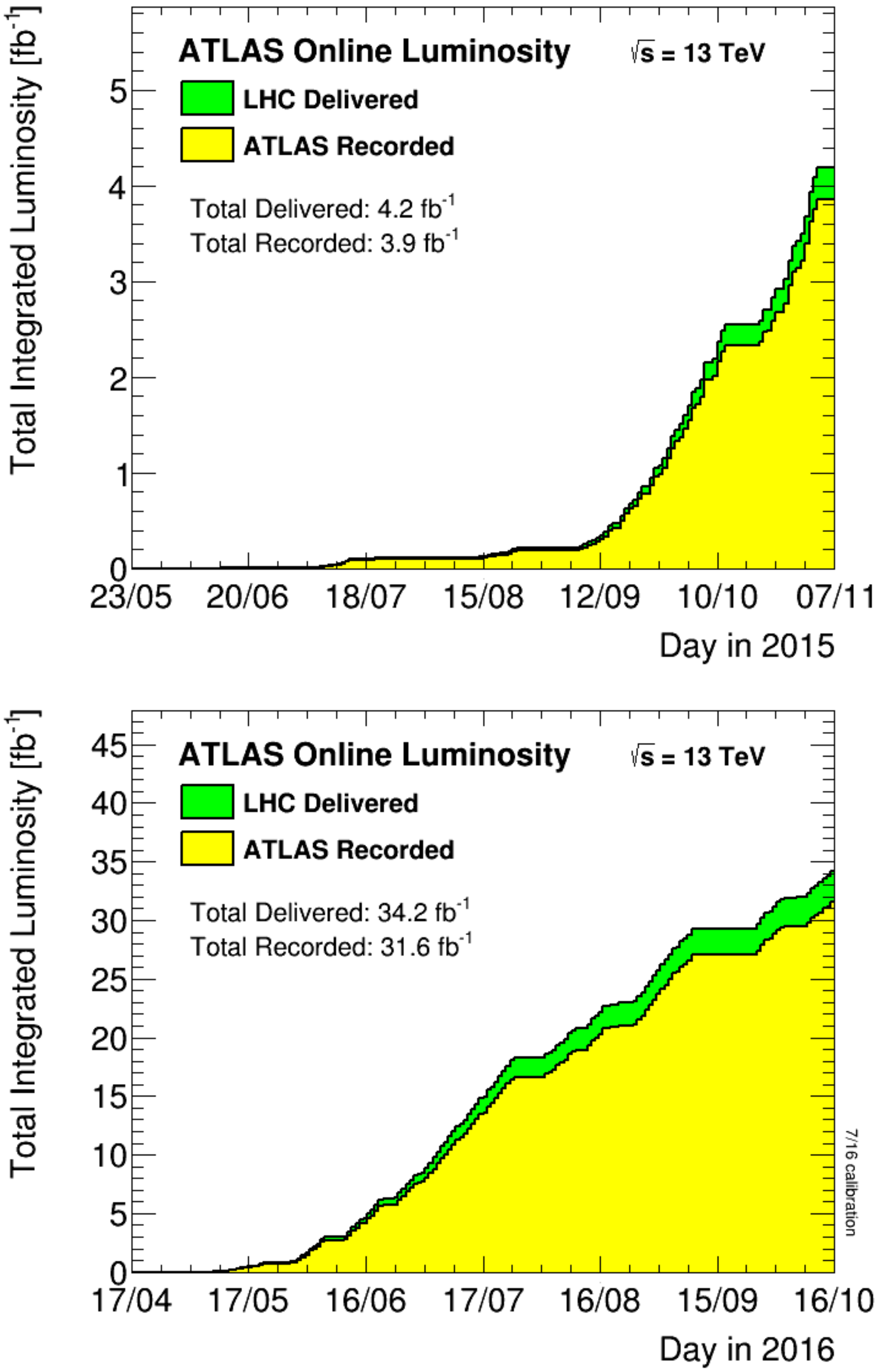

Figure 4.4: Integrated Luminosity delivered by the LHC and collected by ATLAS in the 2015 and 2016 datasets.

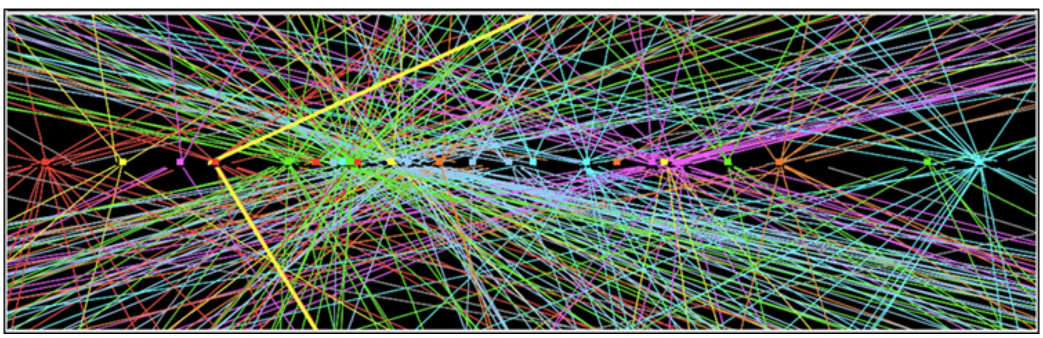

Figure 4.5: Simulated event with many pileup vertices.

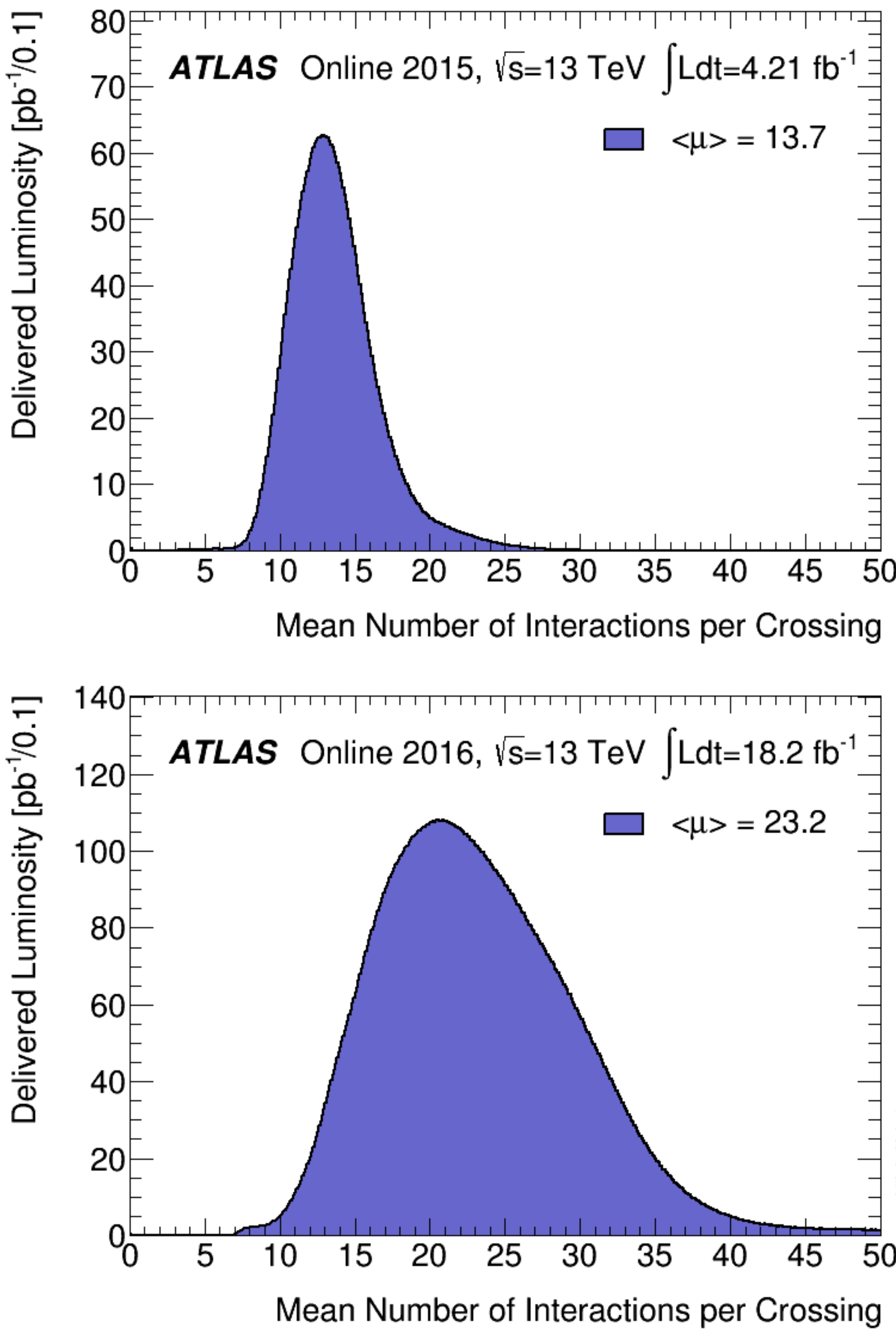

Figure 4.6: Mean number of interactions per bunch crossing in the 2015 and 2016 datasets.

Chapter 5

The ATLAS detector

The dataset analyzed in this thesis was taken by the ATLAS detector [88], which is located at the "Point 1" cavern of the LHC beampipe, just across the street from the main CERN campus. The much-maligned acronym stands for *A T*oriodal *L*HC *A*pparatu*S*. ATLAS is a massive cylindrical detector, with a radius of 12.5 m and a length of 44 m, with nearly hermitic coverage around the collision point. It consists of multiple subdetectors; each plays a role in ATLAS's ultimate purpose of measuring the energy, momentum, and type of the particles produced in collisions delivered by the LHC. These subdetectors are immersed in a hybrid solenoid-toroid magnet system whichs forces charged particles to curve, which allows for precise measurements of their momenta. These magnetic fields are maximized in the central solenoid magnet, which contains a magnetic field of 2 T. A schematic of the detector can be seen in Fig. 5.1.

The *inner detector* (ID) lies closest to the collision point, and contains three separate subdetectors. It provides pseudorapidity[1]coverage of $|\eta| < 2.5$ for charged particles to interact with the tracking material. The tracks reconstructed from the inner detector hits are used to reconstruct the primary vertices, as noted in **??**, and

[1]ATLAS uses a right-handed Cartesian coordinate system; the origin is defined by the nominal beam interaction point. The positive-z direction is defined by the incoming beam travelling counterclockwise around the LHC. The positive-x direction points towards the center of the LHC ring from the origin, and the positive-y direction points upwards towards the sky. For particles of transverse (in the $x-y$ plane) momentum $p_T = \sqrt{p_x^2 + p_y^2}$ and energy E, it is generally most convenient fully describe this particle's kinematics as measured by the detector in the (p_T, ϕ, η, E) basis. The angle $\phi = \arctan(p_y/p_x)$ is the standard azimuthal angle, and $\eta = \ln\tan(\theta/2)$ is known as the pseudorapidity, and defined based on the standard polar angle $\theta = \arccos(p_z/p_T)$. For locations of i.e. detector elements, both (r, ϕ, η) and (z, ϕ, η) can be useful.

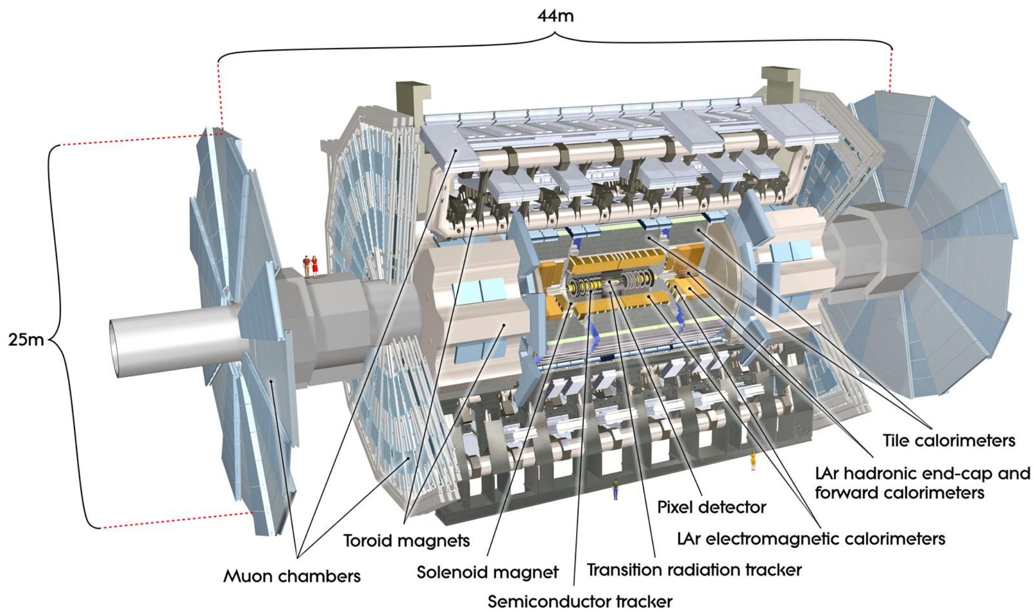

Figure 5.1: The ATLAS detector

to determine the momemta of charged particles. The ATLAS *calorimeter* consists of two subdetectors, known as the *electromagnetic* and *hadronic* calorimeters. These detectors stop particles in their detector material, and measure the energy deposition inside, which measures the energy of the particles deposited. The calorimeters provide coverage out to pseudorapidity of $|\eta| < 4.9$. The muon spectrometer is aptly named; it is specifically used for muons, which are the only particles which generally reach the outer portions of the detector. In this region, we have the large tracking systems of the muon spectrometer, which provide precise measurements of muon momenta. The muon spectrometer has pseudorapidity coverage of $|\eta| < 2.7$.

5.1 Magnets

ATLAS contains multiple magnetic systems; primarily, we are concerned with the solenoid, used by the inner detector, and the toroids located outside of the ATLAS calorimeter. A schematic is shown in Fig. 5.2. These magnetic fields are used to bend

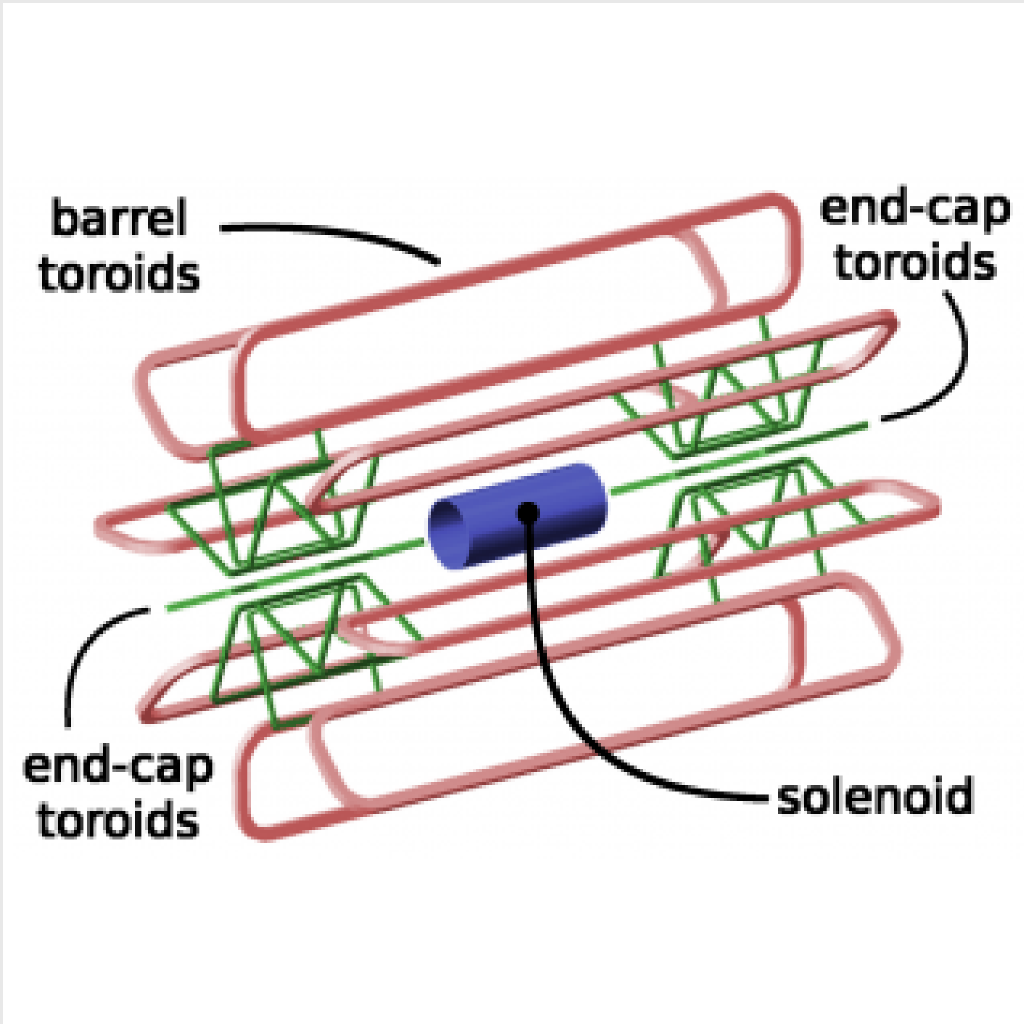

Figure 5.2: The ATLAS magnet system

charged particles under the Lorentz force, which subsequently allows one to measure their momentum.

The ATLAS central solenoid is a 2.3 m diameter, 5.3 m long solenoid at the center of the ATLAS detector. It produces a uniform magnetic field of 2 T; this strong field is necessary to accurately measure the charged particles in this field. An important design constraint for the central solenoid was the decision to place it in between the inner detector and the calorimeters. To avoid excessive impacts on measurements in

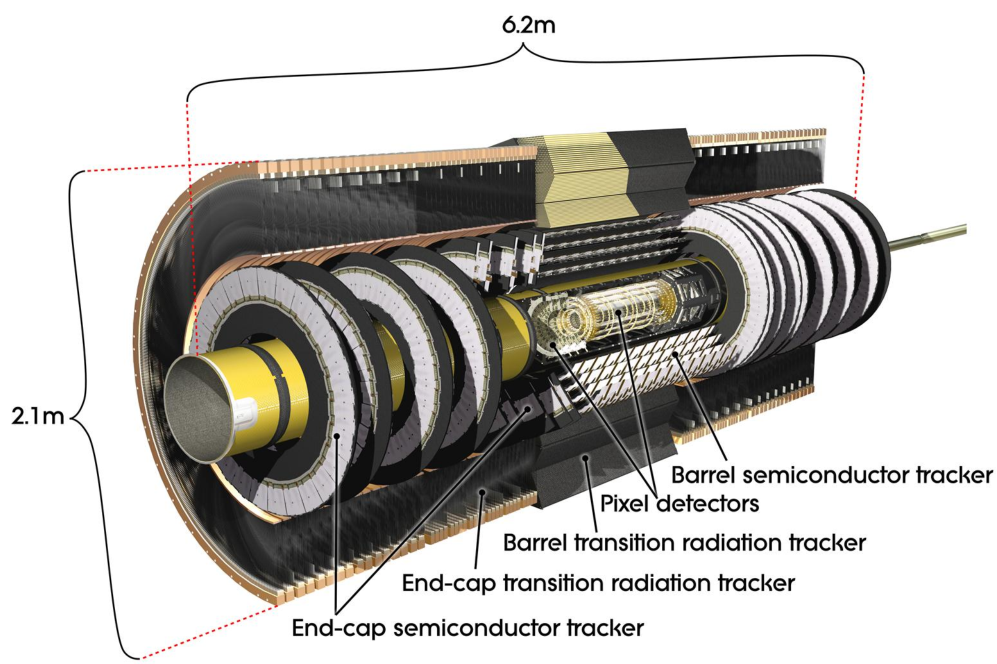

Figure 5.3: The ATLAS inner detector

the calorimetry, the central solenoid must be as transparent as possible[2].

The toroid system consists of eight air-core superconducting barrel loops; these give ATLAS its distinctive shape. There are also two endcap air-core magnets. These produce a magnetic field in a region of approximately 26 m in length and 10 m of radius. The magnetic field in this region is non-uniform, due to the prohibitive costs of a solenoid magnet of that size.

5.2 Inner Detector

The ATLAS inner detector consists of three separate tracking detectors, which are known as, in order of increasing distance from the interaction point, the Pixel Detector, Semiconductor Tracker (SCT), and the Transition Radiation Tracker (TRT). When charged particles pass through these tracking layers, they produce

[2]This is also one of the biggest functional differences between ATLAS and CMS; in CMS, the solenoid is outside of the calorimeters.

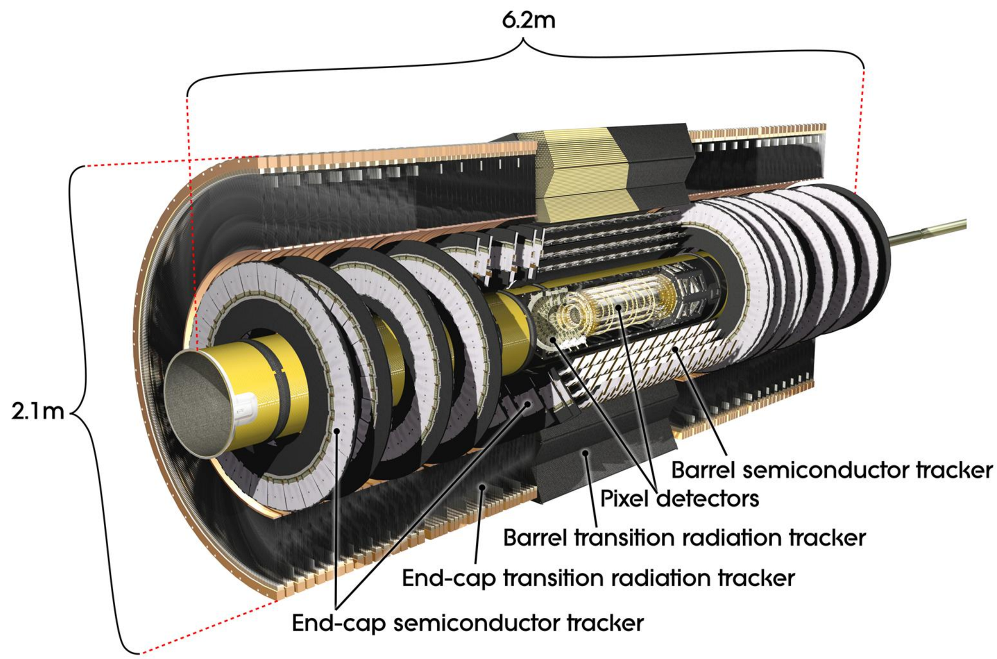

Figure 5.4: The ATLAS pixel detector

hits, which using the known 2 T magnetic field, allows the reconstruction of *tracks*. Tracks are used as inputs for reconstruction of many higher-level physics objects, such as electrons, muons, photons, and $E_{\mathrm{T}}^{\mathrm{miss}}$. Accurate track reconstruction is thus crucial for precise measurements of charged particles.

Pixel Detector

The ATLAS pixel detector consists four layers of silicon "pixels". This refers to the segmentation of the active medium into the pixels; compare to the succeeding silicon detectors, which will use silicon "strips". This provides precise 3D hit locations. The layers are known as the "Insertable"[3]B-Layer (IBL), the B-Layer (or Layer-0), Layer-1, and Layer-2, in order of increasing distance from the interaction point. These layers are very close to the interaction point, and therefore experience a large amount of radiation.

[3] *Very* often, the IBL is mistakenly called the Inner B-Layer, which would have been a much more sensible name.

Layer-1, Layer-2, and Layer-3 were installed with the initial construction of ATLAS. They contain front-end integrated electronics (FEI3s) bump-bonded to 1744 silicon modules; each module is 250 μm in thickness and contains 47232 pixels. These pixels have planar sizes of 50 x 400 μ^2 or 50 x 600 μ^2, to provide highly accurate location information. The FEI3s are mounted on long rectangular structures known as staves, which encircle the beam pipe. A small tilt to each stave allows full coverage in ϕ even with readout systems which are installed. These layers are at radia of 50.5 mm, 88.5 mm, and 122.5 mm from the interaction point.

The IBL was added to ATLAS after Run1 in 2012 at a radius of 33 mm from the interaction point. The entire pixel detector was removed from the center of ATLAS to allow an additional pixel layer to be installed. The IBL was required to preserve the integrity of the pixel detector as radiation damage leads to inoperative pixels in the other layers. The IBL consists of 448 FEI4 chips, arranged onto 14 staves. Each FEI4 has 26880 pixels, of planar size 50 x 250 μm. This smaller granularity was required due to the smaller distance to the interaction point.

In total, a charged particle passing through the inner detector would expect to leave four hits in the pixel detector.

Semiconductor Tracker

The SCT is directly beyond Layer-2 of the pixel detector. This is a silicon strip detector, which do not provide the full 3D information of the pixel detector. The dual-sensors of the SCT contain 2 x 768 individual strips; each strip has area 6.4 cm^2. The SCT dual-sensor is then double-layered, at a relative angle of 40 mrad; together these layers provide the necessary 3D information for track reconstruction. There are four of these double-layers, at radia of 284 mm, 355 mm, 427 mm, and 498 mm. These double-layers provide hits comparable to those of the pixel detector, and we have four additional hits to reconstruct tracks for each charged particle.

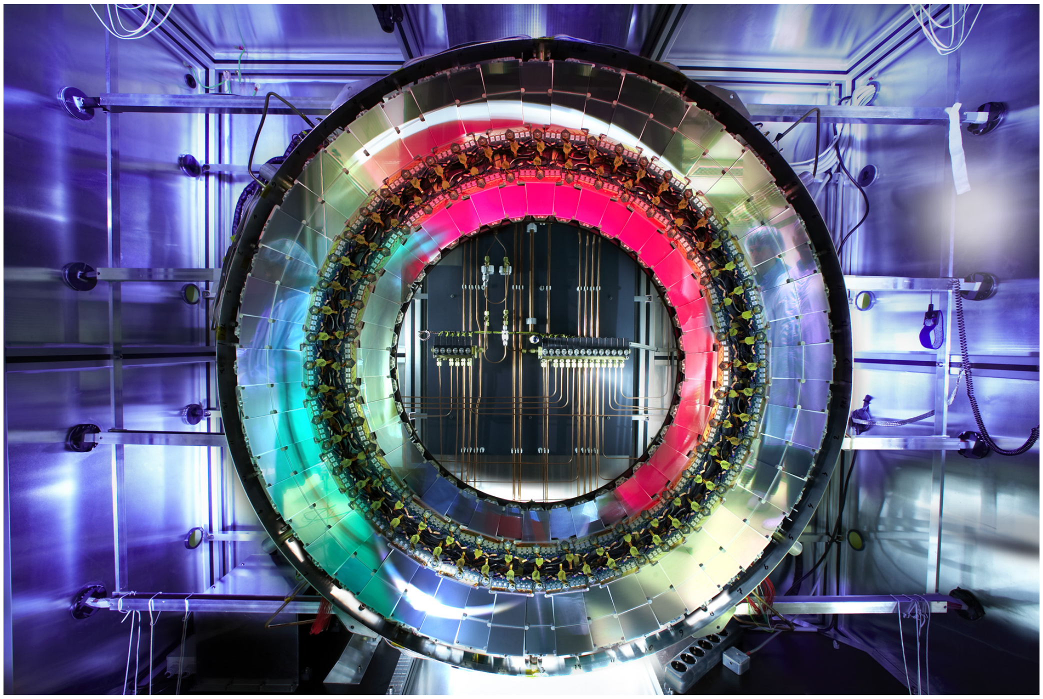

Figure 5.5: A ring of the Semiconductor Tracker

Transition Radiation Tracker

The Transition Radiation Tracker is the next detector radially outward from the SCT. It contains straw drift tubes; these contain a tungsten gold-plated wire of 32 μm diameter held under high voltage (-1530 V) with the edge of the Kapton-aluminum tube. They are filled with a gas mixture of primarily xenon that is ionized when a charged particle passes through the tube. The ions are collected by the "drift" due to the voltage inside the tubes, which is read out by the electronics. This gives so-called "continuous tracking" throughout the tube, due to the large number of ions produced.

The TRT is so-named due to the *transition radiation* (TR) it induces. Due to the dielectric difference between the gas and tubes, TR is induced. This is important for distinguishing electrons from their predominant background of minimum ionizing particles. Generally, electrons have a much larger Lorentz factor than minimum ionizing particles, which leads to additional TR. This can be used as an additional

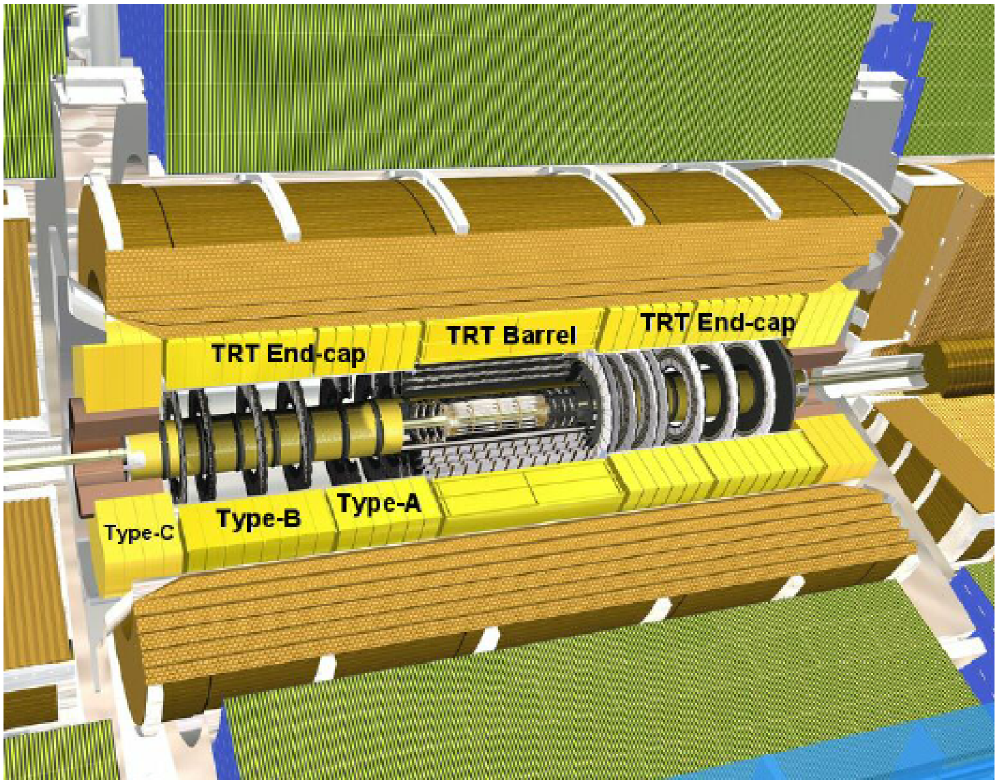

Figure 5.6: A schematic of the Transition Radiation Tracker

handle for electron reconstruction.

5.3 Calorimetry

The calorimetry of the ATLAS detector also includes multiple subdetectors; these subdetectors allow precise measurements of the electrons, photons, and hadrons produced by the ATLAS detector. Generically, calorimeters work by stopping particles in their material, and measuring the energy deposition. This energy is deposited as a cascade particles induce from interactions with the detector material known *showers*. ATLAS uses *sampling* calorimeters; these alternate a dense absorbing material, which induces showers, with an active layer which measures energy depositions by the induced showers. Since some energy is deposited into the absorption layers as well, the energy depositions must be properly calibrated for the detector.

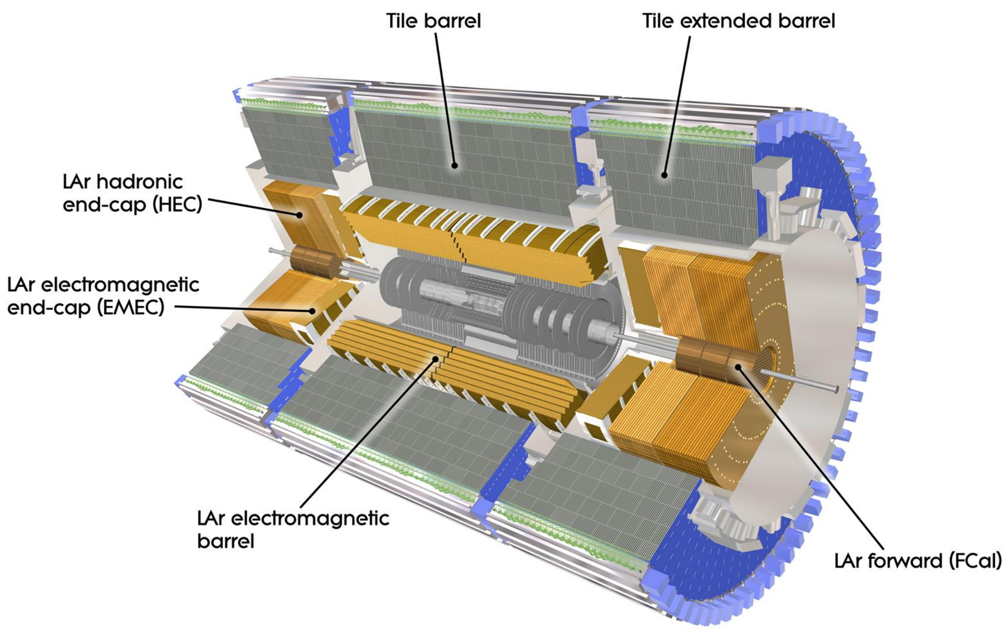

Figure 5.7: The ATLAS calorimeter

Electromagnetic objects (electrons and photons) and hadrons have much different interaction properties, and thus we need different calorimeters to accurately measure these different classes of objects; we can speak of the *electromagnetic* and *hadronic* calorimeters. ATLAS contains four separate calorimeters : the liquid argon (LAr) electromagnetic barrel calorimeter, the Tile barrel hadronic calorimeter, the LAr endcap electromagnetic calorimeter, the LAr endcap hadronic calorimeter, and the LAr Forward Calorimeter (FCal). Combined, these provide full coverage in ϕ up to $|\eta| < 4.9$, and can be seen in Fig. 5.7.

Electromagnetic Calorimeters

The electromagnetic calorimeters of the ATLAS detector consist of the barrel and endcap LAr calorimeters. These are arranged into an ingenious "accordion" shape, shown in Fig. 5.8, which allows full coverage in ϕ and exceptional coverage in η while still allowing support structures for detector operation. The accordion is made of

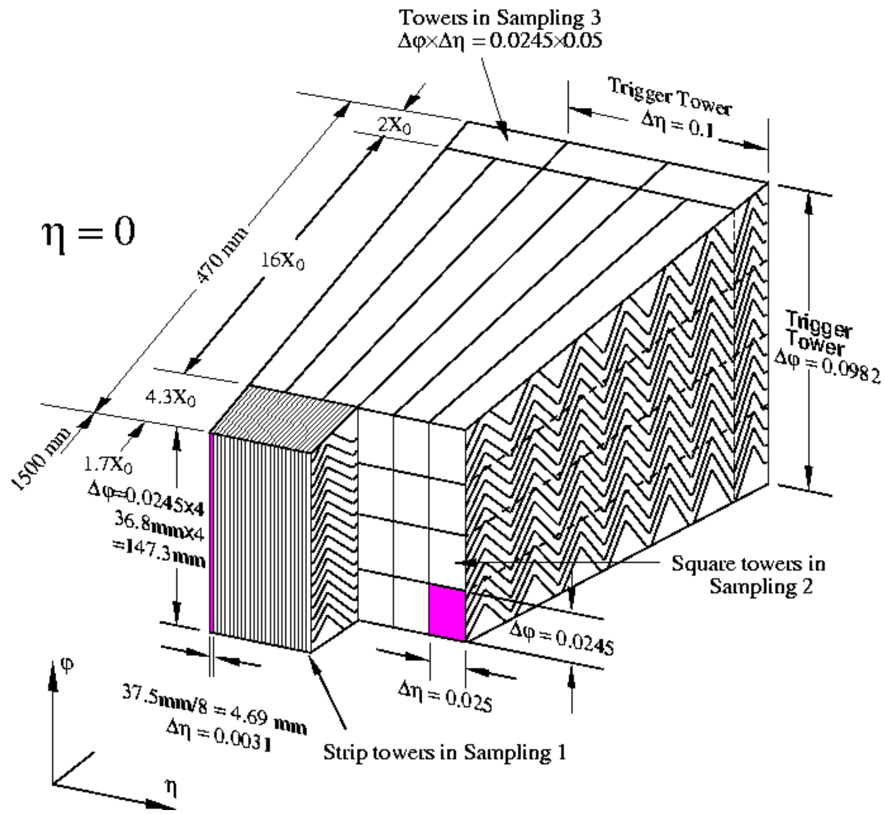

Figure 5.8: A schematic of a subsection of the barrel LAr electromagnetic calorimeter

layers with liquid argon (active detection material) and lead (absorber) to induce electromagnetic showers. The LAr EM calorimeters are each more than 20 radiation lengths deep, which provides the high stopping power necessary to properly measure the electromagnetic showers.

The barrel component of the LAr EM calorimeter extends from the center of the detector out to $|\eta| < 1.475$. The calorimeter has a presampler, which measures the energy of any EM shower induced before the calorimeter. This has segmentation of $\Delta\eta = 0.025, \Delta\phi = .01$ There are three "standard" layers in the barrel, which have decreasing segmentation into calorimeter *cells* as one travels radially outward from the interaction point. The first layer has segmentation of $\Delta\eta = 0.003, \Delta\phi = .1$, and is quite thin relative to the other layers at only 4 radiation lengths deep. It provides precise η and ϕ measurements for incoming EM objects. The second layer is the deepest at 16 radiation lengths, with a segmentation of $\Delta\eta = 0.025, \Delta\phi = 0.025$. It

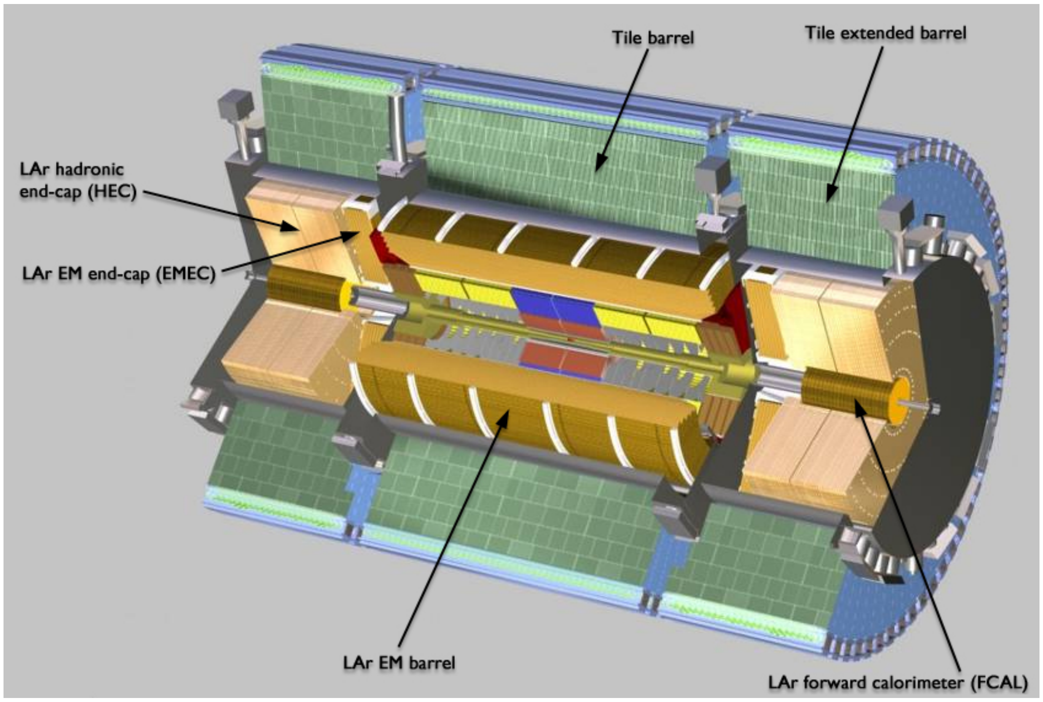

Figure 5.9: A schematic of Tile hadronic calorimeter

is primarily responsible for stopping the incoming EM particles, which dictates its large relative thickness, and measures most of the energy of the incoming particles. The third layer is only 2 radiation lengths deep, with a rough segmentation of $\Delta\eta = 0.05, \Delta\phi = .025$. The deposition in this layer is primarily used to distinguish hadrons interacting electromagnetically and entering the hadronic calorimeter from the strictly EM objects which are stopped in the second layer.

The barrel EM calorimeter has a similar overall structure, but extends from $1.4 < |\eta| < 3.2$. The segmentation in η is better in the endcap than the barrel; the ϕ segmentation is the same. In total, the EM calorimeters contain about 190000 individual calorimeter cells.

Hadronic Calorimeters

The hadronic calorimetry of ATLAS sits directly outside the EM calorimetry. It contains three subdetectors : the barrel Tile calorimeter, the endcap LAr calorimeter, and the Forward LAr Calorimeter. Similar to the EM calorimeters, these are sampling calorimeters that alternate steel (dense material) with an active layer (plastic scintillator).

The barrel Tile calorimeter extends out to $|\eta| < 1.7$. There are again three layers, which combined give about 10 interactions length of distance, which provides excellent stopping power for hadrons. This is critical to avoid excess *punchthrough* to the muon spectrometer beyond the hadronic calorimeters. The first layer has a depth of 1.5 interaction lengths. The second layer is again the thickest at a depth of 4.1 interaction lengths; most of the energy of incoming particle is deposited here. Both the first and second layer have segmentation of about $\Delta\eta = 0.1, \Delta\phi = 0.1$. Generally, one does not need as fine of granularity in the hadronic calorimeter, since the energy depositions in the hadronic calorimeters will be summed into the composite objects we know as jets. The third layer has a thickness of 1.8 interaction lengths, with a segmentation of $\Delta\eta = 0.2, \Delta\phi = 0.1$. The use of multiple layers allows one to understand the induced hadronic shower as it propagates through the detector material.

The endcap LAr hadronic calorimeter covers the region $1.5 < |\eta| < 3.2$. It is again a sampling calorimeter; the active material is LAr with a copper absorbed. It does not use the accordion shape of the other calorimeters; it has a "standard" flat shape perpendicular to the interaction point. The segmentation varies with η. For $1.5 < |\eta| < 2.5$, the cells are $\Delta\eta = 0.1, \Delta\phi = 0.1$; in the region $2.5 < |\eta| < 3.2$, the cells are $\Delta\eta = 0.2, \Delta\phi = 0.2$ in size.

The final calorimeter in ATLAS is the forward LAr calorimeter. Of those subdetectors which are used for standard reconstruction techniques, the FCal sits at the most extreme values of $3.1 < |\eta| < 4.9$. The FCal itself is made of three subdetectors; FCal1 is actually an electromagnetic module, while FCal2 and FCal3 are hadronic. The absorber in FCal1 is copper, with a liquid argon active medium. FCal2 and FCal3 also use a liquid argon active medium, with a tungsten absorber.

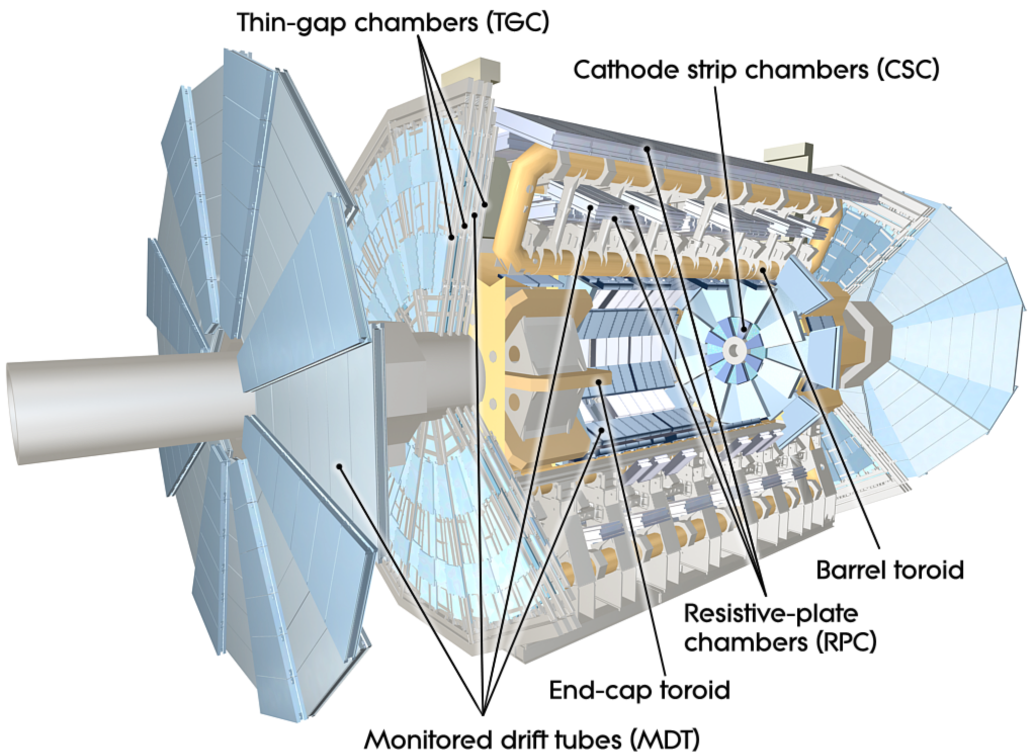

Figure 5.10: The ATLAS muon spectrometer

5.4 Muon Spectrometer

The muon spectrometer is the final major subdetector of the ATLAS detector. The muon spectrometer sits outside the hadronic calorimetry, with pseudorapidity coverage out to $|\eta| < 2.7$. The MS is a huge detector, with some detector elements existing as far as 11 m in radius from the interaction point. This system is used almost exclusively to measure the momenta of muons; these are the only measured SM particles which consistently exit the hadronic calorimeters. These systems provide a rough measurement, which is used in triggering (described in Sec. 5.5), and a precise measurement to be used in offline event reconstruction as described in Ch. 6. The MS produces tracks in a similar way to the ID; the hits in each subdetector are recorded and then tracks are produced from these hits. Muon spectrometer tracks are largely independent of the ID tracks due to the independent solenoidal and toriodal magnet systems used in the ID and MS respectively. The MS consists of four separate

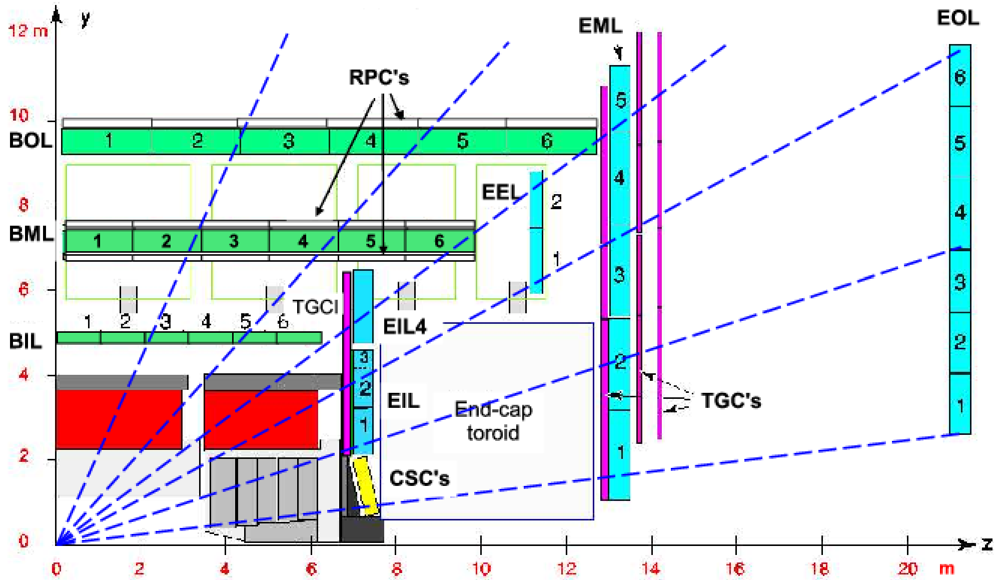

Figure 5.11: A schematic in z/η showing the location of the subdetectors of the muon spectrometer

subdetectors: the barrel region is covered by the Resistive Plate Chambers (RPCs) and Monitored Drift Tubes (MDTs) while the endcaps are covered by MDTs, Thin Gap Chambers (TGCs), and Cathode Strip Chambers (CSCs).

Monitored Drift Tubes

The MDT system is the largest individual subdetector of the MS. MDTs provide precision measurements of muon momenta as well as fast measurements used for triggers. There are 1088 MDT chambers providing coverage out to pseudorapidity $|\eta| < 2.7$; each consists of an aluminum tube containing an argon-CO_2 gas mixture. In the center of each tube there 50μm diameter tungsten-rhenium wire at a voltage of 3080 V. A muon entering the tube will induce ionization in the gas, which will "drift" towards the wire due to the voltage. One measures this ionization as a current in the wire; this current comes with a time measurement related to how long it takes the ionization to drift to the wire.

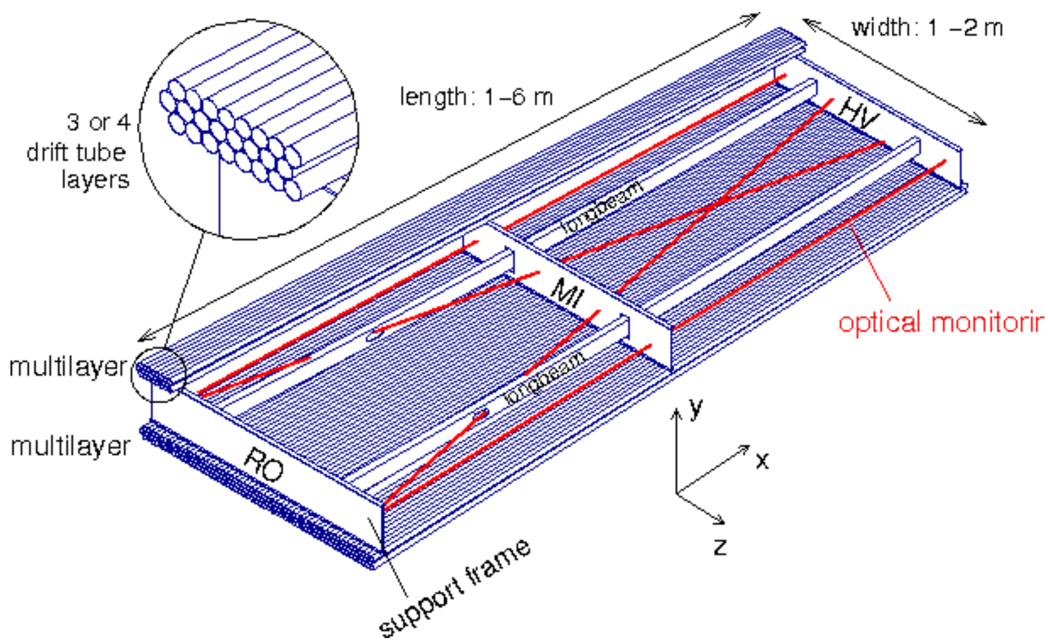

Figure 5.12: Schematic of a Muon Drift Tube chamber

These tubes are layered in a pattern shown in Fig. 5.12. Combining the measurements from the tubes in each layer gives good position resolution. The system consists of three subsystems of these layers, at 5 m, 7m, and 9 m from the interaction point. The innermost layer is directly outside the hadronic calorimeter. The combination of these three measurements gives precise momenta measurements for muons.

Resistive Plate Chambers

The RPC system is alternated with the MDT system in the barrel; the first two layers of RPC detectors surround the second MDT layer while the third is outside the final MDT layer. The RPC system covers pseudorapidity $|\eta| < 1.05$. Each RPC consists of two parallel plates at a distance of 2 mm surrounding a $C_2H_2F_4$ mixture. The electric field between these plates is 4.9k kV/mm. Just as in the MDTs, an incoming muon ionizes the gas, and the deposited ionization is collected by the detector (in this case on the plates). It is quite fast, but with a relatively poor spatial resolution of 1 cm. Still, it can provide reasonable ϕ resolution due to its large distance from the interaction point. This is most useful in triggering, where the timing requirements are quite severe. The RPCs are also complement the MDTs by providing a measurement of the non-bending coordinate.

Cathode Strip Chambers

The CSCs are used in place of MDTs in the first layer of the endcaps. This region, at $2.0 < |\eta| < 2.7$, has higher particle multiplicity at the close distance to the interaction point from low-energy photons and neutrons. The MDTs were not equip to deal with the higher particle rate of this region, so the CSCs were designed to deal with this deficiency.

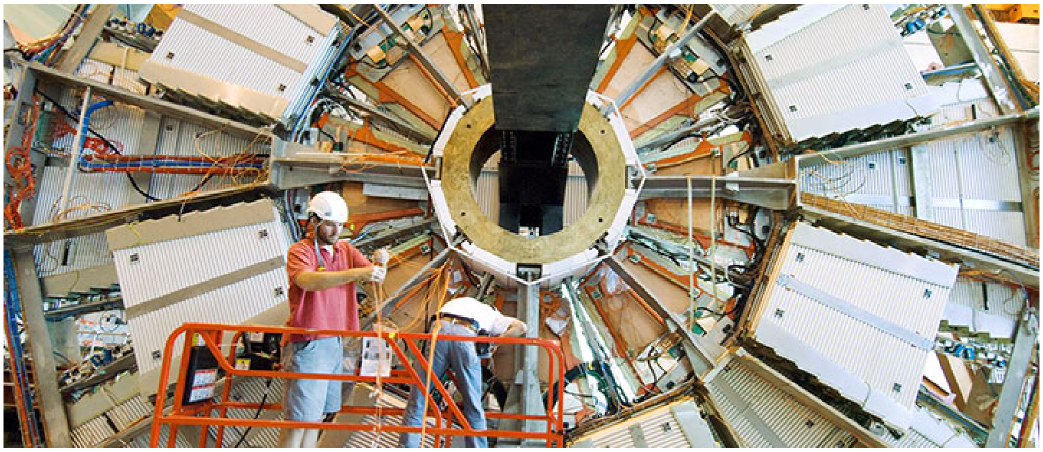

Figure 5.13: Photo of the installation of Cathode Strip Chambers and Monitored Drift Tubes

Each CSC consists multiwire proportional chambers, oriented radially outward from the interaction point. These chambers overlap partially in ϕ. The wires contain a gas mixture of argon and CO_2, which is ionized when muons enter. The detectors operate with a voltage of 1900 V, with much lower drift times than the MDTs. They provide less hits than MDTs, but their lower drift times lower uptime and reduce the amount of detector overload.

The CSCs are arranged into four planes on the wheels of the muon spectrometer, as seen in Fig.**??**. There are 32 CSCs in total, with 16 on each side of the detector in η.

Thin Gap Chambers

The TGCs serve the purpose of the RPCs in the endcap at pseudorapidity of $1.05 < |\eta| < 2.4$; they provide fast measurements used in triggering. The TGCs are also multiwire proportional chambers a la the CSCs. The fast readouts necessary for trigger are provided by a high electric field and a small wire-to-wire distance of 1.8 mm. These detectors provide both η and ϕ information, allowing the trigger to use as much information as possible when selecting events.

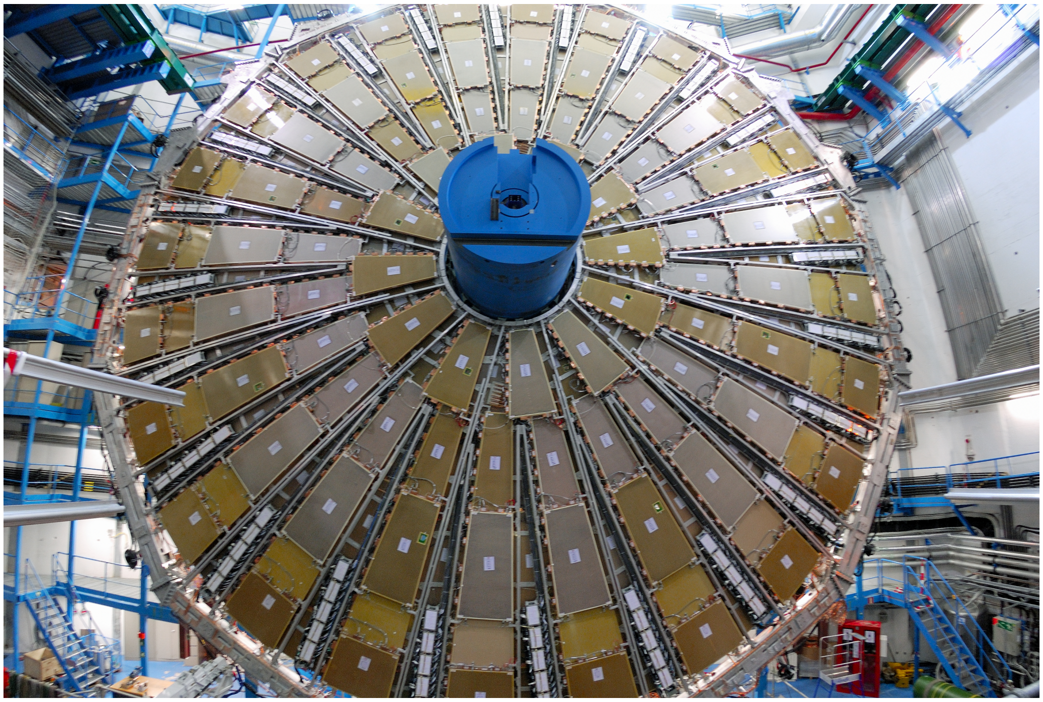

Figure 5.14: Photo of a muon Big Wheel, consisting of Thin Gap Chambers

5.5 Trigger System

The data rate delivered by the LHC is staggering [89]. In the 2016 dataset, the collision rate was 40 MHz, meaning a *bunch spacing* of 25 ns. In each of the event, as we saw in **??**, there are many proton-proton collisions. Most of the collisions are uninteresting, such as elastic scattering of protons, or even inelastic scattering leading to low-energy dijet events. These types of events have been studied in detail in previous experiments.

Even if one is genuinely interested in these events, it's *impossible* to save all of the information available in each event. If all events were written "to tape" (as the jargon goes), ATLAS would store terabytes of data per second. We are limited to only about 1000 Hz readout by computing processing time and storage space. We thus implement a *trigger* which provides fast inspection of events to drastically reduce the data rate from the 40 MHz provided by the LHC to the 1000 Hz we can write to tape for further analysis.

The ATLAS trigger system consists of a two-level trigger, known as the Level-1 trigger (L1 trigger) and the High-Level Trigger (HLT)[4]. Trigger selections are organized into *trigger chains*, where events passing a particular L1 trigger are passed to a corresponding HLT trigger. For example, one would require a particular high-p_{T} muon at L1, with additional quality requirements at HLT. One can also use HLT triggers as prerequisites for each other, as is done in some triggers requiring both jets and $E_{\mathrm{T}}^{\mathrm{miss}}$.

Level-1 Trigger

The L1 trigger is hardware-based, and provides the very fast rejection needed to quickly select events of interest. The L1 trigger uses only what is known as *prompt* data to quickly identify interesting events. Only the calorimeters and the triggering detectors (RPCs and TGCs) of the MS are fast enough to be considered at L1, since the tracking reconstruction algorithms used by the ID and the more precise MS detectors are very slow. This allows quick identification of events with the most interesting physical objects : large missing transverse momentum and high-p_{T} electrons, muons, and jets.

L1 trigger processing is done locally. This means that events are selected without considering the entire available event. Energy deposits over some threshold are reconstructed as *regions of interest*. These RoIs are then compared using pattern recognition hardware to “expected” patterns for the given RoIs. Events with RoIs matching these expected patterns are then handed to the HLT through the Central Trigger Processor. This step alone lowers the data rate down by about three orders of magnitude.

[4] In Run1, ATLAS ran with a three-level trigger system. The L1 was essentially as today; the HLT consisted of two separate systems known as the L2 trigger and the Event Filter (EF). This was changed to the simpler system used today during the shutdown between Run1 and Run2.

High-Level Trigger

The HLT performs the next step, taking the incoming data rate from the L1 trigger of ∼75 kHz down to the ∼1 kHz that can be written to tape. The HLT really performs much like a simplified offline reconstruction, using many common quality and analysis cuts to eliminate uninteresting events. This is done by using computing farms located close to the detector, which process events in parallel. Individually, each event which enters the computing farms takes about 4 seconds to reconstruct; the HLT reconstruction time also has a long tail, which necessitates careful monotoring of the HLT to ensure smooth operation.

HLT triggers are targetted to a particular physics process, such as a $E_{\mathrm{T}}^{\mathrm{miss}}$ trigger, single muon trigger, or multijet trigger. The collection of all triggers is known as the trigger *menu*. Since many low-energy particles are produced in collisions, it is necessary to set a *trigger threshold* on the object of interest; this is really just a fancy naming for a trigger p_{T} cut. Due to the changing luminosity conditions of the LHC, these thresholds change constantly, mostly by increasing thresholds with increasing instaneous luminosity. This allows an approximately constant number of events to be written for further analysis. Triggers which have rates higher than those designated by the menu are *prescaled*. This means writing only some fraction of the triggered events. Of course, for physics analyses, one wishes to investigate all data events passing some set of analysis cuts, so often one uses the "lowest threshold unprescaled trigger". *Turn-on curves* allow one to select the needed offline analysis cut to ensure the trigger is fully efficient. An example turn-on curve for the $E_{\mathrm{T}}^{\mathrm{miss}}$ triggers used in the signal region of this analysis is shown in **??**.

The full set of the lowest threshold unprescaled triggers considered here can be found in Tab. 5.1. These are the lowest unprescaled triggers associated to the SUSY signal models and Standard Model backgrounds considered in this thesis. More information can be found in [89].

Physics Object	Trigger	p_{T} Threshold (GeV)	Level-1 Seed	Additional Requirements	Approximate Rate (Hz)
2015 Data					
$E_{\mathrm{T}}^{\mathrm{miss}}$	HLT_xe70	70	L1_XE50	-	60
Muon	HLT_mu24_iloose_L1MU15	24	L1_MU15	isolated, loose	130
Muon	HLT_mu50	50	L1_MU15	-	30
Electron	HLT_e24_lhmedium_iloose_L1EM20VH	24	L1_EM20VH	medium OR isolated, loose	140
Electron	HLT_e60_lhmedium	60	L1_EM20VH	medium	10
Electron	HLT_e120_lhloose	120	L1_EM20VH	loose	<10
Photon	HLT_g120_loose	120	L1_EM20VH	loose	20
2016 Data					
$E_{\mathrm{T}}^{\mathrm{miss}}$	HLT_xe100_mht_L1XE50	100	L1_XE50	-	180
Muon	HLT_mu24_ivarmedium	24	L1_MU20	medium	120
Muon	HLT_mu50	50	L1_MU20	-	40
Electron	HLT_e24_lhtight_nod0_ivarloose	24	L1_EM22VHI	tight with no d_0 or loose	110
Electron	HLT_e60_lhmedium_nod0	60	L1_EM22VHI	medium with no d_0	10
Electron	HLT_e140_lhloose_nod0	140	L1_EM22VHI	loose with no d_0	<10
Photon	HLT_g140_loose	140	L1_EM22VHI	loose	20

Table 5.1: High-Level Triggers used in this thesis. Descriptions of loose, medium, tight, and isolated can be found in [89]. The d_0 cut refers to a quality cut on the vertex position; this was removed from many triggers in 2016 to increase sensitivity to displaced vertex signals. For most triggers, the increased thresholds in 2016 compared to 2016 were designed to keep the rate approximately equal. The exception is the $E_{\mathrm{T}}^{\mathrm{miss}}$ triggers; see Sec. 5.5.

Razor Triggers

For the analysis presented in this thesis, the *razor triggers* were developed. These are topological triggers, combining both jet and $E_{\mathrm{T}}^{\mathrm{miss}}$ information to select interesting events. In particular, they use the razor variable M_{Δ}^{R}which will be described in Chapter **??**.

Based on 2015 run conditions, these triggers would have allowed the use of a lower offline $E_{\mathrm{T}}^{\mathrm{miss}}$ cut with a similar rate to the nominal $E_{\mathrm{T}}^{\mathrm{miss}}$ triggers. This can be seen in the turn-on curves shown in Fig. 5.15. The razor triggers are fully efficient at nearly 100 GeVlower than the corresponding $E_{\mathrm{T}}^{\mathrm{miss}}$ triggers in M_{Δ}^{R}.

There was a quite big change in the 2016 menu, which increased the rate given to $E_{\mathrm{T}}^{\mathrm{miss}}$ triggers drastically. This can be seen in the difference in rate shown between $E_{\mathrm{T}}^{\mathrm{miss}}$ triggers in 2015 and 2016 in Tab. 5.1. This allowed the $E_{\mathrm{T}}^{\mathrm{miss}}$ triggers to maintain a lower threshold throughout the dataset used in this thesis.

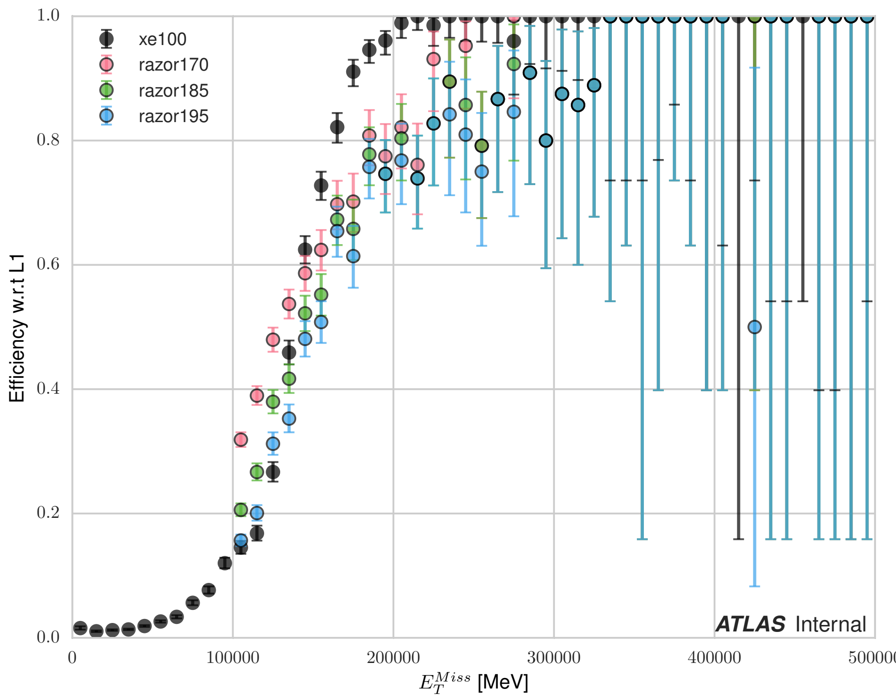

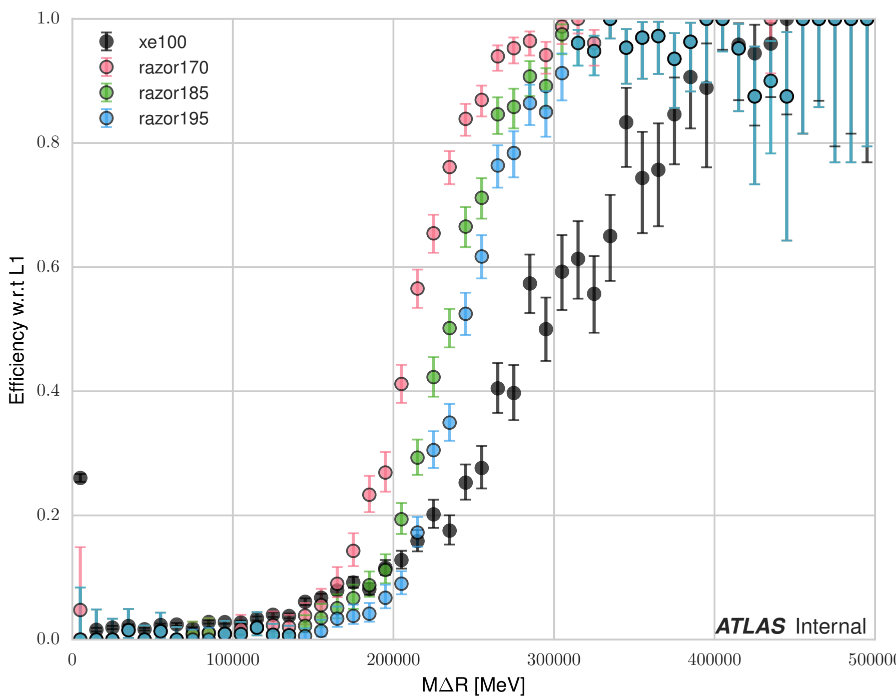

Figure 5.15: Turn-on curves for the razor triggers and nominal $E_{\mathrm{T}}^{\mathrm{miss}}$ trigger. The razor triggers show a much sharper turn-on in M_{Δ}^{R}relative to the $E_{\mathrm{T}}^{\mathrm{miss}}$ trigger. The converse is true for the $E_{\mathrm{T}}^{\mathrm{miss}}$ triggers.

Chapter 6

Object Reconstruction

This chapter describes the reconstruction algorithms used within ATLAS. We will make the distinction between the "primitive" objects which are reconstructed from the detector signals from the "composite" physics objects we use in measurements and searches for new physics.

6.1 Primitive Object Reconstruction

The primitive objects reconstructed by ATLAS are *tracks* and (calorimeter) *clusters*. These are reconstructed directly from tracking hits and calorimeter energy deposits into cells. Tracks can be further divided into inner detector and muon spectrometer tracks. Calorimeter clusters can be divided into sliding-window clusters and topological clusters (topoclusters).

Inner Detector Tracks

Inner detector tracks are reconstructed from hits in the inner detector [90, 91] These hits indicate that a charged particle has passed through the detector material. Due to the 2 T solenoid in the inner detector, the hits associated with any individual particle will be curved. The amount of curvature determines the momentum of the particle. In any given event, there is upwards of 10^4 hits, making it impossible to do any sort of combinatorics to reconstruct tracks. There are two algorithms used by ATLAS track reconstruction, known as *inside-out* and *outside-in*.

ATLAS first employs the inside-out algorithm. One assumes the track begins at the interaction point. Moving out from the interaction point, one creates track seeds. Track seeds are proto-tracks constructed from three hits. These hits can be distributed as three pixel hits, two pixel hits and one SCT hit, or three SCT hits. One extrapolates the track and uses a combinatorial Kalman filter [90], which adds the rest of the pixel and SCT hits to the seeds. This is done seed by seed, so it avoids the combinatorial complexity involved with checking all hits with all seeds. At this point, the algorithm applies an additional filter to avoid ambiguities from nearby tracks. The TRT hits are added to the seeds using the same method. After this procedure, all hits are associated to a track.

The next step is to determine the correct kinematics of the track. This is done by applying a fitting algorithm which outputs the best-fit track parameters by minimizing the track distance from hits, weighted by each hit's resolution. These parameters are $(d_0, z_0, \eta, \phi, q/p)$ where d_0 (z_0) is the transverse (longitudinal) impact parameter and q/p is the charge over the track momenta. This set of parameters uniquely defines the measurement of the trajectory of the charged particle associated to the track. An illustration of a track with these parameters is shown in Fig. 6.1.

The other track reconstruction algorithm is the outside-in algorithm. As the name implies, we start from the outside of the inner detector, in the TRT, and extend the tracks in toward the interaction point. One begins by seeding from TRT hits, and extending the track back towards the center of the detector. The same fitting procedure is used as in the inside-out algorithm to find the optimal track parameters. This algorithm is particularly important for finding tracks which originate from interactions with the detector material, especially the SCT. For tracks from primary vertices, this often finds the same tracks as the inside-out algorithm, providing an important check on the consistency of the tracking procedure.

In the high luminosity environment of the LHC, even the tracks reconstructed

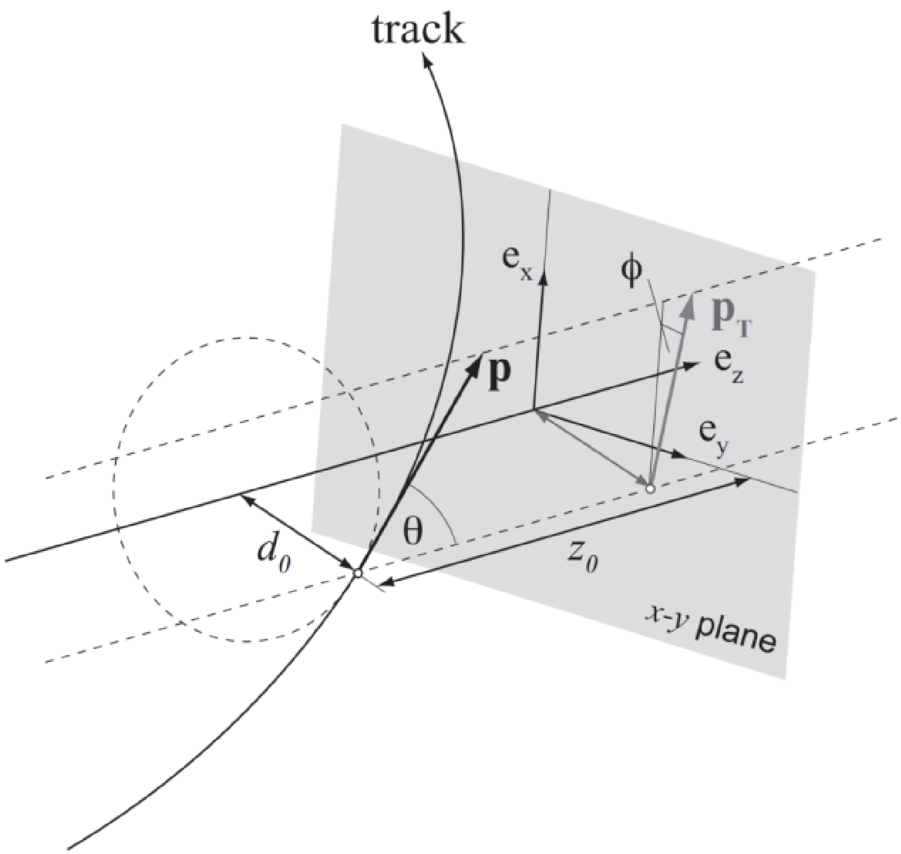

Figure 6.1: The parameters associated to a track.

from precision detectors such as those of ATLAS inner detector can sometimes lead to fake tracks from simple combinatoric chance. Several quality checks are imposed after track fitting which reduce this background. Seven silicon (pixel + SCT) hits are required for all tracks. No more than two *holes* are allowed in the pixel detector. Holes are expected measurements from the track that are missing in the pixel detector. Finally, tracks with poor fit quality, as measured by χ^2/ndf, are also rejected. Due to the high quality of the silicon measurements in the pixel detector and SCT, these requirements give good track reconstruction efficiency, as seen in Fig. 6.2 for simulated events [92].

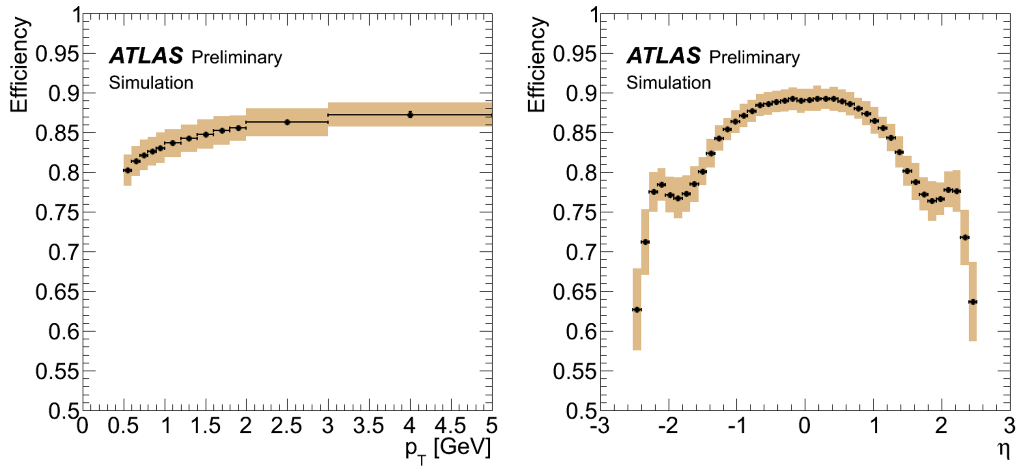

(a) Track reconstruction as a function of $p_{\rm T}$. (b) Track reconstruction as a function of η.

Figure 6.2: Track reconstruction efficiency as a function of track $p_{\rm T}$ and η. The efficiency is defined as the number of reconstructed tracks divided by the number of generate charged particles.

Sliding-window clusters

The sliding-window algorithm is a way to combine calorimeter cells into composite objects (clusters) to be used as inputs for other algorithms [93]. Sliding-window clusters are the primary inputs to electron and photon reconstruction, as described below. The electromagnetic calorimeter has high granularity, with a cell size of $(\eta, \phi) = (.025, .025)$ in the coarsest second layer throughout most of the calorimeter. The “window” consists of 3 by 5 cells in the (η, ϕ) space. All layers are added on this same 2D space. One translates this window over the space and seeds a cluster whenever the energy sum of the cells is maximized. If the seed energy is greater than 2.5 GeV, this seed is called a sliding-window cluster. This choice was motivated to optimize the reconstruction efficiency of proto-electrons and proto-photons while rejecting fakes from electronic noise and additional particles from pileup vertices.

Topological clusters

Topoclusters are the output of the algorithm used within ATLAS to combine hadronic and electromagnetic calorimeter cells in a way which extracts signal from a background of significant electronic noise [94]. They are the primary input to the algorithms which reconstruct jets.

Topological clusters are reconstructed from calorimeter cells in the following way. First, one maps all cells onto a single $\eta - \phi$ plane so one can speak of *neighboring* cells. Two cells are considered neighboring if they are in the same layer and directly adjacent, or if they are in adjacent layers and overlap in $\eta - \phi$ space. The *significance* ξ_{cell} of a cell during a given event is

$$\xi_{\text{cell}} = \frac{E_{\text{cell}}}{\sigma_{\text{noise,cell}}} \tag{6.1}$$

where $\sigma_{\text{noise,cell}}$ is measured for each cell in ATLAS and E_{cell} measures the current energy level of the cell. One thinks of this as the measurement of the energy *over threshold* for the cell.

Topocluster *seeds* are defined as calorimeter cells which have a significance $\xi_{\text{cell}} > 4$. These are the inputs to the algorithm. One iteratively tests all cells adjacent to these seeds for $\xi_{\text{cell}} > 2$. Each cells passing this selection is then added to the topocluster, and the procedure is repeated. When the algorithm reaches the point where there are no additional adjacent cells with $\xi_{\text{cell}} > 2$, every positive-energy cell adjacent to the current proto-cluster is added. The collection of summed cells is a topocluster. An example of this procedure for a simulation dijet event is shown in Fig. 6.3.

There are two calibrations used for clusters [95]. These are known as the electromagnetic (EM) scale [96] and the local cluster weighting (LCW) scale [94]. The EM scale is the energy read directly out of the calorimeters as described. This scale is appropriate for electromagnetic processes. The LCW scale applies additional

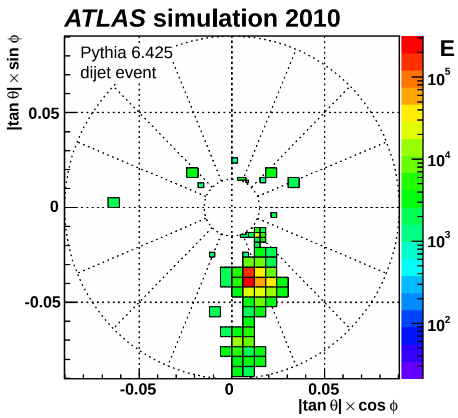

(a) All cells with $\xi_{\text{cell}} > 4$.

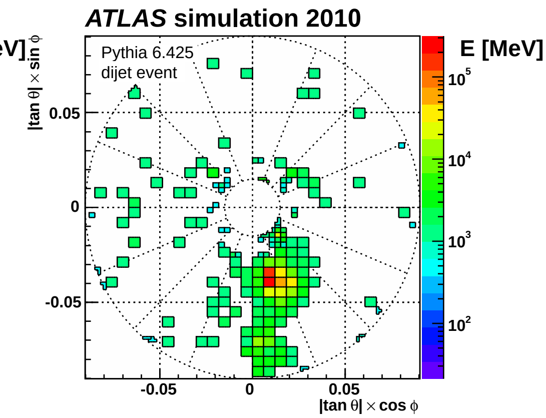

(b) All cells with $\xi_{\text{cell}} > 2$.

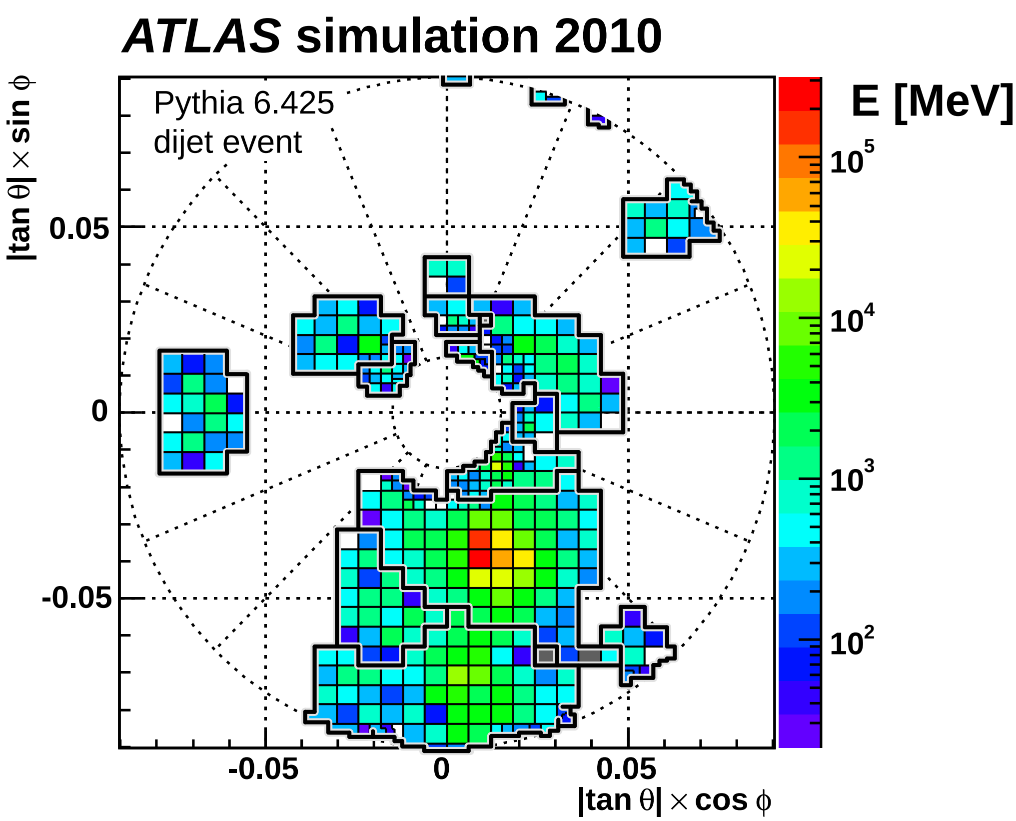

(c) All clustered cells.

Figure 6.3: Example of topoclustering on a simulated dijet event.

scaling to the clusters based on the shower development. The cluster energy can be corrected for calorimeter noncompensation and the differences in the hadronic and electromagnetic calorimeters' responses. This scale provides additional corrections that improve the accuracy of hadronic energy measurements. This thesis only uses the EM scale corrections. LCW scaling requires additional measurements that only became available with additional data. Due to the jet calibration procedure that we will describe below, it is also a relatively complicated procedure to rederive the "correct" jet energy.

Muon Spectrometer Tracks

Muon spectrometer tracks are fit using the same algorithms as the ID tracks, but different subdetectors. The tracks are seeded by hits in the MDTs or CSCs. After seeding in the MDTs and CSCs, the hits from all subsystems are refit as the final MS track. These tracks are used as inputs to the muon reconstruction, as we will see below.

6.2 Physics Object Reconstruction and Quality Identification

There are essentially six objects used in ATLAS searches for new physics: electrons, photons, muons, τ-jets, jets, and $E_{\mathrm{T}}^{\mathrm{miss}}$. The reconstruction of these objects is described here. In this thesis, τ lepton jets are not treated differently from other hadronic jets, and we will not consider their reconstruction algorithms. A very convenient summary plot is shown in Fig. 6.4.

One often wishes to understand "how certain" we are that a particular object is truly the underlying physics object. In ATLAS, we often generically consider, in

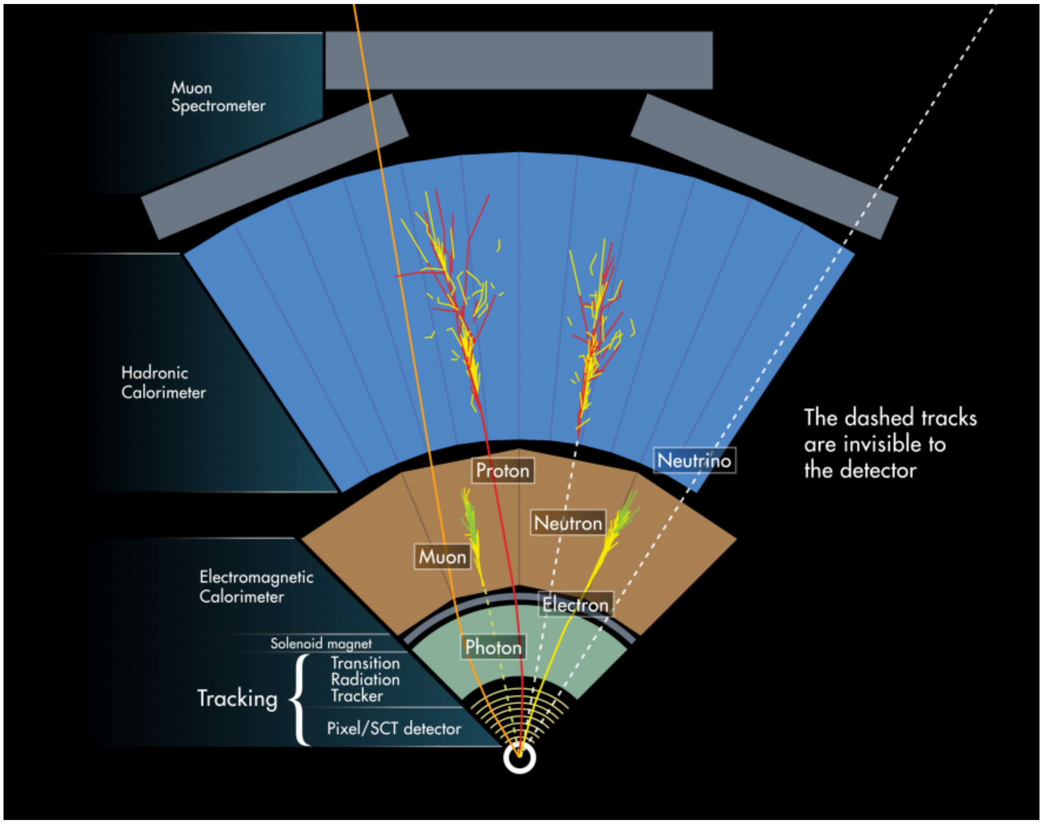

Figure 6.4: The interactions of particles with the ATLAS detector. Solid lines indicate the particle is interacting with the detector, while dashed lines are shown where the particle does not interact.

order, *very loose*, *loose*, *medium*, and *tight* objects[1]. These are ordered in terms of decreasing object efficiency, or equivalently, decreasing numbers of fake objects. We will also describe briefly the classification of objects into these categories.

In this thesis, since we present a search for new physics in a zero lepton final state, we will provide additional details about jet and $E_{\mathrm{T}}^{\mathrm{miss}}$ reconstruction.

[1] These are not all used for all objects, but it's conceptally useful to think of these different categories.

Electrons and Photons

Reconstruction

The reconstruction of electrons and photons (often for brevity called “electromagnetic objects”) is very similar [93, 97, 98]. This is because the reconstruction begins with the energy deposit in the calorimeter in the form of an electromagnetic shower. For any incoming e/γ, many more electrons and photons are produced in the shower. The measurement in the calorimeter is similar for these two objects.

One begins the reconstruction of electromagnetic objects from the sliding-window clusters reconstructed from the EM calorimeter. These $E > 2.5$ GeV clusters the the primary seed for electrons and photons. One then looks for all ID tracks within $\Delta R < 0.3$, where $\Delta R = \sqrt{\Delta\eta^2 + \Delta\phi^2}$. We “match” the track and cluster if they are within $\Delta\phi < 0.2$ in the direction of track curvature, or $\Delta\phi < 0.05$ in the direction opposite the track curvature. Those track-cluster seeds with tracks pointing to the primary vertex are reconstructed as electrons.

For photons, we have two options to consider, known as *converted* and *unconverted* photons. Due to the high energy of the LHC collisions, typical photons have energy $>\sim$ 1 GeV. At this scale, photons interact almost exclusively via pair-production in the presence of the detector material, as shown in Fig. 6.5 [56]. If the track-cluster seed has a track which does not point at the primary vertex, we reconstruct this object as a converted photon. This happens since the photon travels a distance before decay into two electrons, and see the tracks coming from this secondary vertex. Those clusters which do not have any associated tracks are then reconstruced as an unconverted photon.

The final step in electromagnetic object reconstruction is the final energy value. This process is different between electrons and photons due to their differing signatures in the EM calorimeter. In the barrel, electrons energies are assigned as

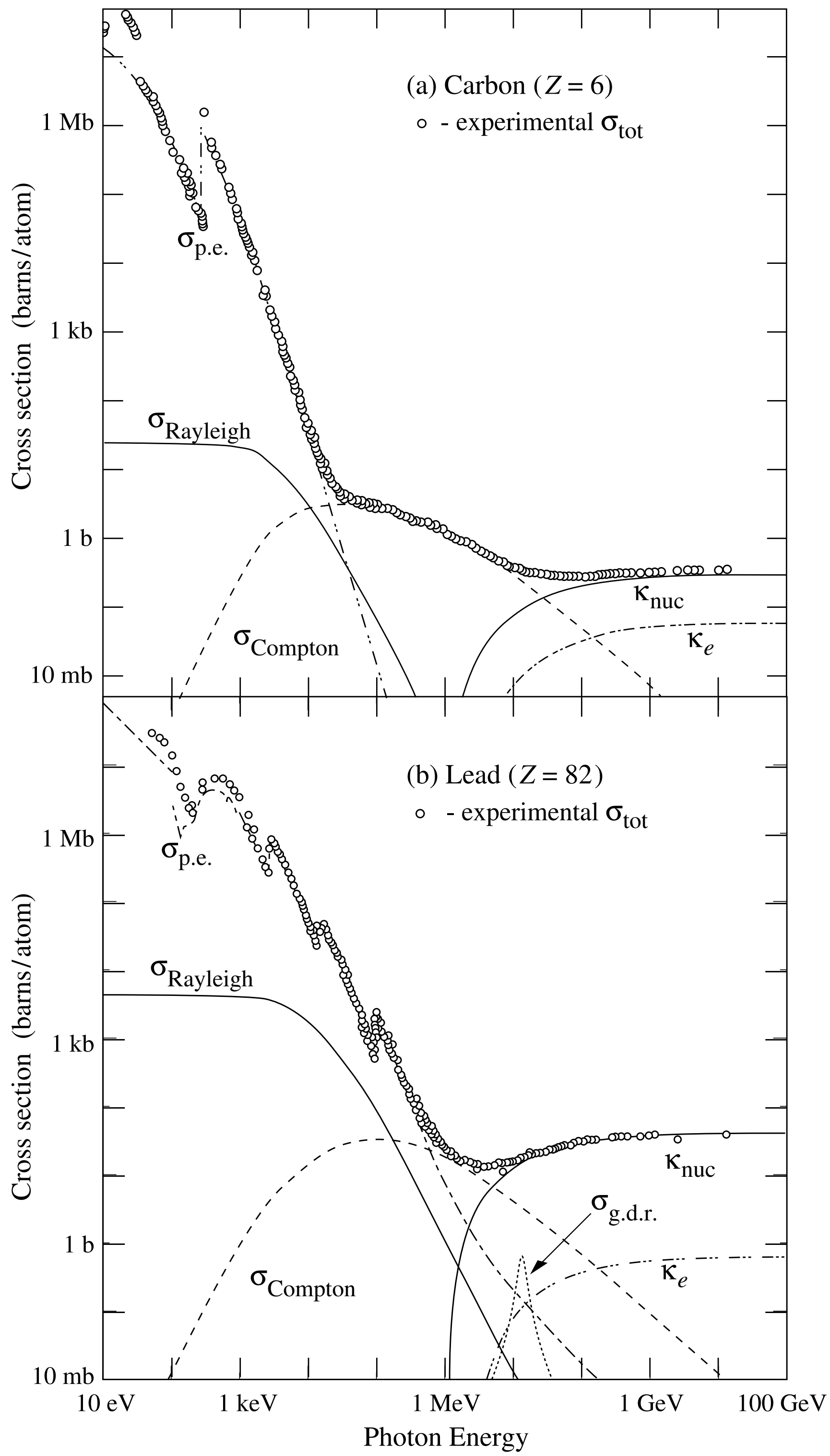

Figure 6.5: Photon total cross sections as a function of energy in carbon and lead, showing the contributions of different processes [56].

the sum of the 3 clusters in η and 7 clusters in ϕ to account for the electron curving in the ϕ direction. Barrel photons are assigned the energy sum of $(3, 5)$ clusters in (η, ϕ) space. In the endcap, the effect of the magnetic field on the electrons is smaller, and there is a coarser granularity. Both objects sum the $(5, 5)$ clusters for their final energy value.

Quality Identification

Electrons have a number of important backgrounds which can give fakes. Fake electrons come primarily from secondary vertices in hadron decays or misidentified hadronic jets. To reduce these backgrounds, quality requirements are imposed on electron candidates. Loose electrons have requirements imposed on the shower shapes in the electromagnetic calorimeter and on the quality of the associated ID track. There is also a requirement that there is a small energy deposition in the hadronic calorimeter behind the electron, to avoid jets being misidentified as electrons (low hadronic leakage). Medium and tight electrons have increasingly stronger requirements on these variables, and additional requirements on the isolation (as measured by ΔR) and matching of the ID track momentum and the calorimeter energy deposit.

Photons are relatively straightforward to measure, since there are few background processes [99]. The primary is pion decays to two photons, which can cause a jet to be misidentified as photon. Loose photons have requirements on the shower shape and hadronic leakage. Tight photons have tighter shower shape cuts, especially on the high granularity first layer of the EM calorimeter. The efficiency for unconverted tight photons as a function of p_{T} is should in

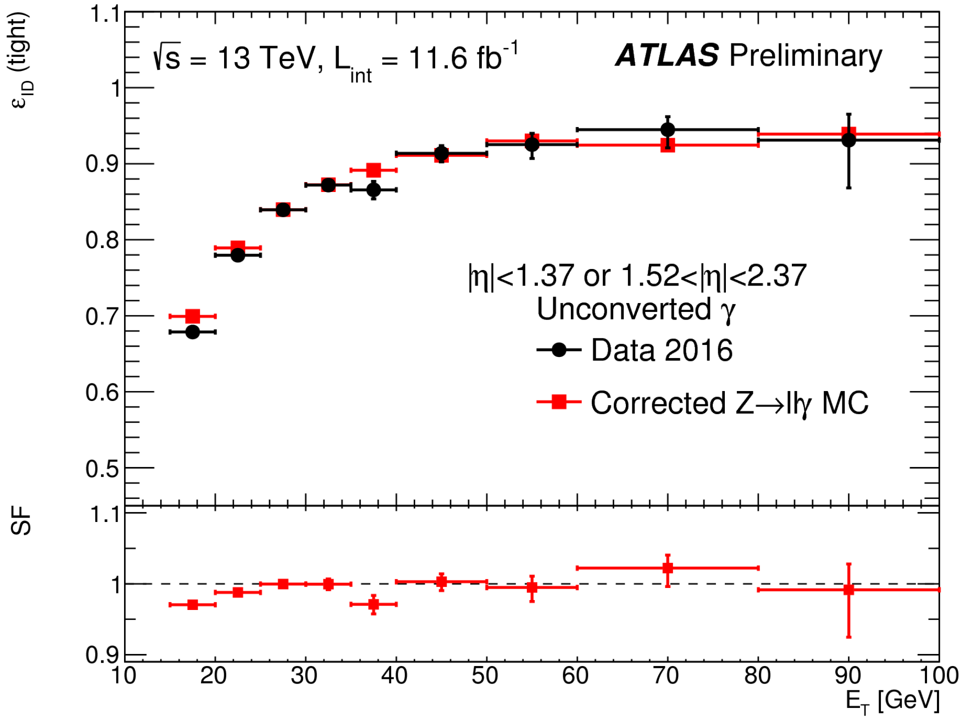

Figure 6.6: Unconverted photon efficiency as measured in [99].

1134 # Muons

1135 ## Reconstruction

1136 Muons are reconstructed using measurements from all levels of the ATLAS detector [100]. They leave a ID track, a small, characteristic deposition in the EM calorimeter, and then a track in the muon spectrometer. The primary reconstruction technique produces a so-called *combined* muon. "Combined" means using a combination of the ID and MS tracks to produce the final reconstruced muon kinematics. This is done by refitting the hits associated to both tracks, and using this refit track for the muon kinematics.

1143 ## Quality Identification

Several additional criteria are used to assure muon measurements are free of significant background contributions, especially from pion and kaon decays to muons.

Muons produced via these decay processes are often characterized by a "kink". Candidate muons with a poor fit quality, characterized by χ^2/n.d.f., are thus rejected. Additionally, the absolute difference in momentum measurements between the ID and MS provide another handle, since the other decay products from hadron decays carry away some amount of the initial hadron momentum. This is measured by

$$\rho' = \frac{|p_{\mathrm{T}}^{\mathrm{ID}} - p_{\mathrm{T}}^{\mathrm{MS}}|}{p_{\mathrm{T}}^{\mathrm{Combined}}}. \tag{6.2}$$

Additionally, there is a requirement on the q/p significance, defined as

$$S_{q/p} = \frac{|(q/p)^{\mathrm{ID}} - (q/p)^{\mathrm{MS}}|}{\sqrt{\sigma_{\mathrm{ID}}^2 + \sigma_{\mathrm{MS}}^2}}. \tag{6.3}$$

The $\sigma_{\mathrm{ID,MS}}$ in the denominator of Eq.Eq. (6.3) are the uncertainties on the corresponding quantity from the numerator. Finally, cuts are placed on the number of hits in the various detector elements.

Subsequently tighter cuts on these variables allow one to define the different muon identification criteria. Loose muons have the highest reconstruction efficiency, but the highest number of fake muons, since there are no requirements on the number of subdetector hits and the loosest requirements on the suite of quality variables. Medium muons consist of Loose muons with tighter cuts on the quality variables. They also require more than three MDT hits in at least two MDT layers. These are the default used by ATLAS analyses. Tight muons have stronger cuts than those of the medium selection, and reducing the reconstruction efficiency. The reconstruction efficiency as a function of p_{T} can be seen for Medium muons in Fig. 6.7.

Jets

Jets are composite objects corresponding to many physical particles [56, 101, 102] This is a striking difference from the earlier particles. Fortunately, we normally (and in this thesis) only need information about the original particle produced in the

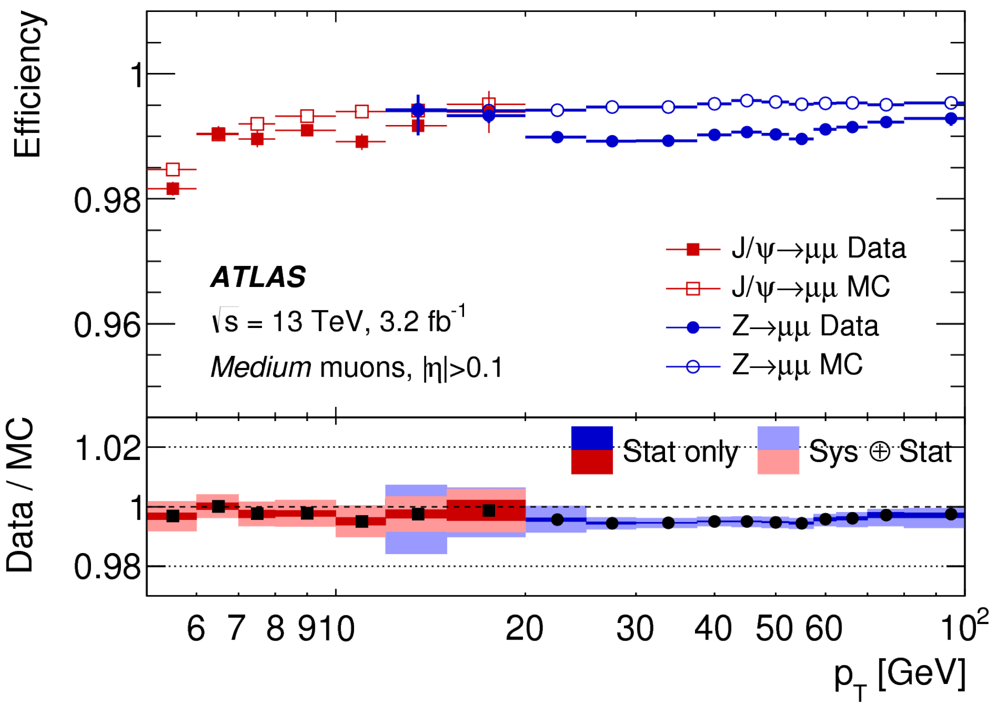

Figure 6.7: Medium muon efficiency as measured in [100].

primary collision. In the SM, this corresponds to quarks and gluons. Due to the hadronization process, free quarks and gluons spontaneously hadronize and produce a hadronic shower, which we call a jet. These showers can be measured by the EM and hadronic calorimeters, and the charged portions can be measured in the ID. The first step is to combine these measurements into a composite object representing the underlying physical parton. This is done via jet algorithms.

Jet Algorithms

It might seem straightforward to combine the underlying physical particles into a jet. There are three important characteristics required for any jet reconstruction algorithm to be used by ATLAS.

- Collinear safety - if any particle with four-vector p is replaced by two particles of p_1, p_2 with $p = p_1 + p_2$, the subsequent jet should not change

- Radiative (infrared) safety - if any particle with four-vector p radiates a particle of energy $\alpha \to 0$, the subsequent jet should not change

- Fast - the jet algorithm should be "fast enough" to be useable by ATLAS computing resources

The first two requirements can be seen in terms of requirements on soft gluon emission. Since partons emit arbitrarily soft gluons freely, one should expect the algorithms to not be affected by this emission. The final requirement is of course a practical limitation.

The algorithms in use by ATLAS (and CMS) which satisfies these requirements are collectively known as the k_T algorithms [103–105]. These algorithms iteratively combine the "closest" objects, defined using the following distance measures :

$$\begin{aligned} d_{ij} &= \min(k_{T,i}^{2p}, k_{T,j}^{2p})\frac{\Delta_{ij}^2}{R^2} \\ d_{iB} &= k_{T_i}^{2p} \end{aligned} \tag{6.4}$$

In Eq.Eq. (6.4), $k_{T,i}$ is the transverse momentum of i-th jet *constituent* and Δ_{ij} is the angular distance ΔR between the constituents. Both R and p are adjustable parameters: R is known as the (jet) *cone size* and p regulates the power of the energy versus the geometrical scales. The algorithm sequence, for a given set of objects i with four-vector k :

1. Find the minimum distance in the set of all d_{ij} and d_{iB}.

2. If the distance is one of the d_{ij}, combine the input pair of object i, j and return to (1). If the distance is one of the d_{iB}, remove the object from the list, call it a jet, and return to (1).

This process ends when all objects i have been added to a jet.

Any choice of (p, R) has requirements of collinear and radiative safety. In essence, the choice is then to optimize based on speed and the potential for new physics discoveries. In ATLAS, we make the choice of $p = -1$ which is also known as the *anti-k_T* algorithm. The choice of $R = 0.4$ is used for the distance parameter of the jets.

The primary "nice" quality of this algorithm can be seen with the following example. Consider three inputs to an anti-$k_T$algorithm, all with $\eta = 0$:

- Object 1 : (p_{T}, ϕ) = (30 GeV, 0)
- Object 2 : (p_{T}, ϕ) = (20 GeV, -0.2)
- Object 3 : (p_{T}, ϕ) = (10 GeV, 0.2)
- Object 4 : (p_{T}, ϕ) = (1 GeV, 0.5)

In the case shown, it seems natural to first combine the "bigger" objects 1 and 2. These then pick up the extra small object 3, and object 4 is not included in the jet. This is what is done by the anti-$k_T$algorithm. The (normal) $k_T$algorithm with $p = 1$ instead combines the smallest objects, 3 and 4, first. Object 1 and 2 combine to form their own jet, instead of these jets picking up object 3. This behavior is not ideal due to effects from pileup, as we will see in the next section.

Jet Reconstruction

In ATLAS, jets are reconstructed using multiple different objects as inputs, including tracks, "truth" objects, calorimeter clusters, and *particle flow objects* (PFOs). For physics analyses, ATLAS primarily uses jets reconstructed from calorimeter clusters, but we will describe the others here, as they are often used for systematic uncertainties.

Calorimeter jets are reconstructed using topoclusters with the anti-$k_T$algorithm with $R = 0.4$. The jet reconstruction algorithm is run on the collection of all topoclusters reconstructed as in Sec. 6.1. Both EM and LCW scale clusters are used in the ATLAS reconstruction software and produce two sets of jets for analysis. As stated above, this thesis presents an analysis using jets reconstructed using EM scale clusters, which we refer to as *EM jets*.

Tracks can be used as inputs to jet reconstruction algorithms. Jets reconstructed from tracks are known as *track jets*. Since the ID tracks do not measure neutral objects, these jets underestimate the true jet energy. However, these are still useful for checks and derivations of systematic uncertainties.

Truth jets are reconstructed from *truth* particles. In this case, truth is jargon for simulation. In simulation, the actual simulated particles are available and used as inputs to the jet reconstruction algorithms. Similarly to track jets, these are not useful in and of themselves, but are used in conjunction with studies of reconstructed jets.

The last object used as inputs to jet reconstruction algorithms are *particle flow objects* (PFOs). These are used extensively as the primary input to jet particle reconstruction algorithms by the CMS collaboration [106]. Particle flow objects are reconstructed by associating tracks and clusters through a combination of angular distance measures and detector response measurements to create a composite object which contains information from both the ID and the calorimeters. For calorimeter clusters which do not have any associated ID track, the cluster is simply the PFO. The natural association between tracks and clusters provides easy pileup subtraction since tracks are easily associated to the primary vertex. As pileup has increased, the utility of using PFOs as inputs to jet reconstruction has increased as well.

Jet Calibration

Jets as described in the last section are still *uncalibrated*. Even correcting the cluster energies using the LCW does not fully correct the jet energy, due to particles losing energy in the calorimeters. This is corrected using the *jet energy scale* (JES). The

JES is a series of calibrations which on average restore the correct truth jet energy for a given reconstructed jet. The steps to derive the JES are described in Fig. 6.8 and described here.

The first step is the origin correction. This adjusts the jet to point at the primary vertex. Next, is the jet-area based pileup correction. This step subtracts the "average" pileup as measured by the energy density ρ outside of the jets and assumes this is a good approximation for the pileup inside the jet. One removes energy $\Delta E = \rho \times A_{\text{jet}}$ in this step. The residual pileup correction applies a final offset correction by parametrizing the change in jet energy as a function of the number of primary vertices N_{PV} and the average number of interactions μ. More details can be found in [102].

The next step is the most important single correction, known as the AbsoluteEtaJES. Due to the use of noncompensation and sampling calorimeters in ATLAS, the measured energy of a jet is a fraction of the true energy of the outgoing parton. Additionally, due to the use of different technologies and calorimeters throughout the detector, there are directional biases induced by these effects. The correction bins a multiplicative factor in p_{T} and η which scales the reconstructed jets to corresponding truth jet p_{T}. This step does not entirely correct the jets, since it is entirely a simulation-based approach.

The final steps are known as the global sequential calibration (GSC) and the residual in-situ calibration. The GSC uses information about the jet showering shape to apply additional corrections based on the expected shape of gluon or quark jets. The final step is the residual in-situ calibration, which is only applied to data. This step uses well-measured objects recoiling off a jet to provide a final correction to the jets in data. In the low p_{T} region (20 GeV$\lesssim p_{T,\text{jet}} \lesssim$ < 200 GeV), $Z \to ll$ events are used as a reference object. In the p_{T} region (100 GeV$\lesssim p_{T,\text{jet}} \lesssim$600 GeV), the reference object is a photon, while in the high p_{T} region ($p_{T,\text{jet}} \lesssim$200 GeV), the high p_{T} jet is

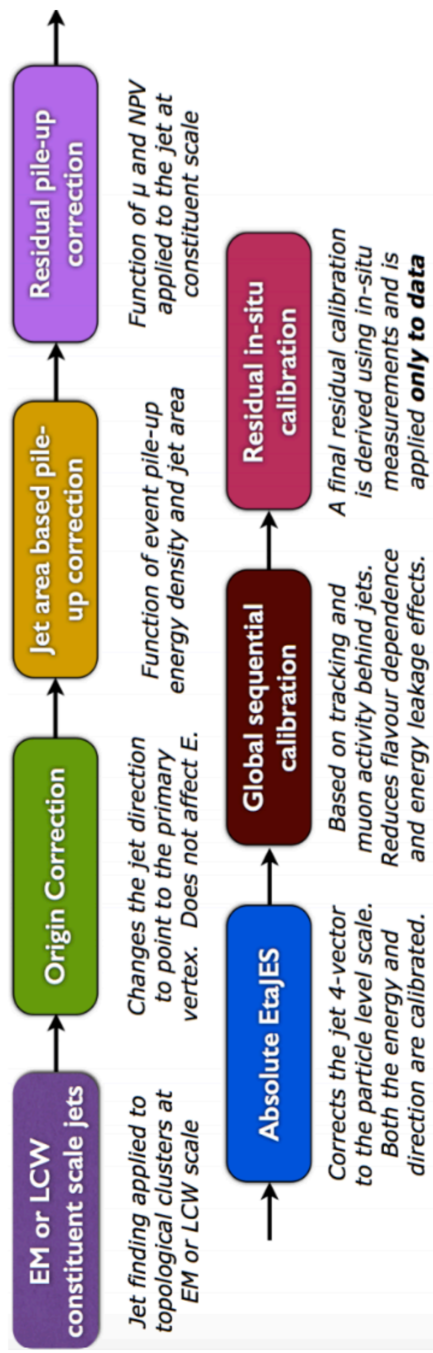

Figure 6.8: The steps used by ATLAS to calibrate jets

compared to multiple smaller p_T jets. The reference object is the group of multijets. After the application of the residual in-situ calibration, the data and MC scales are identical up to corresponding uncertainties. The combined JES uncertainty as a function of p_T is shown in Fig. 6.9.

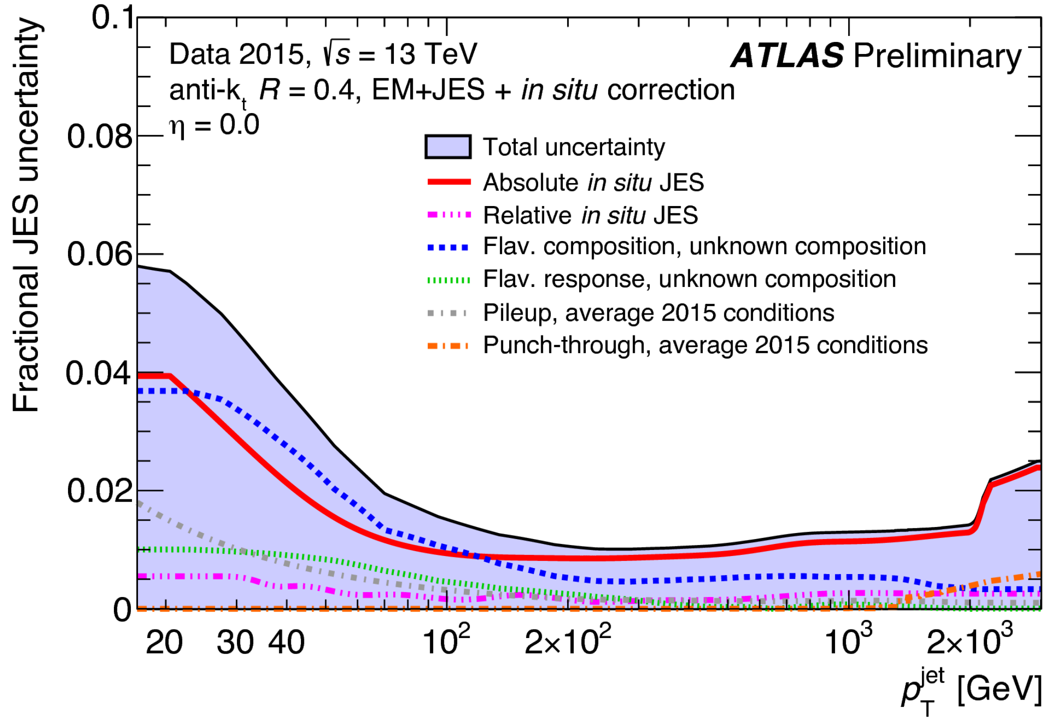

Figure 6.9: Combined jet energy scale uncertainty as a function of p_{T} at $\eta = 0$.

Jet Vertex Tagger

The *jet vertex tagger* (JVT) technique is used to separate pileup jets from those associated to the hard primary vertex [107]. The technique for doing so first involves *ghost association* [108]. Ghost association runs the anti-k_T jet clustering algorithm on a combined collection of the topoclusters and tracks. The tracks *only* momenta are set to zero[2], with only the directional information included. As discussed above, the anti-k_T algorithm is "big to small"; tracks are associated to the "biggest" jet near them in (η, ϕ). This method uniquely associates each track to a jet, without changing the final jet kinematics.

The JVT technique uses a combination of track variables to determine the likelihood that the jet originated at the primary vertex. For jets which have associated tracks from ghost association, this value ranges from 0 (likely pileup jet) to 1 (likely

[2]Not exactly zero, since zero momentum tracks wouldn't have a well-defined (η, ϕ) coordinate, but set to a value obeying $p_{\mathrm{T,track}} << 400$ MeV $= p_{\mathrm{track,min}}$. This is the minimum momentum for a track to reach the ATLAS inner detector.

hard scatter jet). Jets without associated tracks are assigned JVT $= -.1$. The working point of JVT $> .59$ is used for jets in this thesis.

B-jets

Jets originating from bottom quarks (b-jets) can be *tagged* by the ATLAS detector [109, 110]. B-hadrons, which have a comparatively long lifetime compared to hadrons consisting of lighter quarks, can travel a macroscopic distance inside the ATLAS detector. The high-precision tracking detectors identify the secondary vertices from these decays and the jet matched to that vertex is called a *b-jet*. The `MV2c10` algorithm [109, 110], based on boosted decision trees, identifies these jets using a combination of variables sensitive to the difference between light-quark and b-quark jets. The efficiency of this tagger is 77%, with a rejection factor of 134 for light-quarks and 6 for charm jets.

Missing Transverse Momentum

Missing transverse momentum $E_{\mathrm{T}}^{\mathrm{miss}}$ [111] is a key observable in searches for new physics, especially in SUSY searches [112, 113]. However, $E_{\mathrm{T}}^{\mathrm{miss}}$ is not a uniquely defined object when considered from the detector perspective (as compared to the Feynamnn diagram), and it is useful to understand the choices that affect the performance of this observable in searches for new physics.

$E_{\mathrm{T}}^{\mathrm{miss}}$ Definitions

Hard objects refers to all physical objects as defined in the previous sections The $E_{\mathrm{T}}^{\mathrm{miss}}$ reconstruction procedure uses these hard objects and the *soft term* to provide a value and direction of the missing transverse momentum. The $E_{x(y)}^{\mathrm{miss}}$ components are calculated as:

$$E_{x(y)}^{\text{miss}} = E_{x(y)}^{\text{miss, } e} + E_{x(y)}^{\text{miss, } \gamma} + E_{x(y)}^{\text{miss, jets}} + E_{x(y)}^{\text{miss, } \mu} + E_{x(y)}^{\text{miss, soft}}, \tag{6.5}$$

where each value $E_{x(y)}^{\text{miss, } i}$s the negative vectorial sum of the calibrated objects defined in the previous sections.

For purposes of $E_{\text{T}}^{\text{miss}}$ reconstruction, we must assign an *overlap removal* ordering. This is to avoid double counting of the underlying primitive objects (clusters and tracks) which are inputs to the reconstruction of the physics objects. We resolve this in the following order : electrons, photons , jets and muons. This is motivated by the performance of the reconstruction of these objects in the calorimeters.

The soft term $E_{x(y)}^{\text{miss, soft}}$ contains all of the primitive objects which are not associated to any of the reconstructed physics objects. we need to choose which primitive object to use. The primary choices which have been used within ATLAS are the *calorimeter-based soft term* (CST) and the *track-based soft term* (TST) [111]. Based on the soft term choice, we then call $E_{\text{T}}^{\text{miss}}$ built with a CST (TST) soft term simply CST (TST) $E_{\text{T}}^{\text{miss}}$. An additional option, which will be important as pileup continues to increase, is particle flow $E_{\text{T}}^{\text{miss}}$ (PFlow $E_{\text{T}}^{\text{miss}}$).

The CST $E_{\text{T}}^{\text{miss}}$ was used for much of the early ATLAS data-taking. CST $E_{\text{T}}^{\text{miss}}$ is built from the calibrated hard objects, combined with the calorimeter clusters which are *not* assigned to any of those hard objects. In the absence of pileup, it provides the best answer for the “true” $E_{\text{T}}^{\text{miss}}$ in a given event, due to the impressive hermiticity of the calorimeters. Unfortunately, the calorimeters do not know from where their energy deposition came, and thus CST is susceptible to drastically reduced performance with increasing pileup.

TST $E_{\text{T}}^{\text{miss}}$ is the standard for ATLAS searches as currently performed by ATLAS. TST $E_{\text{T}}^{\text{miss}}$ is reconstructed using the calibrated hard objects and a soft term from the tracks which are not assigned to any of those hard objects. In particular, due to the track-vertex association efficiency, one chooses tracks which only come from the primary vertex. This reduces the pileup contributions to the $E_{\mathrm{T}}^{\mathrm{miss}}$ measurement. However, since the ID tracking system is unable to detect neutral objects, the TST $E_{\mathrm{T}}^{\mathrm{miss}}$ is "wrong". In most searches for new physics, the soft $E_{\mathrm{T}}^{\mathrm{miss}}$ is generally a small fraction of the total $E_{\mathrm{T}}^{\mathrm{miss}}$, and thus this bias is not particularly hurtful.

PFlow $E_{\mathrm{T}}^{\mathrm{miss}}$ uses the PFOs described above to build the $E_{\mathrm{T}}^{\mathrm{miss}}$. The PFOs which are assigned to hard objects are calibrated, and the PFOs which are not assigned to any hard object are added to the soft term. In this context, it is convenient to distinguish between "charged" and "neutral" PFOs. Charged PFOs can be seen as a topocluster which has an associated track, while neutral PFOs do not. A charged PFO is essentially a topocluster which is matched with the primary vertex. The neutral PFOs have the same status as the original topoclusters. Thus a "full" PFlow $E_{\mathrm{T}}^{\mathrm{miss}}$ should have performance somewhere between TST $E_{\mathrm{T}}^{\mathrm{miss}}$ and CST $E_{\mathrm{T}}^{\mathrm{miss}}$[3]. A *charged* PFlow $E_{\mathrm{T}}^{\mathrm{miss}}$ should be the same as TST.

Measuring $E_{\mathrm{T}}^{\mathrm{miss}}$ Performance : event selection

The question is now straightforward: how do we compare these different algorithms? We compare these algorithms in $Z \to \ell\ell$ +jets and $W \to \ell\nu$ +jets events. Due to the presence of leptons, these events are well-measured "standard candles". Here we present the results in early 2015 data with $Z \to \mu\mu$ and $W \to e\nu$ events, as shown in [114, 115]. This result was important to assure the integrity of the $E_{\mathrm{T}}^{\mathrm{miss}}$ measurements at the higher energy and pileup environment of Run-2.

The $Z \to \ell\ell$ selection is used to measure the intrinsic $E_{\mathrm{T}}^{\mathrm{miss}}$ resolution of the detector. Neutrinos only occur in these events from heavy-flavor decays inside of jets, and thus $Z \to \ell\ell$ events have very low $E_{\mathrm{T}}^{\mathrm{miss}}$. This provides an ideal event topology to understand the modelling of $E_{\mathrm{T}}^{\mathrm{miss}}$ mismeasurement. Candidate $Z \to \mu\mu$ events are first required to pass a muon or electron trigger, as described in Tab. 5.1. Offline,

[3]Naively, due to approximate isospin symmetry, about 2/3 of the hadrons will be charged and 1/3 will be neutral.

the selection of $Z \to \mu\mu$ events requires exactly two medium muons. The muons are required to have opposite charge and $p_{\mathrm{T}} > 25$ GeV, and mass of the dimuon system is required to be consistent with the Z mass $|m_{ll} - m_Z| < 25$ GeV.

$W \to \ell\nu$ events are an important topology to evaluate the $E_{\mathrm{T}}^{\mathrm{miss}}$ modelling in events with real $E_{\mathrm{T}}^{\mathrm{miss}}$. This $E_{\mathrm{T}}^{\mathrm{miss}}$ is from the neutrino, which is not detected. The $E_{\mathrm{T}}^{\mathrm{miss}}$ in these events has a characteristic distribution with a peak at $\frac{1}{2}m_W$. The selection of $W \to e\nu$ events begins with the selection of exacly one electron of medium quality. A selection on TST $E_{\mathrm{T}}^{\mathrm{miss}} > 25$ GeV drastically reduces the background from multijet events where the jet fakes an electron. The transverse mass is used to select the $W \to e\nu$ events :

$$m_{\mathrm{T}} = \sqrt{2p_{\mathrm{T}}^{\ell}E_{\mathrm{T}}^{\mathrm{miss}}(1 - \cos\Delta\phi)}, \tag{6.6}$$

where $\Delta\phi$ is the difference in the ϕ between the $E_{\mathrm{T}}^{\mathrm{miss}}$ and the electron. m_{T} is required to be greater than 50 GeV.

There are two main ingredients to investigate : the $E_{\mathrm{T}}^{\mathrm{miss}}$ resolution and the $E_{\mathrm{T}}^{\mathrm{miss}}$ scale.

Measuring $E_{\mathrm{T}}^{\mathrm{miss}}$ Performance in early 2015 data : metrics

To compare these algorithms we use the $E_{\mathrm{T}}^{\mathrm{miss}}$ resolution, $E_{\mathrm{T}}^{\mathrm{miss}}$ scale, and linearity. Representative distributions of TST E_x^{miss}, E_y^{miss}, and $E_{\mathrm{T}}^{\mathrm{miss}}$ from early 2015 datataking are shown in Fig. 6.10.

The $E_{\mathrm{T}}^{\mathrm{miss}}$ resolution is an important variable due to the fact that the bulk of the distributions associated to $E_{x(y)}^{\mathrm{miss}}$ are Gaussian distributed [**Aad2012**]. However, to properly measure the tails of this distribution, especially when considering non-calorimeter based soft terms, it is important to use the root-mean square as the proper measure of the resolution. This is strictly larger than resolution as measured using a fit to a Gaussian, due to the long tails from i.e. track mismeasurements. The resolution is measured with respect to two separate variables : $\sum E_{\mathrm{T}}$ and N_{PV}. $\sum E_{\mathrm{T}}$

is an important measure of the “total event activity”. It is defined as

$$\sum E_{\mathrm{T}} = \sum p_{\mathrm{T}}^{e} + \sum p_{\mathrm{T}}^{\gamma} + \sum p_{\mathrm{T}}^{\tau} + \sum p_{\mathrm{T}}^{\mathrm{jets}} + \sum p_{\mathrm{T}}^{\mu} + \sum p_{\mathrm{T}}^{\mathrm{soft}}. \tag{6.7}$$

The measurement as a function of N_{PV} is useful to understand the degradation of $E_{\mathrm{T}}^{\mathrm{miss}}$ performance with increasing pileup. Fig. 6.11 shows the TST $E_{\mathrm{T}}^{\mathrm{miss}}$ resolution in the early 2015 data compared with simulation. The degradation of the TST $E_{\mathrm{T}}^{\mathrm{miss}}$ performance is shown as a function of pileup $N_{\mathrm{PV}}$and total event activity $\sum E_{\mathrm{T}}$. We see that the degradation is significant as a function of these variables, but simulation describes the data well.

Another important performance metric is the $E_{\mathrm{T}}^{\mathrm{miss}}$ scale. This indicates how well we measure the magnitude of the $E_{\mathrm{T}}^{\mathrm{miss}}$, as CST $E_{\mathrm{T}}^{\mathrm{miss}}$ contains additional particles from pileup, while soft neutral particles[4]are ignored by TST $E_{\mathrm{T}}^{\mathrm{miss}}$. To determine this in data, we again use $Z \to \mu\mu$ events, where the $Z \to \mu\mu$ system is treated as a well-measured reference object. The component of $E_{\mathrm{T}}^{\mathrm{miss}}$ which is in the same direction as the reconstructed $Z \to \mu\mu$ system is sensitive to potential biases in the detector response. The unit vector $\boldsymbol{A}_Z$ of the Z system is defined as

$$\boldsymbol{A}_Z = \frac{\vec{p_T}^{\ell+} + \vec{p_T}^{\ell-}}{|\vec{p_T}^{\ell+} + \vec{p_T}^{\ell-}|}, \tag{6.8}$$

where $\vec{p_T}^{\ell+}$ and $\vec{p_T}^{\ell-}$ are the transverse momenta of the leptons from the Z boson decay. The relevant scale metric is the mean value of the $\vec{E}_{\mathrm{T}}^{\mathrm{miss}}$projected onto $\boldsymbol{A}_Z$: $\langle \vec{E}_{\mathrm{T}}^{\mathrm{miss}} \cdot \boldsymbol{A}_Z \rangle$. In Fig. 6.12, the scale is shown for the early 2015 dataset. The negative bias, which is maximized at about 5 GeV, is a reflection of two separate effects. The soft neutral particles are missed by the tracking system, and thus ignored in TST $E_{\mathrm{T}}^{\mathrm{miss}}$. Missed particles due to the limited ID acceptance can also affect the scale.

For events with real $E_{\mathrm{T}}^{\mathrm{miss}}$, one can also look at the *linearity* in simulation. This

---

[4] “Soft“ here means those particles which are not hard enough to be reconstructed as their own particle, using the reconstruction algorithms above.

is defined as

$$\text{linearity} = \langle \frac{E_{\mathrm{T}}^{\mathrm{miss}} - E_{\mathrm{T}}^{\mathrm{miss,Truth}}}{E_{\mathrm{T}}^{\mathrm{miss,Truth}}} \rangle. \tag{6.9}$$

$E_{\mathrm{T}}^{\mathrm{miss,Truth}}$refers to "truth" particles as defined before, or the magnitude of the vector sum of all noninteracting particles. The linearity is expected to be zero if the $E_{\mathrm{T}}^{\mathrm{miss}}$ is reconstructed at the correct scale.

Particle Flow Performance

As described above, the resolution, scale, and linearity are metrics to understand the performance of the different $E_{\mathrm{T}}^{\mathrm{miss}}$ algorithms. In this section, we present comparisons of the different algorithms, including particle flow, in simulation and using a data sample from 2015 of 80 pb^{-1}. In these plots, "MET_PFlow_TST" refers to charged PFlow $E_{\mathrm{T}}^{\mathrm{miss}}$, while the other algorithms are as described above.

Figs. 6.14 and 6.15 show the resolution and scale in simulated $Z \to \mu\mu$ events. The resolution curves follow the expected behavior discussed before. Due to the high pileup in 2015 run conditions, the CST $E_{\mathrm{T}}^{\mathrm{miss}}$ resolution is poor, and further degrades with increasing pileup and event activity. The "regular" PFlow $E_{\mathrm{T}}^{\mathrm{miss}}$ shows reduces pileup and event activity dependence as compared to the CST. PFlow $E_{\mathrm{T}}^{\mathrm{miss}}$ can be seen as a hybrid of TST $E_{\mathrm{T}}^{\mathrm{miss}}$ and CST $E_{\mathrm{T}}^{\mathrm{miss}}$. The charged PFOs ($\sim$2/3) are pileup supressed, while the neutral PFOs (or topoclusters) are not. Both charged PFlow and TST $E_{\mathrm{T}}^{\mathrm{miss}}$ show only a small residual dependence on N_{PV} and $\sum E_{\mathrm{T}}$, since they have fully pileup supressed inputs through track associations.

The scale plots are shown for Z+jets events and Z events with no jets. For the nonsuppressed CST, the scale continues to worsen with increasing p_{T}^{Z}. The standard PFlow algorithm performs the second worst in the region of high p_{T}^{Z}, but is the best at low p_{T}^{Z}. We note the improved scale of the charged PFlow $E_{\mathrm{T}}^{\mathrm{miss}}$ compared to the TST $E_{\mathrm{T}}^{\mathrm{miss}}$. Considering the resolution is essentially identical, the PFlow algorithm is better picking up the contributions from additional neutral particles. In events with no jets,

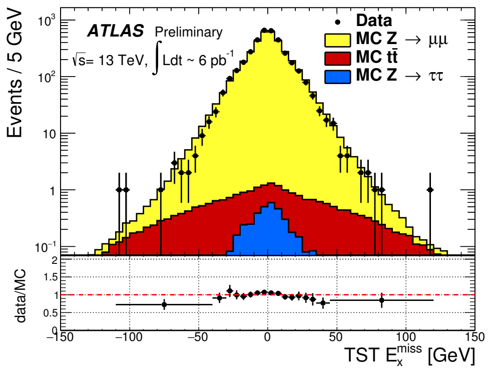

(a)

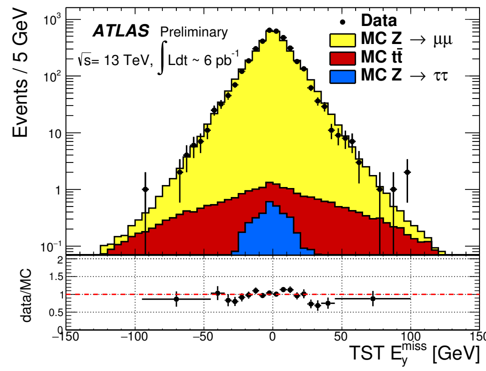

(b)

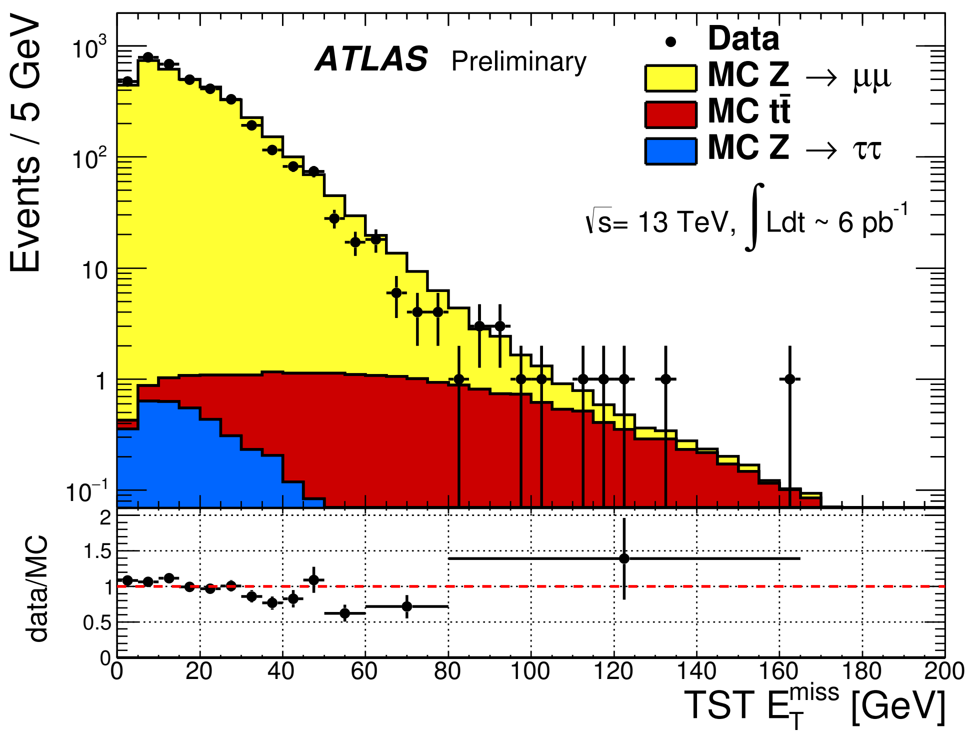

(c)

Figure 6.10: TST E_x^{miss}, E_y^{miss}, and $E_{\mathrm{T}}^{\mathrm{miss}}$ distributions of early $\sqrt{s} = 13$ TeV data compared with simulation after the $Z \to \mu\mu$ selection. The data sample consists of 6 pb^{-1}.

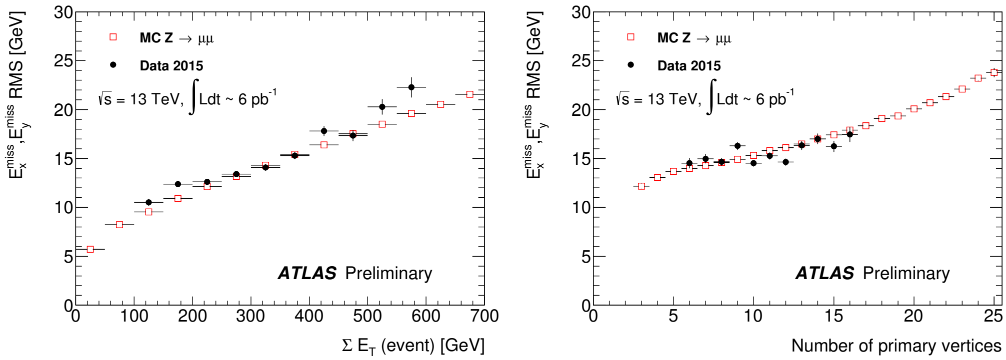

(a) (b)

Figure 6.11: Resolution of TST $E_{\mathrm{T}}^{\mathrm{miss}}$ of early $\sqrt{s} = 13$ TeV data compared with simulation after the $Z \to \mu\mu$ selection. The data sample consists of 6 pb^{-1}.

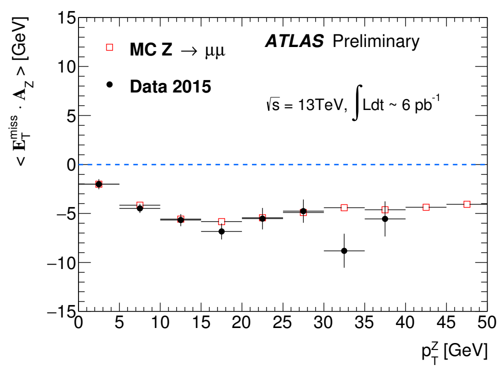

(a)

Figure 6.12: Scale of TST $E_{\mathrm{T}}^{\mathrm{miss}}$ of early $\sqrt{s} = 13$ TeV data compared with simulation after the $Z \to \mu\mu$ selection. The data sample consists of 6 pb^{-1}.

the soft term is essentially the only indication of the $E_{\mathrm{T}}^{\mathrm{miss}}$ mismeasurement, since the muons will be well-measured. In this case, the pileup effects cancel, on average, due to the U(1)$_\phi$ symmetry of the ATLAS detector, and CST performs rather well compared to the more complicated track-based algorithms. The full PFlow algorithm performs best, since it provides a small amount of pileup suppression on the neutral components from CST.

The resolution and linearity are shown in simulated $W \to e\nu$ events in Fig. 6.13. The resolution in $W \to e\nu$ events shows a similar qualitative behavior to $Z \to \mu\mu$ events. The CST $E_{\mathrm{T}}^{\mathrm{miss}}$ has the worst performance, with charged PFlow $E_{\mathrm{T}}^{\mathrm{miss}}$

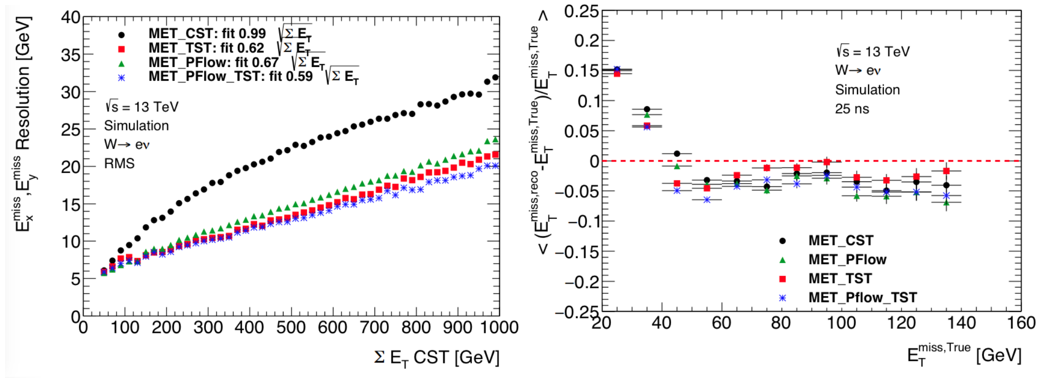

(a) (b)

Figure 6.13: Comparison of $E_{\mathrm{T}}^{\mathrm{miss}}$ resolution and linearity using different $E_{\mathrm{T}}^{\mathrm{miss}}$ algorithms with simulated $W \rightarrow e\nu$ events.

performing best. The surprise here is the scale associated to TST $E_{\mathrm{T}}^{\mathrm{miss}}$ has the strongest performance throughout the space parameterized by $E_{\mathrm{T}}^{\mathrm{miss,Truth}}$, except for one bin at 40 GeV $< E_{\mathrm{T}}^{\mathrm{miss,Truth}} <$ 50 GeV. The scale in these events is best measured using a track-based soft term.

The resolution also investigated in real data passing the $Z \rightarrow \mu\mu$ selection described above. A comparison of the $E_{\mathrm{T}}^{\mathrm{miss}}$ between real data and simulation for each algorithm is presented in Fig. 6.16. The resolution as a function of $\sum E_{\mathrm{T}}$ and N_{PV} is shown in Fig. 6.17 for this dataset. Overall, the real dataset shows the same general features as the simulation dataset in terms of algorithm performance. However, the performance of all algorithms seems to be significantly worse in data. This is likely due to simplifications made in the simulation: soft interactions which are not simulated have a significant effect on an event level variable such as the $E_{\mathrm{T}}^{\mathrm{miss}}$ resolution.

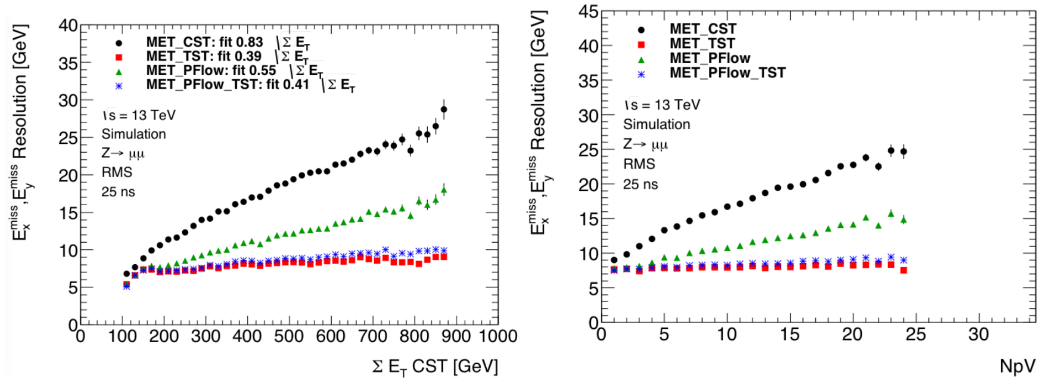

(a) (b)

Figure 6.14: Comparison of $E_{\mathrm{T}}^{\mathrm{miss}}$ resolution using different $E_{\mathrm{T}}^{\mathrm{miss}}$ algorithms with simulated $Z \to \mu\mu$ events.

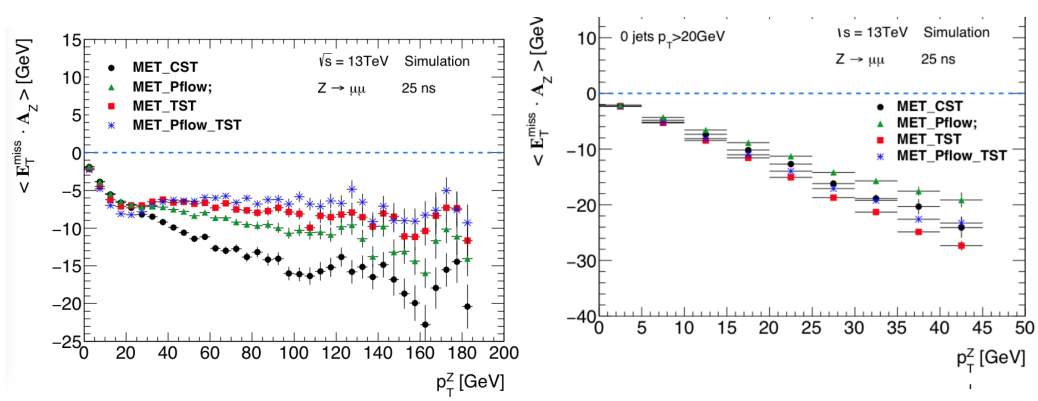

(a) Inclusive in number of jets (b) Zero jet events

Figure 6.15: Comparison of $E_{\mathrm{T}}^{\mathrm{miss}}$ scale using different $E_{\mathrm{T}}^{\mathrm{miss}}$ algorithms with simulated $Z \to \mu\mu$ events.

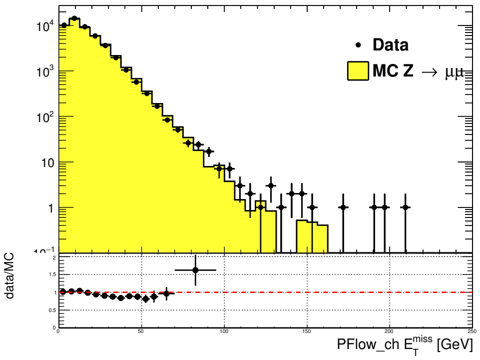

(a)

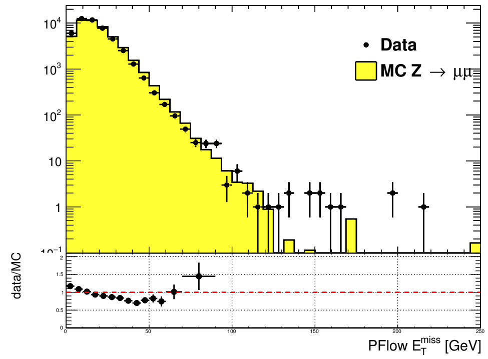

(b)

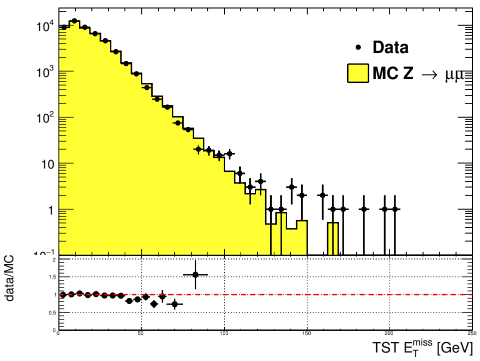

(c)

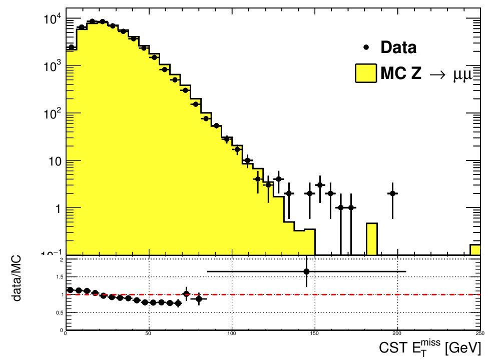

(d)

Figure 6.16: Comparison of $E_{\mathrm{T}}^{\mathrm{miss}}$ distributions using different $E_{\mathrm{T}}^{\mathrm{miss}}$ algorithms with a data sample of 80 pb^{-1}after the $Z \to \mu\mu$ selection

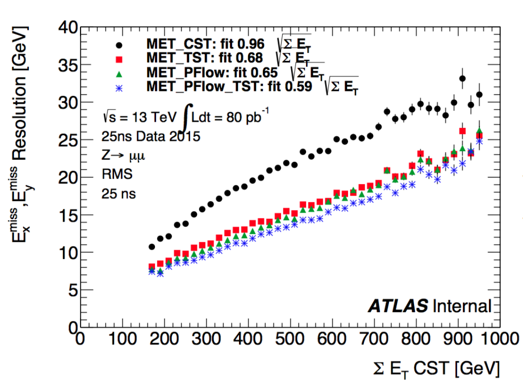

(a)

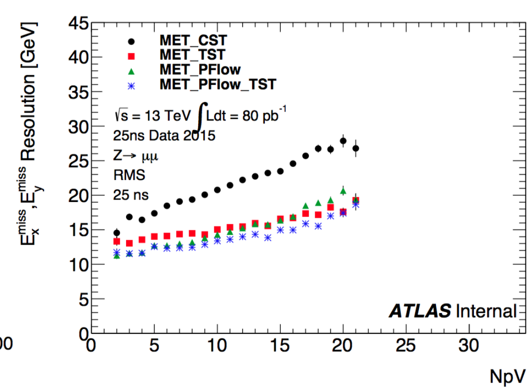

(b)

Figure 6.17: Comparison of $E_{\mathrm{T}}^{\mathrm{miss}}$ resolution using different $E_{\mathrm{T}}^{\mathrm{miss}}$ algorithms with a data sample of 80 pb^{-1}after the $Z \to \mu\mu$ selection

Chapter 7

Recursive Jigsaw Reconstruction

Recursive Jigsaw Reconstruction (RJR) [116, 117] is a novel algorithm used for the analysis presented in this thesis. RJR is the conceptual successor to the razor technique [118, 119], which has been used successfully in many new physics searches [37, 38, 40, 41, 47, 120]. In this chapter, we will first present the razor technique, and describe the razor variables. We will then present the RJR algorithm. After the description of the algorithm, we will describe the precise RJR variables used by this thesis and attempt to provide some physical intuition of what they describe.

7.1 Razor variables

Motivation

In this thesis, we consider SUSY models where gluinos and squarks are pair-produced. Pair-production is a consequence of the R-parity imposed in many SUSY models. $R-$parity violation is highly constrained by limits on proton decay [15], and is often assumed in SUSY model building. The Feynman diagrams considered are shown in Fig. 7.1.

As discussed previously, the consequences of this $\mathbb{Z}_2$ symmetry are drastic. To understand the utility of the razor variables, the stability of the lightest supersymmetric particle is very important. In many SUSY models, including the ones considered in this thesis, this is the lightest neutralino $\tilde{\chi}_1^0$. This means that on either side of a SUSY decay process, where we begin with disparticle production, we have a final

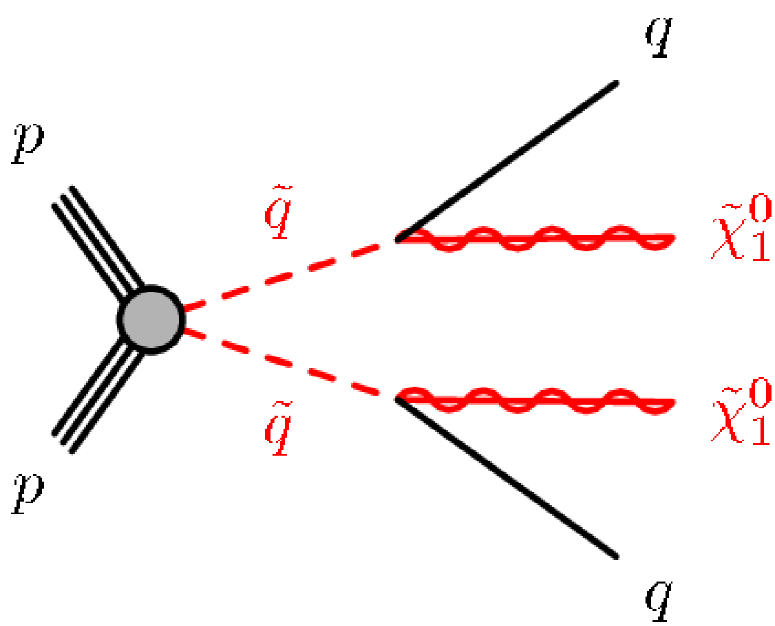

(a) Disquark production

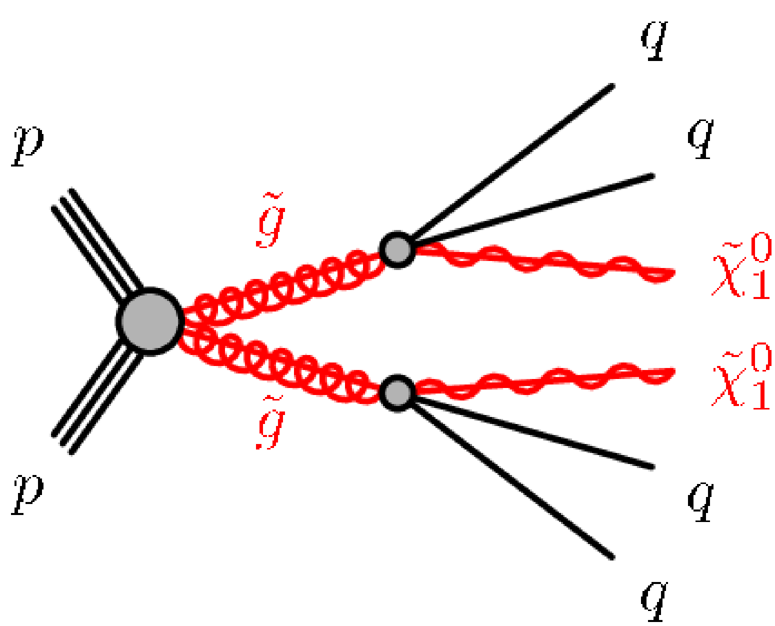

(b) Digluino production

Figure 7.1: Feynman diagrams for the SUSY signals considered in this thesis

state particle which is not detected. Generically, this leads to $E_{\mathrm{T}}^{\mathrm{miss}}$. Selections based on $E_{\mathrm{T}}^{\mathrm{miss}}$ are very good at reducing dominant backgrounds, for example from QCD backgrounds.

However, there are limitations to searches based on $E_{\mathrm{T}}^{\mathrm{miss}}$. Due to jet mismeasurements, instrumental failures, finite detector acceptance, nongaussian tails in the detector response, and production of neutrinos inside of jets, there are many sources of "fake" $E_{\mathrm{T}}^{\mathrm{miss}}$ which does not correspond to a Standard Model neutrino or new physics object such as an LSP. An additional limitation is the complete lack of longitudinal information. As events from i.e. QCD backgrounds tend to have higher boosts along the z-direction, this is ignoring an important handle in searches for new physics. Finally, $E_{\mathrm{T}}^{\mathrm{miss}}$ is only one object, which is a measurement for *two* separate LSPs. If one could factorize this information somehow, this would provide additional information to potentially discriminate against backgrounds. The *razor variables* (M_{Δ}^{R}, R^2) are more robust than standard variables against these effects [118, 119].

Derivation of the razor variables

To derive the razor variables (M_{Δ}^{R}, R^2), we start with a generic situation of the pair production of heavy sparticles with mass m_{Heavy}.[1] Each sparticle decays to a number of observable objects (in this thesis, jets), and an unobservable $\tilde{\chi}_1^0$ of mass $m_{\tilde{\chi}_1^0}$. We will combine all of the jets into a *megajet*; this process will be described below. We begin by analyzing the decay in the "rough-approximation", or in modern parlance, *razor frame* (R-frame). This is the frame where each sparticle is at rest. The complete set of frames considered in the case of the razor variables is shown in Fig. 7.2.

In the R-frame, the decay is straightforward to analyze. By construction, there are in fact two R-frame s, and they have identical kinematics. Each megajet has

[1]The razor variables have undergone confusing notational changes over the years. We will be self-consistent, but the notation used here may be different from references.

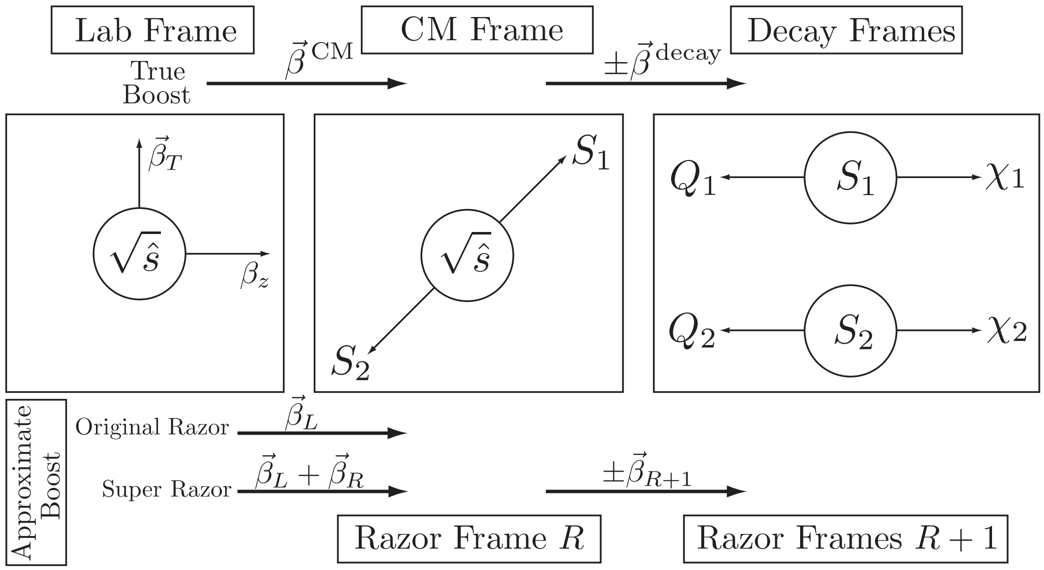

Figure 7.2: Frames considered when applying the razor technique, from [119].

energy E_1^R, E_2^R in the frame of its parent sparticle, and we define a characteristic mass M_R:

$$E_1^R = E_2^R = \frac{m_{\mathrm{Heavy}}^2 - m_{\tilde{\chi}_1^0}^2}{2m_{\mathrm{Heavy}}} \tag{7.1}$$

$$M_R = 2\times E_1^R = 2\times E_2^R = \frac{m_{\mathrm{Heavy}}^2 - m_{\tilde{\chi}_1^0}^2}{m_{\mathrm{Heavy}}}. \tag{7.2}$$

For cases where $m_{\mathrm{Heavy}} >> m_{\tilde{\chi}_1^0}$, M_R is an estimator of m_{Heavy}. This scenario happens in the SM, such as in $t\bar{t}$ and WWevents, where the $\tilde{\chi}_1^0$ is instead a neutrino.

The question now is how to use this simple derivation in the lab frame, where we actually have measurements. There are two related issues: how to combine the jets into the megajets, and how to "transform" (or *boost*) to the R-frame.

To construct the megajets, the procedure is the following. For a given set of jets $j_i, i = 0, ..., n_{\mathrm{jet}}$, we construct *all* combinations of their four-momenta such that there is at least one jet inside each megajet. Among this set of possible megajets $\{J_{1,2}\}$, we make the following unique choice for the megajets. We minimize the following quantity:

$$m_{J_1}^2 + m_{J_2}^2. \tag{7.3}$$

In modern parlance, this is known as a *jigsaw*. It is important to note, this is a *choice*. It may have nice physical qualities or satisfy some convenient intuition about the events, but as we will see later, other choices are possible.

We now describe how we translate our megajet kinematics, measured in the lab frame, to the R-frame. This is a two-step procedure. We perform two *boosts*: a longitudinal boost β_L and a transverse boost β_T. Schematically,

$$J_1^R \xrightarrow{\beta_T} J_1^{CM} \qquad \xrightarrow{\beta_L} J_1^{\text{lab}} \tag{7.4}$$

$$J_2^R \xrightarrow{-\beta_T} J_2^{CM} \qquad \xrightarrow{\beta_L} J_2^{\text{lab}} \tag{7.5}$$

$$\tag{7.6}$$

The $J_{1,2}^{\text{lab}}$ correspond directly to those in the megajet construction. We drop the "lab" designation for the rest of the discussion. The question is how to compute the magnitudes of these boosts, given the missing degrees of freedom.

For the transverse boost β_T, recall the two megajets have equal energies in their R-frame by construction. This constraint can be reexpressed as a constraint on the magnitude of this boost, in terms of the boost velocity β_L (and Lorentz factor γ_L):

$$\beta_T = \frac{\gamma_L(E_1 - E_2) - \gamma_L\beta_L(p_{1,z} - p_{2,z})}{\hat{\beta}_T \cdot (\vec{p_{1,T}} + \vec{p_{2,T}})} \tag{7.7}$$

where we have denoted the lab frame four-vectors as $p_i = (E_i, \vec{p_{i,T}}, p_z)$. We now make the *choice* for the direction of the transverse boost $\hat{\beta}_T$:

$$\hat{\beta}_T = \frac{\vec{p_{1,T}} + \vec{p_{2,T}}}{|\vec{p_{1,T}} + \vec{p_{2,T}}|}. \tag{7.8}$$

This choice forces the denominator of Eq. (7.7) to unity, and corresponds to aligning the transverse boost direction with the sum of the two megajets transverse directions.

For the longitudinal boost, we choose $\vec{\beta_L}$ along the z-direction, with magnitude:

$$\beta_L = \frac{p_{1,z} + p_{2,z}}{E_1 + E_2}. \tag{7.9}$$

Viewed in terms of the original parton-parton interactions, this is the choice which "on average" gives $p_{z,\mathrm{CM}} = 0$, as we would expect. This well-motivated choice due to the total z symmetry.

We now have well-motivated guesses for both boosts, which allow us write our original characteristic mass M_R in terms of the lab frame variables, by application of these two Lorentz boosts to the energies of Eq. (7.1):

$$M_R^2 \xrightarrow{\beta_T} M_{R,\mathrm{CM}}^2 \xrightarrow{\beta_L} M_{R,\mathrm{lab}}^2 \qquad = (E_1 + E_2)^2 - (p_{1,z} + p_{1,z})^2. \tag{7.10}$$

Finally, we define an additional mass variable, which include the missing transverse energy $E_{\mathrm{T}}^{\mathrm{miss}}$. Importantly, note that we did not use the $E_{\mathrm{T}}^{\mathrm{miss}}$ in the definition of M_R, which depends only on the energies of the megajets. Backgrounds with no invisible particles (such as multijet events) must have J_1 and J_2 back to back. Thus, we define the transverse mass:

$$(M_R^T)^2 = \frac{1}{2}\left[E_{\mathrm{T}}^{\mathrm{miss}}(p_{1,T} + p_{2,T}) - \vec{E}_{\mathrm{T}}^{\mathrm{miss}} \cdot (\vec{p_{1,T}} + \vec{p_{2,T}})\right]. \tag{7.11}$$

Generally, we have $M_R^T < M_R$, so we define a dimensionless ratio ("the razor"):

$$R^2 = \left(\frac{M_R^T}{M_R}\right)^2. \tag{7.12}$$

For signal events, we expect R to peak around $R \sim 1/4$, while backgrounds without real $E_{\mathrm{T}}^{\mathrm{miss}}$ are expected to have $R \sim 0$.

7.2 Recursive Jigsaw Reconstruction

Recursive Jigsaw Reconstruction is an algorithm allowing the imposition of a decay tree interpretation on an particular event [116, 117]. The idea is to construct the underlying kinematic variables (the masses and decay angles) on an event-by-event level. This is done "recursively" through a decay tree which corresponds (sometimes approximately) to the Fenymann diagram for the signal process of interest. After each step of the recursive procedure, the objects are “placed” into one bucket (or branch) of the decay tree, and the process is repeated on each frame we have imposed. The imposition of these decay trees is done by *jigsaw* rule: a procedure to resolve combinatoric or kinematic ambiguities while traversing the decay tree. This procedure is performed by the `RestFrames` software packages [121]

In events where all objects are fully reconstructed, this is straightforward, and of course has been used for many years in particle physics experiments. Events which contain $E_{\mathrm{T}}^{\mathrm{miss}}$ are more difficult, due to the loss of information: the potential for multiple mismeasured or simply unmeasureable objects, such as neutrinos or the LSP in SUSY searches. There can also be combinatoric ambiguities in deciding how to group objects of the same type; specifically here, we will be concerned with the jigsaw rule to associate jets to a particular branch of a decay tree. The jigsaw rules we impose will remove these ambiguities. First, we will describe the decay trees used in this thesis, and then describe the jigsaw rules we will use. Finally, we will describe the variables used in the all-hadronic SUSY search presented in this thesis.

Decay Trees

The decay trees imposed in this thesis are shown in Fig. 7.3. Leaving temporarily the question of “how” we apply the jigsaw rules, let us compare these trees to the signal processes of interest. In particular, we want to compare the Feynman diagrams of Fig. 7.1 with the decay trees of Fig. 7.3. The decay tree in **??** corresponds exactly to that expected from disquark production, and matches very closely with the principles of the razor approach. We first apply a jigsaw rule, indicated by a line, to the kinematics of the objects in the *lab* frame. This outputs the kinematics of our event in the *parent-parent* (PP) frame, or in the razor terminology, the CM frame. That is, the kinematics of this frame are an estimator for the kinematics in the center of mass frame of the disquark system. We apply another jigsaw, which splits the objects in the

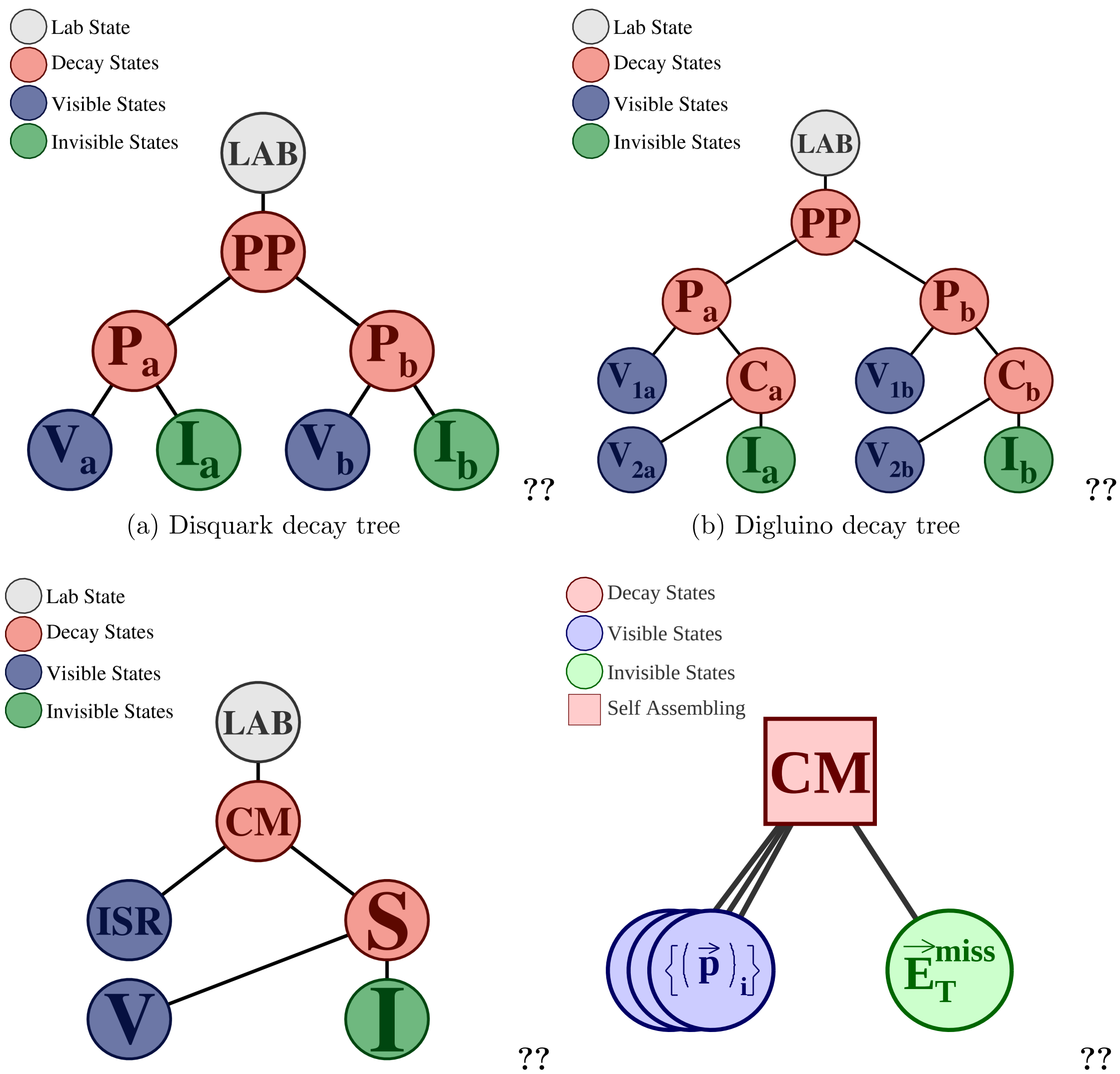

(a) Disquark decay tree

(b) Digluino decay tree

(c) Compressed decay tree

(d) Anti-QCD assembling decay tree

Figure 7.3: RJR decay trees imposed in this thesis

PPframe into two new frames, known as the $P_a$and $P_b$systems. These are equivalent to the razor frames of the razor technique, and represent proxy frames where each squark is at rest. In $P_a(P_b)$, the decay is symmetric between the visible $V_a(V_b)$ objects and the invisible system $I_a(I_b)$. To generate the estimator of the kinematics of the V_a, V_b, I_a, and $I_b$systems in the $P_a$and $P_b$systems, we apply another jigsaw rule to split the total $E_{\mathrm{T}}^{\mathrm{miss}}$ between $P_a$and P_b, which allows calculations of these kinematics in these frames. For the case of disquark production, this is the expected decay tree, and we stop the recursive calculation at that level.

In the case of digluino production, we expect two additional jets, and we can perform an additional boost in each of $P_a$and P_b, to what we call the $C_a$and $C_b$frames. The decay tree is shown in **??**. In this case we apply a jigsaw at the level of $P_a(P_b)$ which separates a single visible object V_{1a} (V_{2a}) from the child frame $C_a(C_b)$. This child frame represents the hypothesized squark after the decay $\tilde{g} \to g\tilde{q}$, which then decays as in the squark case. This gives additional information which will be exploited for the gluino specific search regions.

The third decay tree used in this thesis is the *compressed* decay tree. Compressed refers to signal models which have a small splitting between the mass of the proposed sparticle and the $\tilde{\chi}_1^0$. In this case, the sparticle decay products (i.e. the jets and $E_{\mathrm{T}}^{\mathrm{miss}}$) do not generally have large scale [116]. Instead, the strategy is generally to look for a large-scale initial state radiation (ISR) jet which is recoiling off the disparticle system. In the case where the LSPs receive no momentum from the sparticle decays, the following approximation holds:

$$E_{\mathrm{T}}^{\mathrm{miss}} \sim -p_T^{\mathrm{ISR}} \times \frac{m_{\tilde{\chi}_1^0}}{m_{\mathrm{sparticle}}} \tag{7.13}$$

where $p_{\mathrm{T}}^{\mathrm{ISR}}$ is the transverse momentum associated to the entire ISR system.

RJR offers a natural and straightforward way to exploit this feature in events containing ISR. One imposes the simple decay tree in **??** with associated jigsaw rules. With suitable jigsaw rules, this decay tree "picks out" the large p_{T} ISR jet, recoiling off the $E_{\mathrm{T}}^{\mathrm{miss}}$ and additional radiation from the sparticle decays. This provides a convenient set of variables to understand compressed scenarios.

There is one other decay tree, shown in **??**. This is special, as it is only used for the purpose of QCD rejection, and does not directly map to a sparticle decay chain. Due to the large production cross-sections of QCD events, even very rare large jet mismeasurements can lead to significant $E_{\mathrm{T}}^{\mathrm{miss}}$ which can enter the signal region. To reduce these backgrounds, one usually rejects events which contain jets which are "too close" by some distance metric to the $E_{\mathrm{T}}^{\mathrm{miss}}$ in the event. Generally, in the past, the distance metric has been defined as simply the angular distance ΔR.

The *self-assembling tree* can be seen as defining a distance metric which depends on the magnitudes of the $E_{\mathrm{T}}^{\mathrm{miss}}$ and jets rather than simply their distance inangular space. Depending on the exact kinematics, the one or two closest jets are found, and label the $E_{\mathrm{T}}^{\mathrm{miss}}$ *siblings*.

In this section, we have seen how one imposes particular decay trees on an event to produce a basis of kinematic variables in the approximated frames relevant to the hypothesized sparticle decay chain. This explains why we call this procedure "recursive": we can continue the procedure through as many steps of a decay tree as we want, and each application of a jigsaw rule is dependent on the variables produced in the last step. The question, of course, is *what are these jigsaw rules?*.

Jigsaw Rules

Jigsaw rules are the fundamental step that allow the recursive definitions of the variables of interest. We want rules which allow us to fully define kinematic variables at each step in a decay tree. The only possible solution to fully define the event kinematics in terms of the frames of the hypothesized decays is the imposition of external constraints to eliminate additional degrees of freedom. In principle, these need not have any particular physical motivation. Instead, the jigsaw rules are a way to resolve the mathematical ambiguities to fully reconstruct the full decay chain kinematics. However, most practical jigsaw rules also have some reasonable physical motivation, which we will also elucidate.

In the original razor point of view, some jigsaw rules can be seen as the definitions of the boosts which relate the different frames of interest, while other rules allow one to combine multiple objects and place them into a particular hemisphere (previously megajet). These are the two forms of jigsaw rules: combinatoric and kinematic. As we have stressed before, the jigsaw rules are a *choice*; as long as a particular jigsaw rule allows the definition of variables at each step in a decay tree, it is "as valid" as any other rule.

Practically speaking, in this thesis we use only a small subset of possible jigsaw rules. The combinatoric jigsaw rule we use has already been introduced as megajet construction above. The minimization of

$$m_{J_1}^2 + m_{J_2}^2. \tag{7.14}$$

is a jigsaw rule to deal with the combinatoric ambiguity implicit in which jets go in which hemisphere. This is the jigsaw rule used in the decay trees when going from one frame to two frames such as $PP \rightarrow P_a, P_b$.

We will use three other jigsaw rules, which are both kinematic jigsaw rules. One has already been used in the razor technique. The minimization of β_L will be used as the jigsaw rule in the first step of each decay tree: the lab frame to the PP/CM frame. This is in effect the imposition of longitudinal boost invariance, as we expect on average $p_{z,PP,\mathrm{CM}} = 0$. One defines a unique longitudinal boost by imposition of this external constraint.

The final two jigsaw rules used in this thesis was not used in the razor technique. We describe them here.

The first kinematic ambiguity is the total mass of the invisible system M_I. We guess this to be:

$$M_I^2 = M_V^2 - 4M_{V_a}M_{V_b}. \tag{7.15}$$

As we stated above, there is no need to "justify" the jigsaw rules, as they are in some ways a mathematical trick to fully resolve the event kinematics. However in this case, there is a nice property of this guess. The symmetry of the production mechanism, where we have two decay products V_i and I_i produced from the decay of the same heavy sparticle, is explicit with this jigsaw choice.

The final jigsaw rule we employ in this thesis is used to resolve the "amount" of $E_{\mathrm{T}}^{\mathrm{miss}}$ that "belongs" to each hemisphere, and therefore how to impose the transverse boost onto each of i.e. $P_a$and $P_b$from PP. Equivalently, it can be seen as the resolution of the kinematics of the $I_a$and $I_b$objects in the disquark and digluino decay trees. Recall that at this point, we have already approximated the boost of the PPframe. The choice we use is to minimize the masses P_a and P_b, while simultaneously constraining $P_a = P_b$. As is the case in the last step, there is a straightforward physical interpretation of this choice. In the signal models we are considering, $P_a$and $P_b$are the estimated frames of the squark or gluino pair-produced as a heavy resonance. We then of course expect $M_{P_a} = M_{P_b}$.

The imposition of the decay trees, with ambiguities resolved through the jigsaw rules, give a full set of boosts relating the frames of each decay tree. In each frame, we have estimates for the frame mass and decay angles, which can be used in searches for new physics. In the next section, we describe the variables that are used in this thesis in more details.

7.3 Variables used in the search for zero lepton SUSY

We describe here the variables used in the search described in ??. These were reconstructed using the RJR algorithm as just described, using the RestFrames packages [121]. In these frames, the momenta of all objects placed into that branch of the decay tree are available (after application of the approximated boost), and in principle we can calculate any variable of interest such as invariant masses or the angles between these objects. The truly useful set of variables are highly dependent on the signal process, and we leave their discussion to the subsequent chapters. It is useful to understand the philosophy employed in the construction of these variables.

In general, we can split variables useful for searches for new physics into two categories: *scaleful* and *scaleless* variables. In this search, we will use a set of scaleful variables called the H variables. The scaleless variables will consists of ratios and angles. In general, we want to limit the number of scaleful cuts we apply, for two reasons. Different scaleful variables are often highly correlated, and this of course limts the utility of additional cuts. Addtionally, selections based on many scaleful variables often "over-optimize" for particular signal model of interest, especially as related to the mass difference chosen between the sparticle and the LSP. To avoid this, each decay tree will only use two scale variables, one of which quantifies the overall mass scale of the event, and another which acts as a measure of the event balance.

Squark and gluino variables

Taking our general philosophy to a particular case, we here describe the variables used by the squark and gluino searches. We have a suite of scale variables which we will call the H variables, and a suite of angles and ratios.

As we have described above, the RJR algorithm gives us access to the masses of each frame of interest. It maybe seem natural, then, that these variables would be the most useful for discrimation of the signal from background processes. However, due to the all hadronic state considered in this thesis, the that can be constructed such as M_{PP} can be affected by extra QCD radiation, which can promote the background processes to large scales. The H variables show a resilience to this effect. They take their name from the commonly used variable H_{T}, which is the scalar sum of the visible momentum. However, due to the RJR technique, we can evaluate these variables in the non-lab frame, including longitudinal information. They are also constructed with *aggregrate* momenta using a similar mass minimization procedure as we have already described.

We label these variables as $H^F_{n,m}$.The frame from where they are evaluated is denoted F; practically, this means $F \epsilon \{$lab, PP, P_a, $P_b\}$. When the discussion applies to both $P_a$and P_b, we will write P_i. The subscripts n and m denote the number of visible and invisible vectors considered, respectively. When there are more vectors available than n or m, we add up vectors using the hemisphere (megajet) jigsaw rule until there are n (m) objects.[2] In the opposite case, where n or m is greater than the number of available objects, one simply considers the available objects. The $H^F_{n,m}$ variables are then defined as

$$H^F_{n,m} = \sum_i^n |\vec{p_{\text{vis},i}}^F| + \sum_j^m |\vec{p_{\text{inv},i}}^F|. \tag{7.16}$$

It may not be clear that these variables encode independent information. Fundamentally, this is just an expression of the triangle inequality $\sum|\vec{p}| \geq |\sum \vec{p}|$. The different combinations can then include independent information. The final note on the H variables is that we can also consider purely transverse versions of these variables, which we will denote $H^F_{T,n,m}$. Including this view, it is easy to see how the H variables are extensions of the normal H_{T} variables, as

$$H_{\mathrm{T}} = H^{\text{lab}}_{T,\infty,0}. \tag{7.17}$$

Although the H variables are interesting in their own right, the true power of the RJR technique comes from the construction of scaleless variables with the technique. This is because the scaleless ratios and angles are in fact measured in the "right" frame, where right here means an approximation of the correct frame. This provides a less correlated set of variables than those measured in the lab frame, due to the corrections to the disparticle or sparticle system boosts from the RJR technique.

For the search for noncompressed disquark production, we use will use the following set of RJR variables.

[2]Recall that these vectors are constructed by the imposition of the decay tree with the relevant jigsaw rules.

- $H_{1,1}^{PP}$ - scale variable useful for discrimination against QCD backgrounds and used in a similar way to $E_{\mathrm{T}}^{\mathrm{miss}}$

- $H_{T,2,1}^{PP}$ - scale variable providing information on the overall mass scale of the event for disquark signal production. We will often call this the *full* scale variable.

- $H_{T,1,1}^{PP}/H_{2,1}^{PP}$ - ratio used to prevent imbalanced events where the scale variable is dominated by one high p_{T} jet or high $E_{\mathrm{T}}^{\mathrm{miss}}$

- $p_{PP,z}^{\mathrm{LAB}}/(p_{PP,z}^{\mathrm{LAB}} + H_{T,2,1}^{PP})$ - ratio to used to prevent significant boosts in the $z-$direction. $p_{PP,z}^{\mathrm{LAB}}$is a measure of the total boost of the PPsystem from the lab frame

- $p_{T,j2}^{PP}/H_{T,2,1}^{PP}$- ratio to force the second leading jet in the PPframe to carry a significant portion of the total scalar sum in that frame. This requirement is another balance requirement, on the total p_{T} of that second jet in the PPframe.

First, we note that there is an implicit requirement that each hemisphere has at least one jet (to even reconstruct the $P_a$and $P_b$frames), these variables are implicitly using two or more jets, as we expect in disquark production. The other important thing to note is that all of the ratios use the full scale variable as the denominator. This is sensible, as we expect all of these effects to be scaled with the full scale variable $H_{T,2,1}^{PP}$. We will see a similar behavior for the gluino regions, with a new full scale variable.

For the search for noncompressed digluino production, we use will use the following set of RJR variables. Due to the increased complexity of the event topology with four jets, there are additional handles we can exploit:

- $H_{1,1}^{PP}$ - same as disquark production

- $H_{T,4,1}^{PP}$ - scale variable providing information on the overall mass scale of the event for digluino signal production. As before, we often call this the *full* scale variable. Since this variable allows the jets to be separated in the PPframe, it is more appropriate for digluino production.

- $H_{T,1,1}^{PP}/H_{4,1}^{PP}$ - ratio used to prevent imbalanced events where the scale variable is dominated by one high p_{T} jet or high $E_{\mathrm{T}}^{\mathrm{miss}}$

- $H_{T,4,1}^{PP}/H_{4,1}^{PP}$ - ratio used to measure the fraction of the total scalar sum of the momentum in the transverse plane. Digluino production is expected to be fairly central

- $p_{PP,z}^{\mathrm{LAB}}/(p_{PP,z}^{\mathrm{LAB}} + H_{T,4,1}^{PP})$ - ratio to used to prevent significant boosts in the $z-$direction

- $\min(p_{T,j2_i}^{PP}/H_{T,2,1_i}^{PP})$- ratio to require the second leading jet in *both* squark-like hemispheres $C_a$and $C_b$to contain a significant portion of *that frame's* momenta. This is similar to the $p_{T,j2}^{PP}/H_{T,2,1}^{PP}$disquark discriminator, but applied to both hemispheres $C_a$and C_b.

- $\max(H_{1,0}^{P_i}/H_{2,0}^{P_i})$- ratio requiring one jet in each of the P_i to not take too much of the total momentum of that frame. This ratio is generally a very loose cut.

Compressed variables

As we saw above, the decay tree imposed for compressed spectra is simpler. We do not attempt to fully reconstruct the details of the system recoiling of the ISR system, but use a straightforward set of variables in this case. One additional simplification is that all variables are force to be transverse in this case; we simply do not include the η/z information of the objects as inputs to the RJR reconstruction. We still use the philosophy of limiting our scaleful variables to just two. The compressed scenario uses the following set of RJR variables:

- $p_{T,S}^{\text{ISR}}$- scale variable that is the magnitude of the total transverse momenta of all jets associated to the ISR system, as evaluated in the CM frame

- $R_{\text{ISR}} \equiv p_I^{\vec{\text{CM}}} \cdot p_{T,S}^{\hat{\text{CM}}} / p_{T,S}^{\text{CM}}$ - this ratio is our measurement for the ratio of the LSP mass to the compressed sparticle mass. These are the values in the CM frame In compressed cases, this should be large, as this estimates the amount of the total CM $\rightarrow S$ boost is carried by the invisible system.

- $M_{T,S}$- the transverse mass of the S system

- N_{jet}^{V}- the number of jets associated to the visible system V

- $\Delta\phi_{ISR,I}$- the opening angle between the ISR system and the invisible system measured in the lab frame. As the invisible system is expected to carry much of the total S system momentum, this should be large, as we expect the ISR system to recoil directly opposite the I system in that case.

Anti-QCD variables

For the self-assembling tree, we contruct two variables, which we combine to form a single variable which rejects QCD events. In this case, we use the mass minimzation jigsaw, with a fully transverse version of the event (i.e. we set all jet z/η components to 0). This jigsaw defines the distance metric, and provides us with one or two jets known as the $E_{\text{T}}^{\text{miss}}$ siblings. We define $\vec{p_{\text{sib}}}$as the sum of these jets, and define the following quantities.

We calculate a ratio observable which examines the relative magnitude of the sibling vector $\vec{p_{\text{sib}}}$and $E_{\text{T}}^{\text{miss}}$, and an angle relating $\vec{p_{\text{sib}}}$and $E_{\text{T}}^{\text{miss}}$:

$$R(\vec{p_{\text{sib}}}, E_{\text{T}}^{\text{miss}}) \equiv \frac{\vec{p_{\text{sib}}} \cdot \hat{E}_{\text{T}}^{\text{miss}}}{\vec{p_{\text{sib}}} \cdot \hat{E}_{\text{T}}^{\text{miss}} + |\vec{E}_{\text{T}}^{\text{miss}}|} \tag{7.18}$$

$$\cos\theta(\vec{p_{\text{sib}}}, E_{\text{T}}^{\text{miss}}) \equiv \frac{(\vec{p_{\text{sib}}} + \vec{E}_{\text{T}}^{\text{miss}}) \cdot p^{\text{sib}+\hat{\text{miss}}_{sib}}}{|\vec{p_{\text{sib}}}| + E_{\text{T}}^{\text{miss}}} \tag{7.19}$$

These observables are highly correlated, but taking the following fractional difference provides strong discrimination between SUSY signal and QCD background events:

$$\Delta_{\mathrm{QCD}} \equiv \frac{1 + \cos\theta(\vec{p_{\mathrm{sib}}}, E_{\mathrm{T}}^{\mathrm{miss}}) - 2R(\vec{p_{\mathrm{sib}}}, E_{\mathrm{T}}^{\mathrm{miss}})}{1 + \cos\theta(\vec{p_{\mathrm{sib}}}, E_{\mathrm{T}}^{\mathrm{miss}}) + 2R(\vec{p_{\mathrm{sib}}}, E_{\mathrm{T}}^{\mathrm{miss}})}. \tag{7.20}$$

We will use this variable in the next chapter.

Chapter 8

A search for supersymmetric particles in zero lepton final states with the Recursive Jigsaw Technique

This section presents the details of the first search employing RJR variables as discriminating variables, as described in [117]. We will describe the simulation samples used, and then define the selections where we search for new SUSY phenomena, which we call the *signal regions* (SRs) Afterwards, we describe the background estimation techniques used in the analysis. Finally, we discuss the treatment of systematic uncertainties, and how we combine them using a likelihood method [122].

8.1 Simulation samples

We discussed the collision data sample provided by the LHC for the analysis in this thesis. We analyze a dataset of 13.3 $\text{fb}^{-1}$of collision data, at $\sqrt{s} = 13$ TeV. To select events in data, we use the trigger system as previously discussed, and use the lowest unprescaled trigger which is available for a particular Standard Model background. We now discuss the simulation samples used for this search.

Simulated data is fundamentally important to the ATLAS physics program. Calibrations, measurements, and searches use Monte Carlo (MC) simulations to compare with collision data. In this thesis, MC samples are used to optimize the signal region selections, assist in background estimation, and assess the sensitivity to specific SUSY signal models. The details of Monte Carlo production, accuracy, and utility are far beyond the scope of this thesis, but we provide a short description here.

The first step is MC *generation*. A program is run which does a matrix-element calculation which produces a set of outgoing particles from the parton interactions. The output particles are *interfaced* [123] with the parton decays, showering, and hadronization processes. This can be done by the same program or another tool altogether. This produces a set of *truth* particles with their corresponding kinematics.

Physics process	Generator	Alternative generator	Cross-section normalization	PDF set	Parton shower	Tune
$W(\to \ell\nu)$ + jets	SHERPA 2.2.0	MADGRAPH	NNLO	NNPDF3.0NNLO	SHERPA	SHERPA default
$Z/\gamma^{*}(\to \ell\ell)$ + jets	SHERPA 2.2.0	MADGRAPH	NNLO	NNPDF3.0NNLO	SHERPA	SHERPA default
γ + jets	SHERPA 2.1.1	-	LO	CT10	SHERPA	SHERPA default
$t\bar{t}$	Powheg-Box v2	MC@NLO	NNLO+NNLL	CT10	PYTHIA 6.428	PERUGIA2012
Single top (Wt-channel)	Powheg-Box v2	MC@NLO	NNLO+NNLL	CT10	PYTHIA 6.428	PERUGIA2012
Single top (s-channel)	Powheg-Box v2	MC@NLO	NLO	CT10	PYTHIA 6.428	PERUGIA2012
Single top (t-channel)	Powheg-Box v1	MC@NLO	NLO	CT10f4	PYTHIA 6.428	PERUGIA2012
$t\bar{t} + W/Z/WW$	MG5_aMC@NLO 2.2.3	-	NLO	NNPDF2.3LO	PYTHIA 8.186	A14
WW, WZ, ZZ	SHERPA 2.1.1	-	NLO	CT10	SHERPA	SHERPA default
Multijet	PYTHIA 8.186	-	LO	NNPDF2.3LO	PYTHIA 8.186	A14

Table 8.1: The Standard Model background Monte Carlo simulation samples used in this thesis. The generators, the order in α_s of cross-section calculations used for yield normalization, PDF sets, parton showers and tunes used for the underlying event are shown. Alternative generators are only used for the major backgrounds.

For each major background, we employ a baseline sample and alternative sample, which we will use later to derive uncertainties on the theoretical cross-sections. The choice of generators for each background is itself a quite broad topic, which we avoid discussing here. A summary of the generators used is shown in tab. 8.1. In this thesis, we will use SHERPA [124] to generate boson events: $Z \to \ell\ell$, $W \to \ell\nu$, diboson, and photon events. These are interfaced with the SHERPA's parton showering model [125]. The alternative samples for $Z \to \ell\ell$ and $W \to \ell\nu$ decays are generated with MADGRAPH [126] interfaced with PYTHIA8 [127]. Single top and $t\bar{t}$ events are generated with POWHEGBOX [128] interfaced with itself and the alternative samples are generated with MC@NLO [129] interfaced with HERWIG++ [130] QCD events are generated with PYTHIA8 [127]. Events with $t\bar{t}$ in association with a gauge boson are generated in MG5_aMC@NLO 2.2.3 [129] interfaced with PYTHIA8 [127].

After generation of the truth level particles using the various generators interfaced with their parton showering models, we perform *simulation*. The detector response to the truth particles is simulated, and simulated hits are produced. This procedure ensures "as close as possible" treatment of simulation and collision data. In ATLAS, this is done using the GEANT4 toolkit [131]. This toolkit outputs simulated detector signals, on which we run the exact same reconstruction algorithms as described in the previous chapters. This allows us to produce output simulation datasets for each of the backgrounds in the analysis.

8.2 Event selection

This section describes the selection of the signal region events. We begin by describing the *preselection*, which is used to remove problematic events and reduce the dataset to a manageable size. We then describe the signal region strategy, and present the signal regions used in the analysis.

Preselection

The preselection is used to reduce the dataset to that of interest in this thesis. The preselection cuts are shown in Tab. 8.2. This selection is also used for the samples used for background estimation, except for the lepton veto.

The cuts [1] and [4] are a set of cleaning cuts to remove problematic events. The *Good Runs List* is a centrally-maintained list of data runs which have been determined to be "good for physics". This determination is made by analysis of the various subdetectors, and monitoring of their status. Event cleaning is used to veto events which could be affected by noncollision background, noise bursts, or cosmic rays.

We require the lowest unprescaled $E_{\mathrm{T}}^{\mathrm{miss}}$ trigger for the data run of interest, as described previously, in cut [2]. The lepton veto is applied in cut [5]. These two cuts are only used for the signal region selection.

The rest of the preselection is used for the signal region and control regions used for background estimation. These cuts on scaleful variables used by previous searches are mostly used for the reduction of the dataset to a manageable size. Signal models with sensitivity to lower values of these scaleful variables have been ruled out by previous searches [132]. The final cut is on m_{eff}, which is the scalar sum of all jets and $E_{\text{T}}^{\text{miss}}$. This is the final discriminating variable used in the complementary search to this thesis, which is also presented in [117].

Cut	Description	
1	Good Runs List	Veto events with intolerable detector errors
2	Trigger	HLT_xe70 (2015), HLT_xe80_tclcw_L1XE50, or HLT_xe100_mht_L1XE50 (2016)
3	Event cleaning	Veto for noncollision background, noise bursts, and cosmic rays
4	Lepton veto	No leptons with $p_{\text{T}} >$10 GeV after overlap removal
5	$E_{\text{T}}^{\text{miss}}$ [GeV] $>$	250
6	$p_{\text{T}}(j_1)$ [GeV] $>$	200
7	$p_{\text{T}}(j_2)$ [GeV] $>$	50
8	m_{eff} [GeV] $>$	800

Table 8.2: Preselection for the various event topologies used in the analysis.

Signal regions

We define a set of of signal regions using the RJR variables previously described. These signal regions are split into three general categories: squark pair production SRs, gluino pair production SRs, and compressed production SRs. Within these general SRs, we have a set of signal regions targetting different mass splittings of the sparticle and LSP.

A schematic of this strategy is shown in Fig. 8.1. This type of plane is how most $R-$parity conserving) SUSY searches are organized in both ATLAS and CMS The

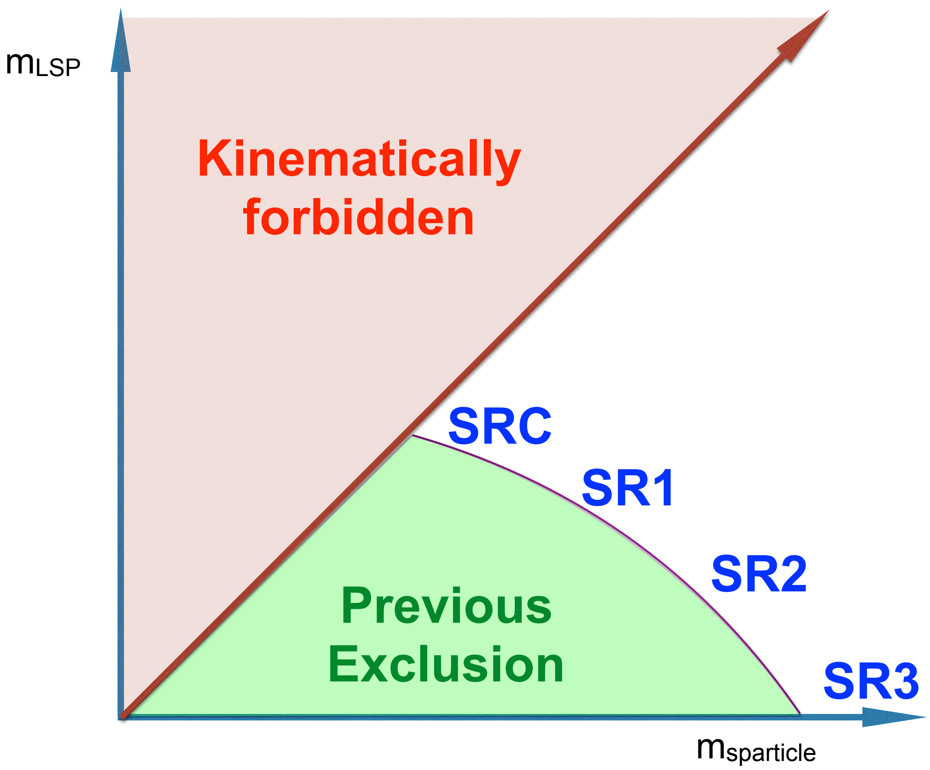

Figure 8.1: Schematic leading the development of the SUSY signal regions in this thesis. A variant of this schematic is used for most SUSY searches on ATLAS and CMS.

horizontal axis is the mass of the sparticle considered. In the case of this thesis, this will the squark or gluino mass. On the horizontal axis, we place the LSP mass. These are the two free parameters of the simplified models considered here. Our search occurs in this two-parameter space. Each signal region targets some portion of this plane. As shown in the figure, a new iteration of a search will use a set of signal regions which have sensitivity just beyond those of the previous exclusions. The choice of how many signal regions to use to fully cover this plane is in many ways a matter of judgment, as it is important to avoid over or under/over-fitting to the signal models of interest. To take the extreme examples, One signal region will obscure the different phenomena in signal events with large versus small mass splittings, leading to underfitting. Binning as finely as possible[1] leads to overfitting due to the fluctuations present in the signal and background events passing the various selections selection. In this thesis, we use six squark signal regions, six gluino signal regions, and five compressed regions.

The full table defining all signal regions is shown in Tab. 8.3. In all cases, the signal region selections contain a combination of scaleful and scaleless cuts. Emphasis on cuts on scaleful variables provide stronger sensitivity to larger mass splittings, while additional sensitivity to smaller mass splittings is found using stronger cuts on scaleless variables. One envisions walking from SR1 (with tight scaleless cuts and loose scaleful cuts) in Fig. 8.1 towards SR3 by loosening the scaleless cuts and tightening the scaleful cuts. We will see this strategy at work in each set of signal regions.

We have already described the useful variables in the previous chapter. The question is how to choose the optimal cuts for a given set of signal models, which are grouped in the mass splitting space. This was done by a brute force scan over the cut values, using a guess of integrated luminosity with a fixed systematic uncertainty scenario; the value of the systematic uncertainty is motivated by that from previous analyses. We choose the lowest cut value that maximizes the Z_{Bi}, as described in [133]. This figure of merit gives conservative estimates, as compared to i.e. $S/\sqrt{B}$. A figure showing an example of this selection tuning procedure is shown in Fig. 8.2.

The compressed selections are split into five regions (SRC1-5), and due to the simplified nature of the compressed decay tree, has sensitivity in both the gluino and squark planes. The compressed regions target mass splittings with $m_{\mathrm{sparticle}} - m_{\mathrm{LSP}} \tilde{<} 200$ GeV. For the compressed region, $M_{T,S}$ is the primary scaleful variable. We can see the general strategy of lowering increasing scale cuts while decreasing the scaleless cuts here. SRC1 targets the most compressed scenarios, with mass splittings of less than 25 GeV, and has the loosest $M_{T,S}$ cut coupled with the tightest $R_{\mathrm{ISR}}$and

[1]This can be defined as having a signal region for each simulated signal sample, which for this analysis is ∼100.

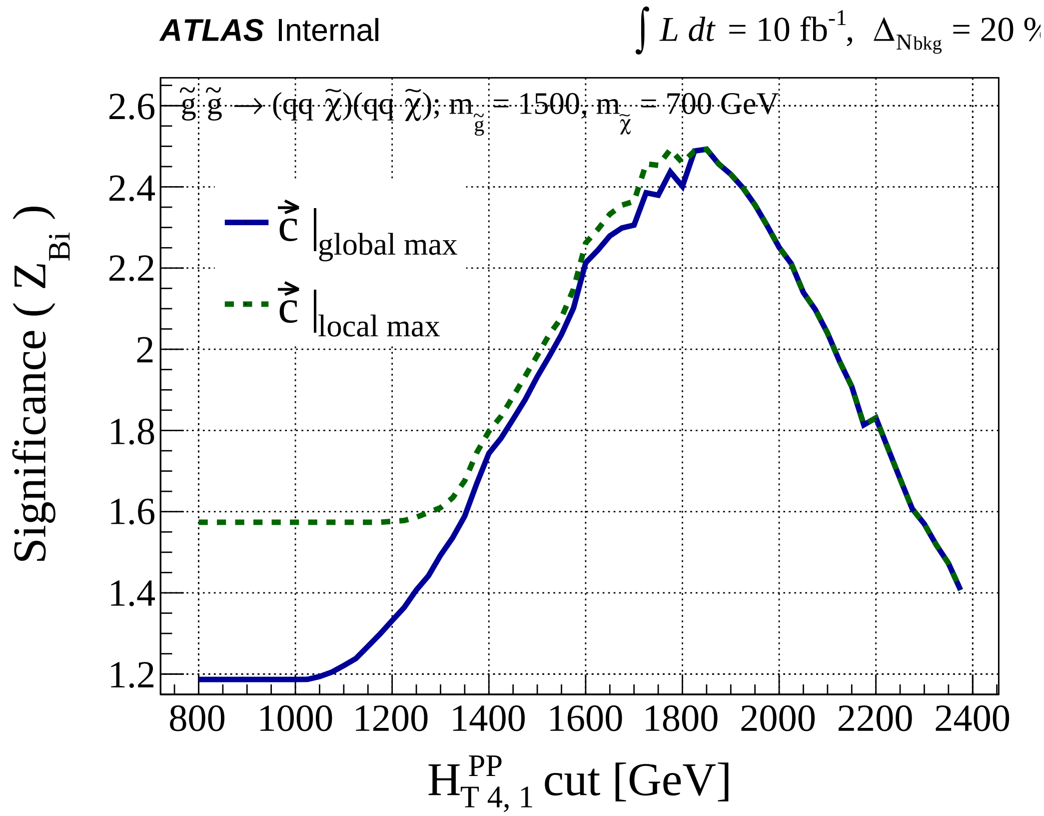

Figure 8.2: Optimization of the $H_{T,4,1}^{PP}$ cut for a gluino signal model with $(m_{\tilde{g}}, m_{\tilde{\chi}_1^0}) =$ $(1500, 700)$ GeV assuming 10 fb^{-1}and an uncertainty of 20% on the background estimate.

$\Delta\phi_{ISR,I}$cuts. SRC4 and SRC5 target mass splittings of ˜200 GeV, and are coupled with the loosest scaleless cuts on $R_{\mathrm{ISR}}$and $\Delta\phi_{ISR,I}$. We also note that SRC4 and SRC5 have differing cuts on N_{jet}^{V}, since these SRs are closest to the noncompressed regions, and can be see as the "crossover" where the differences between squark and gluino production begins to become manifest.

The squark regions (for noncompressed spectra) are organized into six signal regions. These are labeled by a numeral 1-3 and letter a/b. SRs sharing a common numeral i.e. SRS1a and SRS1b share a common set of scaleless cuts, while differing in the main scale variable $H_{T,2,1}^{PP}$. The two SRs for each set of scaless cuts, only differing in the main scale variable, can be seen in a näive way as providing sensitivity to a range of luminosity scenarios[2]. As before, we see that the scaleless cuts are loosened as we tighten the scaleful cuts, as we move across the table from SRS1a to SRS3b. This provides strong sensivity to signal models with intermediate mass splittings with SRS1a to large mass splittings with SR3b.

The gluino signal regions are organized entirely analogously to the squark signal regions. There are six gluino signal regions, again labeled via a numeral 1-3 and letter a/b. Those SRs sharing a common numeral have a common set of scaleless cuts, but differ in their main scale variable $H_{T,4,1}^{PP}$. The SRs follow scaleless vs scaleful strategy, with SRG1 having the loosest scaleful cut cuts coupled with the strongest scaleless cuts, and the converse being true in SRG3. As in the squark case, this strategy provides strong expected sensitivity throughout the gluino-LSP plane.

[2] These SRs were defined before the entire collision dataset was produced, and thus needed to be robust in cases where the LHC provided significantly different than expected performance.

Targeted signal	$\tilde{s}\tilde{s},\ \tilde{s} \rightarrow q\tilde{\chi}_1^0$					
Requirement	Signal Region					
	RJR-S1		**RJR-S2**		**RJR-S3**	
$H_{1,1}^{PP}/H_{2,1}^{PP} \geq$	0.6		0.55		0.5	
$H_{1,1}^{PP}/H_{2,1}^{PP} \leq$	0.95		0.96		0.98	
$p_{\mathrm{PP},\ z}^{lab}/\left(p_{\mathrm{PP},\ z}^{lab} + H_{\mathrm{T}\ 2,1}^{PP}\right) \leq$	0.5		0.55		0.6	
$p_{\mathrm{j2},\ T}^{PP}/H_{\mathrm{T}\ 2,1}^{PP} \geq$	0.16		0.15		0.13	
$\Delta_{\mathrm{QCD}} >$	0.001					
	RJR-S1a	**RJR-S1b**	**RJR-S2a**	**RJR-S2b**	**RJR-S3a**	**RJF**
$H_{\mathrm{T}\ 2,1}^{PP}$ [GeV] $>$	1000	1200	1400	1600	1800	20
$H_{1,1}^{PP}$ [GeV] $>$	1000		1400		1600	

Targeted signal	$\tilde{g}\tilde{g},\ \tilde{g} \rightarrow q\bar{q}\tilde{\chi}_1^0$					
Requirement	Signal Region					
	RJR-G1		**RJR-G2**		**RJR-G**	
$H_{1,1}^{PP}/H_{4,1}^{PP} \geq$	0.35		0.25		0.2	
$H_{\mathrm{T}\ 4,1}^{PP}/H_{4,1}^{PP} \geq$	0.8		0.75		0.65	
$p_{\mathrm{PP},\ z}^{lab}/\left(p_{\mathrm{PP},\ z}^{lab} + H_{\mathrm{T}\ 4,1}^{PP}\right) \leq$	0.5		0.55		0.6	
$\min\left(p_{\mathrm{j2}\ T\ i}^{PP}/H_{\mathrm{T}\ 2,1\ i}^{PP}\right) \geq$	0.12		0.1		0.08	
$\max\left(H_{1,\ 0}^{Pi}/H_{2,\ 0}^{\mathrm{P}i}\right) \leq$	0.95		0.97		0.98	
$\lvert\frac{2}{3}\Delta\phi_{\mathrm{V},P}^{\mathrm{PP}} - \frac{1}{3}\cos\theta_{\mathrm{p}}\rvert \leq$	0.5		–			
$\Delta_{\mathrm{QCD}} >$	0					
	RJR-G1a	**RJR-G1b**	**RJR-G2a**	**RJR-G2b**	**RJR-G3a**	
$H_{\mathrm{T}\ 4,1}^{PP}$ [GeV] $>$	1000	1200	1500	1900	2300	
$H_{1,1}^{PP}$ [GeV] $>$	600		800		900	

Targeted signal	compressed spectra in $\tilde{s}\tilde{s}$ $(\tilde{s} \rightarrow q\tilde{\chi}_1^0)$; $\tilde{g}\tilde{g}$ $(\tilde{g} \rightarrow q\bar{q}\tilde{\chi}_1^0)$				
Requirement	Signal Region				
	RJR-C1	**RJR-C2**	**RJR-C3**	**RJR-C4**	**RJR-C5**
$R_{ISR} \geq$	0.9	0.85	0.8	0.75	0.70
$\Delta\phi_{\mathrm{ISR},\ \mathrm{I}} \geq$	3.1	3.07	2.95	2.95	2.95

8.3 Background estimation

We describe here the method of background estimation. In this thesis, we detail what is colloquially called a “cut-and-count” analysis. This is in contrast to a “shape fit” analysis, where one needs to consider the details of the variable distribution shapes. Instead, we must ensure the overall normalization of the Standard Model backgrounds are correct in the regions of phase space considered in the analysis. In order to do this, we define a set of *control regions* which are free of SUSY contamination based on the previously excluded analysis. We compare the number of events present in the control regions in simulation with that in data to define a *transfer factor* (TF). We extrapolate the number of expected events from each background using this transfer factor to translate from the , which provides our final estimate of the SM background in the corresponding signal region. To be explicit, each signal region SR has a corresponding set of control regions.

More precisely, for a given signal region, we are attempting to estimate the value $N_{\mathrm{SR}}^{\mathrm{data}}$ for a given background. This value is estimated using the following equation:

$$N_{\mathrm{SR}}^{\mathrm{data,est}} = N_{\mathrm{CR}}^{\mathrm{data,obs}} \times \mathrm{TF}_{\mathrm{CR}} \equiv N_{\mathrm{CR}}^{\mathrm{data,obs}} \times \left(\frac{N_{\mathrm{SR}}^{\mathrm{MC}}}{N_{\mathrm{CR}}^{\mathrm{MC}}} \right) \tag{8.1}$$

where the transfer factor TF is taken directly from MC. The two ingredients to our estimation of $N_{\mathrm{SR}}^{\mathrm{data,obs}}$ is thus $N_{\mathrm{CR}}^{\mathrm{data,obs}}$ and the transfer factor taken from MC.

The transfer factor method is potentially more straightforward written in the following way:

$$N_{\mathrm{SR}}^{\mathrm{data,est}} = N_{\mathrm{SR}}^{\mathrm{MC}} \times \left(\frac{N_{\mathrm{CR}}^{\mathrm{data,obs}}}{N_{\mathrm{CR}}^{\mathrm{MC}}} \right) \equiv N_{\mathrm{SR}}^{\mathrm{MC}} \times \mu_{CR}. \tag{8.2}$$

In this form, the correction to the overall normalization is explicit. The ratio $\frac{N_{\mathrm{CR}}^{\mathrm{data,obs}}}{N_{\mathrm{CR}}^{\mathrm{MC}}}$ which we call μ informs us how to scale $N_{\mathrm{SR}}^{\mathrm{MC}}$ in order to get the right overall normalization. The assumption made with this method is that the overall shape of the distribution should not change “that much” as one extrapolates to the signal region.

The CR definitions are motivated and designed according to two (generally competing) requirements:

1. Statistical uncertainties due to low CR statistics

2. Systematic uncertainties related to the extrapolation from the CR to the SR. This motivates the desire to make the control regions as similar as possible to the signal regions without risking signal contamination while ensuring high purity in the targeted SM background.

In principle, one can also apply data-driven corrections to the TF obtained for each CR.

In order to validate the transfer factors obtained from MC, we also develop a series of *validation regions* (VRs). These regions are generally designed to be "in between" the control region and signal region selections in phase space, and thus provide a check on the extrapolation from the control regions into the signal regions. Despite their closeness in phase space to the signal regions, they are also designed to have low signal contamination.

In practice, we perform this estimation procedure simultaneously across all control regions; we describe this later. We only note this here since we can also apply Eq.Eq. (8.1) to measure the contamination of a control region with another background as well. This procedure accounts for the correlations between regions due to correlated systematic uncertainties. We next describe the control region selection for the major SM backgrounds for the analysis.

Control Regions

The primary backgrounds of note in this analysis are Z+jets, W+jets, $t\bar{t}$, and QCD events. There is also a minor background from diboson events which is taken directly from MC with an uncertainty of 50%. We describe the strategy to estimate these various backgrounds here. A summary table is shown in Tab. 8.4. All distributions shown in this section use the scaling factors μ from the background fits, which we describe later.

CR	SM background	CR process	CR event selection
Meff/RJR-CRγ	$Z(\to \nu\bar{\nu})$+jets	γ+jets	Isolated photon
Meff/RJR-CRQ	Multi-jet	Multi-jet	$\Delta_{QCD} < 0$ reversed requirement on $H_{1,1}^{PP}$ (RJR-S/G) or $R_{ISR} < 0.5$ (RJR-C)
Meff/RJR-CRW	$W(\to \ell\nu)$+jets	$W(\to \ell\nu)$+jets	30 GeV$< m_{\mathrm{T}}(\ell, E_{\mathrm{T}}^{\mathrm{miss}}) <$ 100 GeV, b-veto
Meff/RJR-CRT	$t\bar{t}$(+EW) and single top	$t\bar{t} \to b\bar{b}qq'\ell\nu$	30 GeV$< m_{\mathrm{T}}(\ell, E_{\mathrm{T}}^{\mathrm{miss}}) <$ 100 GeV, b-tag

Table 8.4: Control regions used in this thesis.

Events with a Z boson decaying to neutrinos in association with jets are the primary irreducible background in the analysis. These events have true $E_{\mathrm{T}}^{\mathrm{miss}}$ from the decaying neutrinos, and can have significant values of the scaleful variables of interest. Naively, one might expect us to use $Z \to \ell\ell$ as the control process of interest, as $Z \to \ell\ell$ events are quite well-measured. Unfortunately, the $Z \to \ell\ell$ branching ratio is about half of from $Z \to \nu\nu$, which necessitates loosening the control region selection significantly. This leads to unacceptably large systematic uncertainties in the transfer factor.

Instead, photon events are used as the control region for the $Z \to \nu\nu$ events. We label this photon control region as CRY. The photon is required to have $p_{\mathrm{T}} > 150$ GeV to ensure the trigger is fully efficient. The kinematic properties of photon events strongly resemble those of Z events when the boson p_{T} is significantly above the mass of the Z boson. In this regime, the neutral bosons are both scaleless, and can be treated interchangeably, up to the differences in coupling strengths. Additionally,

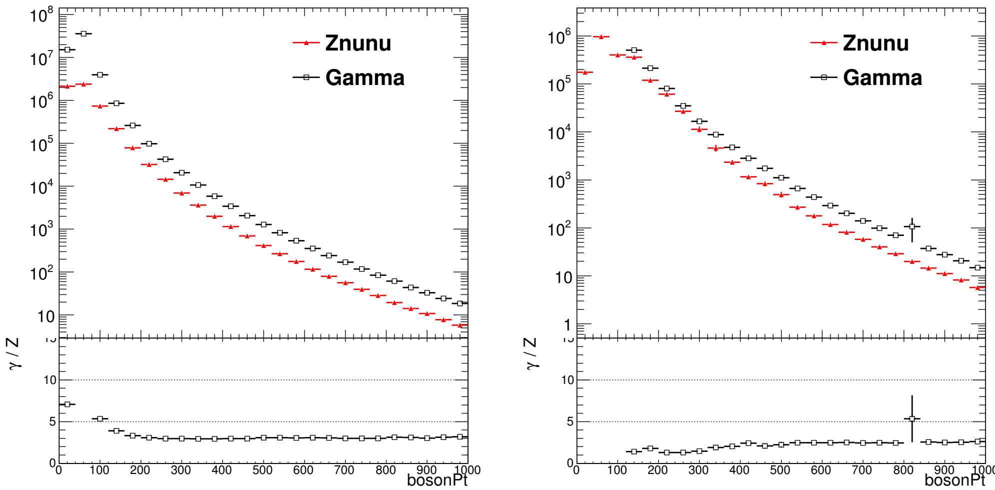

(a) Boson p_{T} ratio as a function of true boson p_{T}

(b) Boson p_{T} ratio as a function of reconstructed boson p_{T}

Figure 8.3

the cross-section for γ+jets events is significantly larger than Z+jets events above the Z mass. These features are shown in Fig. 8.3 in simulated $Z \to \nu\nu$ truth and reconstructed events. The reconstructed $Z \to \nu\nu$ events define the boson p_{T} as simply the $E_{\mathrm{T}}^{\mathrm{miss}}$. In truth events, one clearly sees the effect of the Z mass below $\sim$100 GeV, with a flattening of the ratio above $\sim$300 GeV. In reconstructed events, the effects are less clear at low boson p_{T}, primarily due to cut sculpting from i.e. the trigger requirement on photon events, which necessitates a higher p_{T} cut on photon events for the trigger to remain fully efficient. Still, it is clear that the ratio flattens out at high boson p_{T}, and we are justified in the use of CRY to model the Z+jets background.

The CRY kinematic selection is slightly looser in the scaleful variables for the noncompressed regions to provide sufficient control region statistics. This is chosen to be $H_{1,1}^{PP} > 900$ GeV ($H_{1,1}^{PP} > 550$ GeV) for the squark (gluino) regions to minimize the corresponding statistical and systematic uncertainties.

One additional correction scale factor is applied to γ+jets events before calculating the transfer factors. This is known as the κ method, which is used to determine the disagreement arising from the use of a LO generator for photon events vs. a NLO generator for Z+jets events, which can reduce the theoretical uncertainties from this disagreement. One can see this as a measurement of the k-factor for the LO γ+jets sample. This is effectively done with an auxiliary CRZ region, defined using two leptons with an invariant mass close with 25 GeVof the Z mass. The correction factor derived for this purpose is $\kappa = 1.39 \pm 0.05$.

Distributions of CRY in squark, gluino, and compressed regions are shown in Figs. 8.4 to 8.6. One can see the quite high purity of CRY in photon events from these plots.

Event with a W boson decaying leptonically via W $\rightarrow \ell\nu$ can also enter the signal region. In this case, we use leptonically to include all leptons (e, μ, τ). The W+jets events passing the event selection either have a hadronically-decaying τ, with a neutrion supplying $E_{\mathrm{T}}^{\mathrm{miss}}$, or the case where a muon or electron is misidentified as a jet or missed completely due to the limited detector acceptance. To model this background, we use a sample of one-lepton events with a veto on b-jets, which we label CRW. The lepton is required to have $p_{\mathrm{T}} > 27$ GeV to guarantee a fully efficient trigger. We then treat this single lepton as a jet for purposes of the RJR variable calculations. We apply a kinematic selection on the transverse mass:

$$m_T = \sqrt{2 p_{T,\ell} E_{\mathrm{T}}^{\mathrm{miss}} (1 - \cos\phi_e - E_{\phi}^{miss}}, \tag{8.3}$$

around the W mass: 30 GeV $< m_T <$ 100 GeV. Checks in simulation shows that these requirements give a sample of high purity W $\rightarrow \ell\nu$ background. Due to low statistics using the kinematic cuts imposed in the signal regions, the control region kinematic cuts are slightly loosened with respect to the signal region cuts. We use the loosest cut in any signal region as the control region selection for all signal regions. More clearly, the control region selection corresponding to each signal region is the *same*. As discussed above, this leads to a tolerable increase in the systematic uncertainty from the extrapolation from the CR to the SR when compared to the resulting statistical uncertainty.

Distributions of CRW in squark, gluino, and compressed regions are shown in Figs. 8.7 to 8.9. There is high purity in W+jets events in the control region corresponding to all signal regions.

Top events are also an important background, for the same reasons as the W+jets background, due to the dominant top decay channel of $t \to Wb$. For a top event to be selected by the analysis criteria, as in the case of W+jets, we expect a W to decay via a τ lepton which decays hadronically or one a muon or electron to be misidentified as a jet or be outside the detector acceptance. We are not so worried about hadronic or all dileptonic tops: hadronic $t\bar{t}$ events generally have low $E_{\mathrm{T}}^{\mathrm{miss}}$ (and $H_{1,1}^{PP}$) so they will not pass the kinematic cuts, while dileptonic $t\bar{t}$ events have a lower cross-section and good reconstruction efficiency from the two leptons. We are thus primarily concerned with semileptonic $t\bar{t}$ events with $E_{\mathrm{T}}^{\mathrm{miss}}$ from the neutrino. To model this background, we use the same selection as the W selection, but require that one of the jets chosen by the analysis has at least one b-tag. This selection has quite high purity, as we expect the $t\bar{t}$ background to have two $b-$jets. Thus with the 70% $b-$tagging efficiency working point used in this analysis, ignoring (small) correlations between the two $b-$tags, we expect to tag one of the $b-$jets greater than 90% of the time. As with CRW, we need to loosen the cuts applied to CRT with respect to the signal region in order to gain sufficient expected data statistics. We use exactly the same scheme; the CRT corresponding to each SR is identical, due to using the loosest set of cuts among the SRs. This comes at the cost of an increased systematic uncertainty for this extrapolation, but it was determined that this tradeoff resulted in the lowest overall uncertainty.

Distributions of CRT in squark, gluino, and compressed regions are shown in Figs. 8.10 to 8.12. There is high purity in top events in the control region corresponding to all signal regions.

The final important background is the QCD background. As briefly discussed in the previous chapter, QCD backgrounds are difficult, for a few reasons we describe here. The large cross-section for QCD events means that even very rare extreme mismeasurements can be seen in our signal regions. However, as these events are very rare, one requires extreme confidence in the tails of the distributions to use simulation as an input for background estimation. To avoid this, the strategy in these cases is to apply a strong enough cut to expect *zero* QCD events in the signal regions to avoid this issue. To produce a sample enriched in QCD, which we call CRQ, we reverse the Δ_{QCD} and $H_{1,1}^{PP}$ cuts. This analysis uses the jet smearing method, as described in [134]. This is a data-driven method which applies a resolution function to well-measured QCD events, which also an estimate of the impact of the jet energy mismeasurement on $E_{\mathrm{T}}^{\mathrm{miss}}$ and subsequently the RJR variables.

Distributions of CRQ in squark, gluino, and compressed regions are shown in Figs. 8.13 to 8.15. There is high purity in top events in the control region corresponding to all signal regions.

The final background of note in this background is the diboson background. This background is estimated directly from simulation. Due to the low cross-section of electroweak processes, this background is not significant in the signal regions. We assign a large ad-hoc 50% systematic on the cross-section, and do not attempt to define a control region for this background.

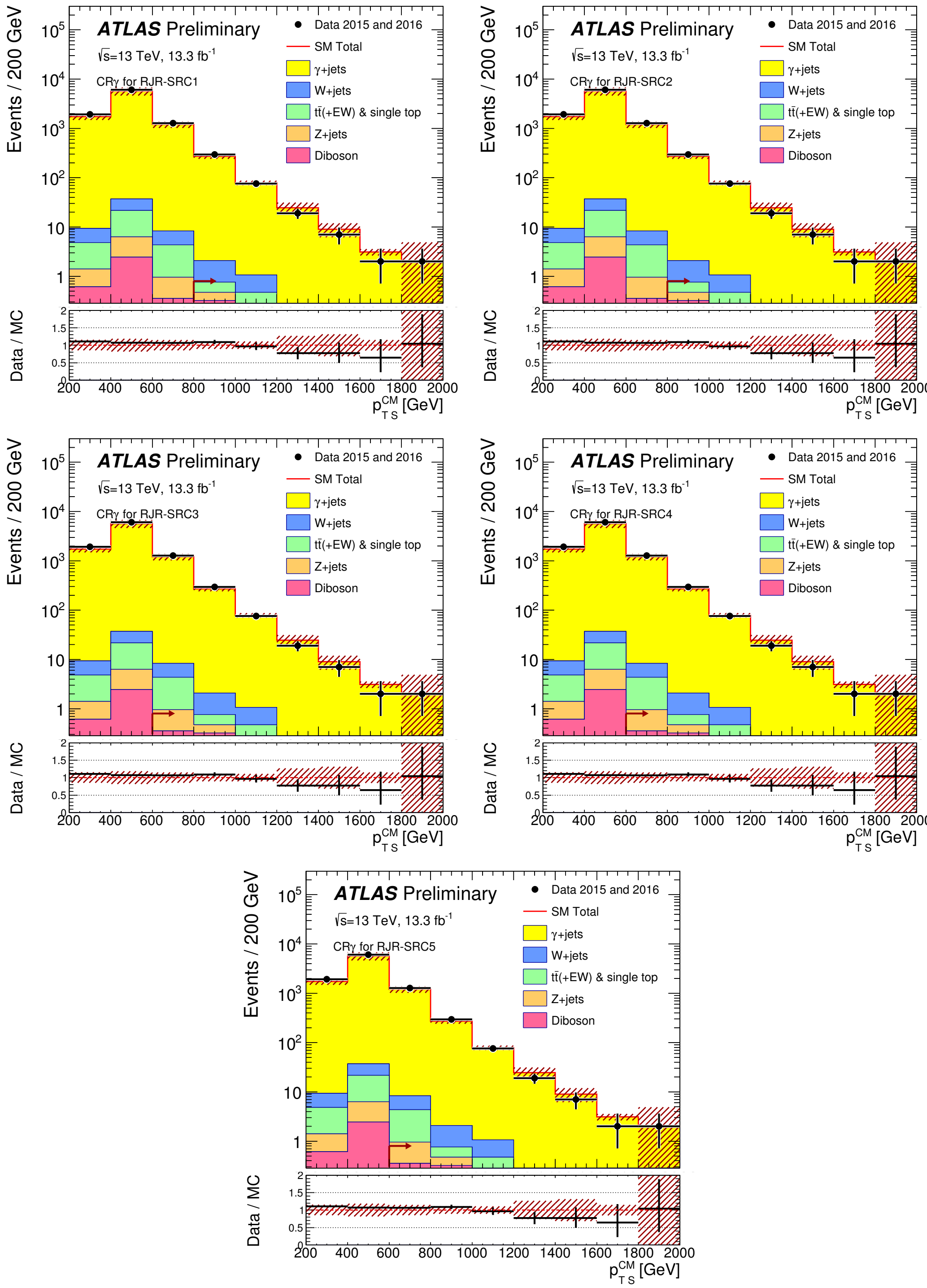

Figure 8.4: Scale variable distributions for the compressed CRY regions.

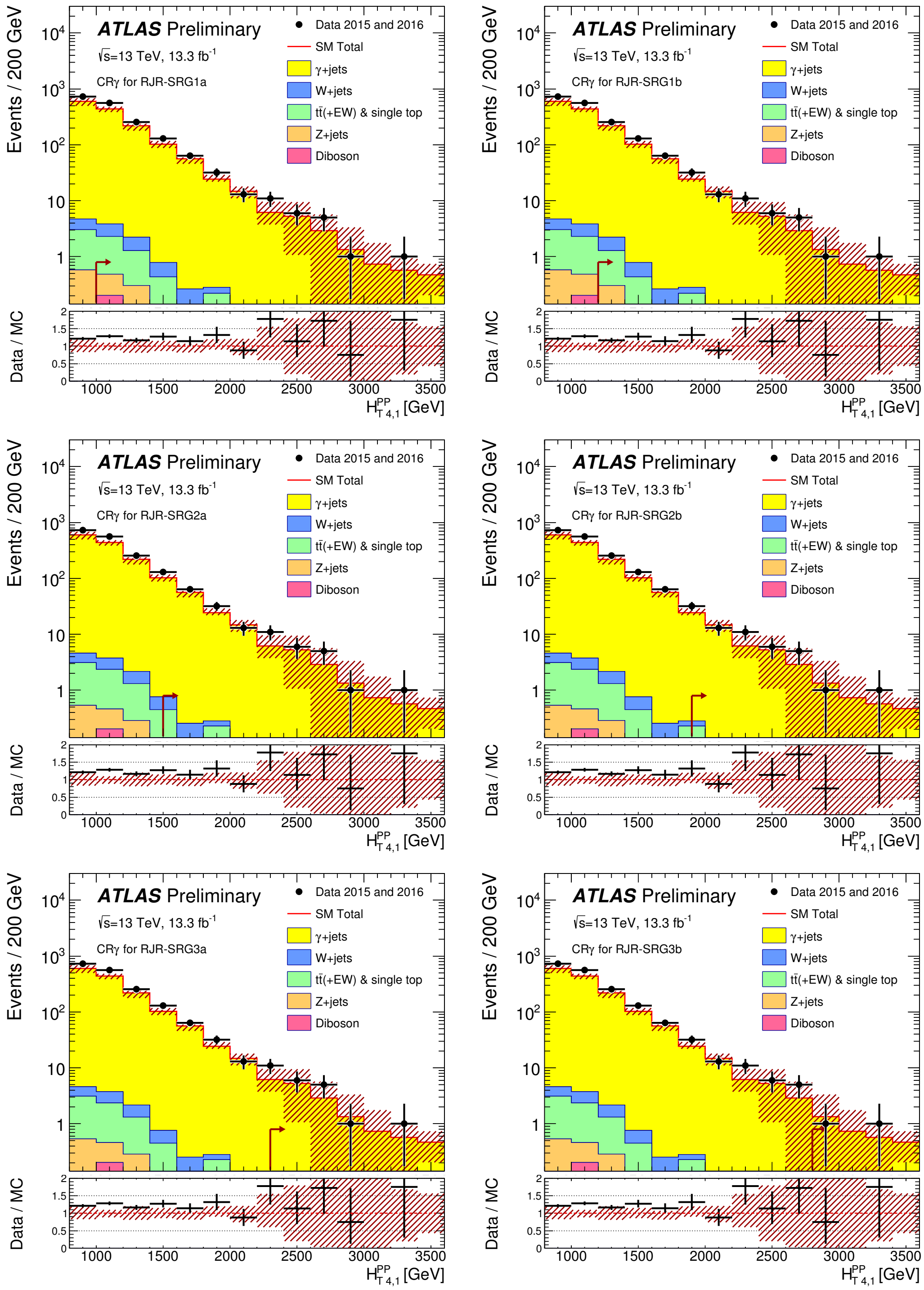

Figure 8.5: Scale variable distributions for the gluino CRY regions.

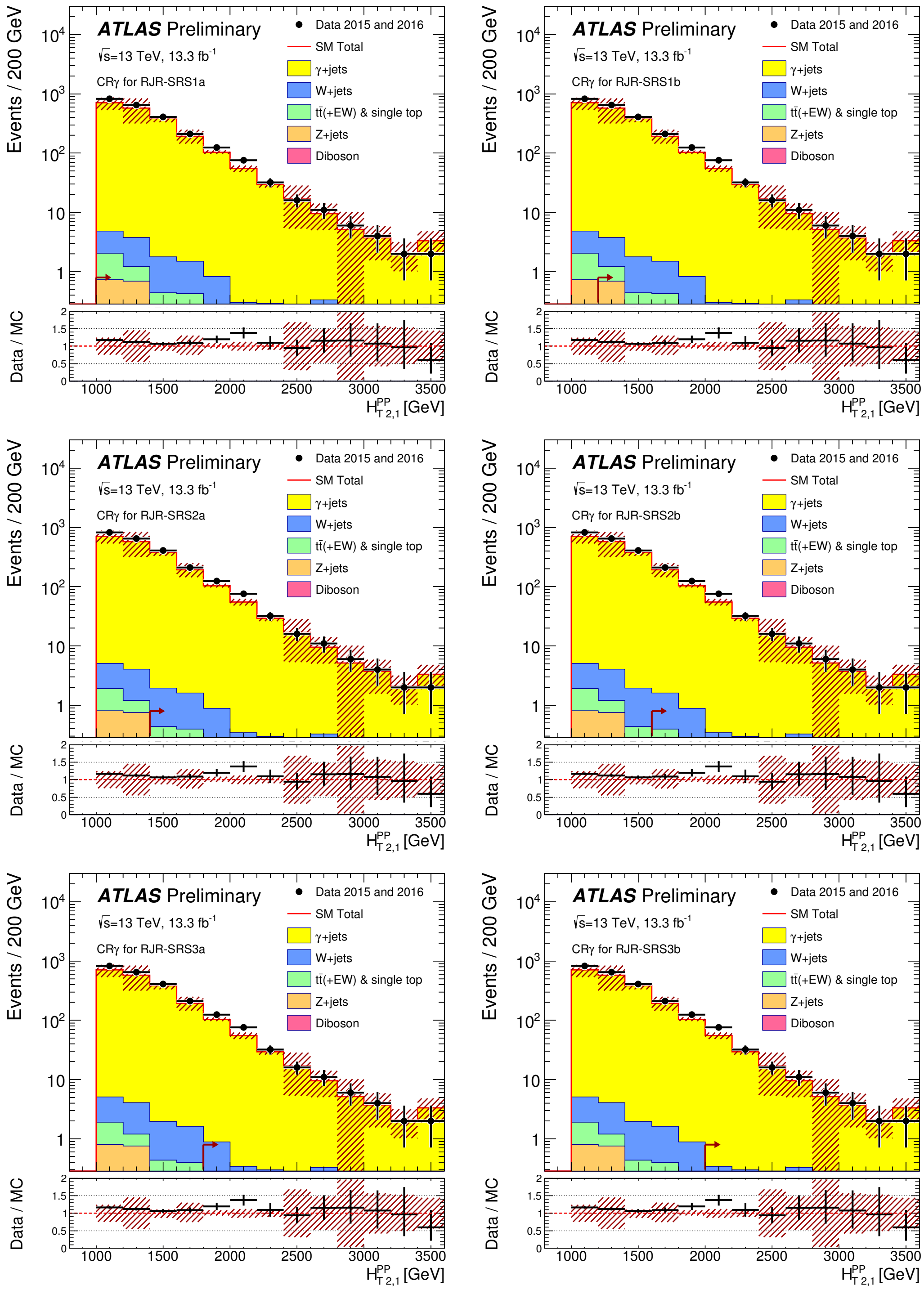

Figure 8.6: Scale variable distributions for the squark CRY regions.

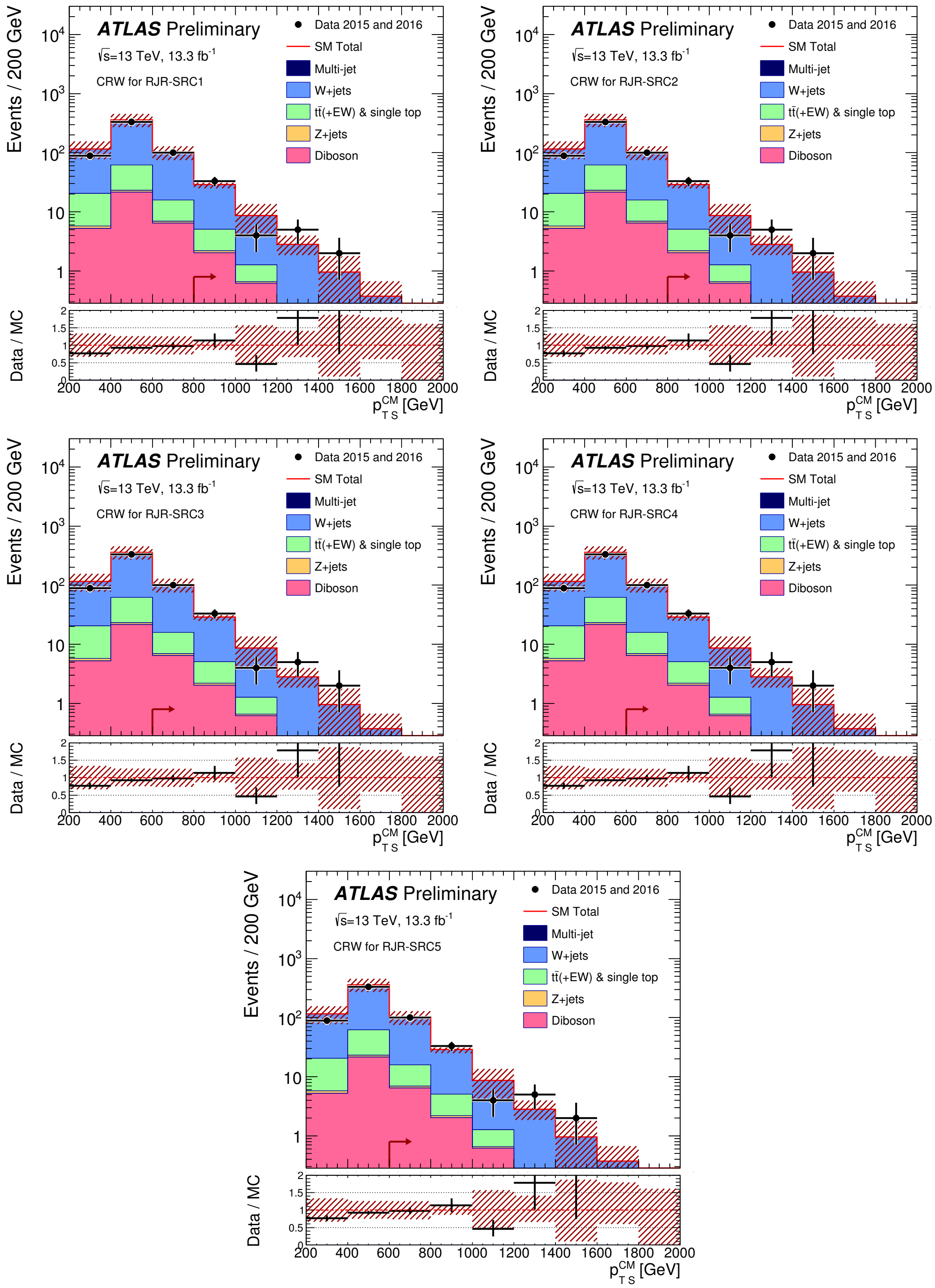

Figure 8.7: Scale variable distributions for the compressed CRW regions.

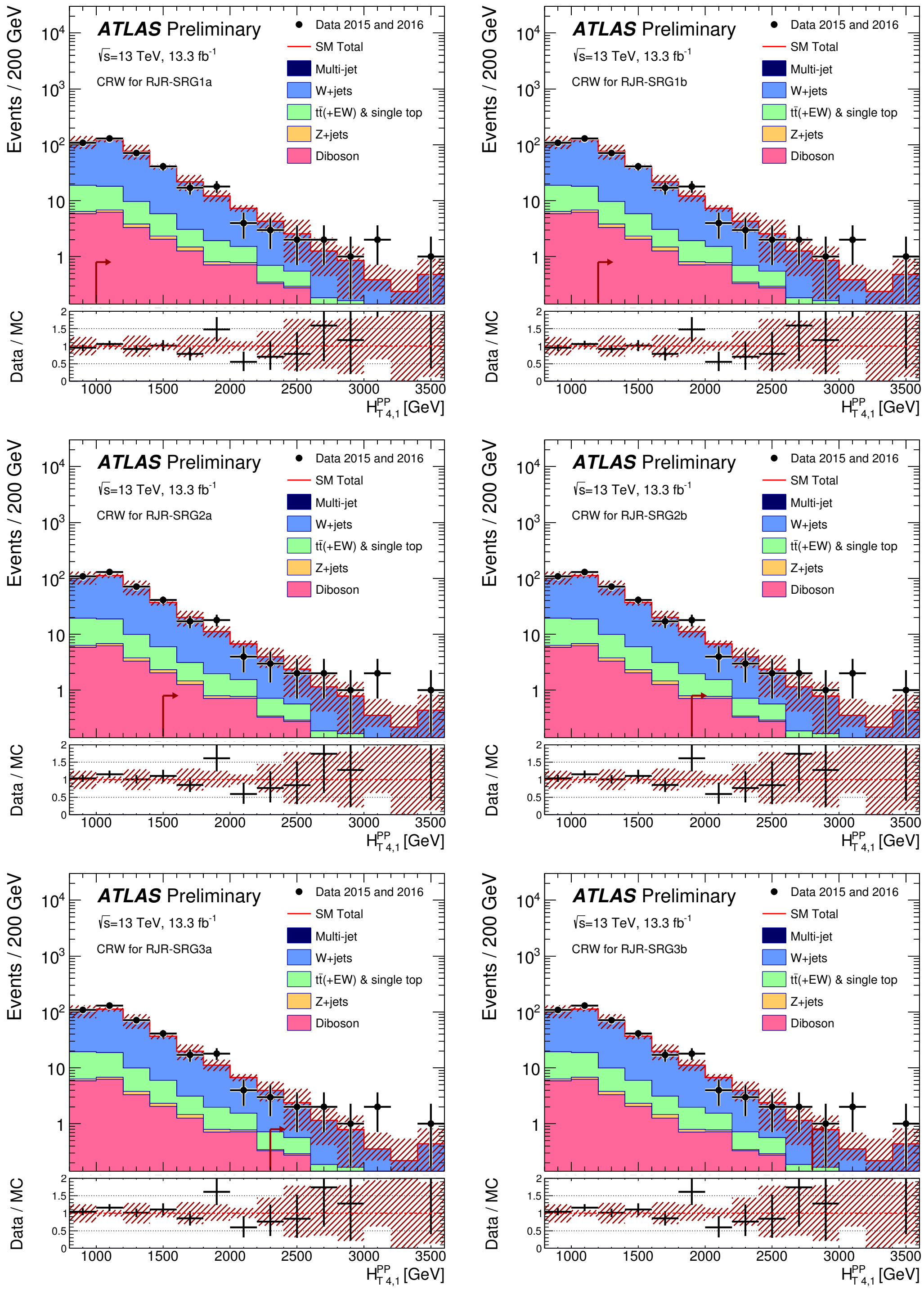

Figure 8.8: Scale variable distributions for the gluino CRW regions.

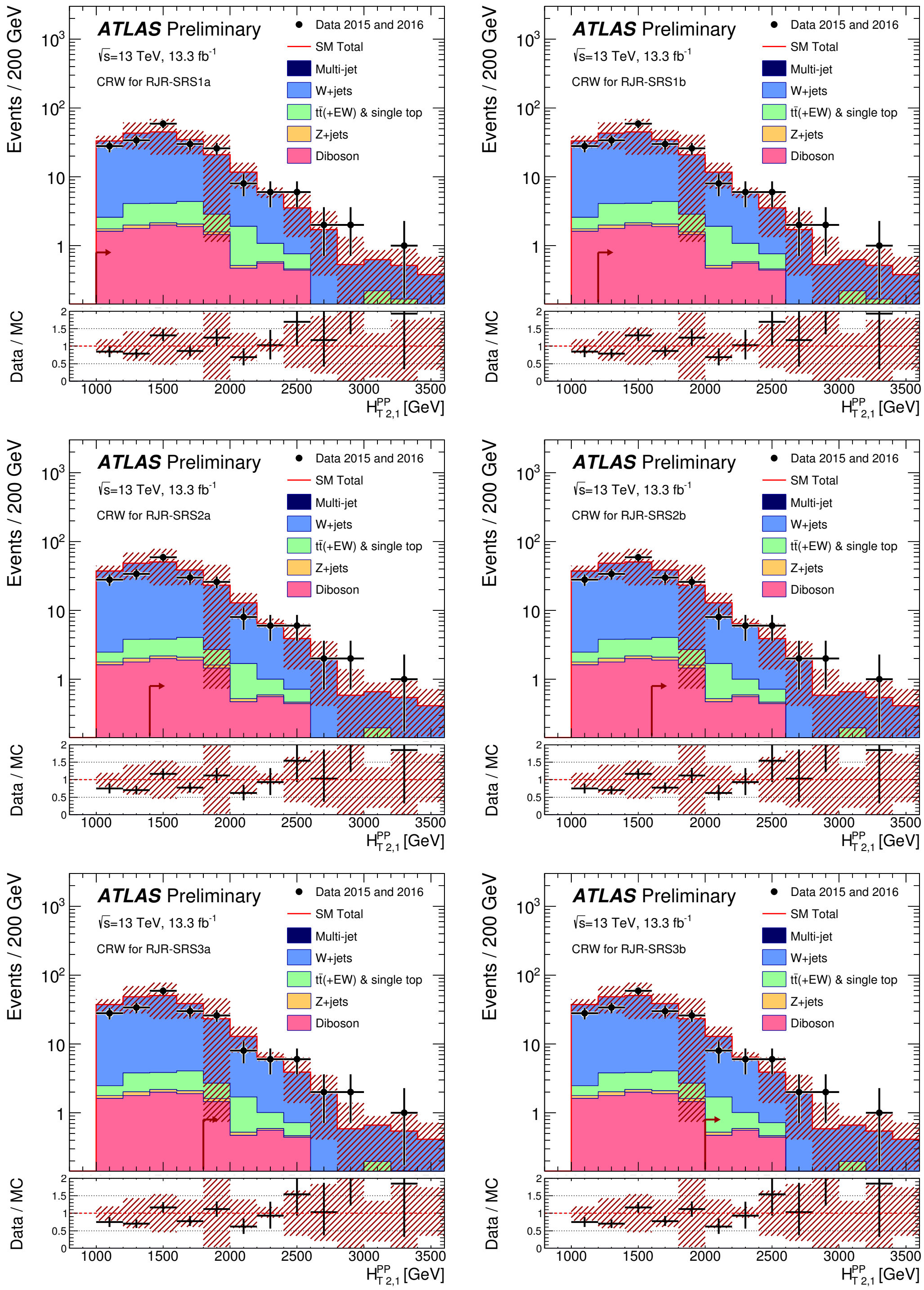

Figure 8.9: Scale variable distributions for the squark CRW regions.

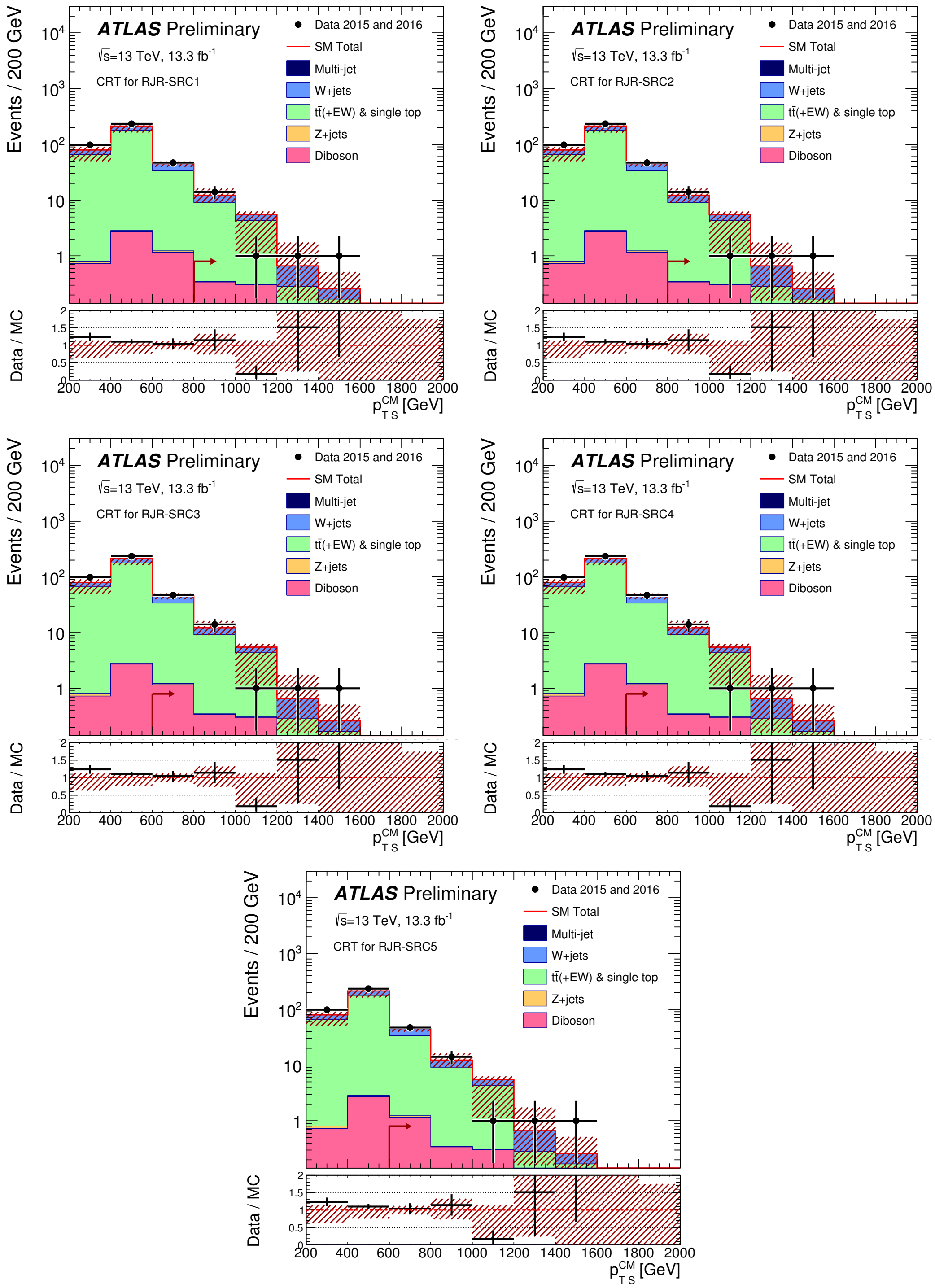

Figure 8.10: Scale variable distributions for the compressed CRT regions.

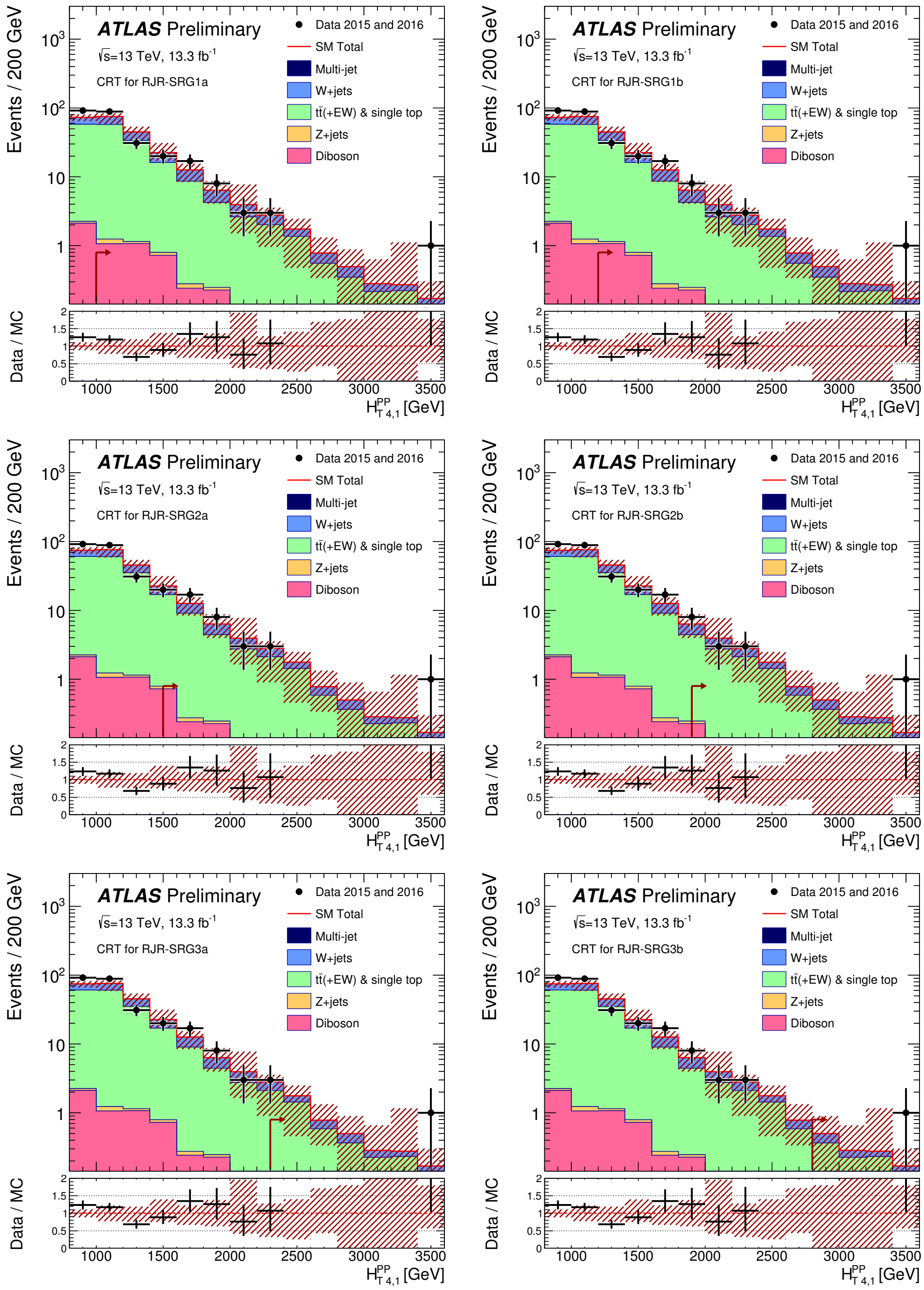

Figure 8.11: Scale variable distributions for the gluino CRT regions.

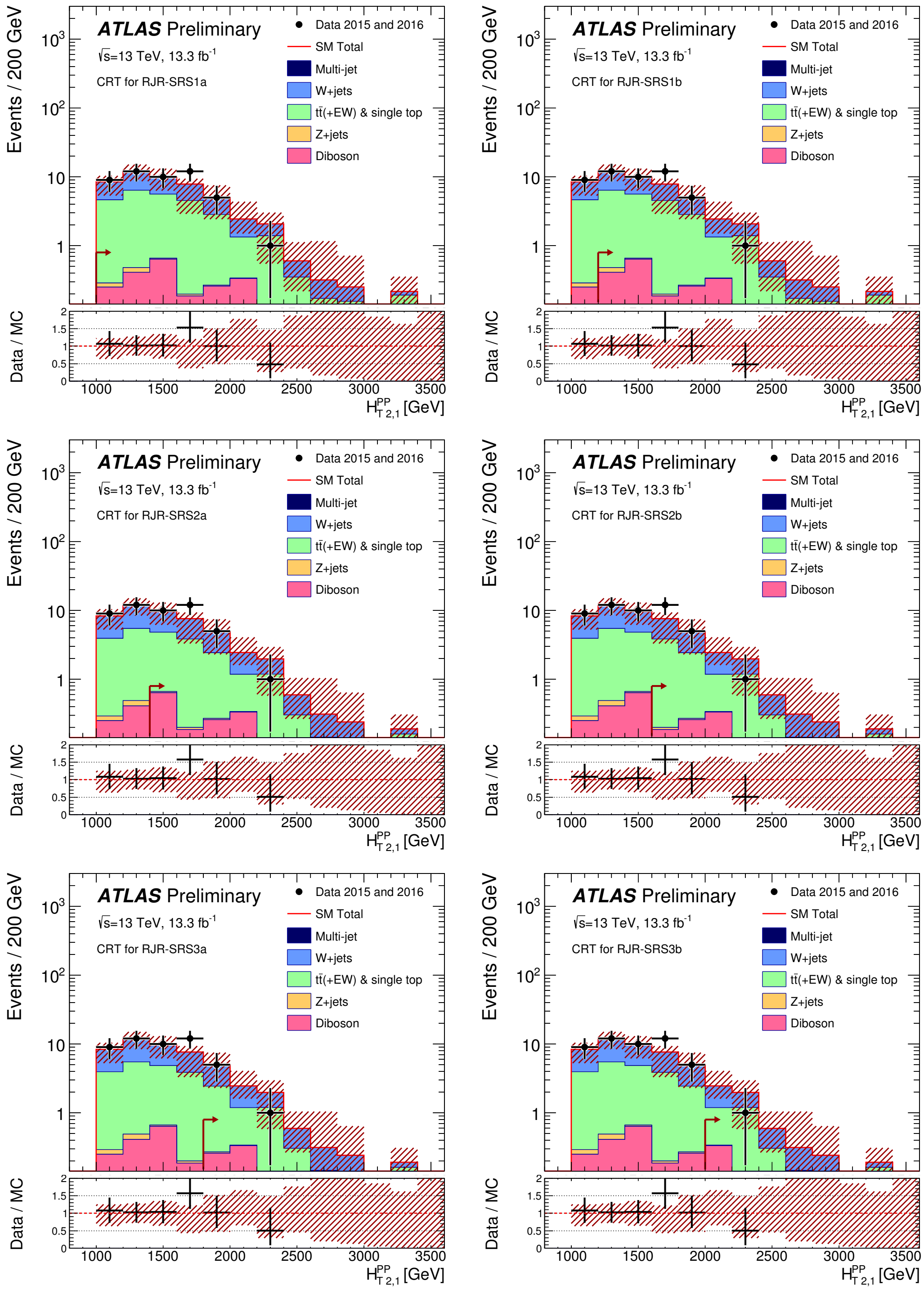

Figure 8.12: Scale variable distributions for the squark CRT regions.

Validation Regions

As discussed in general terms above, we define a set of validations regions to ensure we can properly model the particular backgrounds as we move closer to the SRs in phase space. We define at least one validation region for each major background.

For the most important background $Z \to \nu\nu$, we use a series of validation regions. The primary validation region, which we label as VRZ, is defined by selecting lepton pairs of opposite sign and identical flavor which lie with 25 GeV of the Z boson mass. This selection has high purity for $Z \to \ell\ell$ events as seen in simulation. We treat the two leptons as contributions to the $E_{\mathrm{T}}^{\mathrm{miss}}$ (as we did with the photon in CRY). This selection uses the same kinematic cuts as the signal region. We also define two VRs using the same event selection but looser kinematic cuts, which we label VRZa and VRZb. VRZa has a loosened selection on $H_{1,1}^{PP}$, again to the loosest value among the signal regions, as was done for CRW and CRt. VRZa has a loosened selection on the primary scaleful variable ($H_{T,2,1}^{PP}$ or $H_{T,4,1}^{PP}$), again to the loosest value among the signal regions, as was done for CRW and CRT. These two validation regions allow us to test the modeling of each of these variables individually, as well as allowing more validation region statistics in the signal regions with tighter cuts on these variables.

For the compressed regions, these Z validation region were found lacking. The leptons are highly boosted in the compressed case, and the lepton acceptance was quite low due to lepton isolation requirements in ΔR. Instead, two fully hadronic validation region were developed for the compressed regions. The first, VRZc has identical requirements to the signal regions with an inverted requirement on $\Delta\phi_{ISR,I}$. From simulation, this region was found to be at least 50% pure in Z events, which was considered enough to validate this background in this extreme portion of phase space. For additional validation region statistics, we also developed VRZca, which takes again uses the loosest set of cuts from each signal region. Note this means that each compressed signal region has an identical VRZca.

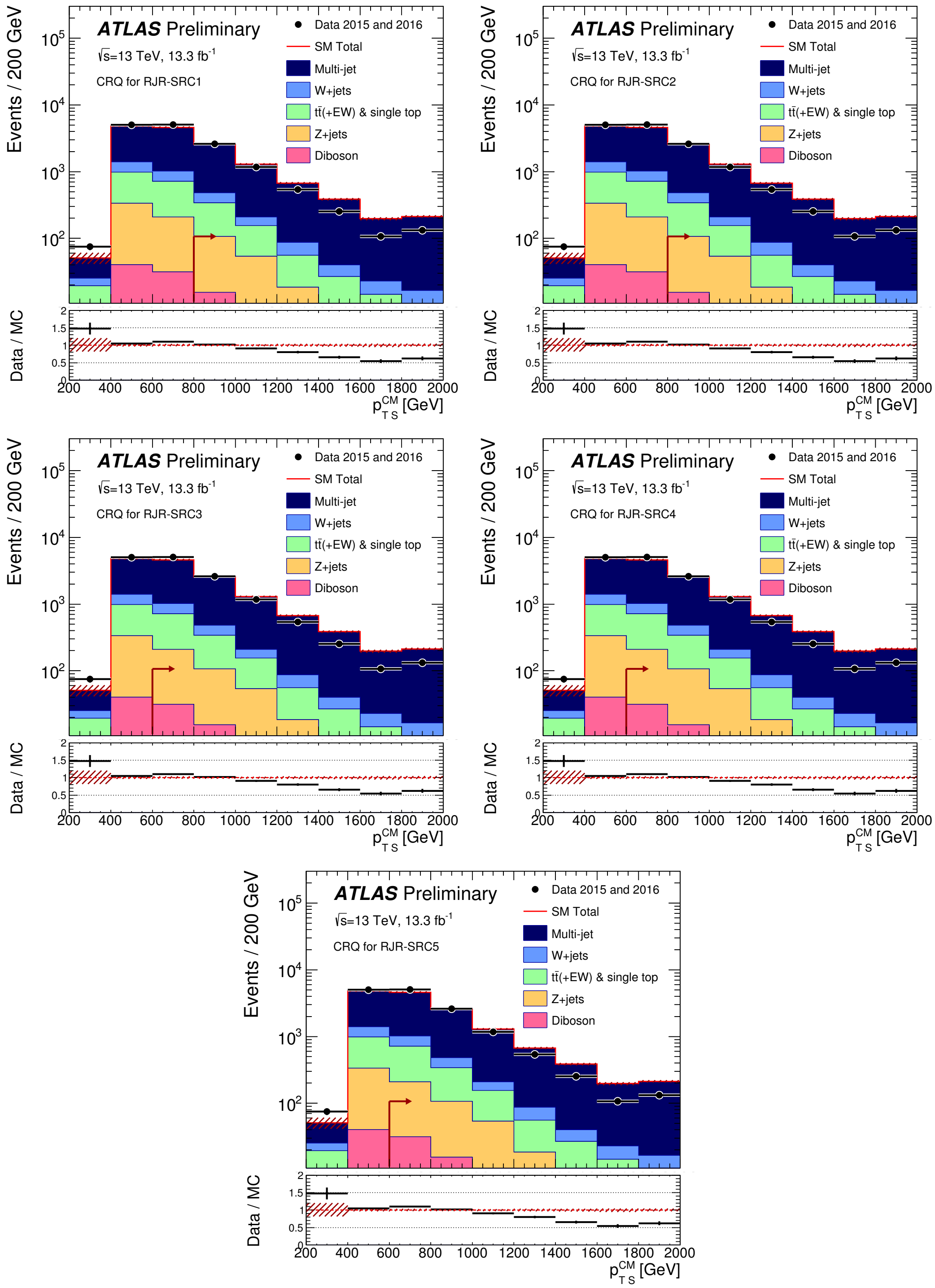

Figure 8.13: Scale variable distributions for the compressed CRQ regions.

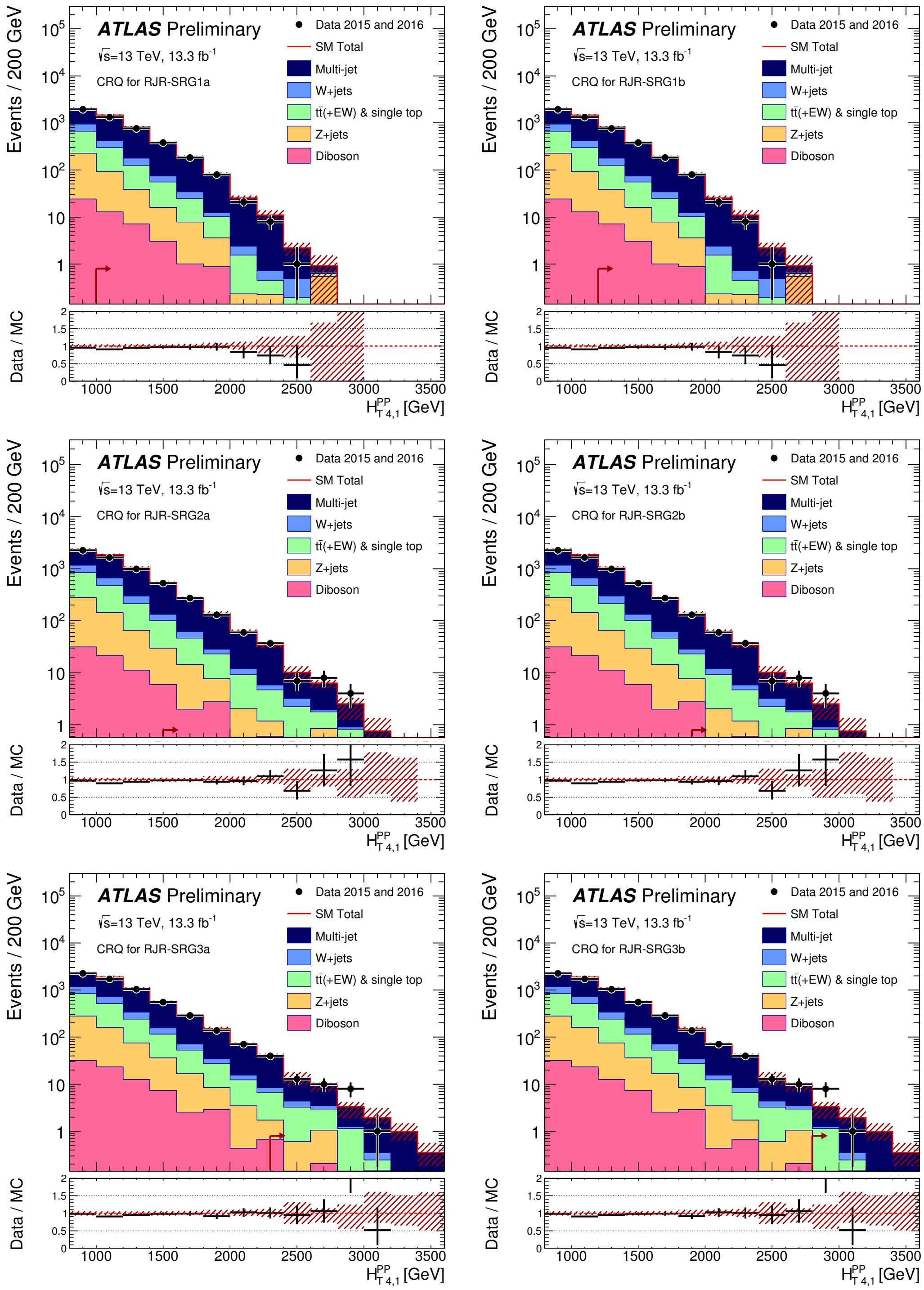

Figure 8.14: Scale variable distributions for the gluino CRQ regions.

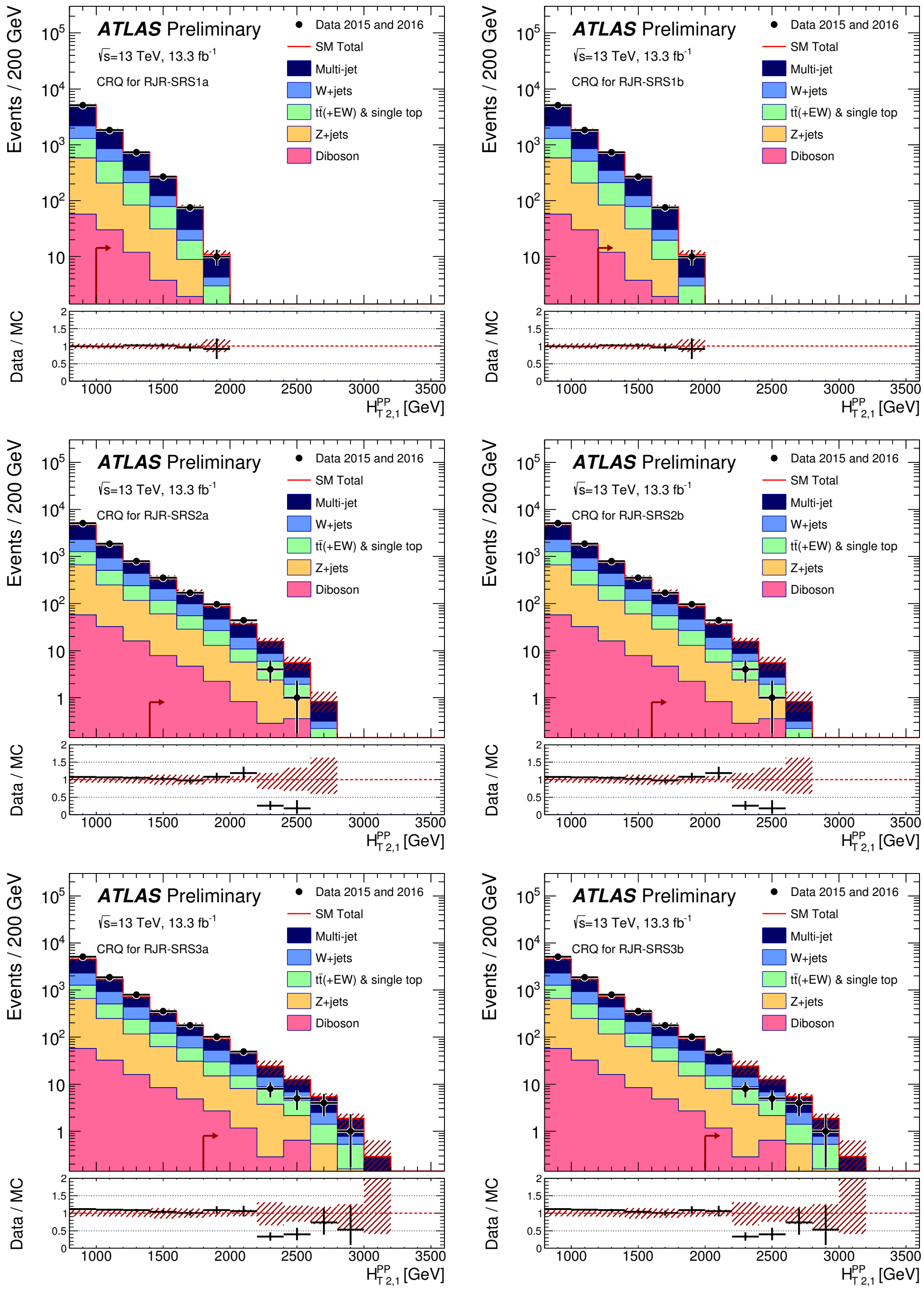

Figure 8.15: Scale variable distributions for the squark CRQ regions.

The top and W validation regions use the same event selection as the corresponding control regions, as described above. However, unlike the control regions, these validation regions reimpose the SR scaleful variable selections, to be closer in phase space to the hadronic signal regions. In the same way as we did for VRZa and VRZb, we also define auxiliary VRs which loosen the cuts on the scale variables. We define VRTa (VRWa) as VRT (VRW) with the same loosened cut on $H_{1,1}^{PP}$ and VRTb (VRWb) as VRT (VRW) with the same loosened cut on the primary scale variable.

The final set of validation regions are those defined to check the estimation of the QCD background. VRQ is defined to be identical to the corresponding CRQ, but again we use the full SR region cuts for the scaleful variables. This selection is then closer to the corresponding signal region to validate the CRQ estimate. We also define the auxiliary validation regions VRQa and VRQb for the noncompressed signal regions. In this case, we reimpose one of the two inverted cuts in CRQ with respect to the signal regions, to make each one even closer to the SRs. In CRQa (CRQb), we reimpose the $H_{1,1}^{PP}$ (Δ_{QCD}).

For the compressed case, we again define a separate validation region, due to the special kinematics probed. We construct a validation region which is the same as CRQ, with $.5 < R_{\mathrm{ISR}} < R_{\mathrm{ISR,\,SR}}$, where $R_{\mathrm{ISR,\,SR}}$ is the cut on R_{ISR}in the corresponding SR. Again, this can be seen as probing "in between" the CR and SR in phase space.

The results of this validation can be seen in Fig. 8.16. Each bin is *pull* of the validation region corresponding to a particular signal region. This is defined

$$\mathrm{Pull} = \frac{N_{\mathrm{obs}} - N_{\mathrm{pred}}}{\sigma_{\mathrm{tot}}}. \tag{8.4}$$

where σ_{tot} is the total uncertainty folding in all systematic uncertainties, which we will describe later. Assuming we have well-measured our backgrounds, we expect a Gaussian distribution of the pulls around 0, with a standard deviation of 1, as this is measuring the number of standard deviations around the mean. We can see there are few postive pulls (indicating an underestimation of the background), indicating

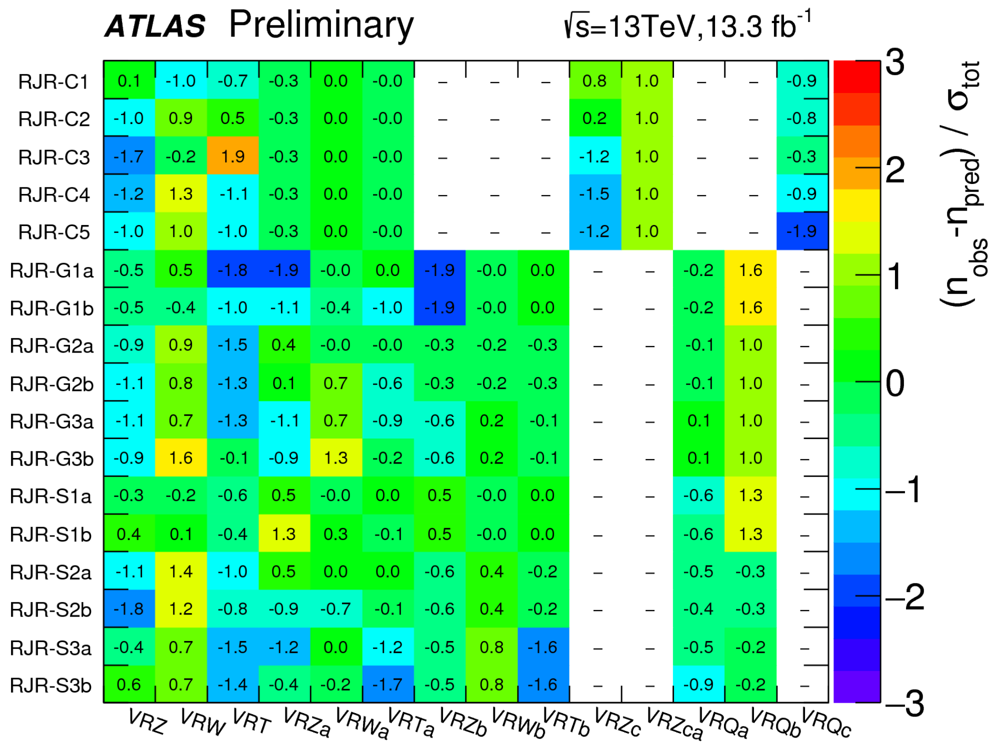

Figure 8.16: Summary of the validation region pulls

we have conservatively measured the Standard Model backgrounds with our control regions.

Systematic Uncertainties

In this section, we discuss the uncertainties considered. These generally fall into four categories: theoretical generator uncertainties, uncertainties on the CR to SR extrapolations, uncertainties on the data-driven transfer factor corrections, and object reconstruction uncertainties. We discuss each of these categories here. A table summarizing this section is in Tab. 8.5

Systematic	Uncertainty Description
alpha_GeneratorZ	Theoretical on Z cross-section
alpha_generatorW	Theoretical on W cross-section
alpha_generatorTop	Theoretical on t cross-section
alpha_radiationTop	Theoretical on t radiation tune
alpha_Pythia8Top	Theoretical on t fragmenation tune
alpha_FlatDiboson	Flat on diboson cross-section
mu_Zjets	CRY extrapolation to SR
mu_Wjets	CRW extrapolation to SR
mu_Top	CRT extrapolation to SR
mu_Multijets	CRQ extrapolation to SR
alpha_Kappa	κ factor
alpha_QCDError	Jet smearing
alpha_JET_GroupedNP_1	JES NP group 1
alpha_JET_GroupedNP_2	JES NP group 2
alpha_JET_GroupedNP_3	JES NP group 3
alpha_JER	JER
alpha_MET_SoftTrk_ResoPerp	Soft $E_{\mathrm{T}}^{\mathrm{miss}}$ resolution perpendicular to hard object system
alpha_MET_SoftTrk_ResoPara	Soft $E_{\mathrm{T}}^{\mathrm{miss}}$ resolution parellel to hard object system
alpha_MET_SoftTrk_Scale	Soft $E_{\mathrm{T}}^{\mathrm{miss}}$ scale

Table 8.5: Description of the systematic uncertainties in the analysis.

The theoretical generator uncertainties are evaluated by using alternative simulation samples or varying scale uncertainties. In the case of the Z+jets and W+jets backgrounds, the related theoretical uncertainties are estimated by varying the renormalization, factorization, and resummation scales by two, and decreasing the nominal CKKW matching scale by 5 GeV and 10 GeV respectively. In the case of $t\bar{t}$ production, we compare the nominal Powheg-Box generator with MG5_aMC@NLO, as well as comparing different radiation and generator tunes. As stated above, we account for the uncertainty on the small diboson bacground by imposition of a flat 50% uncertainty.

The CR to SR extrapolation uncertainties, or what could be called the transfer factor uncertainties, are listed in Tab. 8.5 as $mu\_$. There is one normalization factor μ for each major background, and their uncertainties, especially μ_Z, are often dominant for the measurement in many signal regions. This uncertainty is generally dominated by the statistical uncertainty in the CR.

There are two uncertainties from the data-driven corrections to the transfer factors. The first is the uncertainty on κ, which is measured using an auxiliary $Z \to \ell\ell$ control region. This is labeled alpha_Kappa. The other is the uncertainty is that assigned to the jet smearing method, which is seen in the table as alpha_QCDError.

The final set of uncertainties are those related to object reconstruction. In the case of the hadronic search presented, the important uncertainties are those assigned to the jet energy and $E_{\mathrm{T}}^{\mathrm{miss}}$. The uncertainties on the lepton reconstruction and b-tagging uncertainties were found to be negligible in all SRs. The measurement of the jet energy scale (JES) uncertainty is quite complicated, and described in [135–137]. After a complicated procedure to decorrelate the various components of the JES uncertainty, there are three components which remain, which are labeled as alpha_JET_GroupedNP_1,2,3. The jet energy resolution uncertainty is estimated using the methods discussed in Refs. [137, 138], and is labeled alpha_JER.

The $E_{\mathrm{T}}^{\mathrm{miss}}$ soft term uncertainties are described in [114, 115, 139]. The uncertainty on the $E_{\mathrm{T}}^{\mathrm{miss}}$ soft term resolution is parameterized into a component parellel to direction of the rest of the event (the sum of the hard objects p_{T}) and a component perpendicular to this direction. There is also an uncertainty on the $E_{\mathrm{T}}^{\mathrm{miss}}$ soft term scale. These are labeled as alpha_MET_SoftTrk_ResoPara, alpha_MET_SoftTrk_ResoPerp, and alpha_MET_SoftTrk_Scale.

Fitting procedure

This section describes the fitting procedure to properly account for the correlations between the various uncertainties and the simultaneous fitting of the control and signal regions.

Maximum likelihood fit

To properly account for the systematic uncertainties and simultaneously fit the control regions, we employ a maximum-likelihood fit as described in [122]. The likelihood function $\mathcal{L}$ is the product of the Poisson distributions governing the likelihood in each of the signal regions and the corresponding control regions: We begin by considering our event counts $\boldsymbol{b}$ in the control regions. The systematic uncertainties are included as a set of nuisance parameters $\boldsymbol{\theta}$.

The full likelihood function can be written [122]:

$$\mathcal{L}(n|\mu, b) = P_{\text{SR}} \times P_{\text{CR}} \times C_{\text{syst}} \tag{8.5}$$

$$= P(n_S|\lambda_S(\mu_S, \boldsymbol{b}, \boldsymbol{\theta})) \times \prod_{i \epsilon \text{CR}} P(n_i|\lambda_i(\mu_b, \boldsymbol{b}, \boldsymbol{\theta})) \times C_{\text{syst}}(\boldsymbol{\theta}^0, \boldsymbol{\theta}) \tag{8.6}$$

where $P(n_i|\lambda_i(\mu, \boldsymbol{b}, \boldsymbol{\theta}))$ is a Poisson distribution conditioned on the event counts n_i in the i-th CR with mean parameter $\lambda_i(\mu, \boldsymbol{b}, \boldsymbol{\theta})$. The term $C_{\text{syst}}(\boldsymbol{\theta}^0, \boldsymbol{\theta})$ is the probability density function with central values $\boldsymbol{\theta}^0$ which are varied with the nuisance parameters $\boldsymbol{\theta}$. We model these as Gaussian distributions with unit width and mean zero:

$$C_{\text{syst}}(\boldsymbol{\theta}^0, \boldsymbol{\theta}) = \prod_{s \epsilon S} G(\mu = \theta_s, \sigma = 1), \tag{8.7}$$

where S is the set of systematic uncertainties considered in the analysis.

The terms λ_j for any region j can be expressed as

$$\lambda_j(\mu, \boldsymbol{b}, \boldsymbol{\theta}) = \sum_b \mu_b b_j \prod_{s \epsilon S} (1 + \Delta_{j,b,s} \theta_s) \tag{8.8}$$

The term μ_b is the normalization factor associated to the background b with which has event count b_j in the region j. The terms inside the product represent scale factors freeing the model to account for the systematic uncertainties θ_s.

The process now is to maximize this likelihood function, given the free parameters μ_b and the parameters $\boldsymbol{\Delta}$ associated to the systematics as nuisance parameters.

This is done using the HistFitterpackage [122]. The final expected background prediction in each signal region r_s is then given by

$$N_{\text{total background}} = \sum_b \mu_b N_{b,\text{MC}} \tag{8.9}$$

Background-only fit, model-independent fit, and model-dependent fit

In this section, we describe the fitting procedure employed, which properly accounts for the correlations between the uncertainties through the use of a likelihood fit as described in [122]. We use three classes of likelihood fits: *background-only*, *model-independent*, and *model-dependent* fits. The background-only fits estimate the background yields in each signal region. These fits use only the control region event yields as inputs; they do not include the information from the signal regions besides the simulation event yield. The cross-contamination between CRs is also fit by this procedure. The systematic uncertainties described in the previous section are used as nuisance parameters. This background only fit also estimates the background event yields in the validation regions. When designing the analysis (before unblinding the signal regions), checking the validation region agreement is the primary way to validate the consistency and accuracy of the background estimation procedure.

In the case no excess is observed, we use a model-independent fit to set upper limits on the possible number of possible beyond the Standard Model events in each SR. These limits are derived using the same procedure as the background-only fit, with two additional pieces of information included in the fitting procedure. We include the SR event count, and a parameter known as the *signal strength*, defined as $\mu = \sigma/\sigma_{\text{BG}}$. Using the CL_{S} procedure [140] and neglecting the possible (small) signal contamination in control regions, we derive the the observed and expected limits on the number of events from BSM phenomena in each signal region.

Model-dependent fits are used to set exclusion limits on the specific SUSY models considered in this thesis, particular the gluino or squark pair production with various mass splittings. This can be seen as identical to the background-only fit with an additional simulation input from the particular model of interest, with its corresponding systematic uncertainties from detector effects accounted for as in the background-only fit. As noted when we introduced Fig. 8.1, the exclusion contours from previous model-dependent fits are the primary motivating factor in the design of our signal regions. If no excess is found, we set limits on each of the simplified signal models with various mass splittings.

Chapter 9

Results

This chapter presents the results of the analysis presented in the previous chapter. We present the full set of signal region distributions after applying the μ factors derived from the fitting procedure. We also present the systematic uncertainties in each signal region properly accounting for the correlations of the uncertainties. As no excess is observed, we show exclusion limits in the sparticle-$\tilde{\chi}_1^0$ plane based on the results of the model-dependent fits and present the model-independent limits.

9.1 Signal region distributions

In Figs. 9.1 to 9.3, we can see the unblinded distributions of the last scale cut used for each signal region. These distributions include the μ normalization scale factors derived from the fitting procedure. The systematic uncertainties are also shown. Each plot shows the distribution from a signal model which is targetted by the given signal region.

These distributions have all cuts applied except for the cut on this scale variable, which allows us to see the additional discrimination provided by the given variable. Since signal regions with the same numeral have identical cuts except for that on the main scale variable, we show (a) and (b) on the same figure. The left-most (right-most) arrow shown is the location of the a (b) cut applied in the analysis. We call these plot $N-1$ plots, where N refers to the number of cuts applied in the analysis. The full set of $N-1$ plots in the signal regions for the other variables used in the

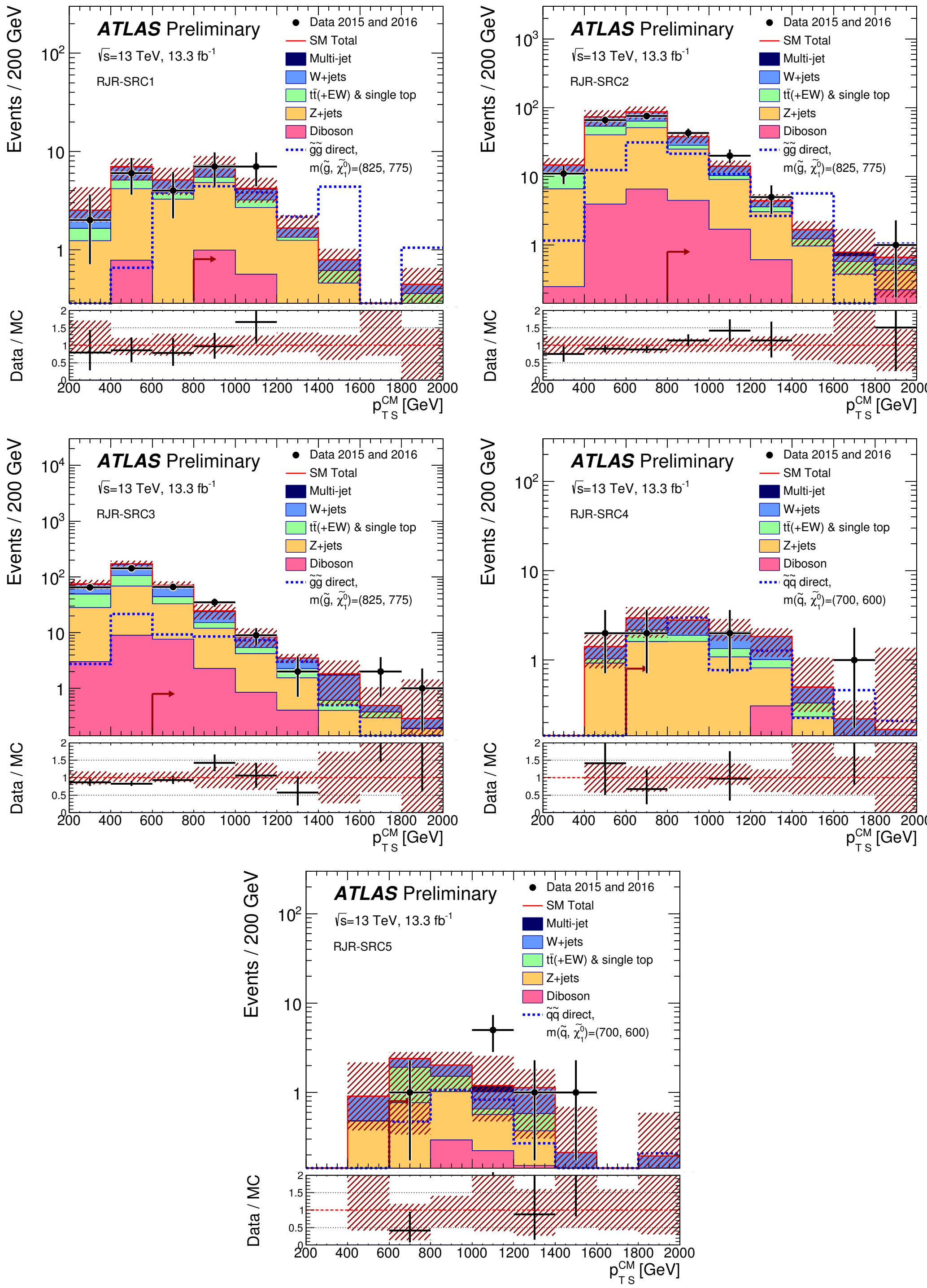

Figure 9.1: Scale variable distributions for the compressed signal regions.

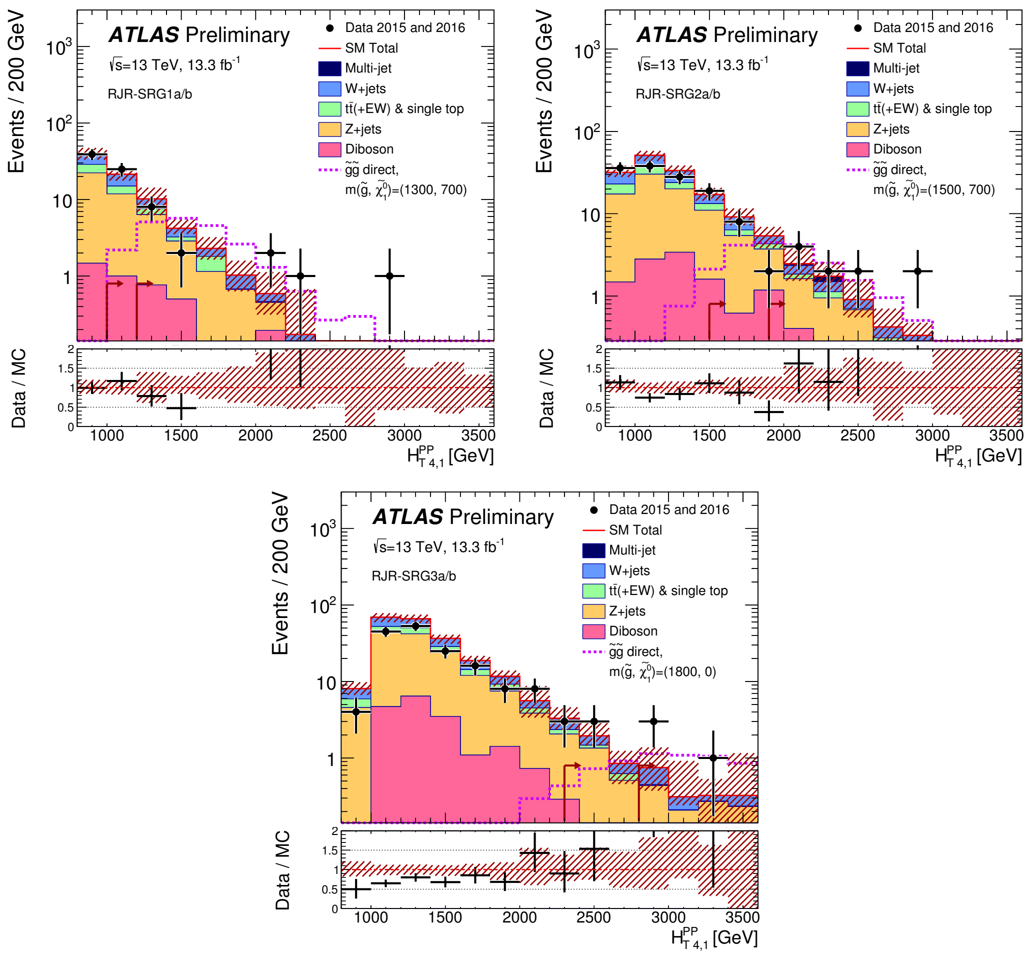

Figure 9.2: Scale variable distributions for the gluino signal regions.

analysis are shown in Sec. 9.4.

A figure showing a summary of the pulls in all of the SRs is shown in Fig. 9.4. This figure shows the integrated data and simulation values above the cut values in the N-1 plots, with the corresponding statistical and systematic uncertainties, for all signal regions simulatneously. The systematic uncertainties will be discussed in the next section. From this plot, we can see there is no significant excess of events over the Standard Model background.

This information is also presented in Tab. 9.2. The table includes the expectations from simulation before applying the μ normalization factor, as well as the model-independent limits we will discuss later.

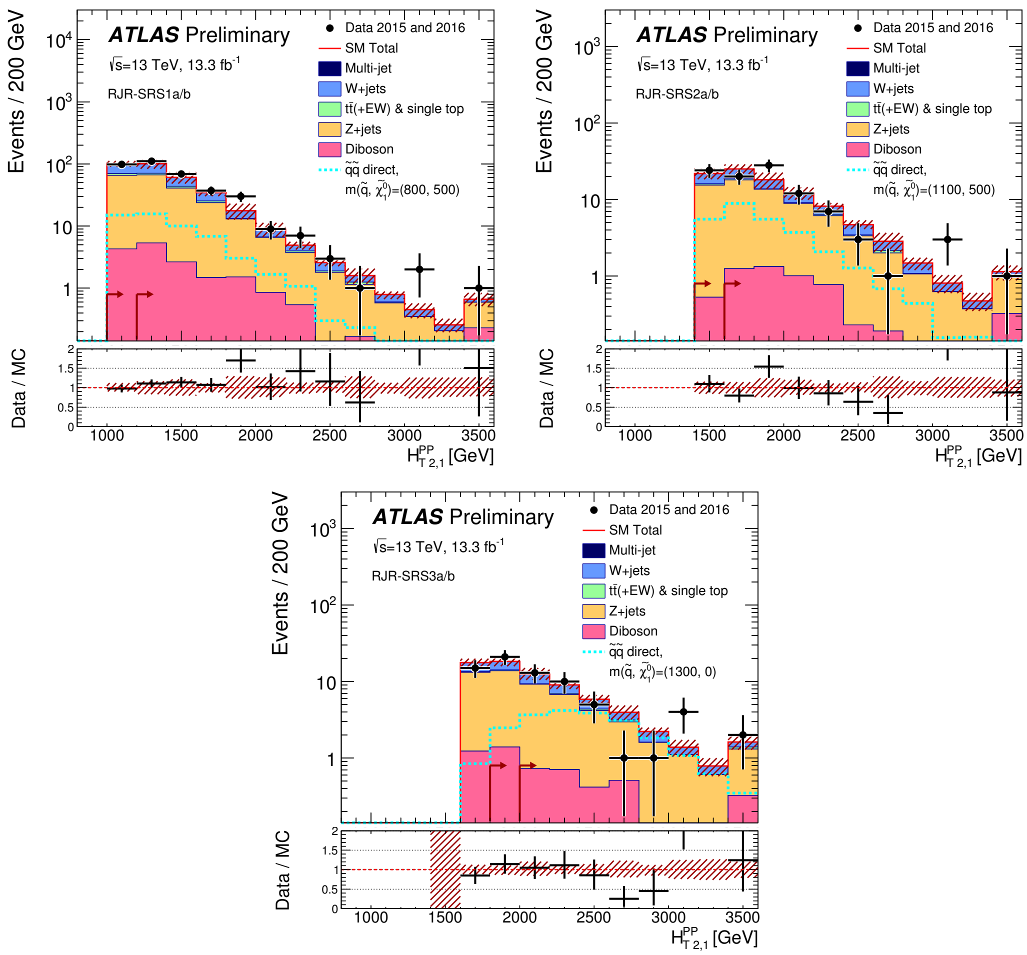

Figure 9.3: Scale variable distributions for the squark signal regions.

We now consider consider the final values of the systematic uncertainties.

9.2 Systematic Uncertainties

This section considers the results of Tab. 9.1. This table is a summary of the resulting systematic uncertainties on the background estimation in each signal region, properly accounting for systematic uncertainties. These uncertainties are expressed both as a relative uncertainty and absolute uncertainty. As correlations are properly treated, the absolute uncertainties do not add in quadrature, although most uncertainties are relatively uncorrelated. We discuss the general trends in the systematic uncertainties for each type of signal region.

In the squark regions, the total uncertainties range from 10% to 11%. We note that the uncertainties on the Z, both theoretical and $\Delta_{\mu,\mathrm{Z+jets}}$ account for the largest on the background estimate in each signal region. The κ factor uncertainty, which is also an uncertainty on the Z estimate, is also significant at 4% in each region. The $Z \to \nu\nu$ contribution to the squark regions is the primary irreducible background, so even when relatively well-measured, the uncertainty on its event yield dominates the overall uncertainty. There are also significant uncertainties from the W, top, and flat diboson uncertainties, although these are subdominant. We note that the uncertainty due to statistics of the MC simulation samples are very small for the squark case; this is a reflection of the "looseness" of these regions, as the MC statistics are sufficient for all of the major backgrounds.

The gluino regions have overall larger uncertainties than the squark regions, between 10% and 25%. due to a multitude of factors. The Z related uncertainties all contribute significantly to the final background yield uncertainties. These are relatively similar to the squark Z uncertainties. The W, top, and diboson uncertainties are all significantly more important than in the squark case however. In the gluino case, we also see that the limited simulation statistics begin to significantly affect the measurement of the Standard Model background. These are all reflections of the overall "tighter" quality of the gluino regions, as indicated by the event yields. The Δ_μ uncertainties are affected by this due to the need to use overall looser control regions, while the theory uncertainties are more affected by small statistical fluctuations between different generators. The low statistics is particularly clear in SRG3b, where the simulation statistics account for a very large 14% uncertainty.

The compressed regions have systematic uncertainties ranging from 10% to 19%. For the tighter regions, SRC1, SRC4, and SRC5, we see a large contribution from the lack of MC statistics. SRC1 and SRC4 should a large value for the W theory uncertainty, while all compressed regions show a large uncertainty on the Z estimate. These large uncertainties result from the fact that we are probing extreme phase space in boson p_{T} with the compressed regions. SRC5 shows large top and jet/$E_{\mathrm{T}}^{\mathrm{miss}}$ uncertainties; these uncertainties are more pronounced in this region than the other compressed region due to the $N_{\mathrm{jet}}^{V} > 3$ cut, and thus the uncertainty in this region is quite affected by fluctuations in the top, jet, or $E_{\mathrm{T}}^{\mathrm{miss}}$ uncertainties.

9.3 Limits and Model-dependent Exclusions

In Tab. 9.1, we show the statistical significance Z for each signal region. We calculate this using the fitted simulation mean compared with the observed event counts in each region. There is no significant excess in each region; the highest excess is in SRG3b, which is only $Z_{\mathrm{SRG3b}} = 1.55$. This information is summarized in Fig. 9.4. We thus set model-independent and model-dependent limits.

As no significant excess is observed in any of the signal regions of this analysis after estimating the background using the background-only fit, we set limits on the model-independent and model-dependent cross sections.

The model-independent limits are shown in Tab. 9.1. We present the limits on the new physics cross section in each SR. The observed and expected limits $S_{\mathrm{obs}}^{95}$and $S_{\mathrm{exp}}^{95}$are reported for the potential contribution from new physics in each region. Including the acceptance ϵ, the model-independent limits in most signal regions are of $\sim 1 - 2$ fb. One should note that the (b) version of each signal region is strictly tighter in the primary scale cut, and thus provides a stronger limit when we observe no excess, as seen here.

Additionally, we derive exclusion limits for the simplified models considered in this thesis. These are the models with pair-production of squark pairs with inaccessible gluinos, and gluino pairs with inaccessible squarks. They correspond directly to the

Channel	**RJR-S1a**	**RJR-S1b**	**RJR-S2a**	**RJR-S2b**	**RJR-S3a**	**RJR-S3b**
Total bkg	334	233	96	75	56	37
Total bkg unc.	±35 [10%]	±25 [11%]	±10 [10%]	±8 [11%]	±6 [11%]	±4 [11%]
MC statistics	–	±2.6 [1%]	±1.5 [2%]	±1.3 [2%]	±1.0 [2%]	±0.7 [2%]
$\Delta\mu_{Z,+\text{jets}}$	±20 [6%]	±14 [6%]	±4 [4%]	±2.9 [4%]	±2.2 [4%]	±1.5 [4%]
$\Delta\mu_{W,+\text{jets}}$	±10 [3%]	±7 [3%]	±3.1 [3%]	±2.3 [3%]	±1.6 [3%]	±1.1 [3%]
$\Delta\mu_{\text{Top}}$	±6 [2%]	±4 [2%]	±1.5 [2%]	±1.1 [1%]	±0.9 [2%]	±0.6 [2%]
$\Delta\mu_{\text{Multijet}}$	±0.09 [0%]	±0.05 [0%]	±0.02 [0%]	–	–	–
CRγ corr. factor	±12 [4%]	±8 [3%]	±4 [4%]	±2.9 [4%]	±2.2 [4%]	±1.4 [4%]
Theory Z	±23 [7%]	±16 [7%]	±7 [7%]	±6 [8%]	±4 [7%]	±2.8 [8%]
Theory W	±4 [1%]	±5 [2%]	±0.4 [0%]	±0.11 [0%]	±1.5 [3%]	±1.2 [3%]
Theory Top	±4 [1%]	±2.7 [1%]	±0.8 [1%]	±0.7 [1%]	±0.6 [1%]	±0.4 [1%]
Theory Diboson	±9 [3%]	±6 [3%]	±2.8 [3%]	±2.6 [3%]	±2.1 [4%]	±1.4 [4%]
Jet/MET	±3.3 [1%]	±1.5 [1%]	±0.6 [1%]	±0.6 [1%]	±1.2 [2%]	±1.0 [3%]
Multijet method	±0.7 [0%]	±0.4 [0%]	±0.08 [0%]	–	–	–

Channel	**RJR-G1a**	**RJR-G1b**	**RJR-G2a**	**RJR-G2b**	**RJR-G3a**	**RJR-G3b**
Total bkg	40	18.8	27.8	8.5	5.8	1.7
Total bkg unc.	±4 [10%]	±2.5 [13%]	±3.4 [12%]	±1.4 [16%]	±1.1 [19%]	±0.4 [24%]
MC statistics	±1.6 [4%]	±1.0 [5%]	±1.2 [4%]	±0.6 [7%]	±0.4 [7%]	±0.23 [14%]
$\Delta\mu_{Z,+\text{jets}}$	±1.5 [4%]	±0.7 [4%]	±1.6 [6%]	±0.5 [6%]	±0.4 [7%]	±0.1 [6%]
$\Delta\mu_{W,+\text{jets}}$	±0.9 [2%]	±0.4 [2%]	±1.2 [4%]	±0.31 [4%]	±0.28 [5%]	±0.1 [6%]
$\Delta\mu_{\text{Top}}$	±0.8 [2%]	±0.33 [2%]	±0.9 [3%]	±0.23 [3%]	±0.07 [1%]	±0.1 [6%]
$\Delta\mu_{\text{Multijet}}$	±0.1 [0%]	–	±0.03 [0%]	±0.02 [0%]	–	–
CRγ corr. factor	±1.2 [3%]	±0.6 [3%]	±0.8 [3%]	±0.26 [3%]	±0.19 [3%]	±0.05 [3%]
Theory Z	±2.3 [6%]	±1.1 [6%]	±1.6 [6%]	±0.5 [6%]	±0.4 [7%]	±0.1 [6%]
Theory W	±1.1 [3%]	±1.3 [7%]	±0.3 [1%]	±0.7 [8%]	±0.6 [10%]	±0.16 [9%]
Theory Top	±1.2 [3%]	±0.7 [4%]	±1.0 [4%]	±0.4 [5%]	±0.4 [7%]	±0.26 [15%]
Theory Diboson	±1.3 [3%]	±0.8 [4%]	±1.5 [5%]	±0.6 [7%]	±0.31 [5%]	±0.13 [8%]
Jet/MET	±1.0 [3%]	±0.6 [3%]	±0.4 [1%]	±0.17 [2%]	±0.22 [4%]	±0.05 [3%]
Multijet method	±0.24 [1%]	±0.12 [1%]	±0.5 [2%]	±0.4 [5%]	–	–

Channel	**RJR-C1**	**RJR-C2**	**RJR-C3**	**RJR-C4**	**RJR-C5**
Total bkg	14.5	59	110	10.5	7.3
Total bkg unc.	±2.2 [15%]	±6 [10%]	±11 [10%]	±1.5 [14%]	±1.4 [19%]
MC statistics	±0.7 [5%]	±1.7 [3%]	±2.4 [2%]	±0.6 [6%]	±0.6 [8%]
$\Delta\mu_{Z,+\text{jets}}$	±0.5 [3%]	±1.9 [3%]	±2.5 [2%]	±0.31 [3%]	±0.13 [2%]
$\Delta\mu_{W,+\text{jets}}$	±0.4 [3%]	±1.7 [3%]	±5 [5%]	±0.4 [4%]	±0.25 [3%]
$\Delta\mu_{\text{Top}}$	±0.33 [2%]	±1.3 [2%]	±4 [4%]	±0.31 [3%]	±0.4 [5%]
$\Delta\mu_{\text{Multijet}}m$	–	±0.1 [0%]	±0.06 [0%]	–	±0.1 [1%]
CRγ corr. factor	±0.5 [3%]	±1.8 [3%]	±2.3 [2%]	±0.29 [3%]	±0.13 [2%]
Theory Z	±0.8 [6%]	±3.5 [6%]	±4 [4%]	±0.6 [6%]	±0.24 [3%]
Theory W	±1.3 [9%]	±0.03 [0%]	±2.0 [2%]	±1.0 [10%]	±0.13 [2%]
Theory Top	±0.5 [3%]	±1.3 [2%]	±3.2 [3%]	±0.6 [6%]	±0.9 [12%]
Theory Diboson	±1.0 [7%]	±4 [7%]	±6 [5%]	±0.27 [3%]	±0.4 [5%]
Jet/MET	±0.5 [3%]	±1.5 [3%]	±3.1 [3%]	±0.24 [2%]	±0.5 [7%]
Multijet method	±0.09 [1%]	±0.4 [1%]	±2.1 [2%]	–	±0.18 [2%]

Table 9.1: Breakdown of the dominant systematic uncertainties in the background estimates for the RJR-based search. The individual uncertainties can be correlated, and do not necessarily add in quadrature to the total background uncertainty. Δ_μ uncertainties are the result of the control region statistical uncertainties and the systematic uncertainties entering a specific control region. In brackets, uncertainties are given relative to the expected total background yield, also presented in the Table. Empty cells (indicated by a '-') correspond to uncertainties <0.1%.

Signal Region	**RJR-S1a**	**RJR-S1b**	**RJR-S2a**	**RJR-S2b**	**RJR-S3a**	**RJR-S3b**
			MC expected events			
Diboson	17	13	5.6	5.1	4.2	2.8
Z/γ^*+jets	231	163	63	48	36	24
W+jets	97	66	22	16	11	7.8
$t\bar{t}$(+EW) + single top	15	10	2.9	2.1	1.7	1.1
			Fitted background events			
Diboson	17 ± 9	13 ± 7	5.6 ± 2.8	5.1 ± 2.6	4.2 ± 2.1	2.8 ± 1.4
Z/γ^*+jets	207 ± 33	146 ± 23	65 ± 9	50 ± 7	37 ± 5	25.0 ± 3.5
W+jets	95 ± 9	65 ± 7	24.1 ± 2.9	18.3 ± 2.3	12.8 ± 2.8	8.7 ± 2.0
$t\bar{t}$(+EW) + single top	14 ± 7	9 ± 5	2.1 ± 1.7	1.6 ± 1.3	1.3 ± 1.0	0.8 ± 0.7
Multi-jet	$0.71^{+0.71}_{-0.71}$	$0.41^{+0.41}_{-0.41}$	$0.08^{+0.09}_{-0.08}$	–	–	–
Total Expected MC	362	253	93	72	53	36
Total Fitted bkg	334 ± 35	233 ± 25	96 ± 10	75 ± 8	56 ± 6	37 ± 4
Observed	368	270	99	75	57	36
$\langle\epsilon\sigma\rangle^{95}_{\mathrm{obs}}$ [fb]	7.6	6.5	2.2	1.7	1.6	1.1
S^{95}_{obs}	101	86	29	23	22	15
S^{95}_{exp}	78^{+27}_{-21}	61^{+22}_{-16}	28^{+11}_{-8}	23^{+9}_{-7}	20^{+8}_{-6}	16^{+7}_{-5}
p_0 (Z)	0.20 (0.84)	0.12 (1.17)	0.44 (0.15)	0.50 (0.00)	0.44 (0.14)	0.50 (0.00)

Signal Region	**RJR-G1a**	**RJR-G1b**	**RJR-G2a**	**RJR-G2b**	**RJR-G3a**	**RJR-G3b**
			MC expected events			
Diboson	2.6	1.6	2.9	1.1	0.62	0.26
Z/γ^*+jets	18	8.8	13	4.2	3.1	0.83
W+jets	11	4.7	7.7	2.0	1.9	0.63
$t\bar{t}$(+EW) + single top	7.4	3.1	4.4	1.1	0.34	0.03
			Fitted background events			
Diboson	2.6 ± 1.3	1.6 ± 0.8	2.9 ± 1.5	1.1 ± 0.6	0.6 ± 0.4	0.26 ± 0.14
Z/γ^*+jets	21.1 ± 3.1	10.2 ± 1.6	14.3 ± 2.5	4.5 ± 0.8	3.3 ± 0.6	0.88 ± 0.19
W+jets	10.8 ± 1.7	4.6 ± 1.4	6.7 ± 1.3	1.7 ± 0.7	1.6 ± 0.7	0.55 ± 0.2
$t\bar{t}$(+EW) + single top	5.4 ± 1.6	2.3 ± 0.9	3.4 ± 1.4	0.8 ± 0.5	$0.26^{+0.45}_{-0.26}$	$0.02^{+0.26}_{-0.02}$
Multi-jet	0.24 ± 0.24	0.12 ± 0.12	0.5 ± 0.5	0.4 ± 0.4	–	–
Total Expected MC	39	18	29	8.7	5.9	1.7
Total Fitted bkg	40 ± 4	18.8 ± 2.5	27.8 ± 3.4	8.5 ± 1.4	5.8 ± 1.1	1.7 ± 0.4
Observed	39	14	30	10	8	4
$\langle\epsilon\sigma\rangle^{95}_{\mathrm{obs}}$ [fb]	1.1	0.56	1.1	0.71	0.64	0.55
S^{95}_{obs}	15	7.5	15	9.4	8.5	7.3
S^{95}_{exp}	16^{+7}_{-4}	10^{+5}_{-3}	14^{+6}_{-4}	$7.6^{+3.5}_{-2.0}$	$7.0^{+2.5}_{-2.1}$	$4.2^{+1.9}_{-0.5}$
p_0 (Z)	0.50 (0.00)	0.50 (0.00)	0.36 (0.35)	0.31 (0.50)	0.21 (0.81)	0.06 (1.55)

Signal Region	**RJR-C1**	**RJR-C2**	**RJR-C3**	**RJR-C4**	**RJR-C5**
			MC expected events		
Diboson	1.9	7.1	11	0.54	0.75
Z/γ^*+jets	8.8	36	46	5.8	2.5
W+jets	3.5	16	43	3.8	2.3
$t\bar{t}$(+EW) + single top	1.9	7.2	20	1.7	2.5
			Fitted background events		
Diboson	1.9 ± 1.0	7 ± 4	11 ± 6	0.54 ± 0.29	0.8 ± 0.5
Z/γ^*+jets	7.7 ± 1.1	32 ± 5	40 ± 6	5.0 ± 0.8	2.2 ± 0.4
W+jets	3.3 ± 1.4	14.5 ± 1.7	40 ± 5	3.56 ± 1.0	2.14 ± 0.35
$t\bar{t}$(+EW) + single top	1.5 ± 0.6	5.8 ± 1.8	16 ± 5	1.4 ± 0.7	2.0 ± 1.1
Multi-jet	0.09 ± 0.09	0.4 ± 0.4	2.1 ± 2.1	–	0.18 ± 0.18
Total Expected MC	16	67	124	12	8.3
Total Fitted bkg	14.5 ± 2.2	59 ± 6	110 ± 11	10.5 ± 1.5	7.3 ± 1.4
Observed	14	69	115	5	8
$\langle\epsilon\sigma\rangle^{95}_{\mathrm{obs}}$ [fb]	0.76	2.2	2.5	0.35	0.61
S^{95}_{obs}	10	29	34	4.7	8.1
S^{95}_{exp}	11^{+5}_{-3}	21^{+9}_{-6}	30^{+12}_{-8}	$8.1^{+3.0}_{-2.3}$	$7.4^{+2.9}_{-1.8}$
p_0 (Z)	0.50 (0.00)	0.18 (0.92)	0.37 (0.32)	0.50 (0.00)	0.39 (0.30)

Table 9.2: Numbers of events observed in the signal regions used in the RJR-based analysis compared with background expectations obtained from the fits described in the text. Empty cells (indicated by a '-') correspond to estimates lower than 0.01. The p-values (p_0) give the probabilities of the observations being consistent with the estimated backgrounds. For an observed number of events lower than expected, the p-value is truncated at 0.5. Between parentheses, p-values are also given as the number of equivalent Gaussian standard deviations (Z). Also shown are 95% CL upper limits on the visible cross-section ($\langle\epsilon\sigma\rangle^{95}_{\mathrm{obs}}$), the visible number of signal events (S^{95}_{obs}) and the number of signal events (S^{95}_{exp}) given the expected number of background events (and $\pm1\sigma$ excursions of the expectation).

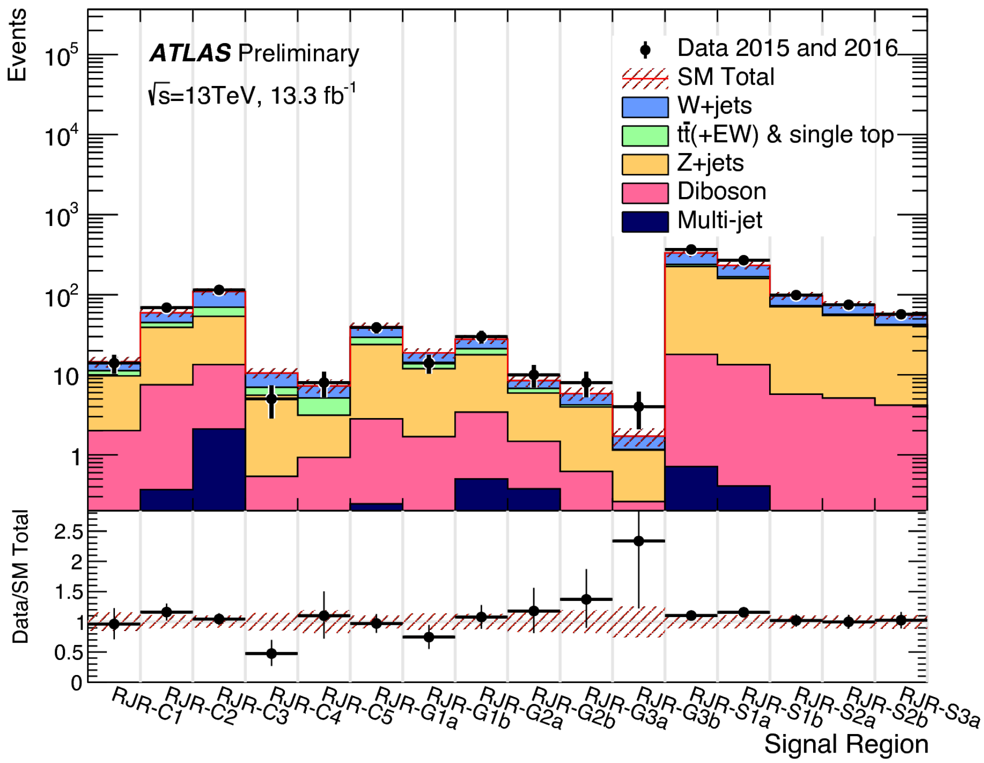

Figure 9.4: Summary of the signal region pulls

Feynman diagrams shown previously. The free parameters of these simplified models are the relevant sparticle mass and the mass of the LSP $\tilde{\chi}_1^0$. We set limits in a plane of these free parameters.

The exclusion limits are shown in Fig. 9.5. Gray text is imposed on the plane at the point of each simplified model with masses $(m_{\text{sparticle}}, m_{\tilde{\chi}_1^0})$. This gray text indicates the signal region which provided the best sensitivity at that point, as measured by the background-only fit. For each simplified signal model, we run the model-dependent fit described in the last chapter, where the signal model signal strength μ_{sig} is included as an additional free parameter. The signal sample is also allowed to freely contribute to the control regions due to signal contamination. This produces a CL$_s$ $p-$value for each signal model in the plane, and we can find those with $p = 0.05$ to set a 95% exclusion limit.

In the squark-$\tilde{\chi}_1^0$ plane, we observe that the limits from the 2015 dataset are far extended in all directions. The expected and observed exclusions are similar, which is a reflection of the compatability of the expected Standard Model event counts and observed event counts in the squark regions. A squark with mass of 1350 GeVor less is excluded by the analysis in direct decays to a quark and LSP. In the compressed spectra, we have extended limits significantly over the 2015 result in the region of 600-700 GeVin squark mass with an LSP of 450 GeVto 600 GeV. We note that directly along the kinematically-forbidden diagonal, the shape of the exclusions is affected by the interpolation between the signal models considered. This could be rectified by inclusion of additional compressed signal models. The limits in the intermediate with an LSP of ∼450-500 GeVare not far extended beyond the previous dataset. We also not that every signal region designed to provide sensitivity to this simplified model (all SRS regions and SRC1-4) is chosen as the best region at least once in the plane, indicating that each signal region provided additional sensitivity to squark phenomena.

Another curiosity is the fact that a gluino region, SRG2a is chosen as the optimal region in the squark-$\tilde{\chi}_1^0$ plane, when the squark mass is ∼700 GeV. Generally, the squark regions are looser than the gluino regions, as seen in their overall event counts. One could see this as an indication that the next iteration of the analysis should have an additional tight squark region here. Another possibility is that this region also benefits from the compressed region strategy of using an ISR jet. As the gluino regions require four jets from the imposition of the gluino decay tree, these could be capturing events where a two jet ISR system recoils off the disquark system.

In the gluino-$\tilde{\chi}_1^0$ plane, the limits on gluino masses in the simplified model where gluinos decay to two jets and an $\tilde{\chi}_1^0$ are again far extended beyond the 2015 dataset. We note in most of the plane, the expected limit is significantly stronger than the observed limit; for example, the gluino mass limit is more than 50GeVstronger in the case of a massless $\tilde{\chi}_1^0$. As much of the phase space is covered by SRG3a and SRG3b, this results from the small statistical fluctuation upward in these regions. Again, we note that every gluino signal region is the best choice at some point in this plane. This is an indication of the utility of the signal region strategy employed in this thesis, as each point provides additional sensitivity to new SUSY models.

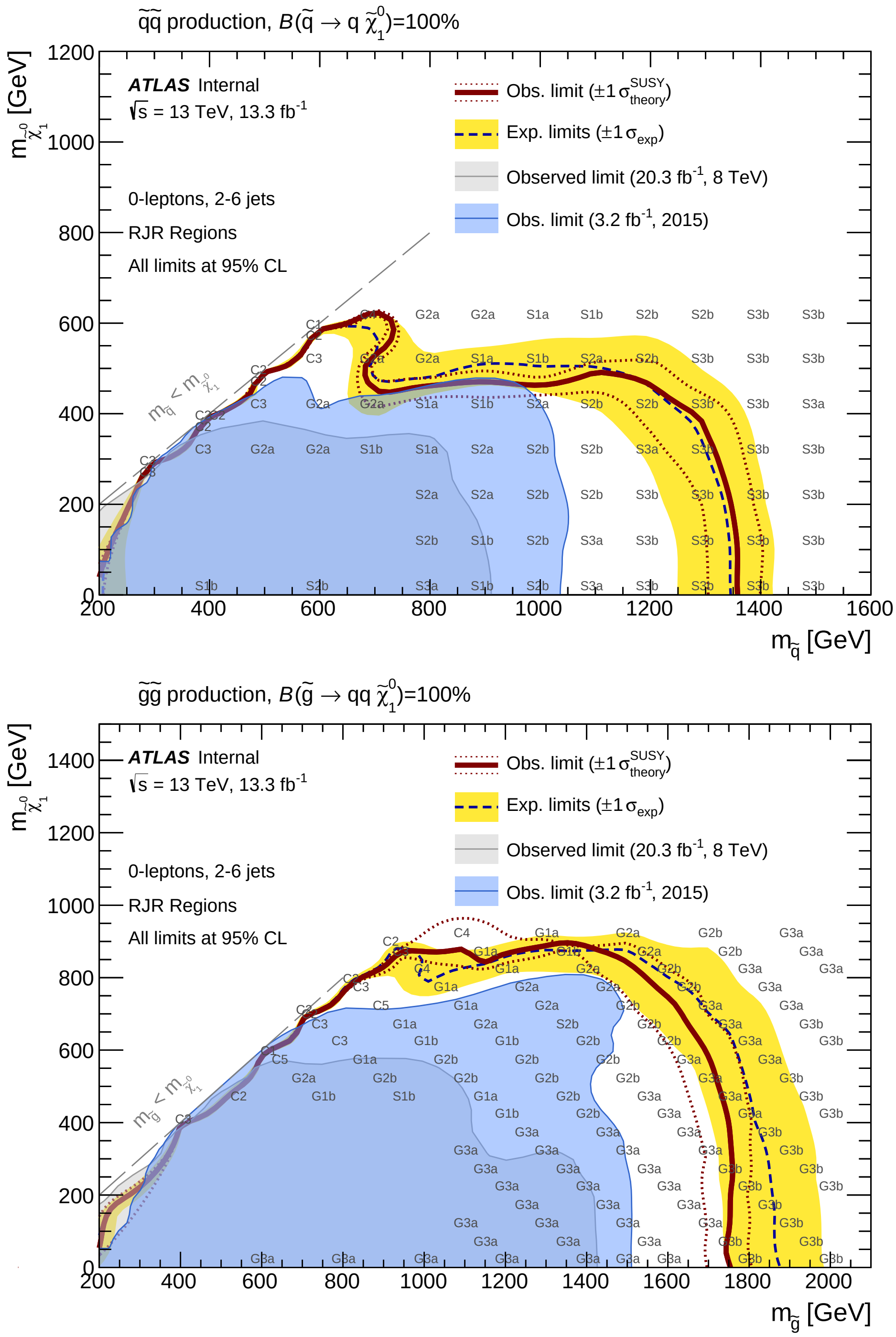

Figure 9.5: Exclusion limits for direct production of (a) light-flavour squark pairs with decoupled gluinos and (b) gluino pairs with decoupled squarks. Exclusion limits are obtained by using the signal region with the best expected sensitivity at each point. The blue dashed lines show the expected limits at 95% CL, with the yellow bands indicating the 1σ excursions due to experimental and background-only theoretical uncertainties. Observed limits are indicated by maroon curves where the solid contour represents the nominal limit, and the dotted lines are obtained by varying the signal cross-section by the renormalization and factorization scale and PDF uncertainties. Results are compared with the observed limits obtained by the previous ATLAS searches with no leptons, jets and missing transverse momentum [132, 141].

Conclusion

Here you can write some introductory remarks about your chapter. I like to give each sentence its own line.

When you need a new paragraph, just skip an extra line.

9.4 New Section

By using the asterisk to start a new section, I keep the section from appearing in the table of contents. If you want your sections to be numbered and to appear in the table of contents, remove the asterisk.

Bibliography

[1] O. Perdereau, *Planck 2015 cosmological results*, AIP Conf. Proc. **1743** (2016) p. 050014.

[2] N. Aghanim et al., *Planck 2016 intermediate results. LI. Features in the cosmic microwave background temperature power spectrum and shifts in cosmological parameters* (2016), arXiv: `1608.02487 [astro-ph.CO]`.

[3] J. S. Schwinger, *On Quantum electrodynamics and the magnetic moment of the electron*, Phys. Rev. **73** (1948) p. 416.

[4] S. Laporta and E. Remiddi, *The Analytical value of the electron (g-2) at order alpha**3 in QED*, Phys. Lett. **B379** (1996) p. 283, arXiv: `hep-ph/9602417 [hep-ph]`.

[5] S. Schael et al., *Precision electroweak measurements on the Z resonance*, Phys. Rept. **427** (2006) p. 257, arXiv: `hep-ex/0509008 [hep-ex]`.

[6] S. L. Glashow, *Partial Symmetries of Weak Interactions*, Nucl. Phys. **22** (1961) p. 579.

[7] S. Weinberg, *A Model of Leptons*, Phys. Rev. Lett. **19** (1967) p. 1264.

[8] A. Salam, *Weak and Electromagnetic Interactions*, Conf. Proc. **C680519** (1968) p. 367.

[9] M. Gell-Mann, *A Schematic Model of Baryons and Mesons*, Phys. Lett. **8** (1964) p. 214.

[10] G. Zweig, “An SU(3) model for strong interaction symmetry and its breaking. Version 2,” *DEVELOPMENTS IN THE QUARK THEORY OF HADRONS. VOL. 1. 1964 - 1978*, ed. by D. Lichtenberg and S. P. Rosen, 1964 p. 22, URL: `http://inspirehep.net/record/4674/files/cern-th-412.pdf`.

[11] S. Weinberg, *Implications of Dynamical Symmetry Breaking*, Phys. Rev. **D13** (1976) p. 974.

[12] S. Weinberg, *Implications of Dynamical Symmetry Breaking: An Addendum*, Phys. Rev. **D19** (1979) p. 1277.

[13] E. Gildener, *Gauge Symmetry Hierarchies*, Phys. Rev. **D14** (1976) p. 1667.

[14] L. Susskind, *Dynamics of Spontaneous Symmetry Breaking in the Weinberg-Salam Theory*, Phys. Rev. **D20** (1979) p. 2619.

[15] S. P. Martin, "A Supersymmetry Primer," 1997, eprint: `arXiv:hep-ph/9709356`.

[16] V. C. Rubin and W. K. Ford Jr., *Rotation of the Andromeda Nebula from a Spectroscopic Survey of Emission Regions*, Astrophys. J. **159** (1970) p. 379.

[17] M. S. Roberts and R. N. Whitehurst, *"The rotation curve and geometry of M31 at large galactocentric distances*, Astrophys. J. **201** (1970) p. 327.

[18] V. C. Rubin, N. Thonnard, and W. K. Ford Jr., *Rotational properties of 21 SC galaxies with a large range of luminosities and radii, from NGC 4605 /R = 4kpc/ to UGC 2885 /R = 122 kpc/*, Astrophys. J. **238** (1980) p. 471.

[19] V. C. Rubin et al., *Rotation velocities of 16 SA galaxies and a comparison of Sa, Sb, and SC rotation properties*, Astrophys. J. **289** (1985) p. 81.

[20] A. Bosma, *21-cm line studies of spiral galaxies. 2. The distribution and kinematics of neutral hydrogen in spiral galaxies of various morphological types.*, Astron. J. **86** (1981) p. 1825.

[21] M. Persic, P. Salucci, and F. Stel, *The Universal rotation curve of spiral galaxies: 1. The Dark matter connection*, Mon. Not. Roy. Astron. Soc. **281** (1996) p. 27, arXiv: `astro-ph/9506004 [astro-ph]`.

[22] M. Lisanti, "Lectures on Dark Matter Physics," 2016, eprint: `arXiv:1603.03797`.

[23] H. Miyazawa, *Baryon Number Changing Currents*, Prog. Theor. Phys. **36** (1966) p. 1266.

[24] J.-L. Gervais and B. Sakita, *Generalizations of dual models*, Nucl. Phys. **B34** (1971) p. 477.

[25] J. Gervais and B. Sakita, *Field theory interpretation of supergauges in dual models*, Nucl. Phys. B **34** (1971) p. 632.

[26] Y. A. Golfand and E. P. Likhtman, *Extension of the Algebra of Poincare Group Generators and Violation of p Invariance*, JETP Lett. **13** (1971) p. 323, [Pisma Zh.Eksp.Teor.Fiz.13:452-455,1971].

[27] A. Neveu and J. H. Schwarz, *Factorizable dual model of pions*, Nucl. Phys. B **31** (1971) p. 86.

[28] A. Neveu and J. H. Schwarz, *Quark Model of Dual Pions*, Phys. Rev. D **4** (1971) p. 1109.

[29] D. V. Volkov and V. P. Akulov, *Is the Neutrino a Goldstone Particle?* Phys. Lett. B **46** (1973) p. 109.

[30] J. Wess and B. Zumino, *A Lagrangian Model Invariant Under Supergauge Transformations*, Phys. Lett. B **49** (1974) p. 52.

[31] A. Salam and J. A. Strathdee, *Supersymmetry and Nonabelian Gauges*, Phys. Lett. B **51** (1974) p. 353.

[32] S. Ferrara, J. Wess, and B. Zumino, *Supergauge Multiplets and Superfields*, Phys. Lett. **B51** (1974) p. 239.

[33] J. Wess and B. Zumino, *Supergauge Transformations in Four-Dimensions*, Nucl. Phys. B **70** (1974) p. 39.

[34] J. D. Lykken, "Introduction to supersymmetry," *Fields, strings and duality. Proceedings, Summer School, Theoretical Advanced Study Institute in Elementary Particle Physics, TASI'96, Boulder, USA, June 2-28, 1996*, 1996 p. 85, arXiv: `hep-th/9612114 [hep-th]`, URL: `http://lss.fnal.gov/cgi-bin/find_paper.pl?pub-96-445-T`.

[35] A. Kobakhidze, "Intro to SUSY," 2016, URL: `https://indico.cern.ch/event/443176/page/5225-pre-susy-programme`.

[36] G. R. Farrar and P. Fayet, *Phenomenology of the Production, Decay, and Detection of New Hadronic States Associated with Supersymmetry*, Phys. Lett. B **76** (1978) p. 575.

[37] ATLAS Collaboration, *Search for the electroweak production of supersymmetric particles in* $\sqrt{s} = 8$ *TeV pp collisions with the ATLAS detector*, Phys. Rev. D **93** (2016) p. 052002, arXiv: 1509.07152 [hep-ex].

[38] ATLAS Collaboration, *Summary of the searches for squarks and gluinos using* $\sqrt{s} = 8$ *TeV pp collisions with the ATLAS experiment at the LHC*, JHEP **10** (2015) p. 054, arXiv: 1507.05525 [hep-ex].

[39] ATLAS Collaboration, *ATLAS Run 1 searches for direct pair production of third-generation squarks at the Large Hadron Collider*, Eur. Phys. J. C **75** (2015) p. 510, arXiv: 1506.08616 [hep-ex].

[40] CMS Collaboration, *Search for supersymmetry with razor variables in pp collisions at* $\sqrt{s} = 7$ *TeV*, Phys. Rev. D **90** (2014) p. 112001, arXiv: 1405.3961 [hep-ex].

[41] CMS Collaboration, *Inclusive search for supersymmetry using razor variables in pp collisions at* $\sqrt{s} = 7$ *TeV*, Phys. Rev. Lett. **111** (2013) p. 081802, arXiv: 1212.6961 [hep-ex].

[42] CMS Collaboration, *Search for Supersymmetry in pp Collisions at* 7 *TeV in Events with Jets and Missing Transverse Energy*, Phys. Lett. B **698** (2011) p. 196, arXiv: 1101.1628 [hep-ex].

[43] CMS Collaboration, *Search for Supersymmetry at the LHC in Events with Jets and Missing Transverse Energy*, Phys. Rev. Lett. **107** (2011) p. 221804, arXiv: 1109.2352 [hep-ex].

[44] CMS Collaboration, *Search for supersymmetry in hadronic final states using* M_{T2} *in pp collisions at* $\sqrt{s} = 7$ *TeV*, JHEP **10** (2012) p. 018, arXiv: 1207.1798 [hep-ex].

[45] CMS Collaboration, *Searches for supersymmetry using the* M_{T2} *variable in hadronic events produced in pp collisions at* 8 *TeV*, JHEP **05** (2015) p. 078, arXiv: 1502.04358 [hep-ex].

[46] CMS Collaboration, *Search for new physics with the* M_{T2} *variable in all-jets final states produced in pp collisions at* $\sqrt{s} = 13$ *TeV*, JHEP (2016), arXiv: 1603.04053 [hep-ex].

[47] ATLAS Collaboration, *Multi-channel search for squarks and gluinos in* $\sqrt{s} = 7$ *TeV pp collisions with the ATLAS detector at the LHC*, Eur. Phys. J. C **73** (2013) p. 2362, arXiv: 1212.6149 [hep-ex].

[48] Y. Grossman, "Introduction to the SM," 2016, URL: https://indico.fnal.gov/sessionDisplay.py?sessionId=3&confId=11505#20160811.

[49] W Buchmuller and C Ludeling, *Field Theory and Standard Model* (Sept. 2006) p. 70, URL: https://cds.cern.ch/record/984122.

[50] P. W. Higgs, *Broken Symmetries and the Masses of Gauge Bosons*, Phys. Rev. Lett. **13** (1964) p. 508.

[51] ATLAS Collaboration, *Observation of a new particle in the search for the Standard Model Higgs boson with the ATLAS detector at the LHC*, Phys. Lett. B **716** (2012) p. 1, arXiv: 1207.7214 [hep-ex].

[52] CMS Collaboration, *Observation of a new boson at a mass of 125 GeV with the CMS experiment at the LHC*, Phys. Lett. B **716** (2012) p. 30, arXiv: 1207.7235 [hep-ex].

[53] A. Chodos et al., *A New Extended Model of Hadrons*, Phys. Rev. **D9** (1974) p. 3471.

[54] A. Chodos et al., *Baryon Structure in the Bag Theory*, Phys. Rev. **D10** (1974) p. 2599.

[55] J. C. Collins, D. E. Soper, and G. F. Sterman, *Factorization of Hard Processes in QCD*, Adv. Ser. Direct. High Energy Phys. **5** (1989) p. 1, arXiv: hep-ph/0409313 [hep-ph].

[56] K. A. Olive et al., *Review of Particle Physics*, Chin. Phys. **C38** (2014) p. 090001.

[57] N. Cabibbo, *Unitary Symmetry and Leptonic Decays*, Phys. Rev. Lett. **10** (1963) p. 531, [,648(1963)].

[58] M. Kobayashi and T. Maskawa, *CP Violation in the Renormalizable Theory of Weak Interaction*, Prog. Theor. Phys. **49** (1973) p. 652.

[59] W. F. L. Hollik, *Radiative Corrections in the Standard Model and their Role for Precision Tests of the Electroweak Theory*, Fortsch. Phys. **38** (1990) p. 165.

[60] D. Yu. Bardin et al., *ELECTROWEAK RADIATIVE CORRECTIONS TO DEEP INELASTIC*

SCATTERING AT HERA! CHARGED CURRENT SCATTERING, Z. Phys. **C44** (1989) p. 149.

[61] D. C. Kennedy et al., *Electroweak Cross-Sections and Asymmetries at the Z0*, Nucl. Phys. **B321** (1989) p. 83.

[62] A. Sirlin, *Radiative Corrections in the SU(2)-L x U(1) Theory: A Simple Renormalization Framework*, Phys. Rev. **D22** (1980) p. 971.

[63] S. Fanchiotti, B. A. Kniehl, and A. Sirlin, *Incorporation of QCD effects in basic corrections of the electroweak theory*, Phys. Rev. **D48** (1993) p. 307, arXiv: `hep-ph/9212285 [hep-ph]`.

[64] C. Quigg, "Cosmic Neutrinos," *Proceedings, 35th SLAC Summer Institute on Particle Physics: Dark matter: From the cosmos to the Laboratory (SSI 2007): Menlo Park, California, July 30- August 10, 2007*, 2008, arXiv: `0802.0013 [hep-ph]`, URL: `http://lss.fnal.gov/cgi-bin/find_paper.pl?conf-07-417`.

[65] S. R. Coleman and J. Mandula, *All Possible Symmetries of the S Matrix*, Phys. Rev. **159** (1967) p. 1251.

[66] R. Haag, J. T. Lopuszanski, and M. Sohnius, *All Possible Generators of Supersymmetries of the s Matrix*, Nucl. Phys. **B88** (1975) p. 257.

[67] A. Salam and J. A. Strathdee, *On Superfields and Fermi-Bose Symmetry*, Phys. Rev. **D11** (1975) p. 1521.

[68] S. Dimopoulos and H. Georgi, *Softly Broken Supersymmetry and SU(5)*, Nucl. Phys. B **193** (1981) p. 150.

[69] S. Dimopoulos, S. Raby, and F. Wilczek, *Supersymmetry and the Scale of Unification*, Phys. Rev. **D24** (1981) p. 1681.

[70] L. E. Ibanez and G. G. Ross, *Low-Energy Predictions in Supersymmetric Grand Unified Theories*, Phys. Lett. **B105** (1981) p. 439.

[71] W. J. Marciano and G. Senjanovic, *Predictions of Supersymmetric Grand Unified Theories*, Phys. Rev. **D25** (1982) p. 3092.

[72] L. Girardello and M. T. Grisaru, *Soft Breaking of Supersymmetry*, Nucl. Phys. **B194** (1982) p. 65.

[73] D. J. H. Chung et al., *The Soft supersymmetry breaking Lagrangian: Theory and applications*, Phys. Rept. **407** (2005) p. 1, arXiv: `hep-ph/0312378 [hep-ph]`.

[74] J. Hisano et al., *Lepton flavor violation in the supersymmetric standard model with seesaw induced neutrino masses*, Phys. Lett. **B357** (1995) p. 579, arXiv: `hep-ph/9501407 [hep-ph]`.

[75] F. Gabbiani et al., *A Complete analysis of FCNC and CP constraints in general SUSY extensions of the standard model*, Nucl. Phys. **B477** (1996) p. 321, arXiv: `hep-ph/9604387 [hep-ph]`.

[76] F. Gabbiani and A. Masiero, *FCNC in Generalized Supersymmetric Theories*, Nucl. Phys. **B322** (1989) p. 235.

[77] J. S. Hagelin, S. Kelley, and T. Tanaka, *Supersymmetric flavor changing neutral currents: Exact amplitudes and phenomenological analysis*, Nucl. Phys. **B415** (1994) p. 293.

[78] J. S. Hagelin, S. Kelley, and V. Ziegler, *Using gauge coupling unification and proton decay to test minimal supersymmetric SU(5)*, Phys. Lett. **B342** (1995) p. 145, arXiv: `hep-ph/9406366 [hep-ph]`.

[79] D. Choudhury et al., *Constraints on nonuniversal soft terms from flavor changing neutral currents*, Phys. Lett. **B342** (1995) p. 180, arXiv: `hep-ph/9408275 [hep-ph]`.

[80] R. Barbieri and L. J. Hall, *Signals for supersymmetric unification*, Phys. Lett. **B338** (1994) p. 212, arXiv: `hep-ph/9408406 [hep-ph]`.

[81] B. de Carlos, J. A. Casas, and J. M. Moreno, *Constraints on supersymmetric theories from mu —¿ e gamma*, Phys. Rev. **D53** (1996) p. 6398, arXiv: `hep-ph/9507377 [hep-ph]`.

[82] J. A. Casas and S. Dimopoulos, *Stability bounds on flavor violating trilinear soft terms in the MSSM*, Phys. Lett. **B387** (1996) p. 107, arXiv: `hep-ph/9606237 [hep-ph]`.

[83] C. Borschensky et al., *Squark and gluino production cross sections in pp collisions at $\sqrt{s}$ = 13, 14, 33 and 100 TeV*, Eur. Phys. J. **C74** (2014) p. 3174, arXiv: `1407.5066 [hep-ph]`.

[84] M. Klasen, M. Pohl, and G. Sigl, *Indirect and direct search for dark matter*, Prog. Part. Nucl. Phys. **85** (2015) p. 1, arXiv: `1507.03800 [hep-ph]`.

[85] L. Evans and P. Bryant, *LHC Machine*, JINST **3** (2008) S08001.

[86] Vladimir Shiltsev, "Accelerator Physics and Technology," Aug. 2016, URL: `{https://indico.fnal.gov/sessionDisplay.py?sessionId=3&confId=11505#20160811}`.

[87] *LEP design report*, Copies shelved as reports in LEP, PS and SPS libraries, Geneva: CERN, 1984, URL: `https://cds.cern.ch/record/102083`.

[88] ATLAS Collaboration, *The ATLAS Experiment at the CERN Large Hadron Collider*, JINST **3** (2008) S08003.

[89] ATLAS Collaboration, *2015 start-up trigger menu and initial performance assessment of the ATLAS trigger using Run-2 data*, ATL-DAQ-PUB-2016-001 (2016), URL: `https://cds.cern.ch/record/2104298`.

[90] ATLAS Collaboration, *Performance of the ATLAS Inner Detector Track and Vertex Reconstruction in High Pile-Up LHC Environment*, ATLAS-CONF-2012-042, 2012, URL: `https://cds.cern.ch/record/1435196`.

[91] ATLAS Collaboration, *Early Inner Detector Tracking Performance in the 2015 Data at* $\sqrt{s} = 13$ *TeV*, ATL-PHYS-PUB-2015-051, 2015, URL: `https://cds.cern.ch/record/2110140`.

[92] K Hamano, A Morley, and A Salzburger, "Track Reconstruction Performance and Efficiency Estimation using different ID geometry samples," tech. rep. ATL-COM-PHYS-2012-1541, plots for a poster at HCP: CERN, Oct. 2012, URL: `https://cds.cern.ch/record/1489674`.

[93] ATLAS Collaboration, *Electron reconstruction and identification efficiency measurements with the ATLAS detector using the 2011 LHC proton–proton collision data*, Eur. Phys. J. C **74** (2014) p. 2941, arXiv: `1404.2240 [hep-ex]`.

[94] ATLAS Collaboration, *Topological cell clustering in the ATLAS calorimeters and its performance in LHC Run 1* (2016), arXiv: `1603.02934 [hep-ex]`.

[95] ATLAS Collaboration, *Jet energy resolution in proton–proton collisions at $\sqrt{s} = 7$ TeV recorded in 2010 with the ATLAS detector*, Eur. Phys. J. C **73** (2013) p. 2306, arXiv: 1210.6210 [hep-ex].

[96] ATLAS Collaboration, *Electron performance measurements with the ATLAS detector using the 2010 LHC proton–proton collision data*, Eur. Phys. J. C **72** (2012) p. 1909, arXiv: 1110.3174 [hep-ex].

[97] M. Aaboud et al., *Measurement of the photon identification efficiencies with the ATLAS detector using LHC Run-1 data* (2016), arXiv: 1606.01813 [hep-ex].

[98] ATLAS Collaboration, *Electron and photon energy calibration with the ATLAS detector using LHC Run 1 data*, Eur. Phys. J. C **74** (2014) p. 3071, arXiv: 1407.5063 [hep-ex].

[99] "Electron and photon energy calibration with the ATLAS detector using data collected in 2015 at $\sqrt{s} = 13$ TeV," tech. rep. ATL-PHYS-PUB-2016-015, CERN, Aug. 2016, URL: https://cds.cern.ch/record/2203514.

[100] ATLAS Collaboration, *Muon reconstruction performance of the ATLAS detector in proton–proton collision data at $\sqrt{s} = 13$ TeV*, Eur. Phys. J. C **76** (2016) p. 292, arXiv: 1603.05598 [hep-ex].

[101] ATLAS Collaboration, *Jet energy measurement with the ATLAS detector in proton–proton collisions at $\sqrt{s} = 7$ TeV*, Eur. Phys. J. C **73** (2013) p. 2304, arXiv: 1112.6426 [hep-ex].

[102] ATLAS Collaboration, *Jet energy measurement and its systematic uncertainty in proton–proton collisions at $\sqrt{s} = 7$ TeV with the ATLAS detector*, Eur. Phys. J. C **75** (2015) p. 17, arXiv: 1406.0076 [hep-ex].

[103] S. D. Ellis and D. E. Soper, *Successive combination jet algorithm for hadron collisions*, Phys. Rev. **D48** (1993) p. 3160, arXiv: hep-ph/9305266 [hep-ph].

[104] M. Cacciari and G. P. Salam, *Dispelling the N^3 myth for the k_t jet-finder*, Phys. Lett. B **641** (2006) p. 57, arXiv: hep-ph/0512210.

[105] M. Cacciari, G. P. Salam, and G. Soyez, *The anti-k_t jet clustering algorithm*, JHEP **04** (2008) p. 063, arXiv: 0802.1189 [hep-ph].

[106] *Particle-Flow Event Reconstruction in CMS and Performance for Jets, Taus, and MET* (2009).

[107] ATLAS Collaboration, *Tagging and suppression of pileup jets with the ATLAS detector*, ATLAS-CONF-2014-018, 2014, URL: https://cds.cern.ch/record/1700870.

[108] M. Cacciari, G. P. Salam, and G. Soyez, *The Catchment Area of Jets*, JHEP **04** (2008) p. 005, arXiv: 0802.1188 [hep-ph].

[109] G. Aad et al., *Performance of b-Jet Identification in the ATLAS Experiment*, JINST **11** (2016) P04008, arXiv: 1512.01094 [hep-ex].

[110] ATLAS Collaboration, *Optimisation of the ATLAS b-tagging performance for the 2016 LHC Run*, ATL-PHYS-PUB-2016-012 (2016), URL: https://cds.cern.ch/record/2160731.

[111] G. Aad et al., *Performance of algorithms that reconstruct missing transverse momentum in $\sqrt{s} = 8$ TeV proton-proton collisions in the ATLAS detector* (2016), arXiv: 1609.09324 [hep-ex].

[112] ATLAS Collaboration, *Prospects for Supersymmetry discovery based on inclusive searches at a 7 TeV centre-of-mass energy with the ATLAS detector*, ATL-PHYS-PUB-2010-010, 2010, URL: https://cds.cern.ch/record/1278474.

[113] ATLAS Collaboration, *Expected sensitivity studies for gluino and squark searches using the early LHC 13 TeV Run-2 dataset with the ATLAS experiment*, ATL-PHYS-PUB-2015-005, 2015, URL: https://atlas.web.cern.ch/Atlas/GROUPS/PHYSICS/PUBNOTES/ATL-PHYS-PUB-2015-005.

[114] ATLAS Collaboration, *Expected performance of missing transverse momentum reconstruction for the ATLAS detector at $\sqrt{s} = 13$ TeV*, ATL-PHYS-PUB-2015-023, 2015, URL: https://cds.cern.ch/record/2037700.

[115] ATLAS Collaboration, *Performance of missing transverse momentum reconstruction with the ATLAS detector in the first proton–proton collisions at $\sqrt{s} = 13$ TeV*,

ATL-PHYS-PUB-2015-027, 2015, URL: https://cds.cern.ch/record/2037904.

[116] P. Jackson, C. Rogan and M. Santoni, *Sparticles in Motion - getting to the line in compressed scenarios with the Recursive Jigsaw Reconstruction* (2016), arXiv: 1607.08307 [hep-ph].

[117] ATLAS Collaboration, *Further searches for squarks and gluinos in final states with jets and missing transverse momentum at $\sqrt{s} = 13$ TeV with the ATLAS detector*, ATLAS-CONF-2016-078, 2016, URL: https://cds.cern.ch/record/2206252.

[118] C. Rogan, *Kinematical variables towards new dynamics at the LHC* (2010), arXiv: 1006.2727 [hep-ph].

[119] M. R. Buckley et al., *Super-Razor and Searches for Sleptons and Charginos at the LHC*, Phys. Rev. **D89** (2014) p. 055020, arXiv: 1310.4827 [hep-ph].

[120] CMS Collaboration, *Search for supersymmetry using razor variables in events with b-tagged jets in pp collisions at $\sqrt{s} = 8$ TeV*, Phys. Rev. D **91** (2015) p. 052018, arXiv: 1502.00300 [hep-ex].

[121] Chris Rogan, "RestFrames," URL: {http://restframes.com}.

[122] M. Baak et al., *HistFitter software framework for statistical data analysis*, Eur. Phys. J. **C75** (2015) p. 153, arXiv: 1410.1280 [hep-ex].

[123] M. L. Mangano et al., *Matching matrix elements and shower evolution for top-quark production in hadronic collisions*, JHEP **01** (2007) p. 013, arXiv: hep-ph/0611129 [hep-ph].

[124] T. Gleisberg et al., *Event generation with SHERPA 1.1*, JHEP **02** (2009) p. 007, arXiv: 0811.4622 [hep-ph].

[125] S. Schumann and F. Krauss, *A Parton shower algorithm based on Catani-Seymour dipole factorisation*, JHEP **03** (2008) p. 038, arXiv: 0709.1027 [hep-ph].

[126] F. Maltoni and T. Stelzer, *MadEvent: Automatic event generation with MadGraph*, JHEP **02** (2003) p. 027, arXiv: hep-ph/0208156 [hep-ph].

[127] T. Sjöstrand et al., *An Introduction to PYTHIA 8.2*, Comput. Phys. Commun. **191** (2015) p. 159, arXiv: `1410.3012 [hep-ph]`.

[128] S. Alioli et al., *A general framework for implementing NLO calculations in shower Monte Carlo programs: the POWHEG BOX*, JHEP **06** (2010) p. 043, arXiv: `1002.2581 [hep-ph]`.

[129] J. Alwall, R. Frederix, S. Frixione, V. Hirschi, F. Maltoni, O. Mattelaer, H. -S. Shao, T. Stelzer, P. Torrielli, M. Zaro, *The automated computation of tree-level and next-to-leading order differential cross sections, and their matching to parton shower simulations*, JHEP **07** (2014) p. 079, arXiv: `1405.0301 [hep-ph]`.

[130] S. Frixione et al., *NLO QCD corrections in Herwig++ with MC@NLO*, JHEP **01** (2011) p. 053, arXiv: `1010.0568 [hep-ph]`.

[131] S. Agostinelli et al., *GEANT4: A simulation toolkit*, Nucl. Instrum. Meth. A **506** (2003) p. 250.

[132] ATLAS Collaboration, *Search for squarks and gluinos in final states with jets and missing transverse momentum at $\sqrt{s} = 13$ TeV with the ATLAS detector*, Eur. Phys. J. C **76** (2016) p. 392, arXiv: `1605.03814 [hep-ex]`.

[133] R. D. Cousins, J. T. Linnemann, and J. Tucker, *Evaluation of three methods for calculating statistical significance when incorporating a systematic uncertainty into a test of the background-only hypothesis for a Poisson process*, Nucl. Instrum. Meth. **A595** (2008) p. 480.

[134] ATLAS Collaboration, *Search for squarks and gluinos with the ATLAS detector in final states with jets and missing transverse momentum using 4.7 fb^{-1} of $\sqrt{s} = 7$ TeV proton–proton collision data*, Phys. Rev. D **87** (2013) p. 012008, arXiv: `1208.0949 [hep-ex]`.

[135] ATLAS Collaboration, *Jet energy measurement with the ATLAS detector in proton-proton collisions at $\sqrt{s} = 7$ TeV*, Eur. Phys. J. C **73** (2013) p. 2304, arXiv: `1112.6426 [hep-ex]`.

[136] ATLAS Collaboration, *Single hadron response measurement and calorimeter jet energy scale uncertainty with the ATLAS detector at the LHC*, Eur. Phys. J. C **73** (2013) p. 2305, arXiv: `1203.1302 [hep-ex]`.

[137] ATLAS Collaboration, *Jet Calibration and Systematic Uncertainties for Jets Reconstructed in the ATLAS Detector at $\sqrt{s} = 13$ TeV*,

ATL-PHYS-PUB-2015-015, 2015,
URL: https://cds.cern.ch/record/2037613.

[138] ATLAS Collaboration, *Jet energy resolution in proton-proton collisions at* $\sqrt{s} = 7$ *TeV recorded in 2010 with the ATLAS detector*, Eur. Phys. J. C **73** (2013) p. 2306, arXiv: 1210.6210 [hep-ex].

[139] ATLAS Collaboration, *Performance of algorithms that reconstruct missing transverse momentum in* $\sqrt{s} = 8$ *TeV proton–proton collisions in the ATLAS detector* (2016), arXiv: 1609.09324 [hep-ex].

[140] G. J. Feldman and R. D. Cousins, *A Unified approach to the classical statistical analysis of small signals*, Phys. Rev. **D57** (1998) p. 3873, arXiv: physics/9711021 [physics.data-an].

[141] ATLAS Collaboration, *Search for squarks and gluinos with the ATLAS detector in final states with jets and missing transverse momentum using* $\sqrt{s} = 8$ *TeV proton–proton collision data*, JHEP **09** (2014) p. 176, arXiv: 1405.7875 [hep-ex].

The Standard Model

add some text or cut this

Compressed region N-1 plots

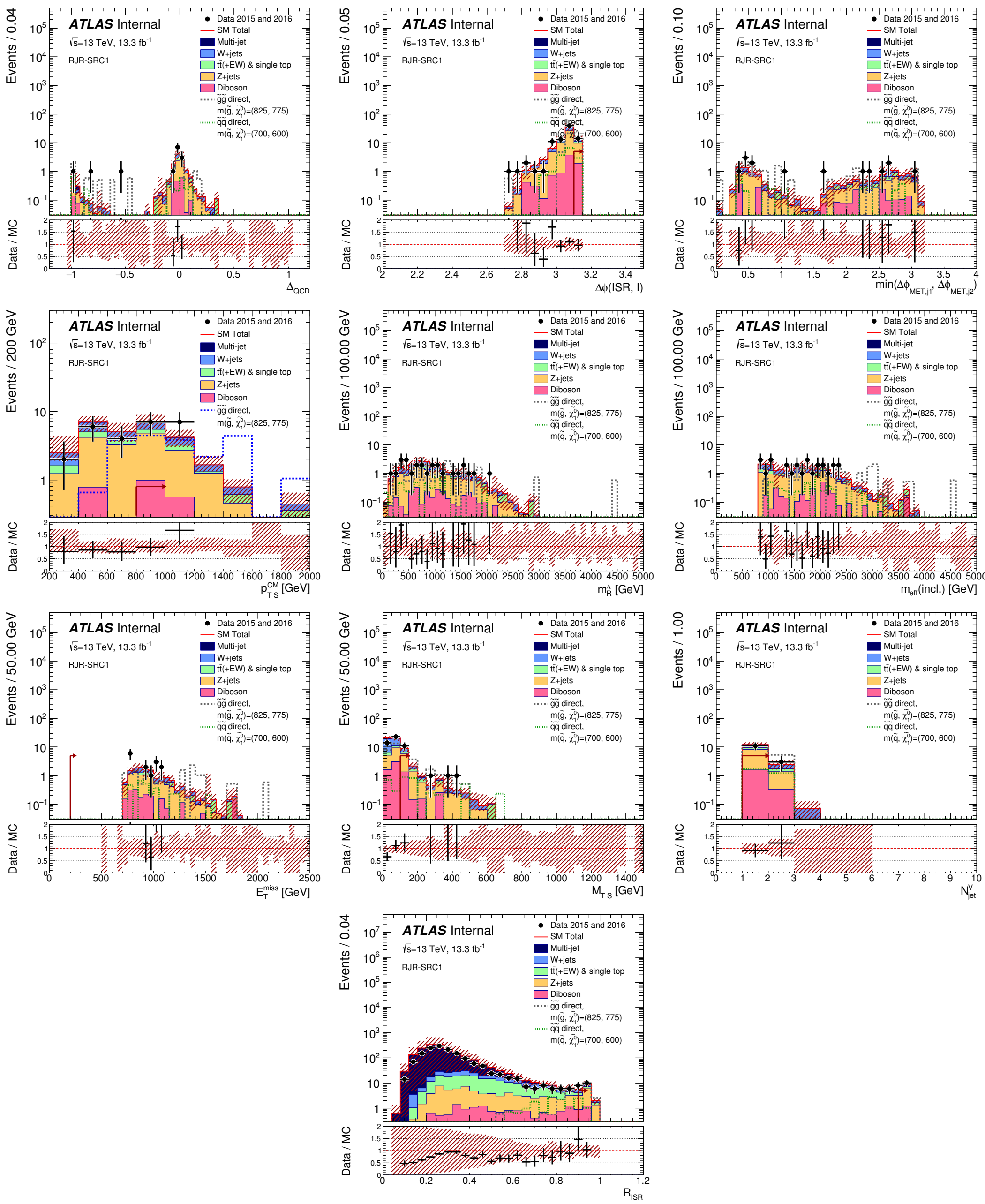
ATLAS Internal
√s=13 TeV, 13.3 fb⁻¹
RJR-SRC1
Data 2015 and 2016
SM Total
Multi-jet
W+jets
tt̄(+EW) & single top
Z+jets
Diboson
g̃g̃ direct,
m(g̃, χ̃⁰₁)=(825, 775)
q̃q̃ direct,
m(q̃, χ̃⁰₁)=(700, 600)
Events / 0.04
Events / 0.05
Events / 0.10
Events / 200 GeV
Events / 100.00 GeV
Events / 50.00 GeV
Events / 1.00
Data / MC
Δ_QCD
Δφ(ISR, I)
min(Δφ_MET,j1, Δφ_MET,j2)
p_T S^CM [GeV]
m_R^Δ [GeV]
m_eff(incl.) [GeV]
E_T^miss [GeV]
M_T S [GeV]
N_jet^V
R_ISR

Figure 1

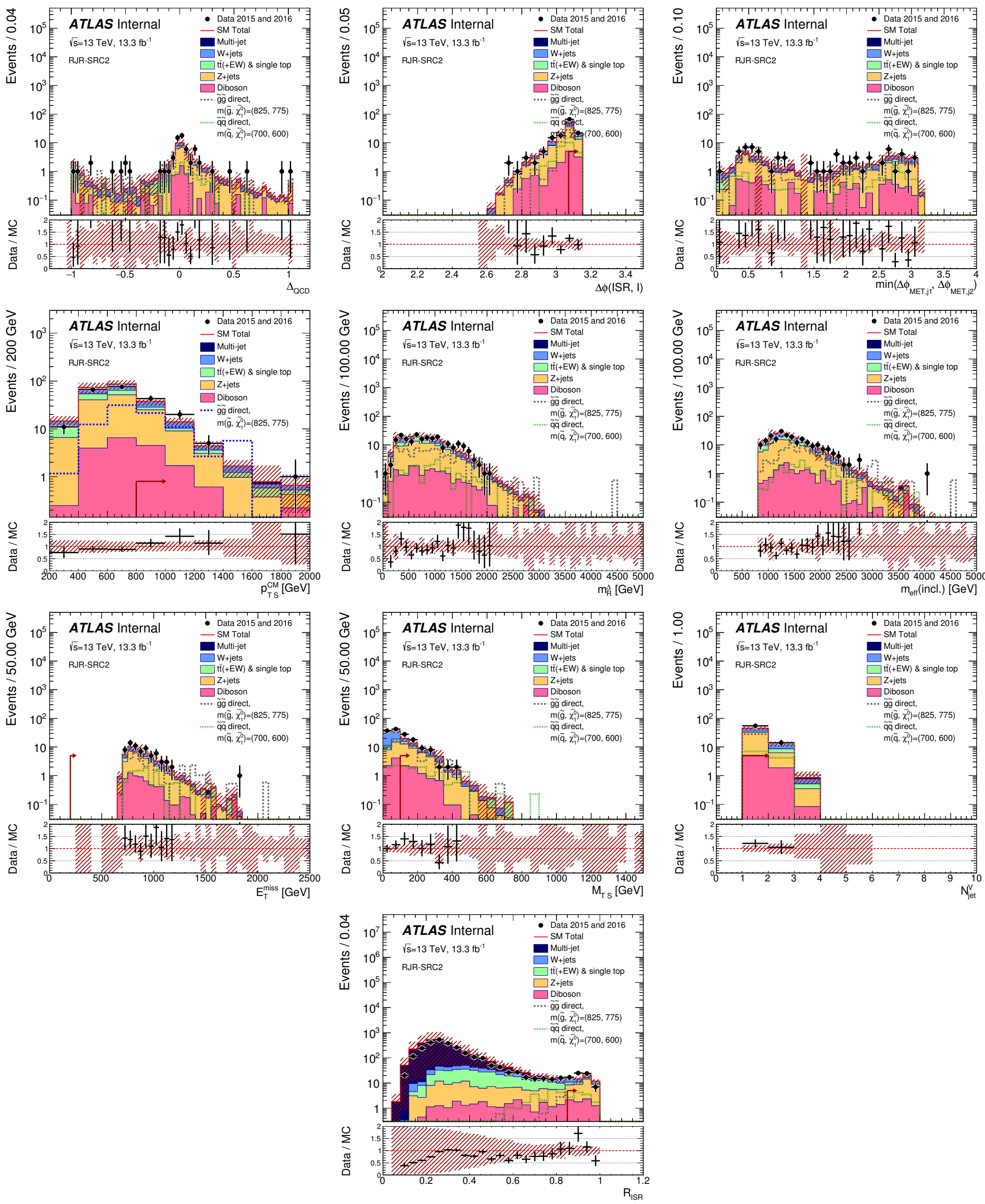
ATLAS Internal
√s=13 TeV, 13.3 fb⁻¹
RJR-SRC2
Data 2015 and 2016
SM Total
Multi-jet
W+jets
tt̄(+EW) & single top
Z+jets
Diboson
g̃g̃ direct, m(g̃, χ̃⁰₁)=(825, 775)
q̃q̃ direct, m(q̃, χ̃⁰₁)=(700, 600)
Data / MC
Events / 0.04
Δ_QCD
Events / 0.05
Δφ(ISR, I)
Events / 0.10
min(Δφ_MET,j1, Δφ_MET,j2)
Events / 200 GeV
p_T S^CM [GeV]
Events / 100.00 GeV
m_R^λ [GeV]
m_eff(incl.) [GeV]
Events / 50.00 GeV
E_T^miss [GeV]
M_T S [GeV]
Events / 1.00
N_jet^V
R_ISR

Figure 2

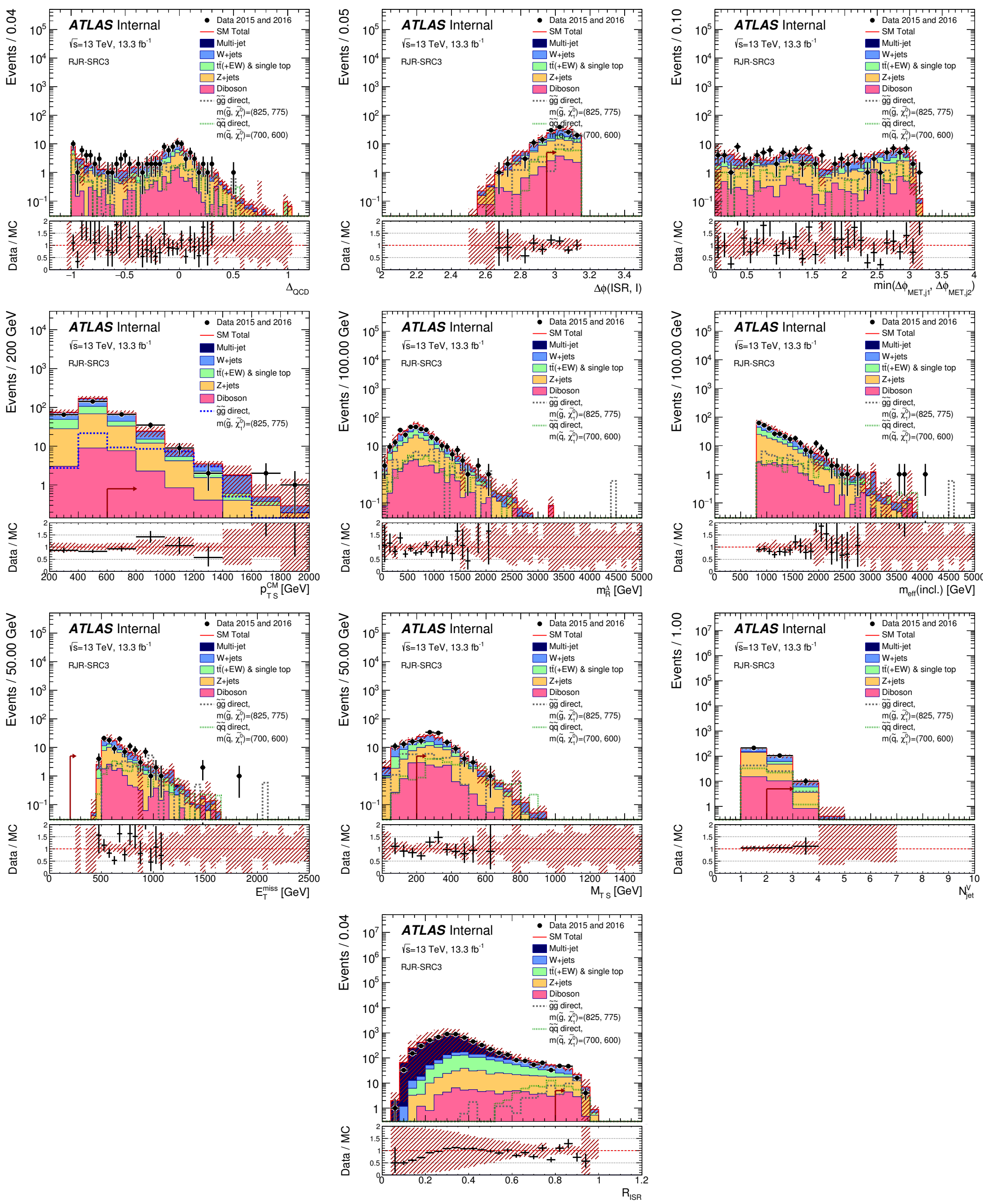
ATLAS Internal
√s=13 TeV, 13.3 fb⁻¹
RJR-SRC3
Data 2015 and 2016
SM Total
Multi-jet
W+jets
tt̄(+EW) & single top
Z+jets
Diboson
g̃g̃ direct, m(g̃, χ̃⁰₁)=(825, 775)
q̃q̃ direct, m(q̃, χ̃⁰₁)=(700, 600)
Data / MC
Events / 0.04
Δ_QCD
Events / 0.05
Δφ(ISR, I)
Events / 0.10
min(Δφ_MET,j1, Δφ_MET,j2)
Events / 200 GeV
p_TS^CM [GeV]
Events / 100.00 GeV
m_R^Λ [GeV]
m_eff(incl.) [GeV]
Events / 50.00 GeV
E_T^miss [GeV]
M_TS [GeV]
Events / 1.00
N_jet^V
R_ISR

Figure 3

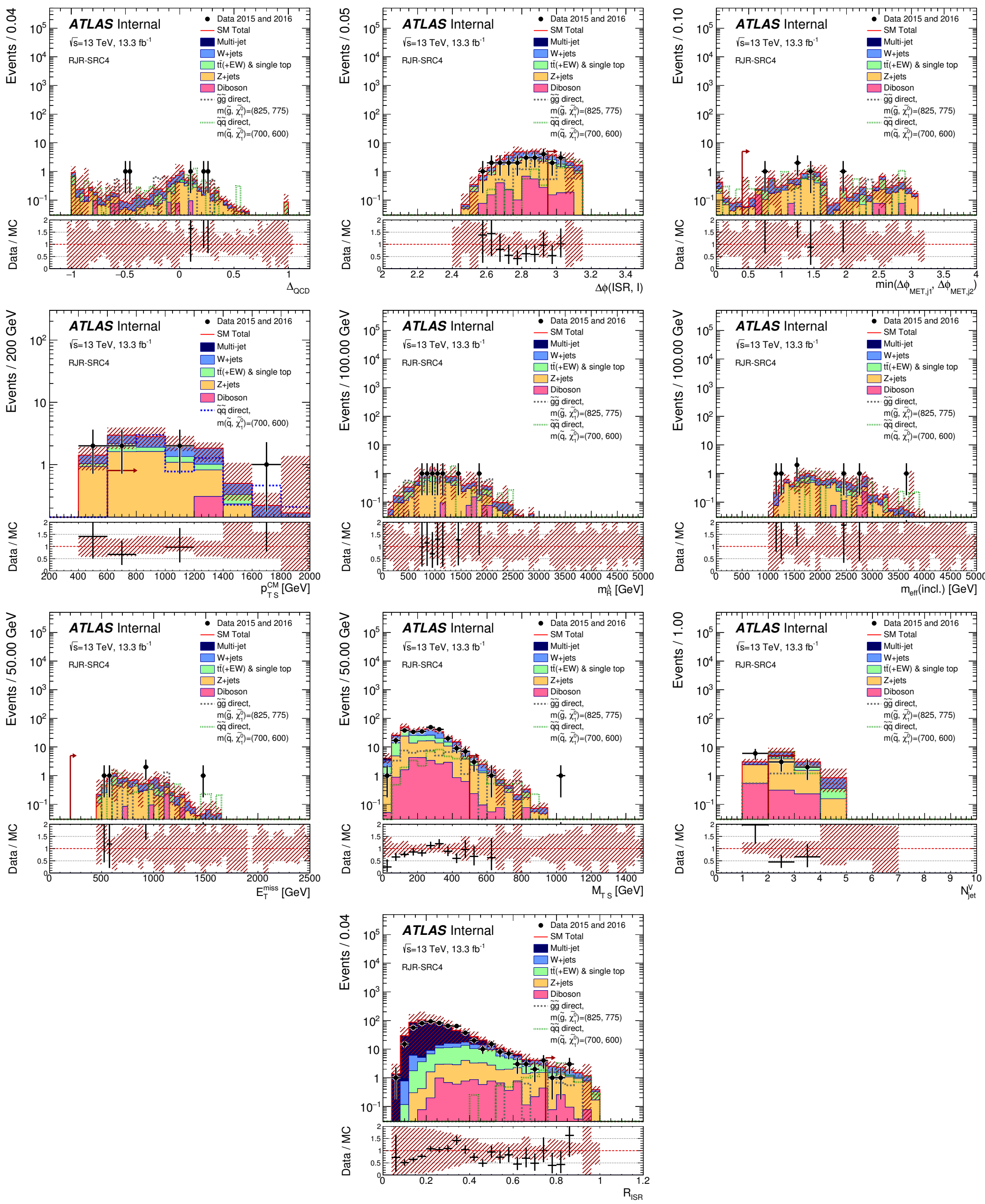
ATLAS Internal
√s=13 TeV, 13.3 fb⁻¹
RJR-SRC4
Data 2015 and 2016
SM Total
Multi-jet
W+jets
tt̄(+EW) & single top
Z+jets
Diboson
g̃g̃ direct, m(g̃, χ̃⁰₁)=(825, 775)
q̃q̃ direct, m(q̃, χ̃⁰₁)=(700, 600)
Data / MC
Events / 0.04
Events / 0.05
Events / 0.10
Events / 200 GeV
Events / 100.00 GeV
Events / 50.00 GeV
Events / 1.00
Δ_QCD
Δφ(ISR, I)
min(Δφ_MET,j1, Δφ_MET,j2)
p^CM_T S [GeV]
m^Λ_R [GeV]
m_eff(incl.) [GeV]
E^miss_T [GeV]
M_T S [GeV]
N^V_jet
R_ISR

Figure 4

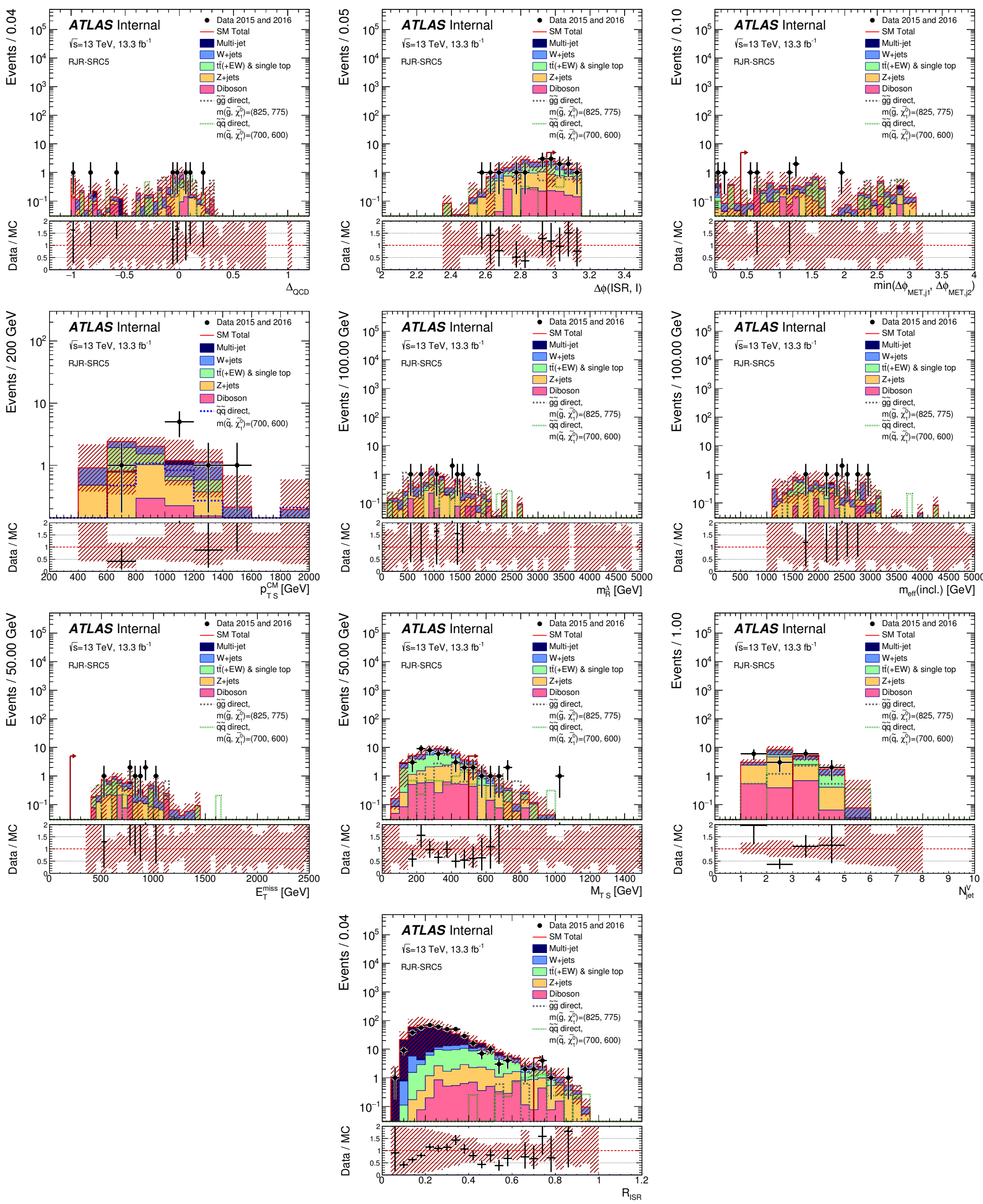

Figure 5

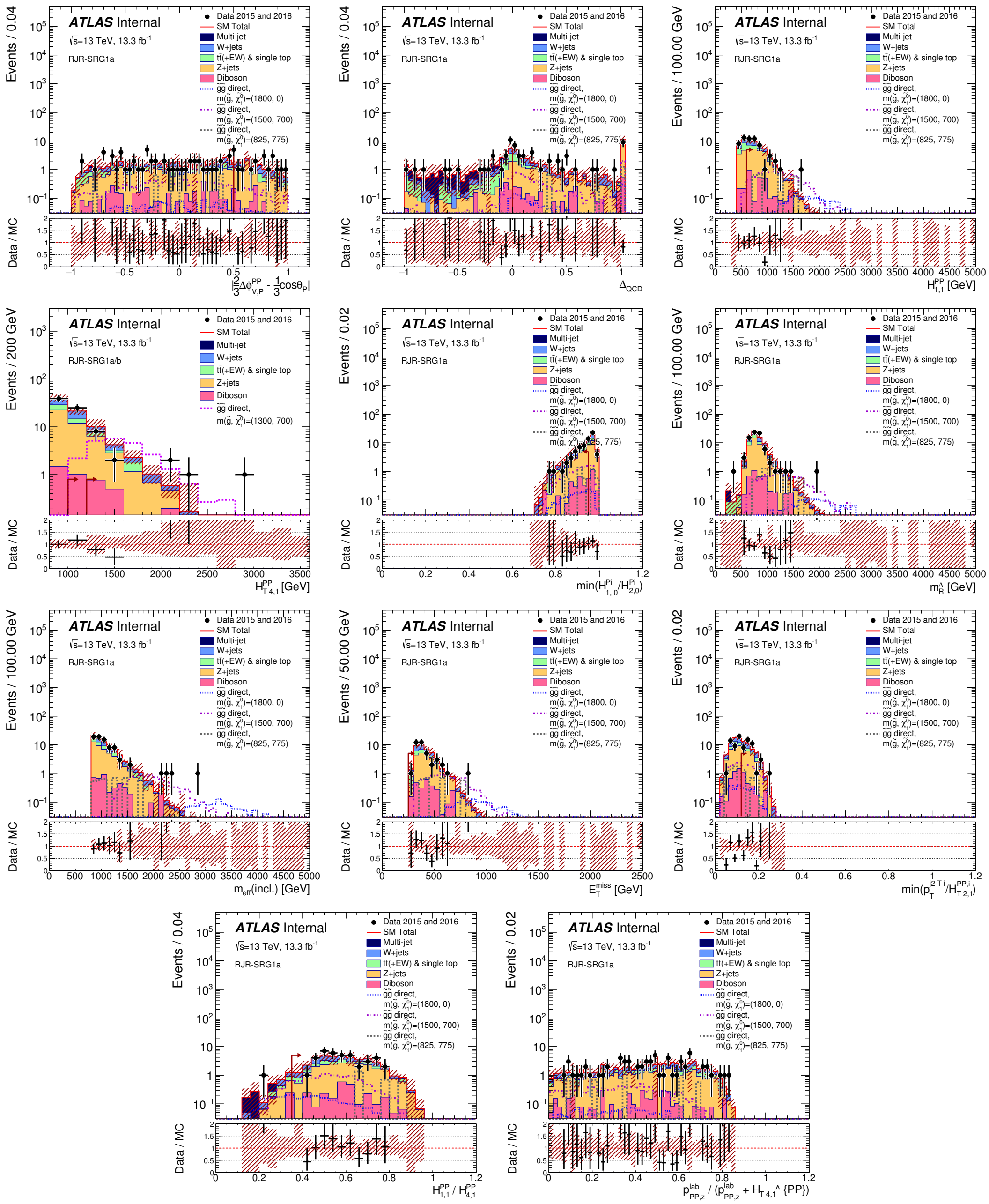

Figure 6

Figure 7

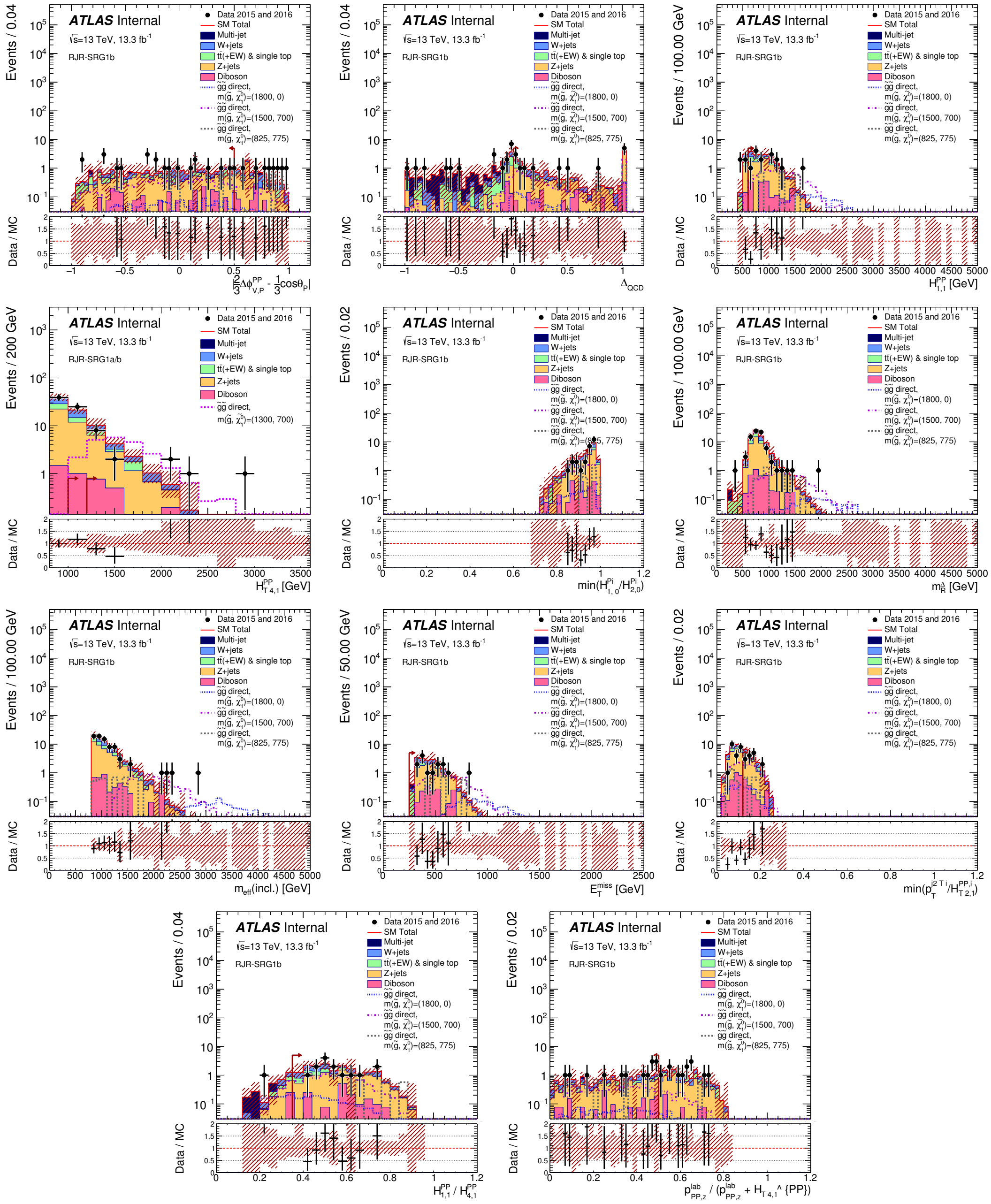
ATLAS Internal
√s=13 TeV, 13.3 fb⁻¹
RJR-SRG1b
RJR-SRG1a/b
Data 2015 and 2016
SM Total
Multi-jet
W+jets
tt̄(+EW) & single top
Z+jets
Diboson
g̃g̃ direct, m(g̃, χ̃₁⁰)=(1800, 0)
g̃g̃ direct, m(g̃, χ̃₁⁰)=(1500, 700)
g̃g̃ direct, m(g̃, χ̃₁⁰)=(825, 775)
g̃g̃ direct, m(g̃, χ̃₁⁰)=(1300, 700)
Events / 0.04
Events / 0.02
Events / 100.00 GeV
Events / 200 GeV
Events / 50.00 GeV
Data / MC
Δ_QCD
H^PP_1,1 [GeV]
H^PP_T 4,1 [GeV]
m^Λ_R [GeV]
m_eff(incl.) [GeV]
E^miss_T [GeV]
H^PP_1,1 / H^PP_4,1

Figure 8

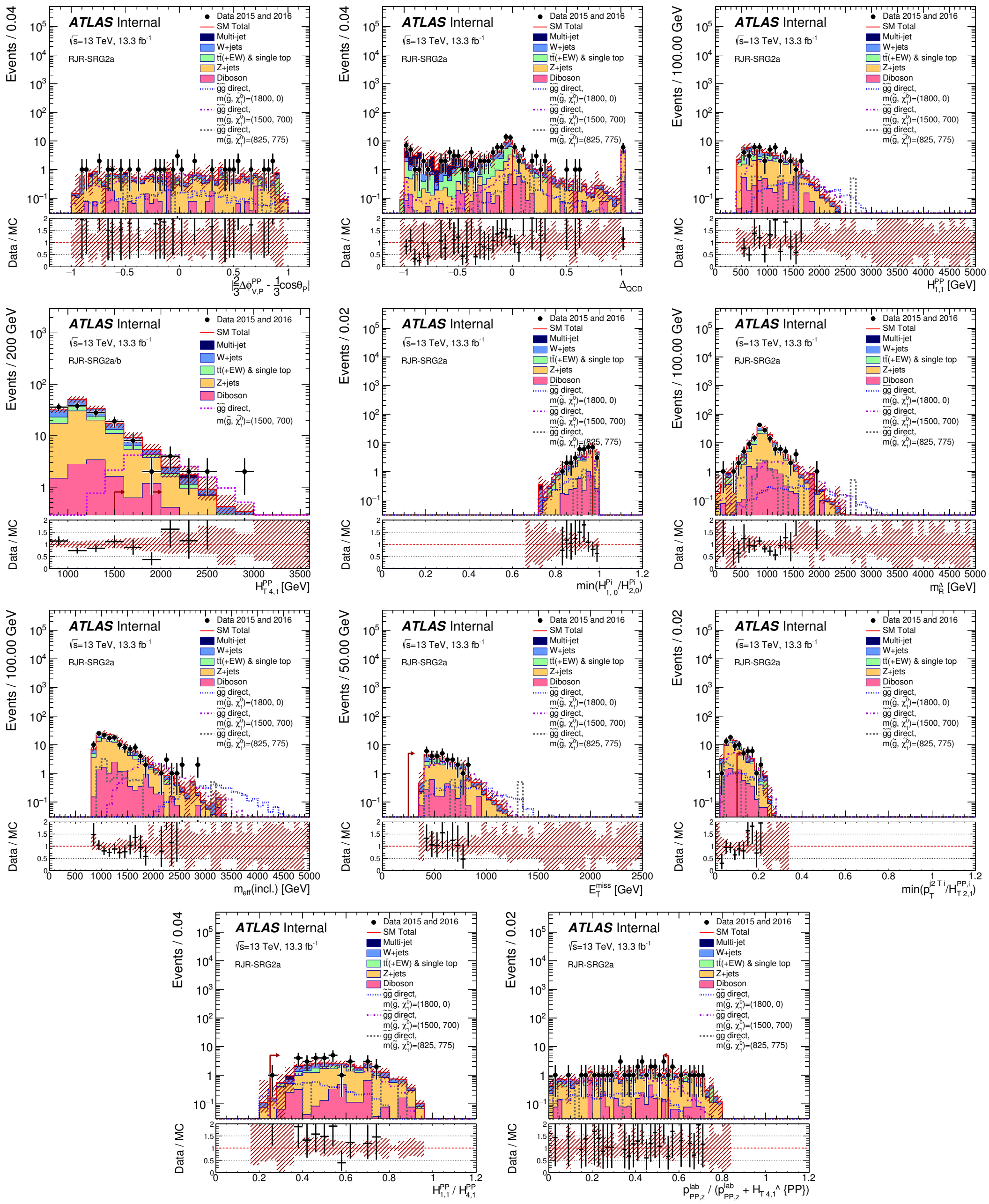

Figure 9

Figure 10

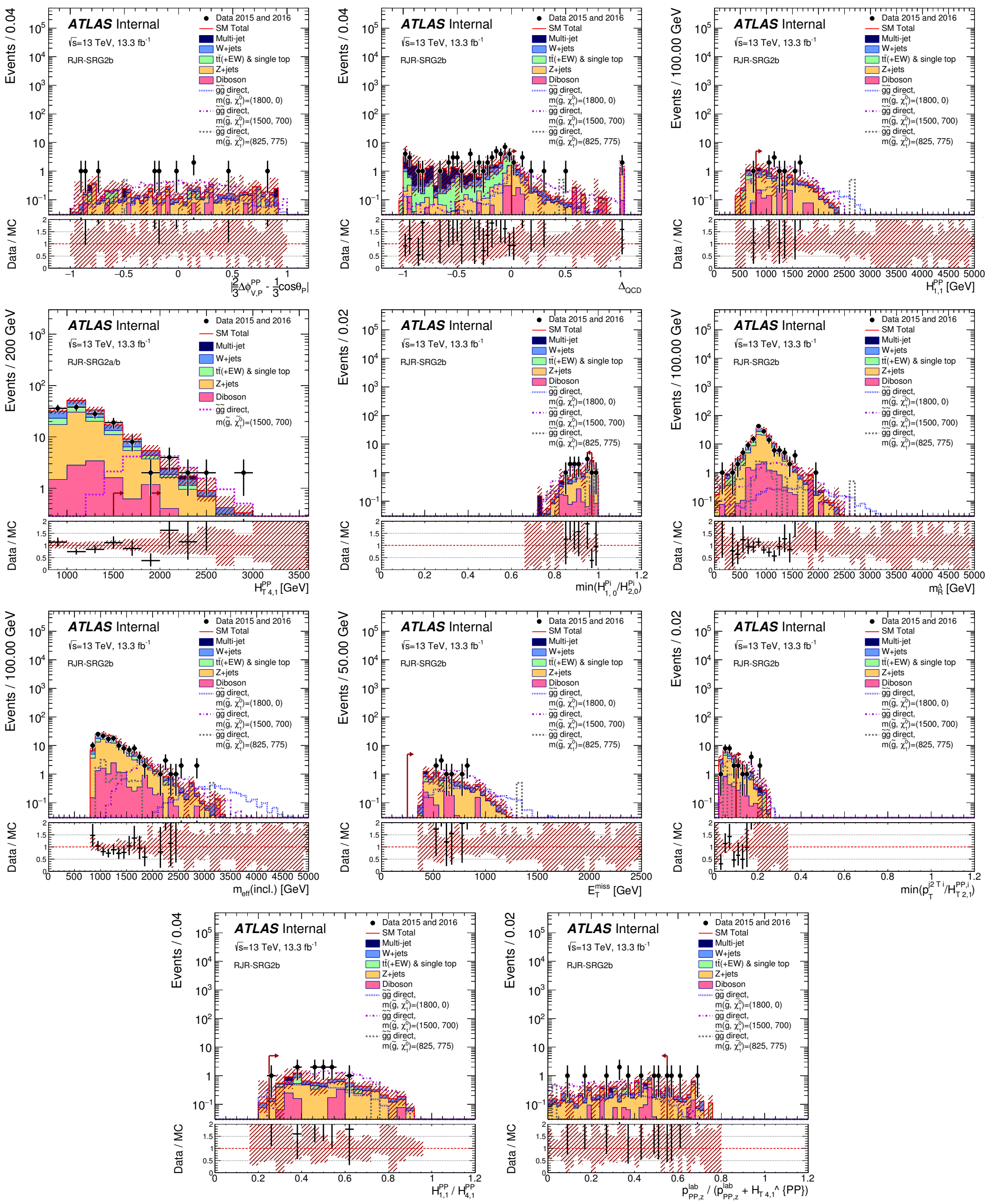
ATLAS Internal
√s=13 TeV, 13.3 fb⁻¹
RJR-SRG2b
RJR-SRG2a/b
Data 2015 and 2016
SM Total
Multi-jet
W+jets
tt̄(+EW) & single top
Z+jets
Diboson
g̃g̃ direct, m(g̃, χ̃₁⁰)=(1800, 0)
g̃g̃ direct, m(g̃, χ̃₁⁰)=(1500, 700)
g̃g̃ direct, m(g̃, χ̃₁⁰)=(825, 775)
Events / 0.04
Events / 100.00 GeV
Events / 200 GeV
Events / 0.02
Events / 50.00 GeV
Data / MC
Δ_QCD
H_{1,1}^{PP} [GeV]
H_{T 4,1}^{PP} [GeV]
m_{δ} [GeV]
m_eff(incl.) [GeV]
E_T^miss [GeV]
H_{1,1}^{PP} / H_{4,1}^{PP}

Figure 11

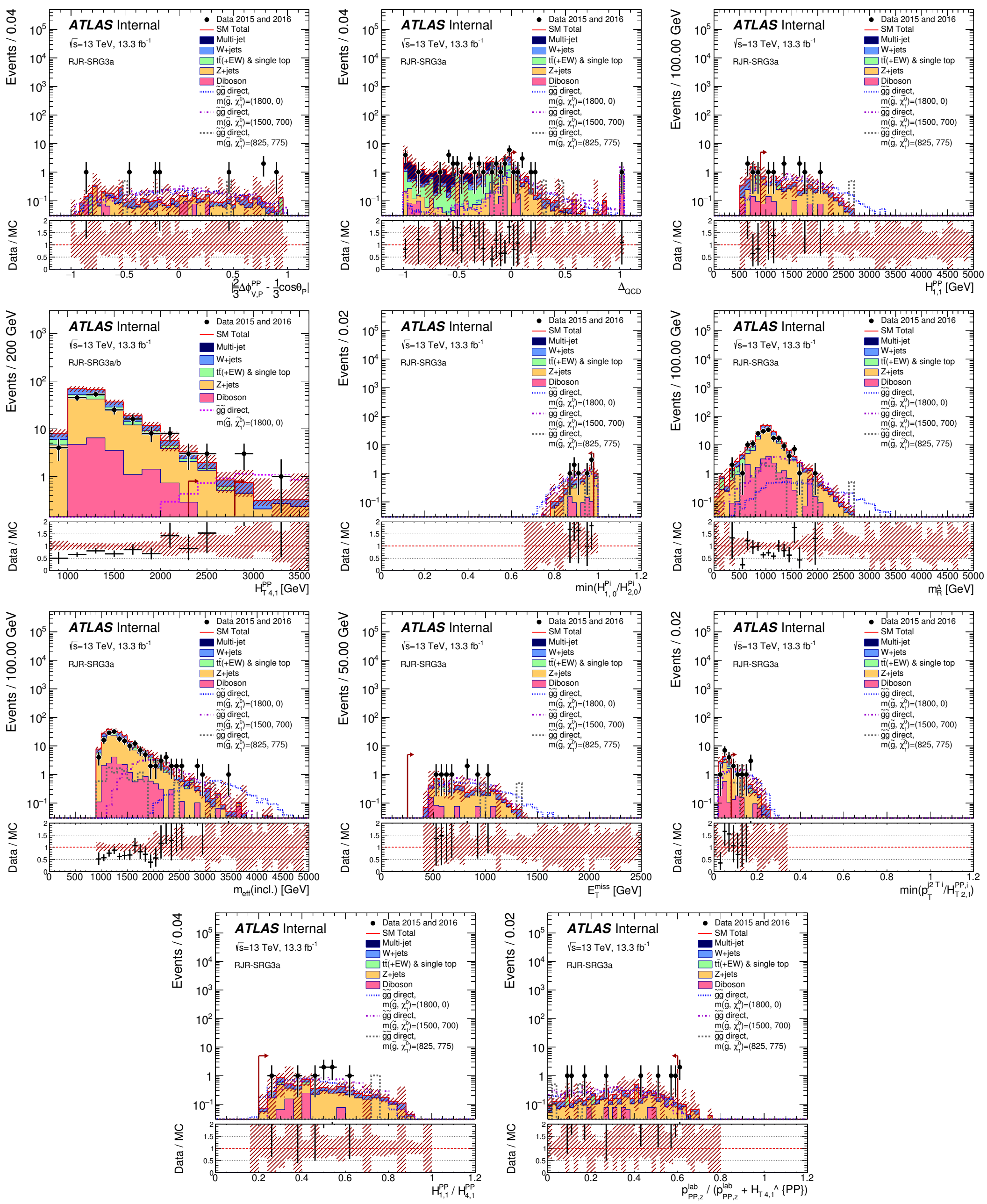

Figure 12

Figure 13

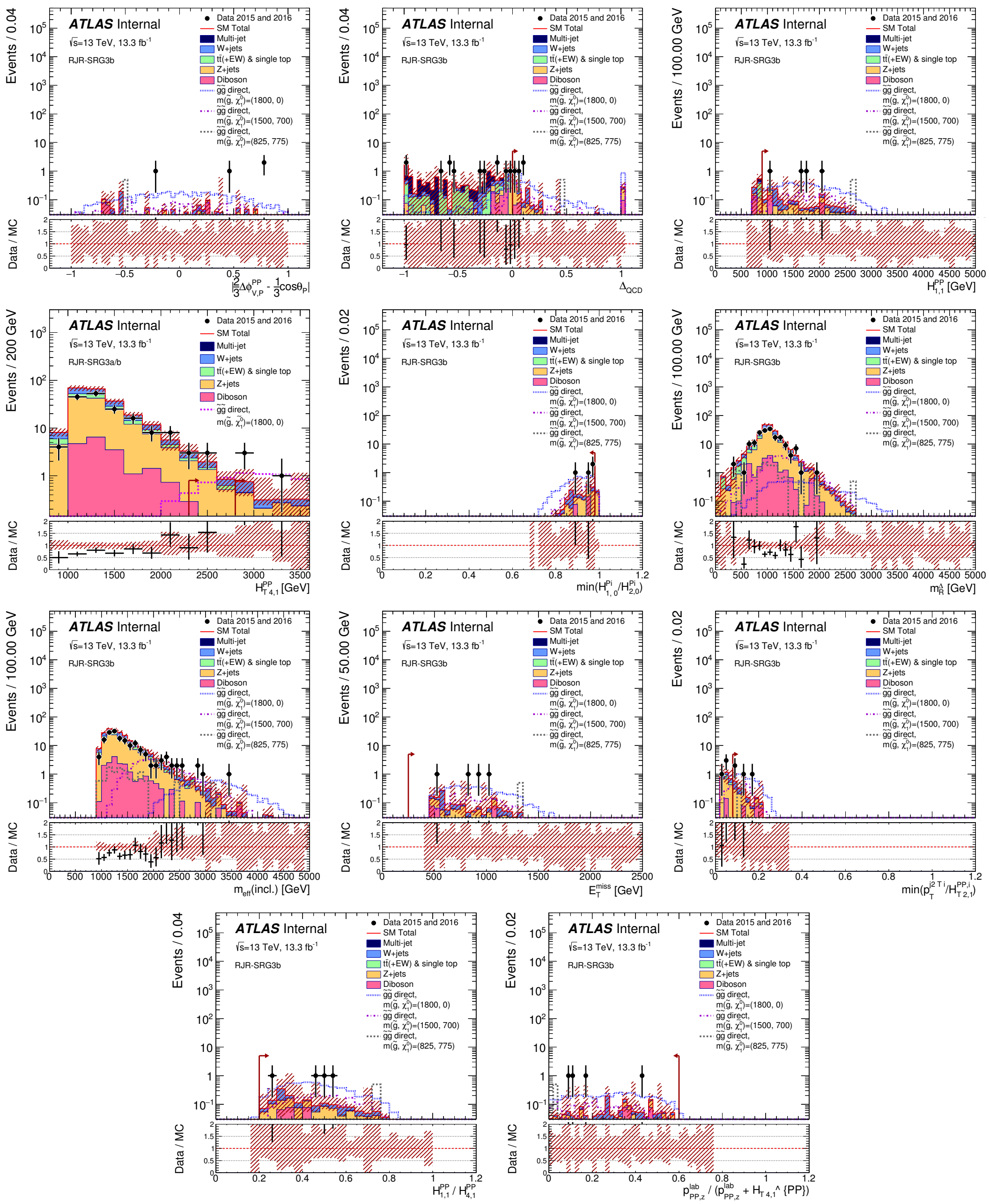

Figure 14

Figure 15

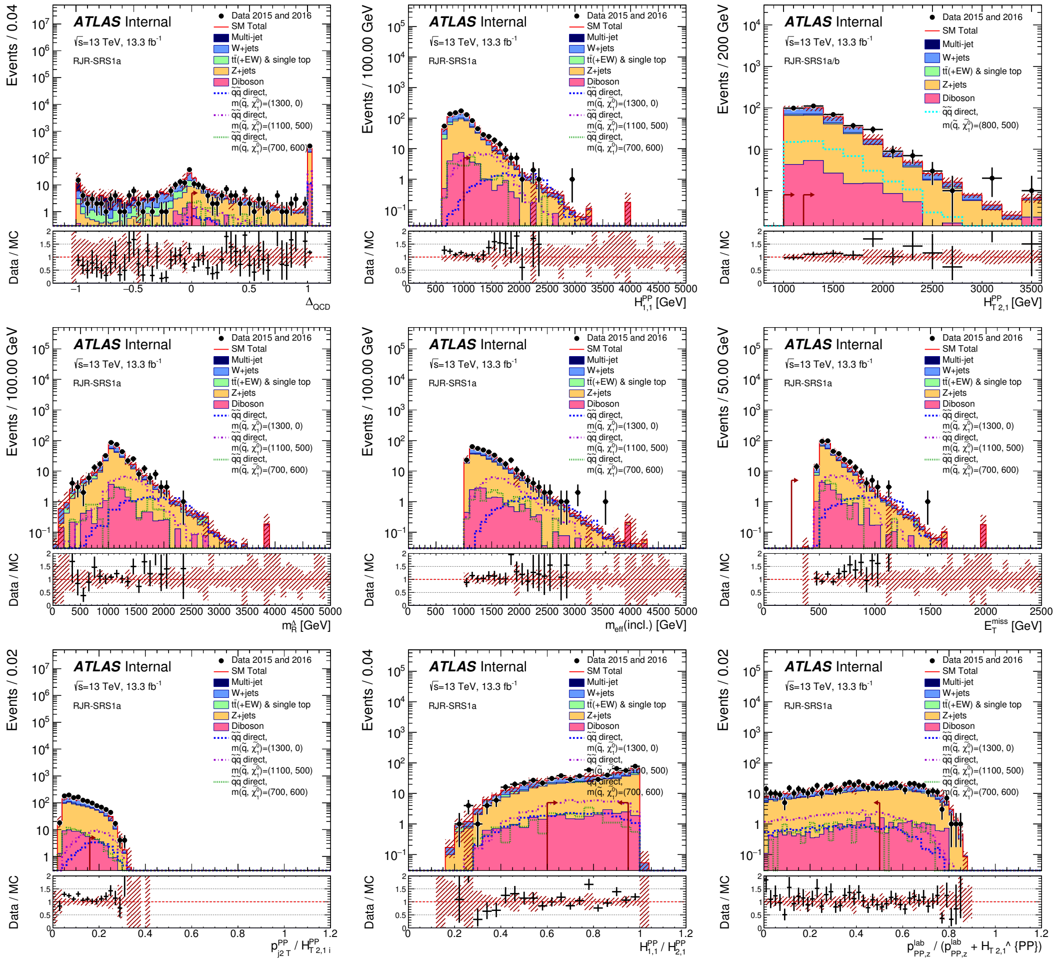

Figure 16

Figure 17

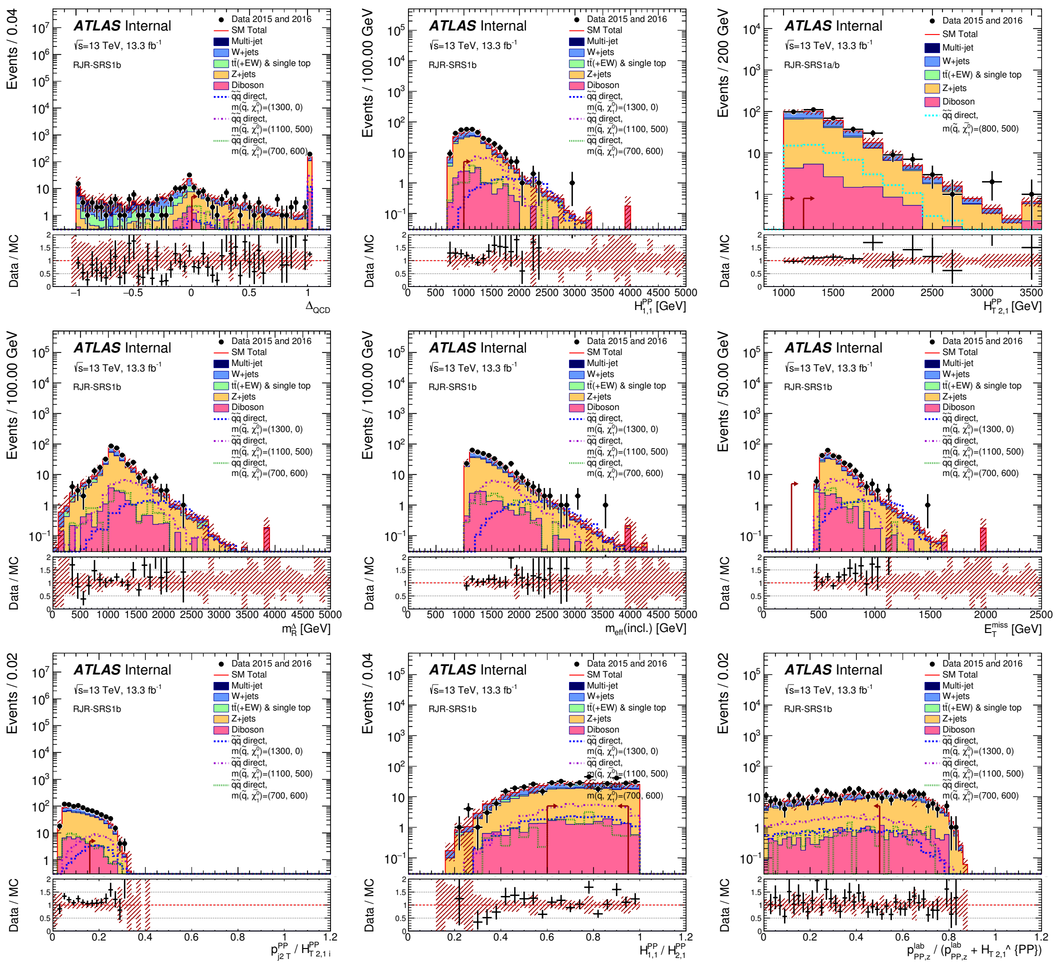
ATLAS Internal
√s=13 TeV, 13.3 fb⁻¹
RJR-SRS1b
RJR-SRS1a/b
Data 2015 and 2016
SM Total
Multi-jet
W+jets
tt̄(+EW) & single top
Z+jets
Diboson
q̃q̃ direct, m(q̃, χ̃₁⁰)=(1300, 0)
q̃q̃ direct, m(q̃, χ̃₁⁰)=(1100, 500)
q̃q̃ direct, m(q̃, χ̃₁⁰)=(700, 600)
q̃q̃ direct, m(q̃, χ̃₁⁰)=(800, 500)
Events / 0.04
Events / 100.00 GeV
Events / 200 GeV
Events / 50.00 GeV
Events / 0.02
Data / MC
Δ_QCD
H^PP_1,1 [GeV]
H^PP_T 2,1 [GeV]
m^Δ_R [GeV]
m_eff(incl.) [GeV]
E_T^miss [GeV]
p^PP_j2 T / H^PP_T 2,1 i
H^PP_1,1 / H^PP_2,1
p^lab_PP,z / (p^lab_PP,z + H_T 2,1^ {PP})

Figure 18

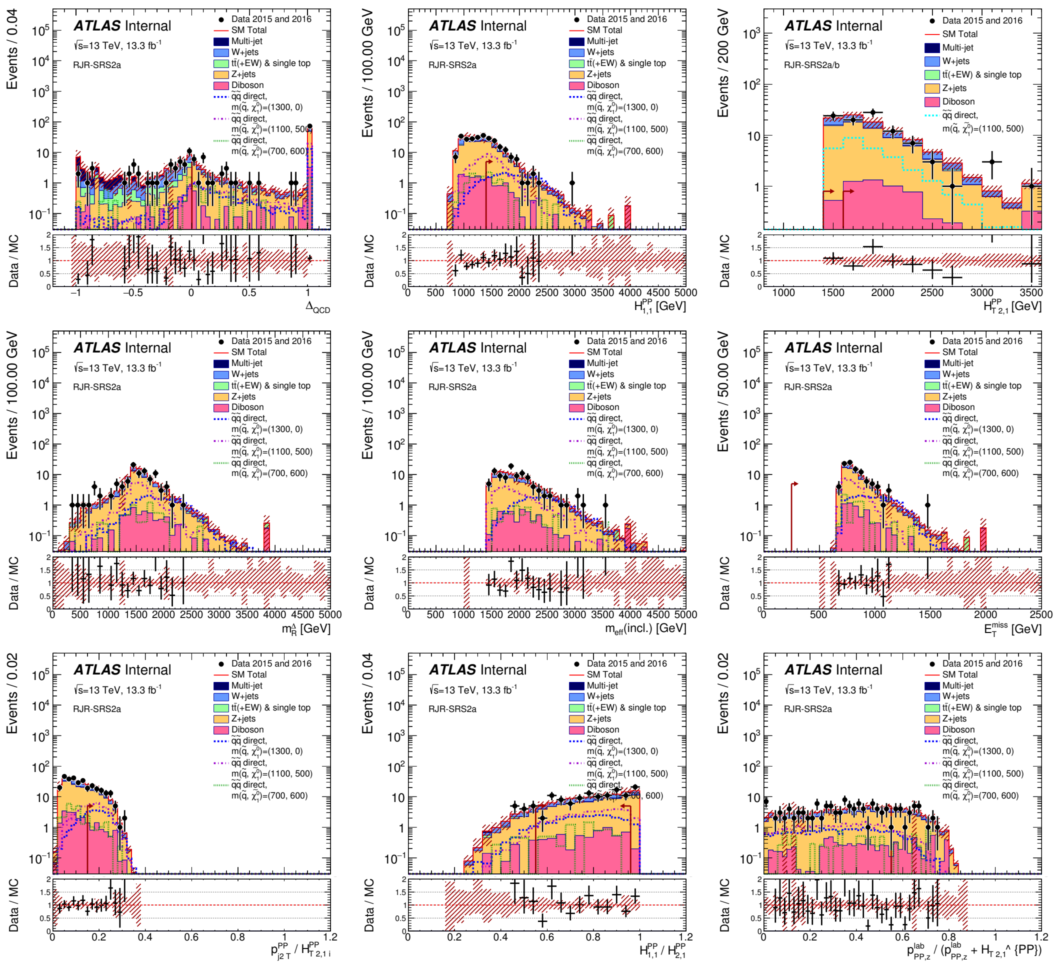
ATLAS Internal
√s=13 TeV, 13.3 fb⁻¹
RJR-SRS2a
RJR-SRS2a/b
Data 2015 and 2016
SM Total
Multi-jet
W+jets
tt̄(+EW) & single top
Z+jets
Diboson
Data / MC
Events / 0.04
Events / 100.00 GeV
Events / 200 GeV
Events / 50.00 GeV
Events / 0.02
Δ_QCD
H^PP_1,1 [GeV]
H^PP_T 2,1 [GeV]
m^Δ_R [GeV]
m_eff(incl.) [GeV]
E^miss_T [GeV]
H^PP_1,1 / H^PP_2,1

Figure 19

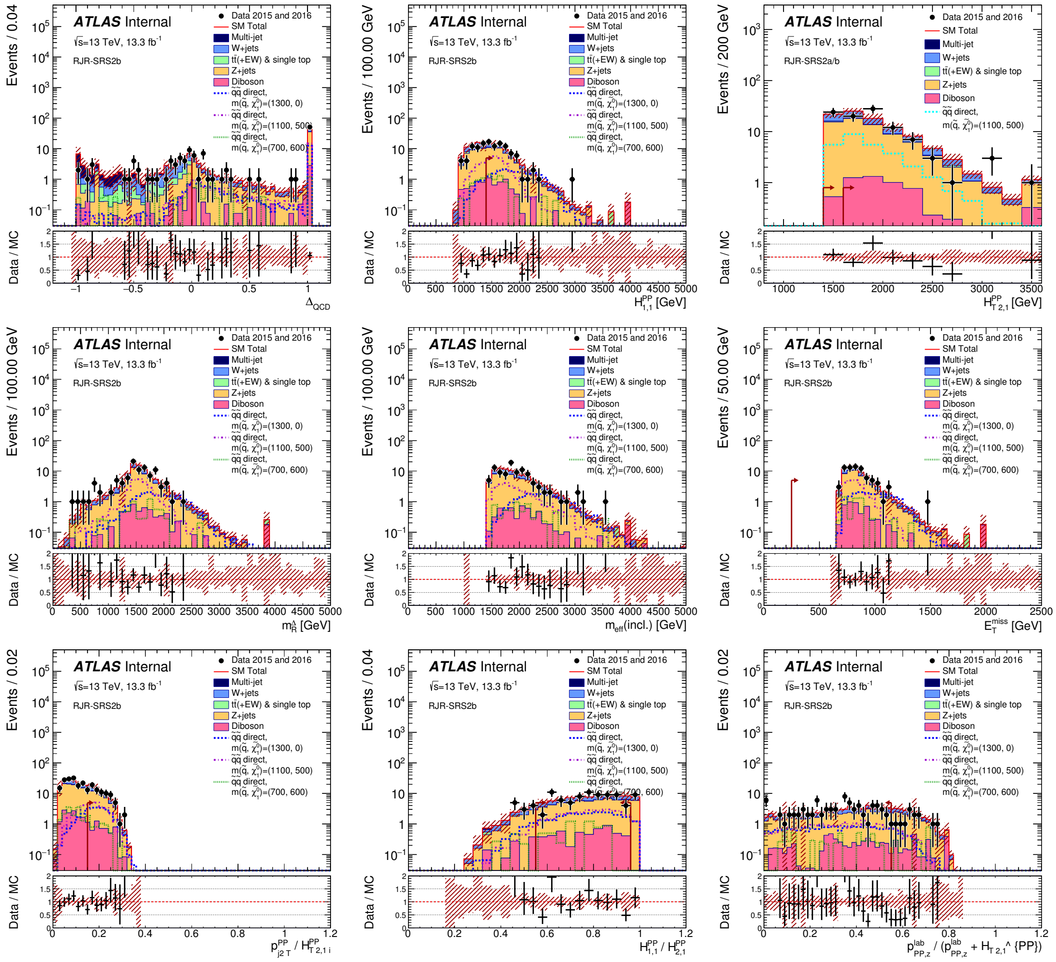

Figure 20

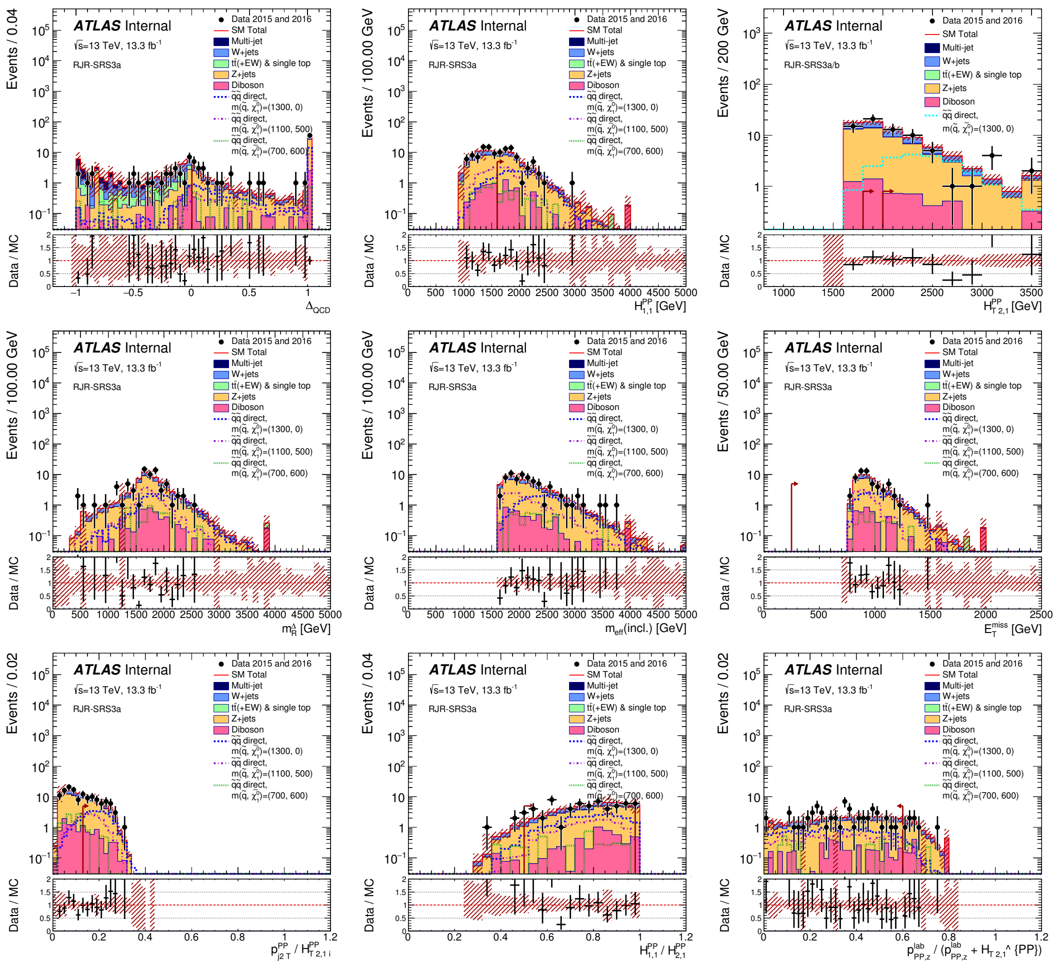

Figure 21

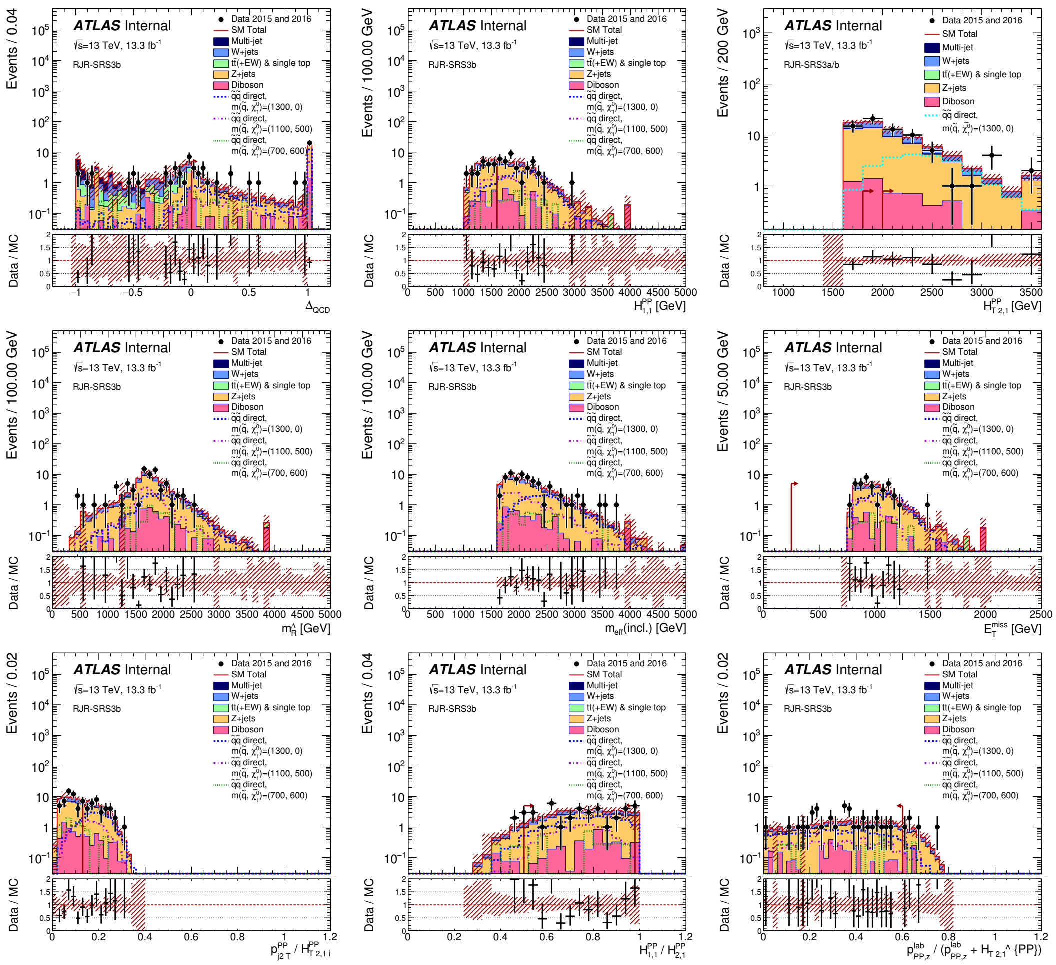

Figure 22